LASER/OPTICS TECHNIQUES

SUMMARY REPORT

Prepared For: National Aeronautics and Space Administration,
George C. Marshall Space Flight Center, Huntsville, Alabama

PERKIN-ELMER

PERKIN-ELMER

ELECTRO-OPTICAL DIVISION   NORWALK, CONNECTICUT

ENGINEERING REPORT NO. _____8387_____

LASER/OPTICS TECHNIQUES
SUMMARY REPORT

DATE: 29 APRIL 1966

PREPARED FOR: GEORGE C. MARSHALL SPACE FLIGHT CENTER

NATIONAL AERONAUTICS AND SPACE ADMINISTRATION

HUNTSVILLE, ALABAMA

Prepared by: _Morley S. Lipsett_
Morley S. Lipsett, Senior Physicist

Approvals: _H. Wischnia_
H. Wischnia, Sr. Staff Engineer

R. Crane
R. Crane, Jr., Advanced Technology Manager

PERKIN-ELMER

<u>Contributors</u>

M. S. Lipsett, Project Manager

R. J. Arguello

S. R. Habijanec

S. A. Myers

W. N. Peters

E. R. Schlesinger

D. T. Thompson

H. F. Wischnia

PRECEDING PAGE BLANK NOT FILMED.

TABLE OF CONTENTS

PRECEDING PAGE BLANK NOT FILMED,

TABLE OF CONTENTS (Continued)

LIST OF ILLUSTRATIONS

LIST OF ILLUSTRATIONS (Continued)

LIST OF ILLUSTRATIONS (Continued)

LIST OF ILLUSTRATIONS (Continued)

LIST OF ILLUSTRATIONS (Continued)

LIST OF ILLUSTRATIONS (Continued)

LIST OF ILLUSTRATIONS (Continued)

LIST OF TABLES

ABSTRACT

$3 5 2 4 5$

The subject of the present program (NAS8-20115) is laser and optical techniques applicable to future deep space optical communication systems. Analysis and laboratory work have been conducted in the following areas: stability of laser beam intensity distribution in the far field; remote boresight alignment of receiving and transmitting optical channels; isolation of the transmitter channel from the receiver channel; determination of a rotational coordinate reference system about the line of sight; and ways of implementing fine guidance tracking and pointing offset capabilities. Laboratory breadboard equipment which was developed as building blocks for this program is described, and a summary of project activities to date is presented. Fluctuations in the far field of a He-Ne laser are shown to be of insufficient magnitude to be detrimental to an optical communication link. Further, it is shown that, by special dielectric multilayer filter techniques, channel isolation of at least 115 db is readily achieved for the purpose of optical duplexing.

SECTION I

INTRODUCTION

The Laser/Optics Techniques Program is directed towards the goal of demonstrating the feasibility of high-channel-capacity deep space optical communications by providing the key techniques which will lead from laser promise to laser practice. The properties of lasers which substantiate this promise are well known; the high degree of spatial coherence, which makes for potentially tremendous antenna gain, and the extremely narrow optical bandwidth, which lends itself to narrow-band signal detection techniques. The present program was directed towards studying some of the principal factors influencing the design of a future spaceworthy optical communications system. As defined by MSFC Contract NAS8-20115 functioning hardware was developed while experimental and theoretical studies were carried out in the following areas: stability of laser beam intensity distribution in the far field; remote alignment of receiving and transmitting optical channels; isolation of the transmitter channel from the receiver channel; determination of a rotational coordinate reference system about the line of sight; and ways of implementing fine guidance beacon tracking and transmitter pointing offset capabilities.

The modus operandi of the laboratory work was to make direct measurements and gain experience with critical components of an actual breadboard optical communications system based on a 1/2 scale version of the OTS[1] configuration. The project breadboard was constructed from modular subsystems,

---

[1]Determination of Optical Technology Experiments for a Satellite (OTS) Phase I and II Reports, No. 7846 and 7924, Perkin-Elmer Corporation, 1964-1965, NASA Contract NAS8-11408.

PERKIN-ELMER

each of which was amenable in principle to eventual space qualification. As a corollary, the ground rule was imposed that the basic hardware shall be simple in concept so as to minimize the complexity of the entire system and to enhance its inherent reliability.

The breadboard employs a 16-inch aperture telescope which, together with other specially developed breadboard equipment, is capable of tracking a laser beacon and pointing a transmitted beam to within a fraction of its 0.3 arc-second diffraction spread. A helium-neon laser functions as the spaceborne transmitter. The guidance optics and detectors are designed with maximum sensitivity for use with a distant argon-laser beacon.

As in the original OTS design, the system employs the concept of optical duplexing, and requires an effective transmit channel to receive channel isolation of many decades. The required degree of isolation exceeds by a large factor the isolation capabilities of conventional microwave duplexing techniques. The question of whether it could be achieved in practice by optical techniques was one of the most important areas of investigation of the present program. Special dielectric multilayer techniques were developed which provided an affirmative answer.

The basic layout of the system under study is illustrated in Figure 1-1. The current status of each component is listed in Table 1-1. The tasks specified by the contractual work statement and described in this report are designated in Table 1-1 by an asterisk.
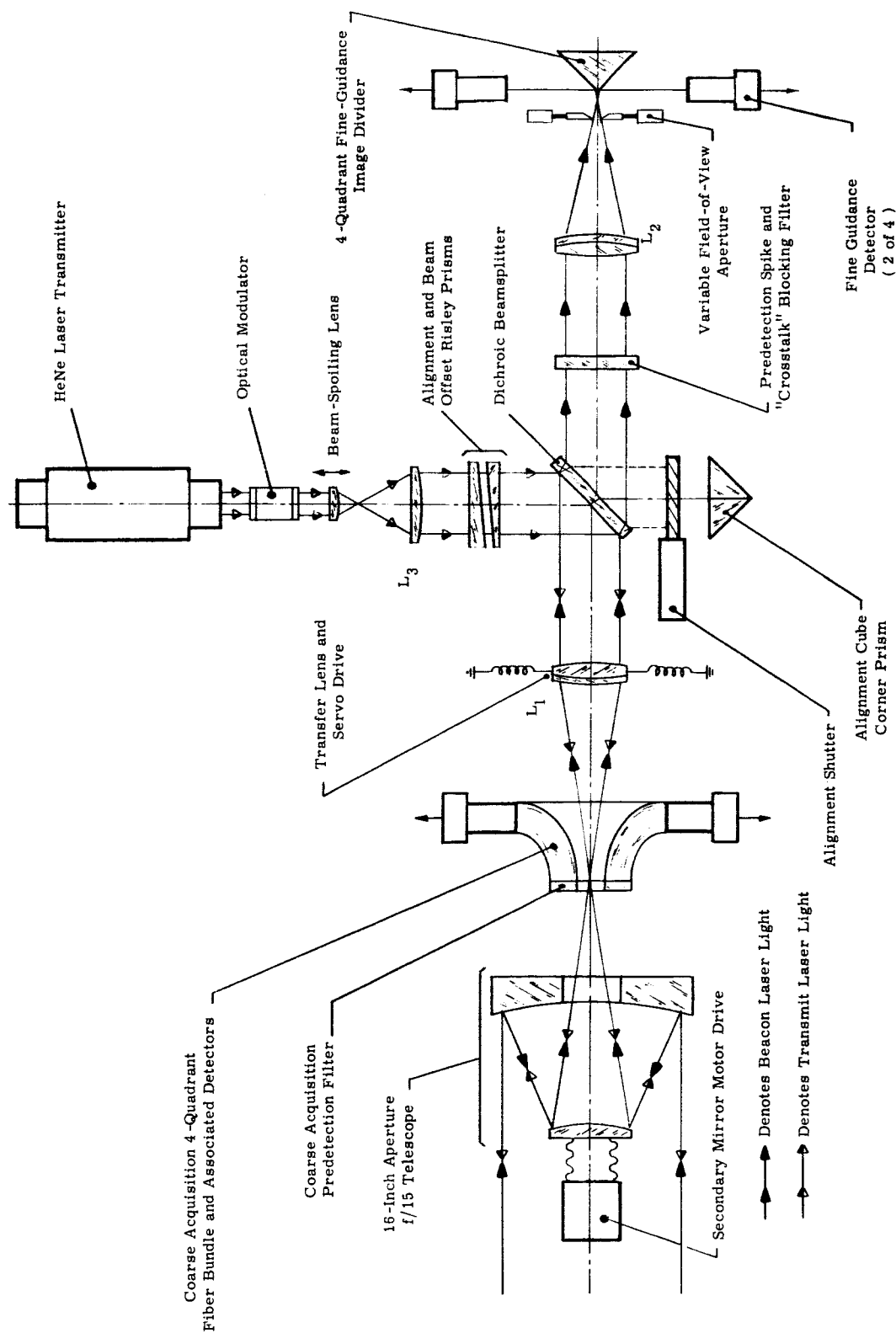
Figure 1-1. Layout of Basic Optical Communications System Hardware

TABLE I

STATUS OF CRITICAL HARDWARE

ITEM DESCRIPTION (Laser/Optics Techniques Tasks Designated By*)	STATUS
1.* Telescope "Front End"	Sixteen-inch diameter Cassegrain with motor driven focus control built for MSFC as breadboard hardware.
2. Coarse Acquisition Subsystem	Not yet breadboarded, but telescope provides for 1° coarse acquisition field.
3.* Image Transfer Optics	Designed and breadboarded — diffraction-limited 2-arc minute fine-guidance f.o.v. working at f/70.
4.* Transfer Lens Servo Drive	Designed, built and tested for MSFC as breadboard hardware. Specially designed for diffraction-limited laser-beacon tracking purposes.
5.* Techniques for Remote System Focusing Operations	Investigated. Principal conclusion that focus can be taken care of by secondary mirror motor drive and monitored by fine-guidance sensors when transfer-lens is dithered. Transfer lens servo electronics have provision for dither input and focal condition output.
6.* Dichroic Beamsplitter	Developed for breadboard. Present level of development: transmission to argon laser light is on the order of 85% and to helium-neon laser light is about 0.1%. (i.e., highly reflective at 6328Å) for 45° incidence.
7.* Channel Separation Techniques (elimination of transmitter crosstalk in receive channel)	115 db achieved in breadboard with special dielectric multilayers on mainly two optical elements: the beam-splitter and the pre-detection spike filter. Techniques can be used for more or less isolation as needed. 115 db is enough for ∼3 milliwatts of transmit laser light.
8.* Predetection Spike Filter	Transmit light blocking filter developed for use with spike. All dielectric spike with half bandwidth of 25Å incorporated into breadboard. Further development recommended to reduce bandwidth to 5Å and to lessen scattering effects.
9.* Fine-Guidance Image Position Sensor	Breadboarded with 4-quadrant optical image divider and four photomultipliers. Used with transfer lens servo drive and capable of diffraction limited tracking over 2 arc-minute f.o.v.
10. Variable Field-Of-View Aperture	Development recommended.
11.* Alignment and Beam Offset Techniques	Manual operation demonstrated with breadboard equipment. Equipment for remote operation (shutter, Risley Prisms, etc.) not yet added to breadboard.
12. Beam Spoiling Optics	Not breadboarded.
13.* RLOS Techniques	Studied for MSFC. Auxiliary subsystem indicated as best approach.
14. Optical Modulator	Not breadboarded.
15.* Transmit Laser Intensity Fluctuation in Far Field	Measured and found to be less than 1% and not a detrimental effect.

SECTION II

THE SYSTEM

2.1 GENERAL

Figure 1-1 was previously used to illustrate the principal elements of a 1/2 scale version of the OTS optical communications system. A 16-inch aperture telescope acts as the front end of the system and is used for both transmission of He-Ne laser light and reception of argon laser beacon light. A four-quadrant fiber bundle with a central aperture is shown located at the f/15 focus of this telescope. Its purpose is to divide the field of view into a 2-arc-minute fine guidance field (transmitted through the aperture) and a 1-degree coarse acquisition field (accepted by the outer annulus). Although the work to be described in this report mainly concerns the fine guidance field, the coarse acquisition field was not excluded from our consideration in the development of hardware for this project.

In Figure 1-1 the focal plane of the first lens, L_1, beyond the field dividing fiber bundle lies in the focal plane of the telescope. This produces a region of collimated light to the right of L_1 with an axial bundle diameter equal to the clear aperture of the telescope multiplied by the ratio of the focal length of L_1 to the effective focal length of the telescope.

The next item in the optical chain is a dichroic beamsplitter, designed for maximum reflectance at 6328Å and maximum transmission at 4880Å, and 5145Å. It produces two conjugate light paths as illustrated. This

arrangement is used to implement optical duplexing, although the details of obtaining adequate channel separation are somewhat more complicated and will be discussed in Section VI of this report.

Two additional lenses, L_2 and L_3, shown in Figure 1-1, form conjugate f/70 images at the apex of a fine-guidance image-divider prism and at an equivalent image of the transmit laser, respectively. The required point ahead function of the system is shown implemented by means of a pair of Risley prisms. Relative and joint rotation of these prisms accomplishes two-coordinate angular offset of the transmitted laser beam from the line of sight of the receive channel. A lateral translation of either laser lens would have an identical effect.

Telescope pointing errors are sensed by the fine-guidance image-divider and associated photomultipliers illustrated in Figure 1-1. The resulting error signals are used to close a feedback loop that causes an x-y servo drive to translate lens L_1 and reposition the beacon image on the apex of the image-dividing prism.

In this way, the system can point at and track an earth beacon to within the diffraction limit of the telescope. Since the transmit channel is conjugate to the receive channel, the light transmitted back to earth is constrained to point and track to the same accuracy.

A rotational reference about the line of sight (RLOS reference) is a required input for the transmit beam offset subsystem indicated in Figure 1-1 Ways of obtaining this reference were investigated in the present program and the results are discussed in detail in Section IV of this report.

This completes a cursory view of the system. Details of the actual breadboard hardware developed for this work are given in Section III, where some specific system tolerances are dealt with in context. Other system tolerances enter into the discussion of alignment and point ahead techniques given in Section VII.

SECTION III

LABORATORY PROCEDURES AND EQUIPMENT

3.1 INTRODUCTION

Because of the wide variety of laboratory investigations planned for this program, it was necessary to have ready access to an entire breadboard optical communication system, to individual subsystems and even to separate components. A modular approach was therefore adopted for equipment design.

First, the basic system parameters were established. These are summarized in Table 3-1. Then, all of the hardware, including such major subsystems as the 16-inch aperture telescope, was designed as a set of detachable subassemblies, each of which could be fastened anywhere on the surface of a 3 foot by 6 foot steel optical bench. A typical arrangement is illustrated in Figure 3-1.

Small components, such as filters and beamsplitters were attached to magnetic bases which could be slid into position and locked firmly in place magnetically. Critical components such as transfer lenses were held and adjusted by three-axis micropositioners bolted to the optical bench. Examples of the former device are illustrated in Figure 3-2; an example of the latter is illustrated in Figure 3-3.

As a result of this approach, within wide latitude the equipment could be positioned in any configuration dictated by the requirements of a particular experiment.

TABLE 3-1

SYSTEM PARAMETERS	
Clear Aperture of Main Telescope	16 inches
f-number of Primary Mirror	f/3
Secondary Magnification	5X
Location of f/15 Focal Plane	7 inches behind vertex of primary mirror.
Field of View for Coarse Acquisition	1 degree
Fine-Guidance Field of View	2 minutes
Magnification of Image Transfer Optics (Resulting in Final f/70 Image)	4.67X
Diameter of 2-Minute Field at f/15	0.14 inch
Diameter of 2-Minute Field at f/70	0.65 inch
Diameter of 1-degree Field at f/15	4-1/16 inches
Operating Wavelengths	6328Å, 4880Å, and 5145Å
Image Quality	Diffraction-limited pointing and tracking capability over central 2-minute field.
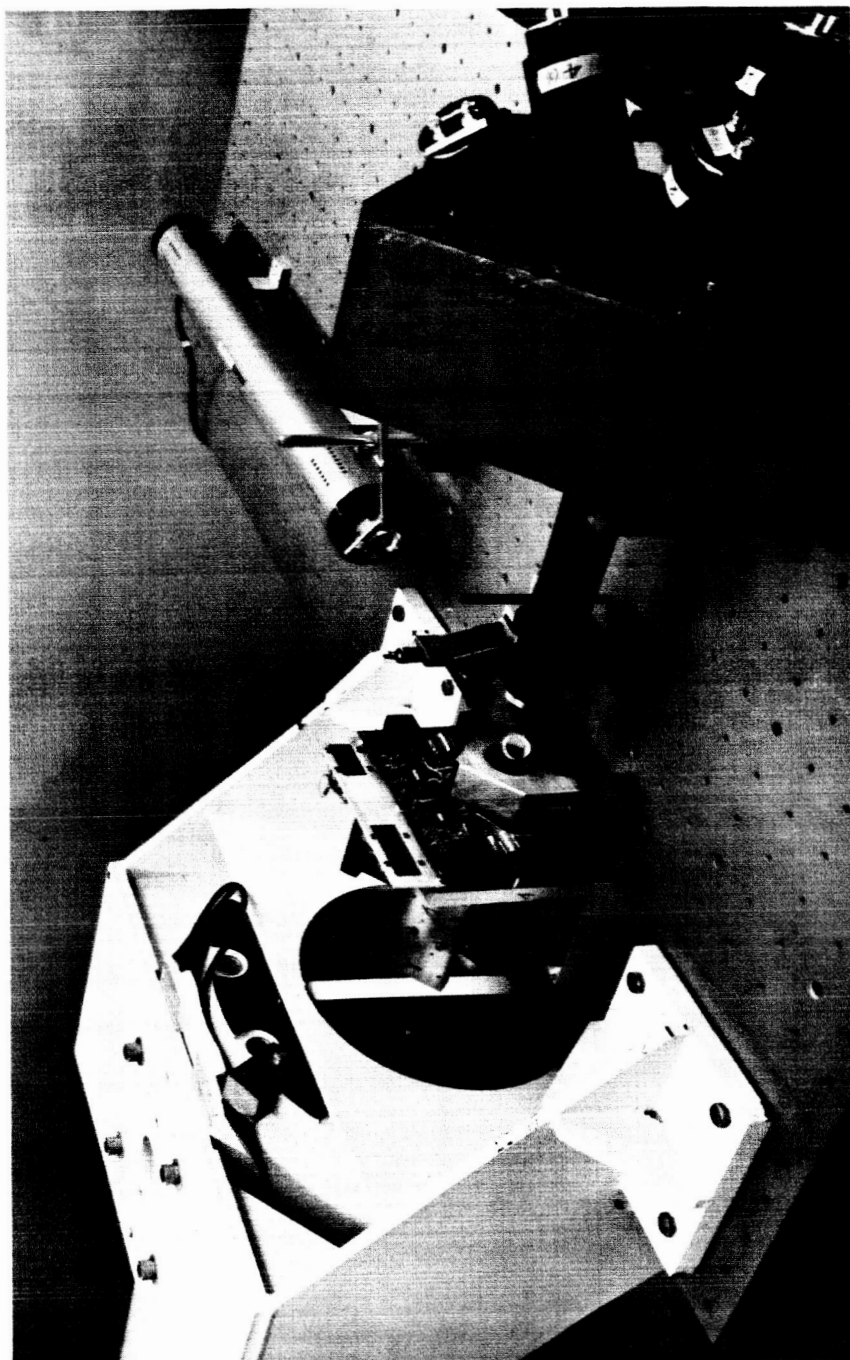
Figure 3-1. Typical Arrangement of Experimental Breadboard Equipment
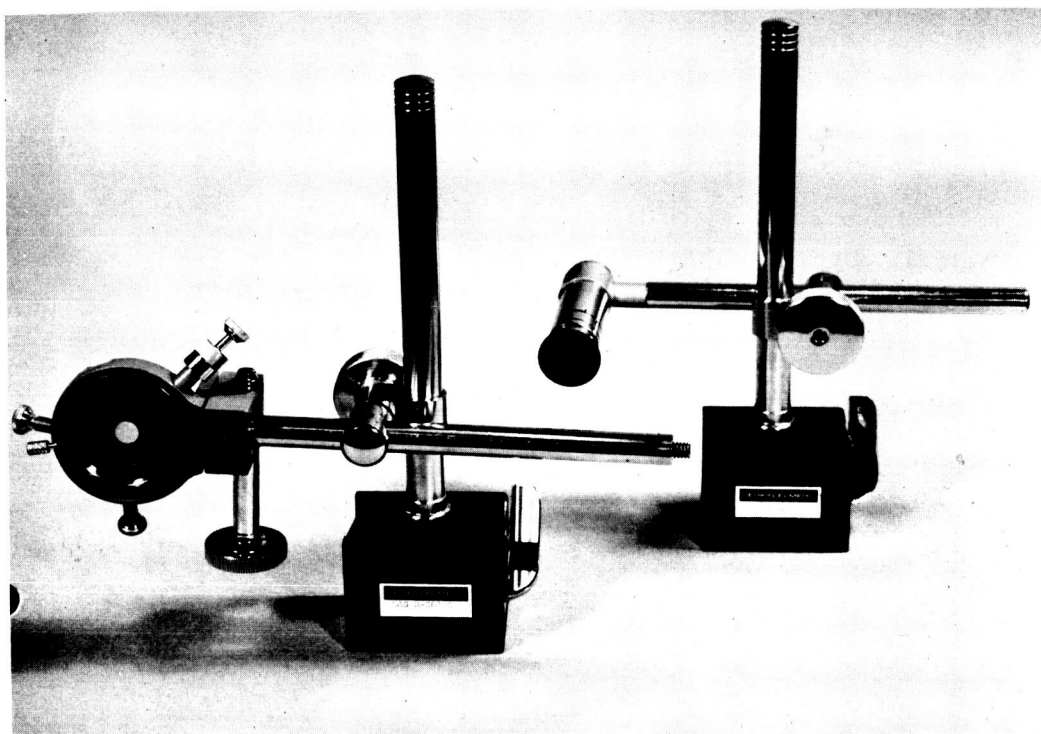
Figure 3-2. Component Fixtures Held by
             Magnetic Clamps
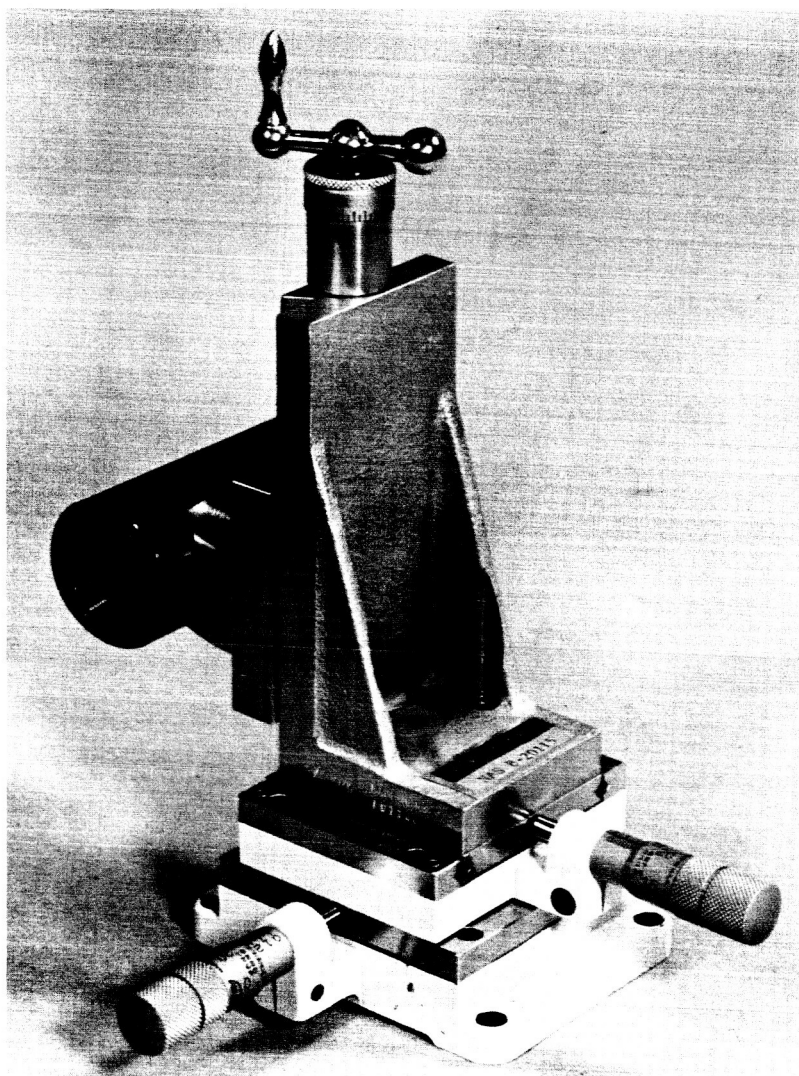
Figure 3-3.   Lens Cell Held in
              Three-Axis Micropositioner

3.2 TELESCOPE OPTICS

The project breadboard uses a Cassegrain form of telescope with a 16-inch diameter f/3 paraboloidal primary mirror. This choice of form was based on somewhat conflicting optical and manufacturing requirements. The optical requirements are for 1/10 arc-second rms tracking accuracy over the central 2-minute fine-guidance field, and reasonably good imagery over a full 1-degree field. The manufacturing requirements are for mirror shapes that are readily tested and are capable of being made scatter-free.

Computer-aided design calculations showed that diffraction-limited performance is attainable over the fine-guidance field whether the main telescope be an f/15 Dall-Kirkham (ellipsoidal primary, spherical secondary) Ritchey-Chretien (hyperboloid-hyperboloid) or classical Cassegrain (paraboloid-hyperboloid). The Dall-Kirkham, however, could be ruled out for reasons of having excessively bad wide-field performance for coarse acquisition, despite the manufacturing simplification inherent in a spheroidal secondary.

Assuming similar design parameters (i.e., f-number of primary, location of conjugates of secondary, etc.), it turned out that the difference between a Cassegrain and Ritchey-Chretien is almost academic. As shown in Figure 3-4, the hyperboloidal Ritchey-Chretien primary mirror is within $\lambda/8$ of a true paraboloid over the central 11.2-inch aperture and is within about $\lambda/2$ over the full 16-inch aperture. This departure makes for somewhat better off-axis performance of the Ritchey-Chretien design, but the improvement is not worth the additional manufacturing steps entailed.
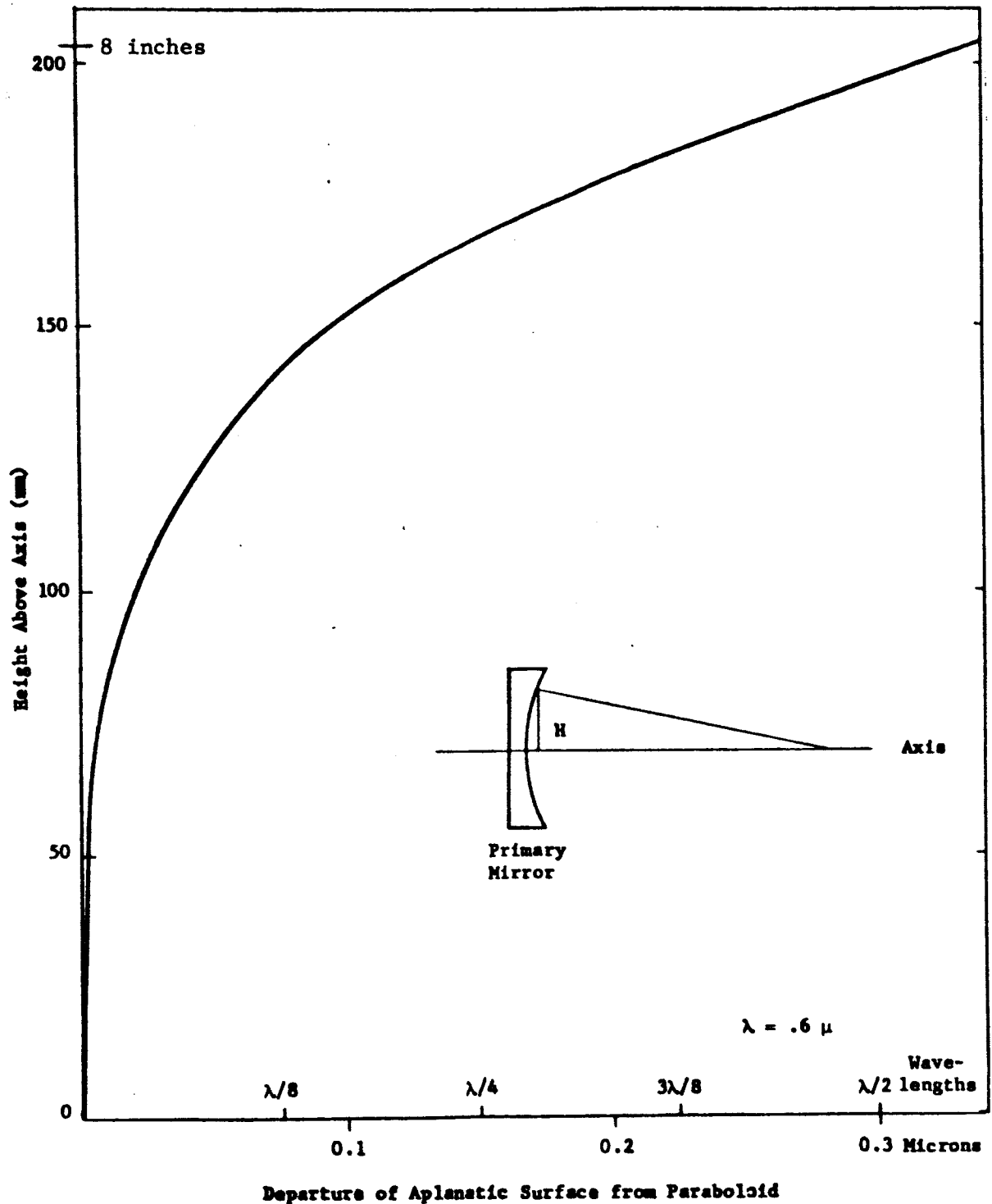
Figure 3-4. Plot of Departure of Aplanatic Primary Mirror Surface
            From Paraboloid. The Aplanatic Surface is Slightly
            Shallower than the Paraboloid.

It was therefore decided to manufacture the Cassegrainian design, but to use system correction to optimize the figure of the secondary mirror with respect to the primary.

System correction is the final manufacturing operation of the telescope mirrors. Mounted in their correct supports, the fused silica primary and secondary mirrors are tested together as a working telescope. To the extent indicated by these tests, the secondary mirror is withdrawn and its surface figure corrected until the mirrors perform to adequate precision in combination.

It was necessary to have a sufficiently large hole in the primary mirror to accommodate the 1-degree coarse acquisition field. This had the desirable consequence of conveniently allowing for center mounting of the primary mirror, which, for the dimensions used, is an ideal way of obtaining rigid mirror support and maximum figure stability.

As part of the optical design, it was important to bear in mind that sky shields (light baffles) are needed to exclude light from outside the 1-degree field in the focal plane of the telescope. The sky shielding of Cassegrain-type telescopes usually requires a compromise between the size of the protected field and the size of the field unvignetted by the baffles. We were fortunate in that our particular design obtained a 4-1/16 inch diameter (1 degree) shielded field and a 4 inch diameter completely unvignetted field. The baffle at the secondary mirror blocks very little more of the central area of the primary mirror than is required in any event by its hole and mirror support.

The design results in a total unobstructed area of 80 percent of the primary mirror. A layout of the telescope optics is shown in Figure 3-5 which illustrates that the telescope is focused by an axial translation of the secondary mirror.

Highly annealed mirror quality fused silica was decided on for the telescope mirrors in order to ensure minimum surface scatter and maximum figure accuracy.

3.3 TELESCOPE STRUCTURE

Center mounting of the primary mirror was accomplished by the telescope structure illustrated in cross section in Figure 3-6. This structure was adapted for the project breadboard by Boller and Chivens, Inc. (Astro-Optical Division, Perkin-Elmer) from a standard and very successful design for an observatory telescope. The rear of the actual structure is shown in the upper left of Figure 3-1. A front view is shown in Figure 3-7.

The secondary mirror is supported at the end of a remote focusing drive assembly, visible in the center foreground of Figure 3-7, which is electrically driven and imparts an extremely fine control over the telescope focus without otherwise affecting the mirror alignment.

3.4 IMAGE TRANSFER OPTICS

The image transfer optics were designed in accordance with the basic layout shown in Figure 2-1. It was specified that the design be

PERKIN-ELMER

Figure 3-5. Layout of 16-Inch Aperture Telescope Optics

PRIMARY MIRROR:

Clear Aperture —— 16" Diameter
Focal Length —— 48" ± 1/2

SECONDARY MIRROR:

Clear Aperture —— 3.71
Focal Length —— 11.46
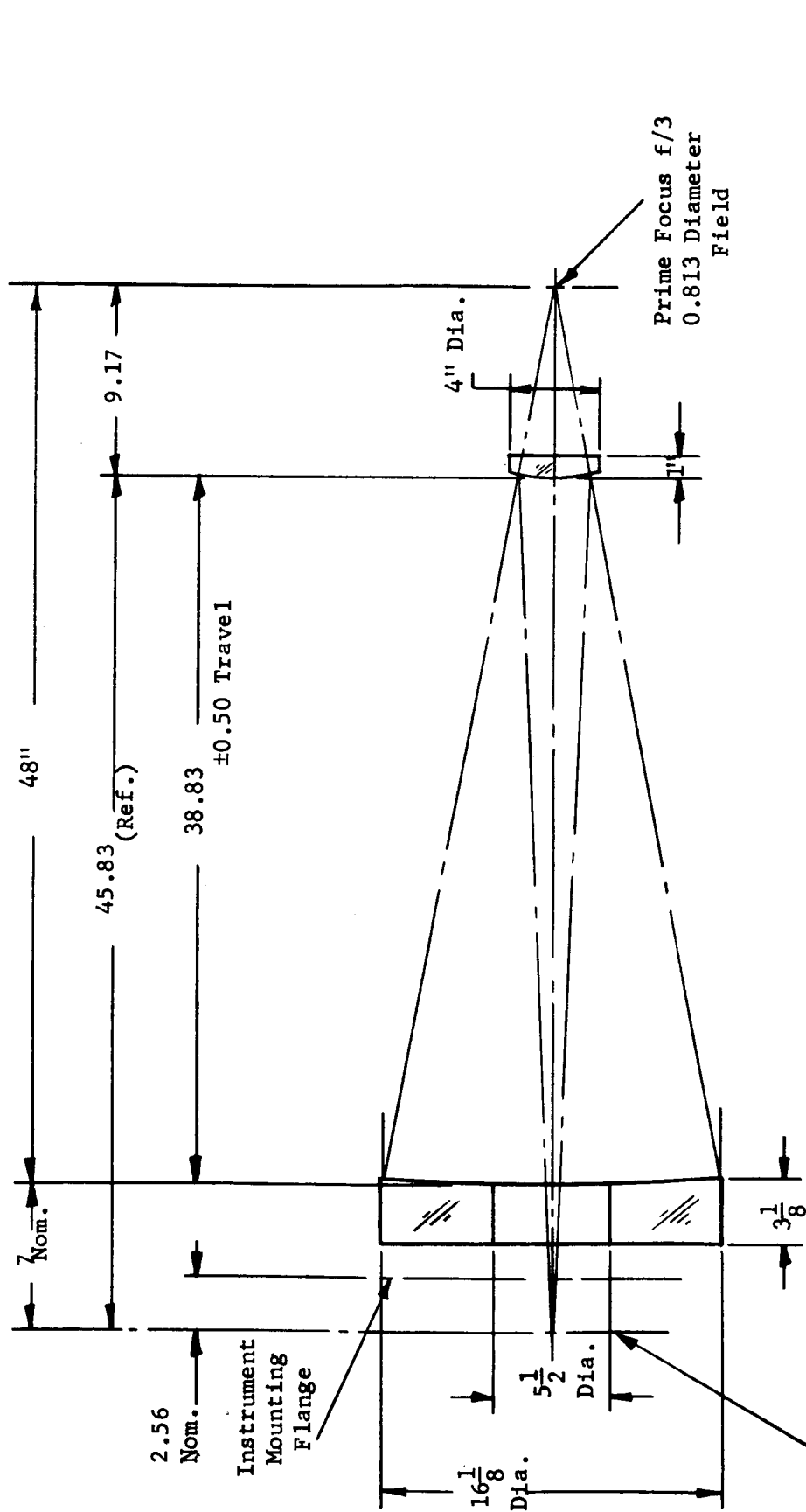
CASSEGRAIN FOCUS:

f/15
4" Diameter Unvignetted Field
$4\frac{1}{16}$ Diameter Protected Field

F.L. = 240"

Prime Focus f/3
0.813 Diameter Field
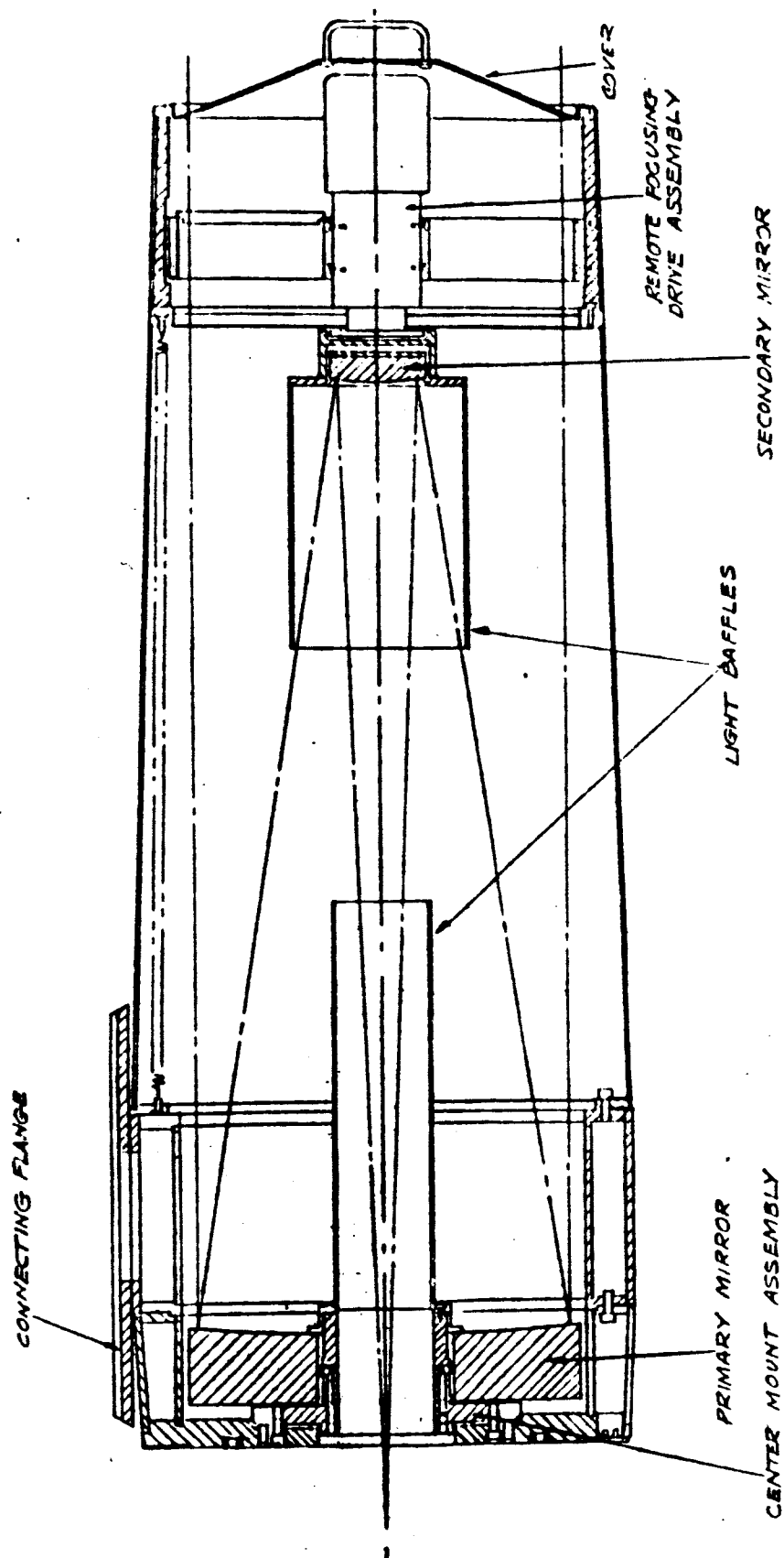
Figure 3-6. Drawing of the 16-Inch Aperture Laser/Optics Techniques Telescope Structure
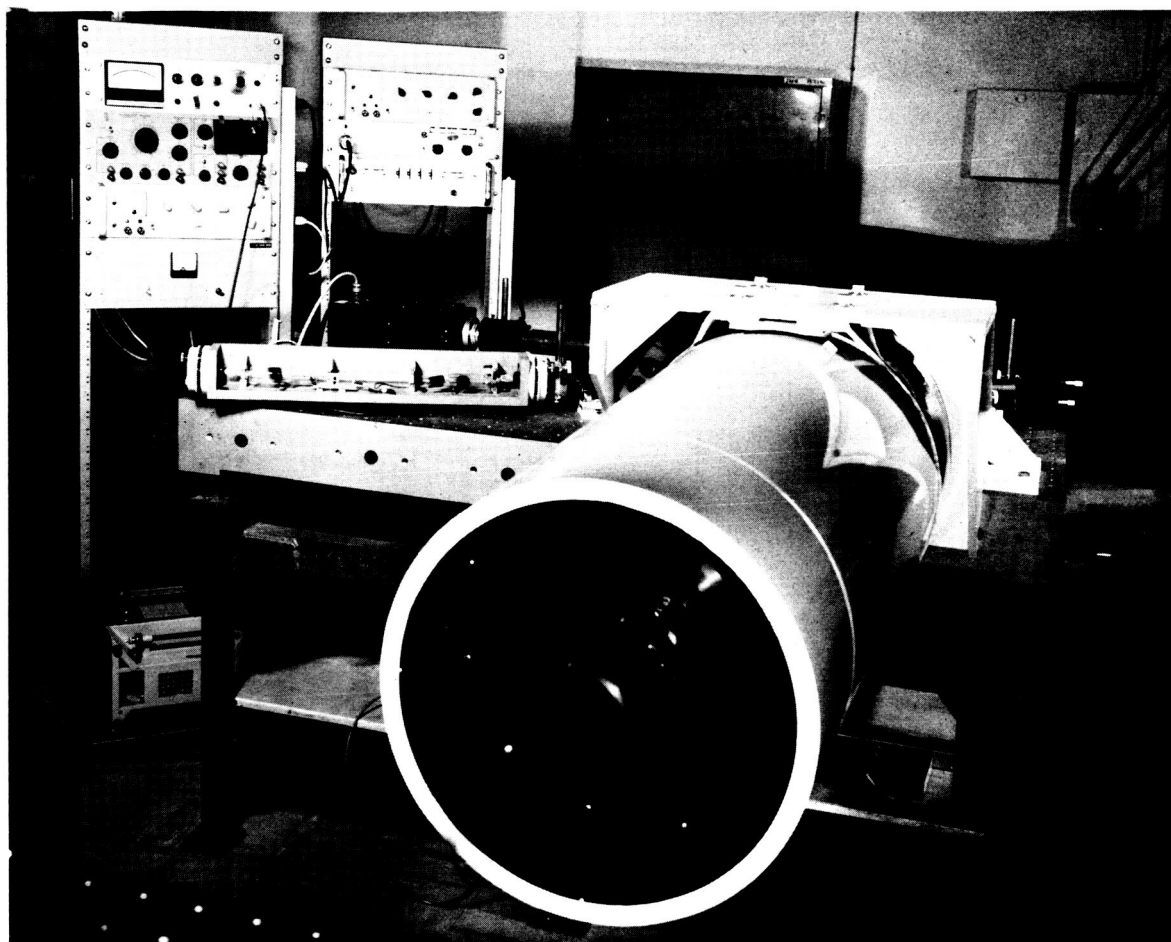
Figure 3-7. Optical Bench Showing
Telescope Subassembly

achromatized for He-Ne laser light at 6328Å and argon laser light at 4880Å and 5145Å. It was further specified that the image transfer optics provide a net magnification of 4.67X and result in an f/70 diffraction-limited image of the main telescope's central 2-minute field. In addition, because these optics were required for use with laser light, it was specified that a minimum of surfaces be used and that parallel or concentric surfaces be avoided. A computer-aided design was obtained which meets these criteria and consists of a special doublet at L_1, with a focal length of about 6 cm, and another special doublet at L_2 with a focal length of about 28 cm. Between these lenses is a region of collimated light 10 to 20 cm long in which zero-power beamsplitters, Risley prisms, filters, etc., can be located without introducing systematic aberrations into the system.

These doublets resemble, and in a sense act as, telescope objectives. The first, which we have denoted the transfer lens, collimates an image falling within the central 2-minute field of the telescope. The second lens de-collimates light from the first and forms the f/70 image required for fine-guidance purposes.

Lens L_3, which works with a conjugate image formed by the transmitter channel may be considered identical to L_2.

An axial bundle of the relayed collimated light has a diameter of about 4mm, which is a demagnification of 100X of the 16-inch (400mm) aperture of the main telescope.

Field angle considerations lead to a minimum clear aperture of about 12mm for L_1 and a similar value or greater for L_2, depending on the spacing between L_1 and L_2.

But to standardize on cells for the lenses and to provide for experimental flexibility, L_1 and L_2 were manufactured with a clear aperture of about 22mm. One of these cells was previously illustrated in Figure 3-3.

3.5 SYSTEM FOCUS

By considering the depth of focus at each focal plane of the project optical system, it becomes evident that only the spacing of the secondary mirror to the primary is critical for correct system focus. At f/70, for example, the focus tolerance ΔZ is $\simeq$ ±5mm as given by the usual formula[1] ($\lambda/4$ criterion)

$$\Delta Z \simeq \pm \frac{1}{2} (f/a)^2 \lambda$$

where f/2a is the f-number and λ is the wavelength ($\sim$ 5000Å).

At f/15 the focus tolerance is $\sim$ ± 0.23mm (± 0.009 inch). But at the f/3 prime focus of the telescope the tolerance is only $\sim$ ±9 microns (3×10^{-4} inches). It therefore follows that all of the image transfer optics can be mechanically positioned and fixed with respect to the primary mirror if system focus is left to be accomplished by adjusting the position of the secondary mirror. The motor drive shown in Figure 3-6 and incorporated into the project breadboard is provided for this function. An automatic procedure for achieving correct system focus in practice is discussed in Paragraph 3.11.

---

[1] M.Born and E.Wolf: Principles of Optics, MacMillan, New York (1964).

3.6 OPTICAL TOLERANCES

The optical system of the Laser/Optics Techniques project must be capable of pointing and tracking to within a fraction of the angular diffraction spread of its 16-inch aperture telescopic front end. Optical tolerances must therefore be held to an extent which ensures that the final f/70 image, falling on the apex of the fine-guidance image divider, contains an adequate amount of energy symmetrically disposed within the focal spot. This spot ideally corresponds to the area enclosed by the first dark ring of the f/70 Airy pattern; a theoretical maximum of 84 percent of the total light intensity in the image can be so enclosed.

If the theoretical peak intensity at the prime image of a telescope mirror is I_o, then the ratio of the expected intensity peak I to I_o is given for high frequency figure errors by the expression

$$I/I_o = 1 - 4\pi^2 \Delta^2 \lambda^{-2}$$

where λ is the wavelength of operation and Δ is the rms (root mean square) wavefront departure of the wavefront from a sphere centered on the image;[2] i.e., Δ is twice the rms mirror figure error.

It follows this expression that, to result in a peak intensity, I, of 94 percent of theoretical, the rms figure error cannot exceed $\lambda/50$. This exceedingly stringent tolerance was selected for the 36-inch aperture primary mirror of Stratoscope II because its principal function is to carry out celestial photography in such a way that resolution in the recorded image is limited mainly by the finite primary mirror diameter.

---

[2] R.M. Scott: Optical Engineering, Applied Optics, Vol.1, No. 4, July 1962, pp.387-397

Diffraction-limited pointing and tracking functions, where the need is to locate and lock onto the centroid of an image, is best accomplished with optics made to a similar tolerance. This ensures the most efficient collection of the beacon energy for tracking purposes and the most efficient transmission of light from space to earth. An effective figure tolerance of $\lambda/20$ rms ($\Delta = \lambda/10$) leads to a peak intensity, I, of only 60 percent of theoretical and the tracking S/N suffers accordingly. However, for the breadboard system parameters this tolerance is capable of leading to 1/10 arc-second rms tracking and pointing accuracy.

Equal-path interferometer measurements were carried out on the 16-inch project telescope to show whether the combined figure tolerance of the mirrors was within $\lambda/20$ as required.

The telescope was arranged in autocollimation with a test flat in a test-tunnel. The interferometer was set up on axis to measure variations in the wavefront at the f/15 telescope focus. Photographs were taken of the fringe patterns obtained, from which it was estimated that the wavefront variations introduced by the telescope mirror were less than $\pm \lambda/10$.

Taking into account the fact that telescope errors are doubled on autocollimation and the rms of the wavefront errors must be considerably less than $\lambda/10$, it is conservative to state that the Δ of the telescope system was shown to be of order $\lambda/10$ or better at the f/15 focus. This corresponds to a system figure tolerance of about $\lambda/20$, which is of significantly higher quality than needed for ground-based applications.

The image transfer optics used in the project breadboard were
designed so as not to add further degradation to the optical system perform-
ance. We recall that these optics consist essentially of two doublets. The
first operates at f/15 and collimates an image falling within the central
2-minute fine-guidance field of the telescope. The second operates at f/70,
de-collimates light from the first lens, and produces a relayed image of the
fine-guidance field magnified by f/70 by the combination of the two lenses.

These lenses were tested individually on an optical bench equip-
ped with a collimator supplying point-source illumination at infinity. By
varying the orientation of the lens under test, images were made to fall
throughout the image plane corresponding to the 2-minute fine-guidance field.
The lenses were apertured so as to operate at their designed working f-numbers
of f/15 (6 cm f.l.) and f/70 (28 cm f.l.).

When the images were observed under high magnification, both
lenses were found to produce essentially perfect Airy patterns over the full
designed field. The measured diameter of the first dark ring was approxi-
mately 19 microns for white-light illumination of the f/15 lens, which is
close to the theoretical value of 20 microns for 5500Å illumination. The
f/70 lens produced an approximately 90 micron diameter dark ring, which com-
pares equally favorably with the theoretical value of 92 microns.

Photographs of the magnified images showed that the great major-
ity of the energy appeared in the central spot of each image. The secondary
rings were symmetrical and very much fainter, as would be expected from

theory. This is illustrated by Figure 3-8, which is a reproduction of photographs of the focal pattern of the 28 cm f.l. lens taken with increasing exposure times.

3.7 FINE-GUIDANCE IMAGE POSITION SENSOR

The Laser/Optics Techniques breadboard is designed to incorporate an image position sensor subsystem at the f/70 fine-guidance image plane. One such subsystem was previously illustrated schematically in Figure 1-1 by a pyramid-shaped prism and four photomultipliers. Basically the same function can be carried out by a variety of techniques which for our purposes may be classified according to whether or not image division is accomplished optically somewhere along the line. A brief comparison of the different techniques suited to the needs of the project breadboard is given in Table 3-2. Only the most immediately relevant properties of each are highlighted.

The technique adopted for the Laser/Optics Techniques breadboard appears near the end of the table and consists of an optical image divider in conjunction with four photomultipliers. This is a particularly versatile technique as different image stops can be employed for field reduction, and different photodetectors can be substituted for a variety of spectral responses.

For the optical image divider, we employed a modified version of the design employed in Stratoscope II.

The original design consists of a modified cube-corner retro-reflector. A star image is divided four ways on retro-reflection from a
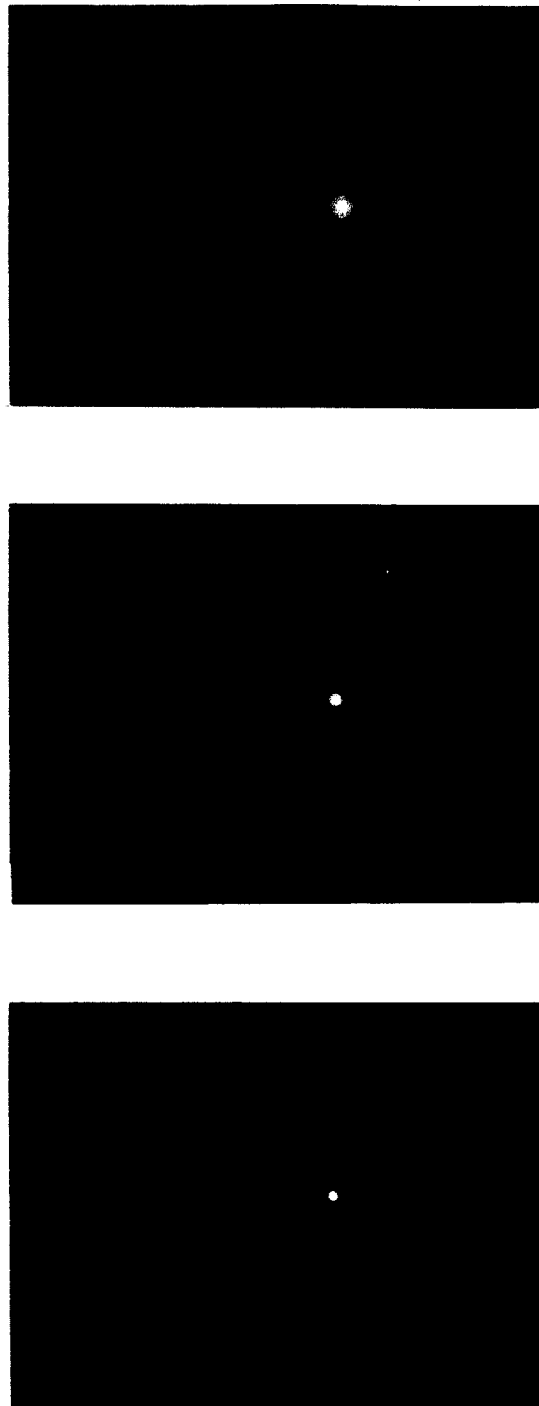
Figure 3-8. Focal Pattern of the 28 cm f.1 Lens With Increasing Exposure Times

cube-corner prism whose three reflective surfaces depart by a calculated amount from mutual orthogonality. The design results in the ability to discriminate against image motions that are small compared with the size of the diffraction-limited star image. Image division occurs at the point of intersection of three planes of one glass element, and as this point can be made to have a blunt region of very small extent only a correspondingly small fraction of light in the image fails to reach the four photomultipliers which subsequently sense the image division.

Because of space restrictions, an image divider of this type was employed in the project breadboard on transmission--not on reflection as is more usually the case. This modification carries the divided image out to a region behind the divider where photomultipliers can be mounted conveniently, and is easily accomplished with the Stratoscope divider by leaving uncoated one of its three reflecting surfaces.

3.8   PROJECT PHOTOMULTIPLIERS

The prime function of the photomultipliers employed in the image position sensor subsystem is to detect argon laser beacon light at $4880\overset{\circ}{A}$ and/or $5145\overset{\circ}{A}$. And they must carry out this function in the presence of whatever residual red light at $6328\overset{\circ}{A}$ is incompletely blocked from the transmitter channel. The subject of channel separation is discussed much more fully in Section VI. We note here only that because of the channel separation problem it is desirable to choose receive-channel photomultipliers that not only have maximum blue response but also minimum red response.

TABLE 3-2

COMPARISON OF IMAGE DIVIDERS AND TRACKERS

DEVICE DESCRIPTION	PROPERTIES	CONSEQUENCES OF PROPERTIES
Magnetically focused image dissector (e.g., ITT type FW-146, F4011, etc.)	Furnished with fixed aperture sizes ranging from 0.0005 inch to 0.350 inch. Typical equivalent photocathode aperture sizes: 0.005 inch. Senses image position by magnetic scanning of electron image across aperture.	Aperture can function as a virtual image stop. This eliminates noise due to background light in remainder of image. But as a concomitant property this necessitates a search mode if image is not centered. Necessity for scanning decreases available signal power in each of two axes by 1/2 for 100% modulation. Requires magnetic coil power supplies and drive circuitry.
Electrostatically focused image dissector (e.g., C.B.S. Type CL-1147 Reconotron).	Aperture fixed as in above device. Typical aperture diameter 0.002 inches for a typical useful photocathode diameter of 0.75 inch. Senses image position by electrostatic deflection system.	As for all image dissector devices the virtual image-stop is not adjustable. This limits the field of view drastically and requires a scanning mode for initial acquisition and for acquisition on loss of track. Low power requirements but worse resolution than by magnetic focus and deflection. Also loses useful signal power by the need for position modulation by electron image.
EMR Quadrant Multiplier Phototube (e.g., model 568A-01-14) (consists of 4-quadrant photocathode followed by a common multiplier chain)	Sensitive area of photocathode 0.4 in dia. gap size (dead region between quadrants) 0.0015 inches + 0.0005 -0. Image position determined by sequential switching on of each quadrant.	Maximum number of resolution elements limited $\frac{0.4}{0.0015} \sim 270$ in either axis. Loses 75% of available signal power.
ITT Quadrant Multiplier Phototube (e.g., Model F4002) (consists of 1	Useful cathode diameter 0.97 inches. The splitting reticle is used to direct photo electrons from each quadrant of the photo-	Unspecified but probably small numbers of resolution elements.

Device	Characteristics	Advantages
Optical Image Divider with Associated Photomultiplier tubes (e.g., Perkin-Elmer retor-divider design for Stratoscope II)	...specified by the manufacturer) exists near the electrical center of the photocathode. Functions as four photomultiplier tubes in one package. Image division takes place at intersection point of three optically polished planes. Useful apertures in excess of 1.5 inches readily obtained with essentially no dead zone at apex. (i.e., apex can be made to have a blunt region no greater than a few microns in diameter.) Entire field of view is exposed to photomultipliers.	No loss of signal power except at electrical center of photocathode. Compact unit as compared with four separate photomultipliers. No loss of signal power as each quadrant of divided image falls on its own photomultiplier tube. Tremendous number of resolution elements. No appreciable amount of signal power lost when image is centered. Tracking information available over entire field of view. Requires an additional image stop if field of view is to be reduced to cut down on noise due to background light. Field of view can be adjusted by external stop. The choice of detector is not restricted. Hence this technique is versatile and experimentally convenient.
Optical Image divider with Associated Quadrant Multiplier Phototube (e.g., Perkin-Elmer retro-divider design for Stratoscope II with ITT Model F4002 Quadrant Multiplier Phototubes.)	Requires external photodetectors. Critical manufacturing tolerances can be maintained with optical precision. Image division is still carried out optically, but sensing is carried out as if by four photomultiplier tubes in one envelope. Requires image stop if noise due to background light must be reduced by reducing the field of view	The finished optical element is basically rugged and the critical surfaces can be so constructed as to be self-protecting. Other mechanical tolerances (e.g., positioning of photodetectors) are non-critical as a result of the optical design at the divider. Uses signal power as efficiently as four photomultipliers yet mechanical configuration is much more compact. The field of view can be varied at will by changing the size of the image stop.

3-22

We settled on EMI photomultipliers for this application as they were both readily available and suited to the requirements. More over, photomultipliers of this general kind can be ruggedized and space-qualified.

The main characteristics of the EMI 9514S photomultipliers are summarized in Table 3-3. The spectral response characteristics of the type-S photocathodes which are employed are shown in Figure 3-9 where the characteristics of S-11 and S-20 surfaces are also shown for comparison. A selected set of four of these photomultipliers, matched for maximum photocathode sensitivity and minimum dark current, was obtained for the image position sensor subsystem.

In addition, a selected pair of similar, but red sensitive, EMI 9558A photomultipliers having S-20 photocathodes was obtained. These were employed, as discussed in Section VI, in our investigation of channel separation techniques.

A photograph of the complete image position sensor subsystem is shown in Figure 3-10. The tube on the left contains the de-collimating lens previously denoted in Figure 2-1 as L_2 and the image divider at the apex of which is formed the f/70 fine-guidance image plane. The four quadrants of the divided image plane fall on the photocathodes of four respective photo-multipliers. These are housed in the cylinders visible in the right-hand side of the photograph.

TABLE 3-3

<u>TYPICAL CHARACTERISTICS OF EMI 9514S PHOTOMULTIPLIER</u>

Photocathode Sensitivity	40 μa/𝓁m
Useful Photocathode Diameter	1.75 inches
Number of Dynodes	13
Spectral Response	S (special blue response with reduced red sensitivity)
Dark Current (at 2000 a/𝓁m)	0.02 μa at 25°C
Tube Temperature for Dark Current within a Factor of 2 of Ultimate Minimum	−10°C
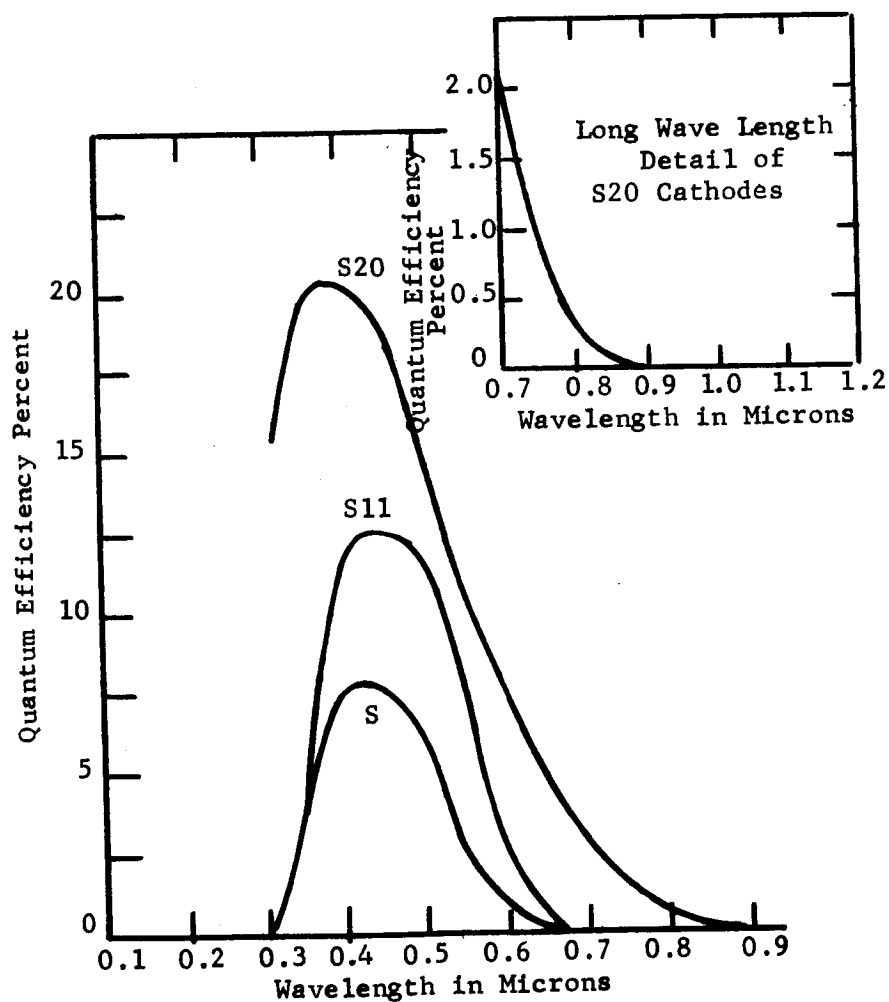
Figure 3-9. Photocathode Spectral Response Curves
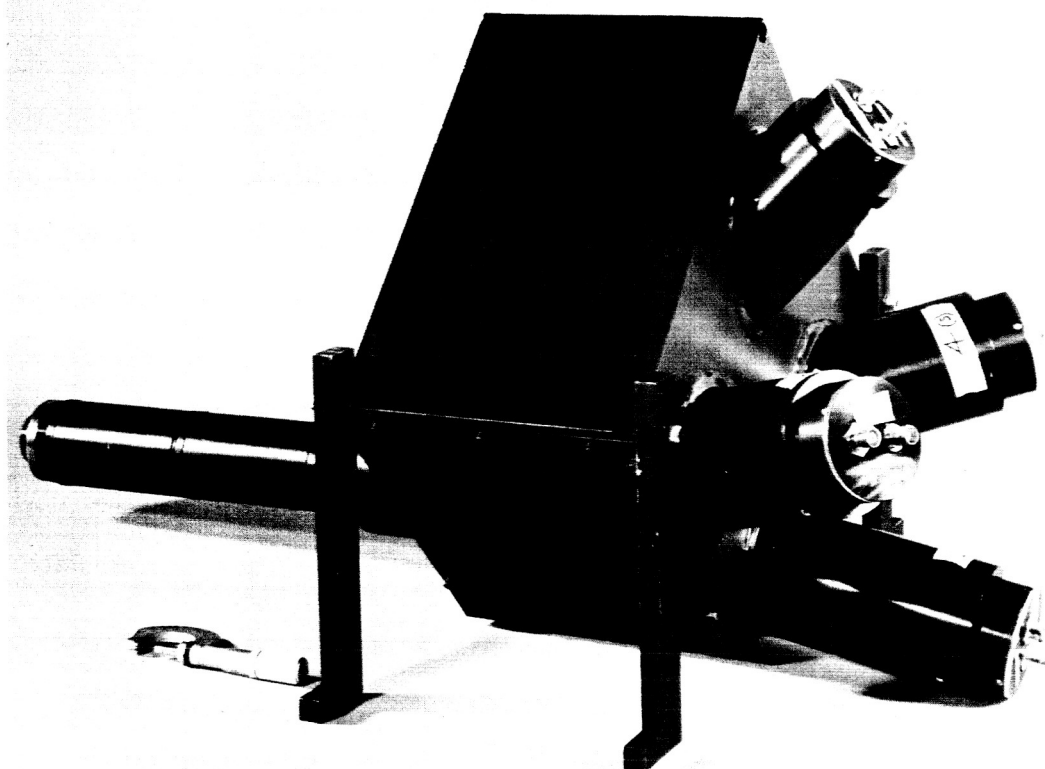
Figure 3-10. Image-Position Sensor Subsystem

3.9   LASER DESIGN

To meet the needs of the basic project breadboard as well as those of the experimental investigation of laser beam fluctuation the He-Ne laser illustrated in Figure 3-11 was constructed. The plasma tube was of conventional design with Brewster-angle windows and oxide-coated cathode filaments, but the supporting structure was made especially rigid so as to avoid microphonic effects. Provision was made for easy substitution of different laser mirrors as well as for varying the mirror spacing. This facilitated obtaining stable operation in the fundamental transverse mode using a hemispherical mirror configuration.

Both the filament and the gas discharge were powered by highly regulated DC supplies which avoided introducing hum and noise modulation of the resulting laser light output.

At various times, plasma tubes with either a 3mm or 2mm bore were employed. The active length of the gas discharge was about 24 inches (60 cm) in each case and an output of from 5 to 10 milliwatts at 6328Å was generally obtained.

For some of the later experiments, when it was no longer useful to have the laser mirrors exposed, a Perkin-Elmer Model 5300 laser was incorporated into the breadboard. This laser is illustrated in Figure 3-1 as part of a typical experimental setup.
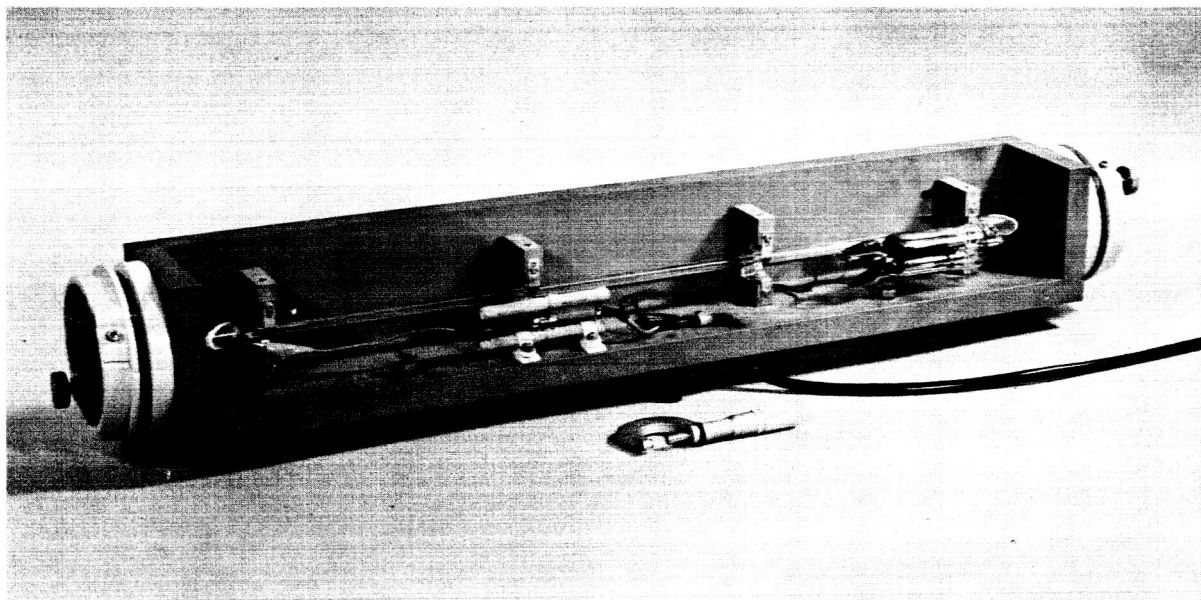
Figure 3-11. He-Ne Laser

3.10 PREVIEW OF THE TRANSFER LENS SERVO SUBSYSTEM

As indicated in Figure 1-1, fine-guidance is carried out not by maneuvering the entire optical system, but by two-axis electromechanical translations of the transfer lens L_1 alone. The major resulting benefits are system simplicity and fast transmit beam pointing correction.

A transfer lens servo subsystem was designed, constructed, tested and incorporated into the project breadboard. A full description forms Section IX of this report. Some salient points are as follows:

(a) The transfer lens servo subsystem comprises 1) the transfer lens in its cell 2) supported by flexure bearings that are so arranged as to allow motion only in an x-y plane when 3) the lens is driven by x-y magnetic drives in response to signals from 4) the image position sensor subsystem, shown in Figure 3-10. These signals are processed by an electronics control box and an auxiliary hold-mode and electronics control unit. A 1 Kc/s square-wave modulated f/15 point-source was employed in tests on the transfer-lens servo subsystem independently of the main telescope.

(b) The transfer lens servo subsystem is illus-
trated in Figure 3-12. Seen from left to
right in the photograph are: the f/15 test
light source and chopper blade, the transfer
lens mechanism, the electronics control boxes
(the hold-mode and electronics control unit
is on the bottom), and finally the image posi-
tion sensor subsystem.

(c) A top view of the transfer lens mechanism
situated in place behind the main telescope
is shown in Figure 3-13. The photograph is
a time exposure and shows graphically how
focused light from the 10 milliwatt He-Ne
laser is collimated by one lens (L_3 of
Figure 1-1), deflected at right angles by
the dichroic beamsplitter and then is focused
to a spot in the f/15 focal plane of the sys-
tem after which it diverges to "fill" the
telescope.

(d) The hold-mode and electronics control unit
(HMECU) facilitates testing of the complete
subsystem and has three primary functions:

  (1) To meter the transfer lens position in
      the fine-guidance image plane. The
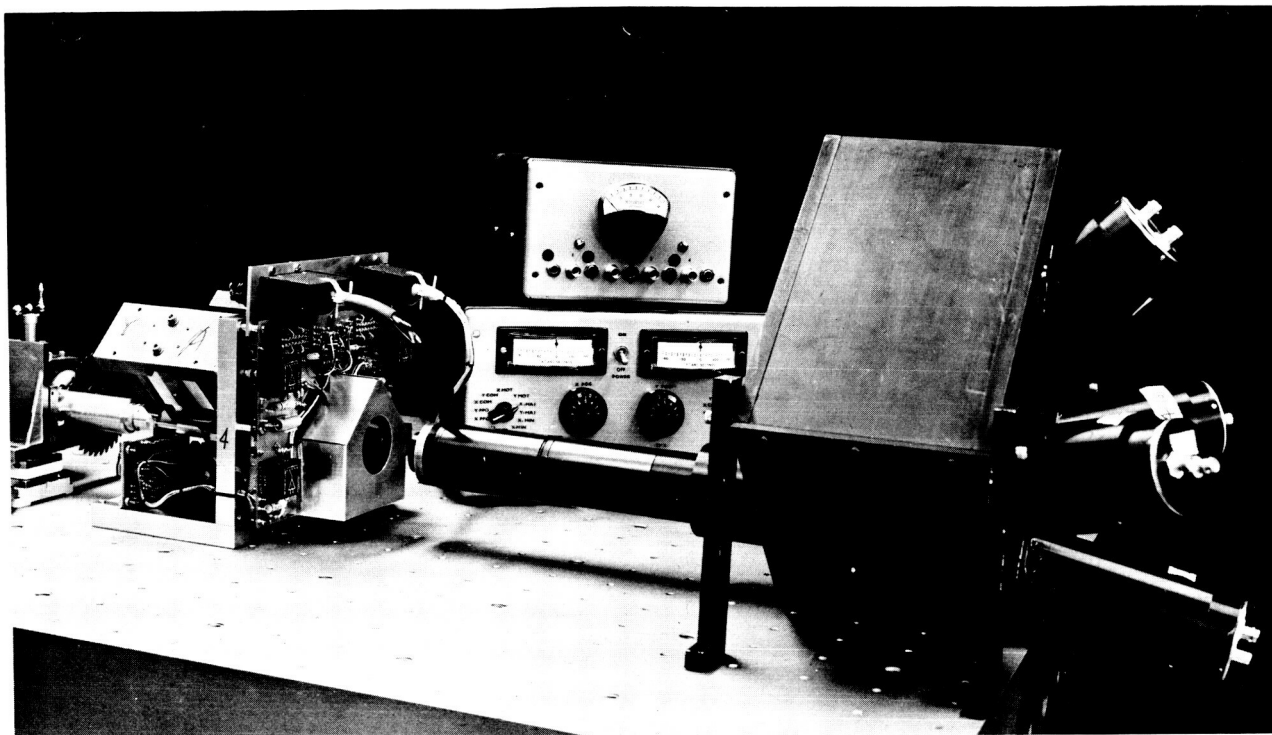
Figure 3-12.   Transfer Lens Servo Subsystem
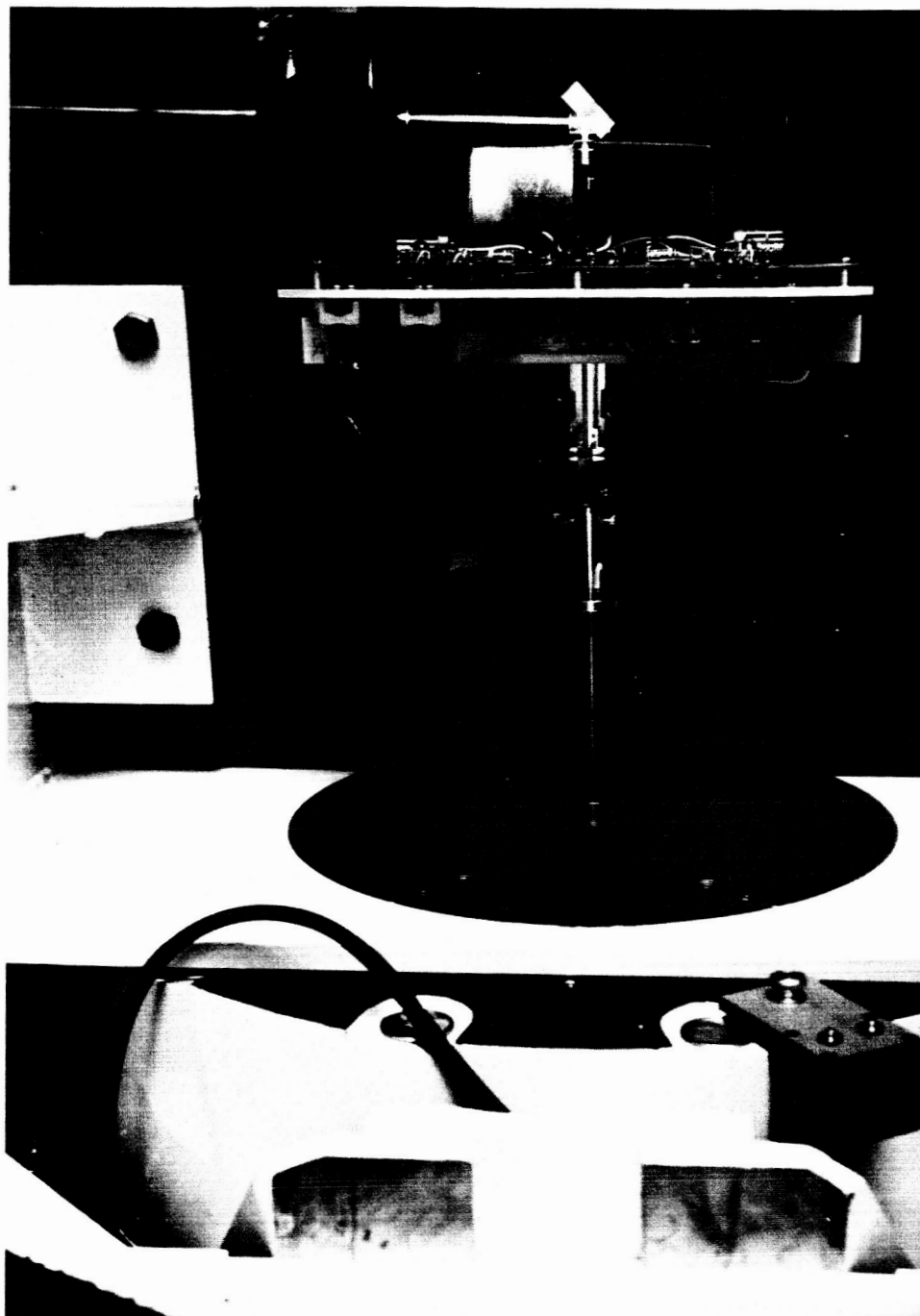
Figure 3-13. Top View of Transfer Lens Mechanism

panel meters are calibrated in equivalent

pointing error of the 16-inch aperture

f/15 telescope.

(2) To provide, by means of a two-axis hold-
mode servo, a stable central lens position
for rapid and dependable acquisition, and
to provide a means of precisely locating
the transfer lens for alignment and test
purposes.

(3) To provide test points and signal injection
for measurement of servo parameters and
tracking stability.

(e) The servo has approximately the response we would
expect to be needed by a spaceborne beacon tracker.
The 3 db bandwidth is approximately 40 cps, and
the response is very stiff at low frequencies.

(f) Newly developed two-axis capacitance-operated position-
pickoff sensors are utilized for velocity feedback
and they work simply and reliably. A previous need
for tachometer motor coils and large associated magnets
has been effectively dispensed with.

(g)   The transfer lens servo subsystem is capable of

detecting optimum system focus and forms a nat-

ural link in a remote focusing procedure.

3.11 REMOTE FOCUS PROCEDURE

Brief mention was made in Paragraph 3.5 of system focus consid-
erations. It was shown that, with the exception of the secondary mirror,
all of the optical elements can be permanently spaced with respect to the
primary mirror. This leaves the axial spacing of the secondary mirror as
the one parameter to vary to readjust the system focus. The motor drive
mechanism, which is provided in the project breadboard for this purpose, was
previously illustrated in Figure 3-6. The motor drive is manually operated
by two pushbuttons (one for each direction of travel) which are shown attached
to the rear of the telescope structure (lower left-hand corner) in
Figure 3-13.

The motor drive, then, is the system focus controller. Detection
of focus errors is accomplished by the transfer lens servo subsystem. The
focusing procedure is carried out while the complete system is tracking the
earth beacon or its equivalent. An electrical dither signal is injected
into one axis of the transfer lens servo drive. The response of the closed
loop is to exactly compensate for the electrical dither by moving the trans-
fer lens. This motion produces an equal and opposite error signal in the
image position sensor subsystem, since the dither acts on the servo drive
the same as would a sinusoidal torque disturbance on the telescope. The
motion of the transfer lens is then monitored while the secondary mirror is

moved in and out of focus by the motor drive. At optimum focus the f/70 beacon image has a minimum diameter and the transfer lens experience minimum dither induced displacement. In practice this is a rather broad minimum. On either side of focus, the beacon image is broadened and the transfer lens has to move further to produce the same compensation. This relationship is illustrated in Figure 3-14.

Position pickoff sensors are incorporated into the transfer lens servo subsystem and may be used to monitor the optimum focus condition. In practice it is preferable to determine a position of the secondary mirror on either side of focus both of which result in the same dither-induced lens motion. Then the secondary mirror is moved to the half-way position, which is taken to be optimum. It also turns out to be preferable, for reasons of accuracy in the presence of spacecraft disturbances, to measure dither-induced velocity of the transfer lens rather than position.

This remote focus procedure originates in the Stratoscope II design and has also been adapted for OAO-C (Princeton Experiment Package).

The HMECU supplied with the transfer lens servo subsystem provides convenient access points to the electronics for this focusing procedure to be carried out.
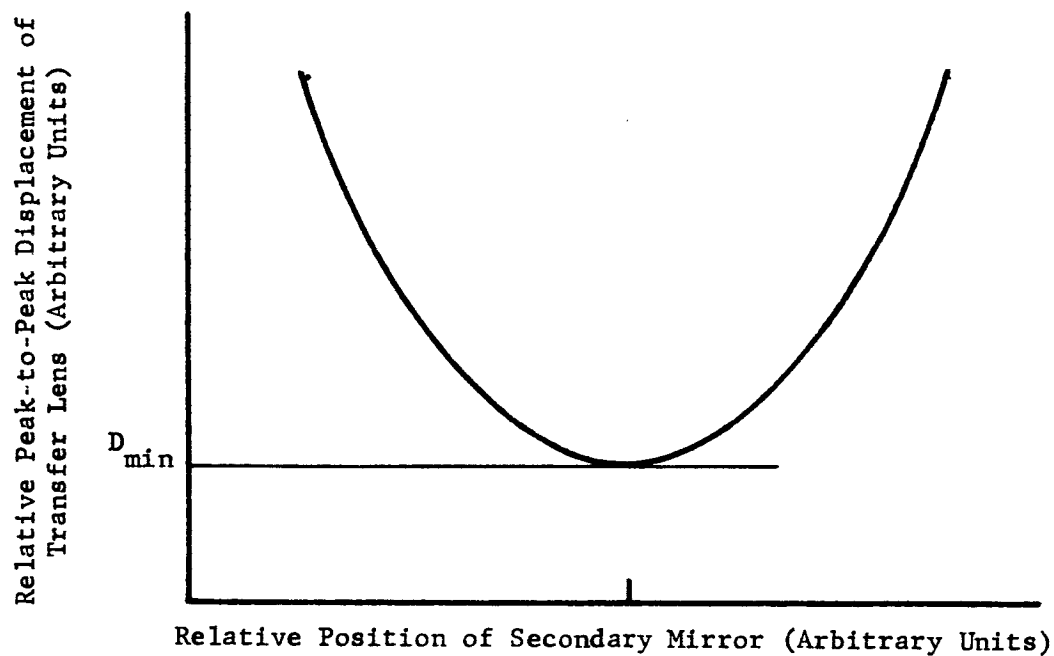
Figure 3-14. Relationship Between Dither Induced
Peak-to-Peak Displacement of Transfer
Lens and System Focus as Determined
by Secondary Mirror Position

SECTION IV

ROTATION ABOUT LINE OF SIGHT (RLOS)

4.1   GENERAL

If a diffraction-limited laser beam is to intercept a given earth station 10^8 miles or more away, then, as discussed in the Phase II OTS Report, it must be biased forward from the apparent line of sight of an earth beacon by, for example, 36 arc-seconds. The correct aim of the transmitter may be specified by two coordinates, one describing the magnitude of the forward bias angle, and the other describing the rotational orientation about the line of sight. A reference, from which rotation about the line of sight (RLOS) may be determined, must somehow be obtained by the space vehicle.

A polarization scheme that relies upon sensing the plane of polarization of the incoming beacon light, and which originally looked like a promising approach, was analyzed in the Phase II OTS Report and was shown to have inadequate signal-to-noise ratio for what were then reasonable deep-space parameters based on GaAs laser beacons.

Because powerful argon lasers operating at more favorable wavelengths have subsequently been developed, and because the polarization technique is appealingly simple to implement, this technique was re-investigated as called for in the present program. A summary of this investigation is given in Paragraph 4.2 where it is shown that, within the present state of the art, the polarization technique is unsuitable for RLOS determination over ranges beyond about 10^7 miles.

An interesting alternative approach to the RLOS problem is discussed in Paragraph 4.3. It employs two coherent earth beacons in such a way that the beams are superimposed at the spaceborne receiver and form parallel interference fringes. The orientation of the fringes is detected optically thus yielding an RLOS reference. This interference fringe method turns out to be an extremely powerful technique for RLOS or twist angle measurement at close and intermediate ranges of less than a few million miles. Its practical limit is less than 50 million miles and is set mainly by the required baseline separation of the beacons.

Another alternate approach to the RLOS problem makes use of an auxiliary star tracker and is discussed briefly in the OTS Phase II Report. We have analyzed this method vis-a-vis the capabilities of the polarization method. This work is described in Paragraph 4.3. It is concluded that, with an auxiliary star tracker of modest size and performance, the required RLOS accuracy of 1 arc-minute can easily be obtained at the requisite distances with an adequate signal-to-noise ratio. The disadvantage of the approach is the increase in system complexity due to the addition of a star-tracker subsystem.

It is probably safe to conclude from these calculations that over ranges of 10^8 miles the required signal-to-noise ratio for the required RLOS accuracy cannot in fact be met conveniently without resorting to an auxiliary subsystem. We are therefore led to recommend that for a deep space optical communications system based on an argon laser beacon on the earth surface, RLOS determination in the spacecraft should be implemented by the auxiliary star-tracker method.

Irrespective of the RLOS technique, an integration-time or servo-bandwidth parameter always enters into calculations of attainable signal-to-noise ratios. An investigation was carried out to provide a fundamental basis for choosing a value for this parameter. The results are summarized in Paragraph 4.5. The analysis is valid in general for any spaceborne servo that must operate in the presence of vehicle-induced torque disturbances.

4.2 PERFORMANCE OF ARGON LASER EARTH BEACON FOR DETERMINATION OF RLOS

The determination of RLOS by the polarization technique described in the Phase II OTS Report has been re-evaluated for an argon laser earth beacon. Plots of RLOS signal-to-noise ratio versus range with low-pass filter bandwidths (0.1, 1.0 and 10 cps) as a parameter are presented in Figures 4-1 through 4-6. The RLOS uncertainty $\Delta\alpha$ is taken as 1 arc-minute and diameter of the satellite receiver aperture is set at 32 inches. The cw earth transmitter power is taken at 100 and 1000 watts. The parameter of earth transmitter beam divergence varies over the range 3, 5, and 10 arc-seconds. The quantum efficiency is set at 0.1.

Table 4-1 lists the values of range for which signal-to-noise ratio is unity for the various cases considered. The RLOS determination by the polarization technique for the argon earth beacon case at 5145Å, appears marginal at best at the Martian range (10^8 miles) even with the 1000 watt laser.

If one compares RLOS performance of the argon beacon with the gallium arsenide beacon, it is evident that the argon beacon provides more photons per watt, and a transmitter power capability that is potentially greater. The detector quantum efficiency attainable for operating at 5145Å is also substantially greater than that at 8400Å. However, the atmospheric attenuation is somewhat greater at 5145Å than at 8400Å.
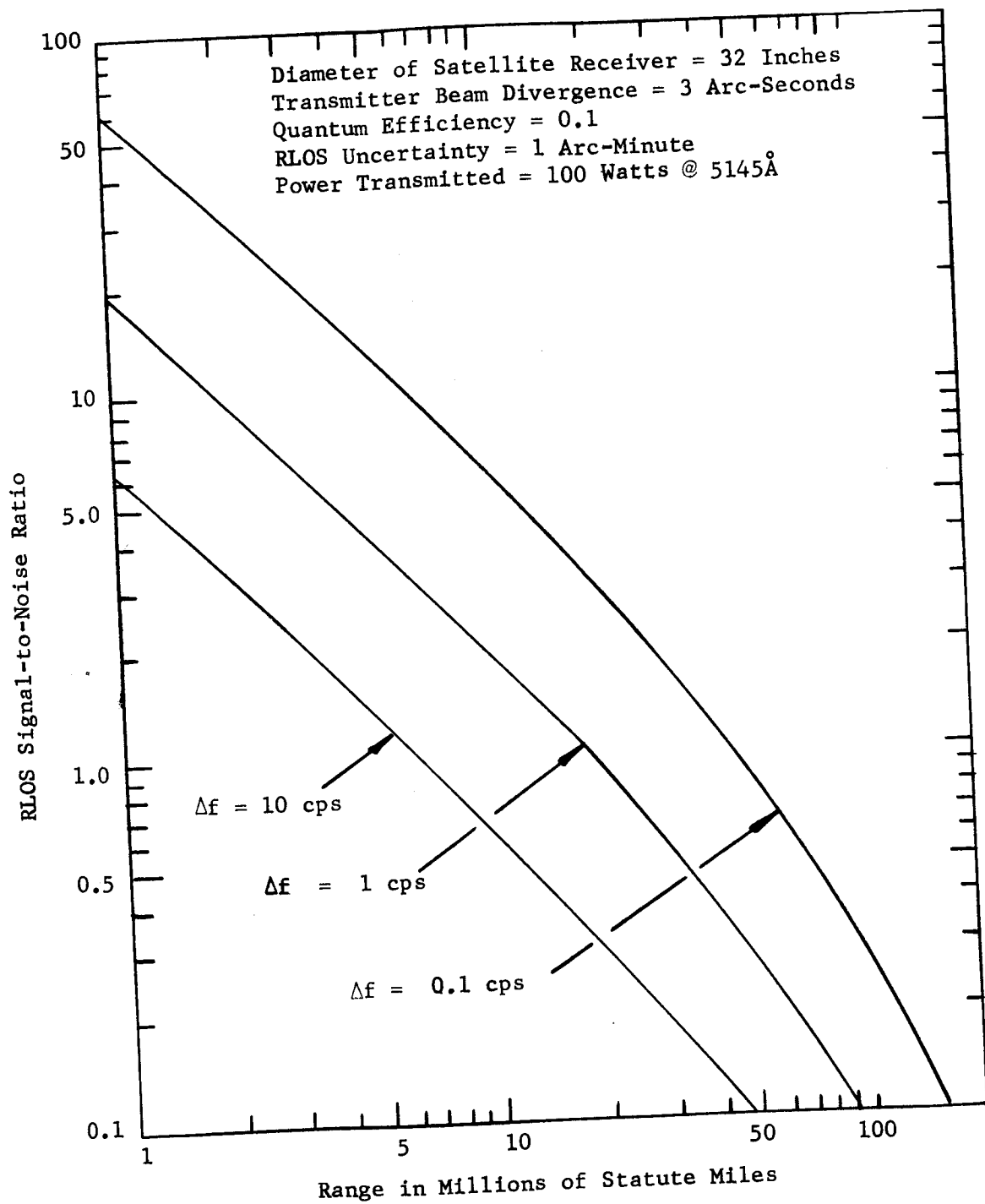
Figure 4-1. RLOS Signal-to-Noise Ratio with Beam Divergence of
3 Arc-Seconds (100 Watt Laser)
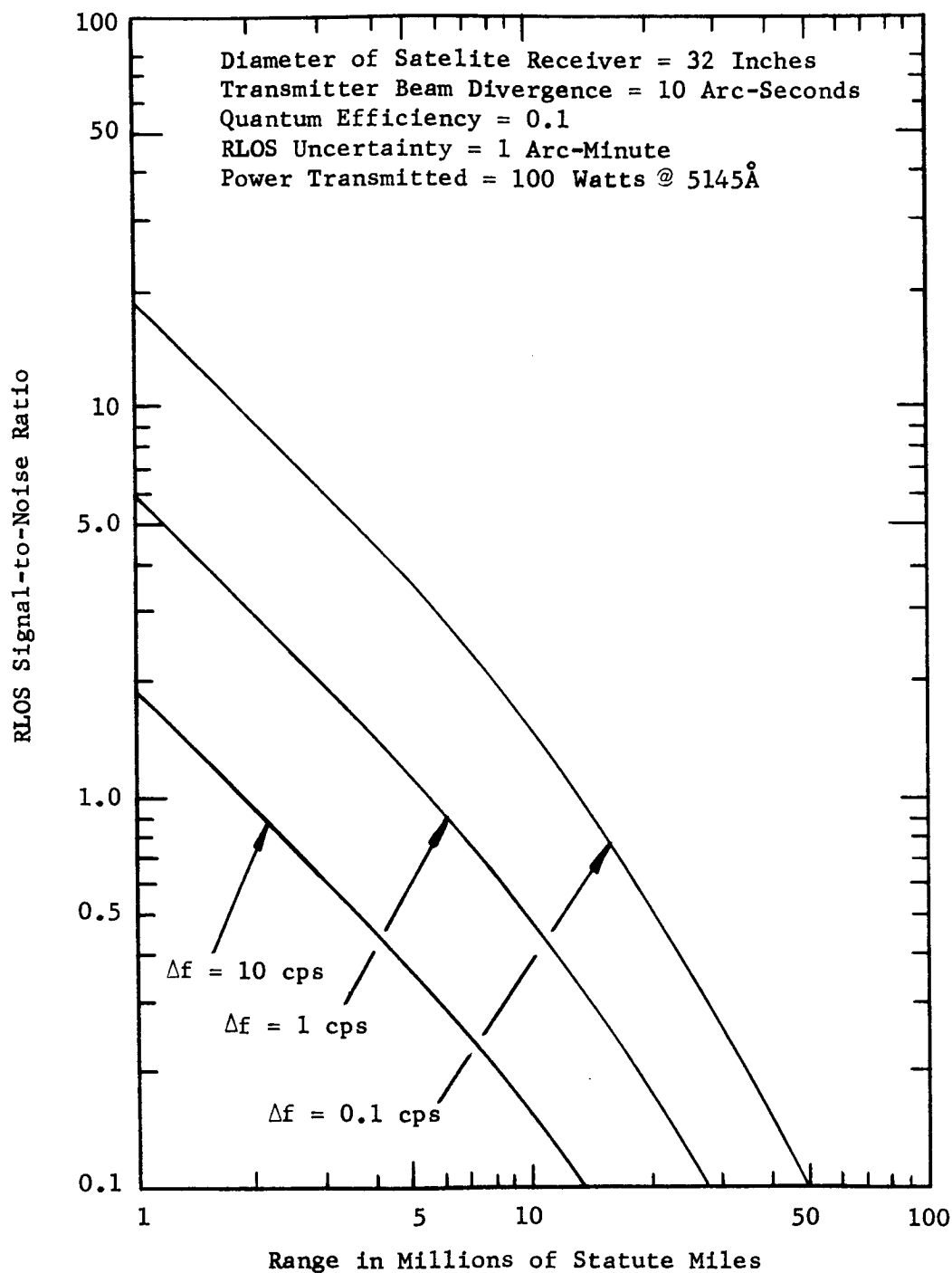
Figure 4-3. RLOS Signal-to-Noise Ratio with Beam Divergence
of 10 Arc-Seconds (100 Watt Laser)
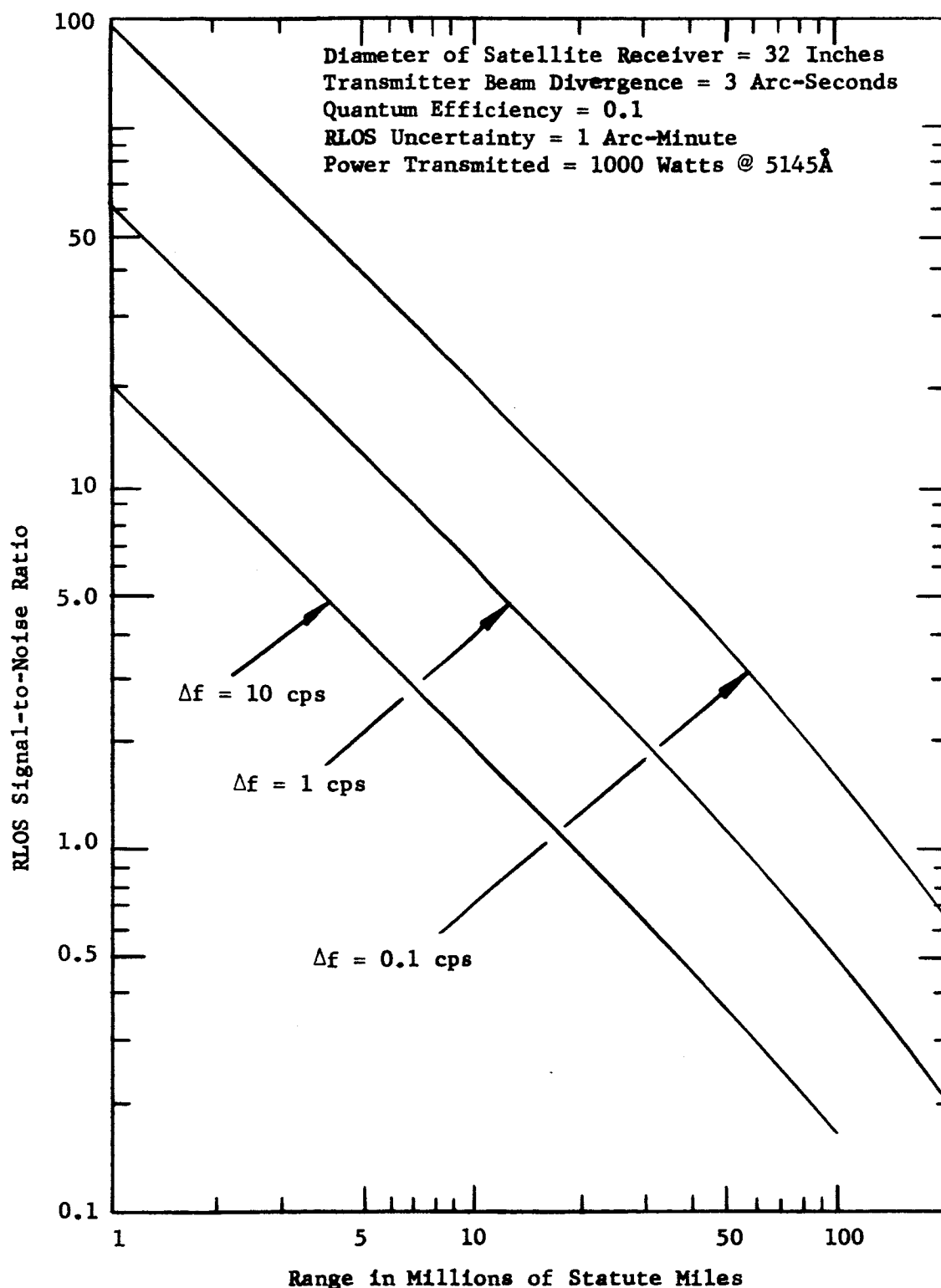
Figure 4-4. RLOS Signal-To-Noise Ratio with Beam Divergence of
             3 Arc-Seconds (1000 Watt Laser)

Diameter of Satellite Receiver = 32 Inches
Transmitter Beam Divergence = 5 Arc-Seconds
Quantum Efficiency = 0.1
RLOS Uncertainty = 1 Arc-Minute
Power Transmitted = 1000 Watts @ 5145Å

Δf = 10 cps

Δf = 1 cps

Δf = 0.1 cps

RLOS Signal-to-Noise Ratio

Range in Millions of Statute Miles
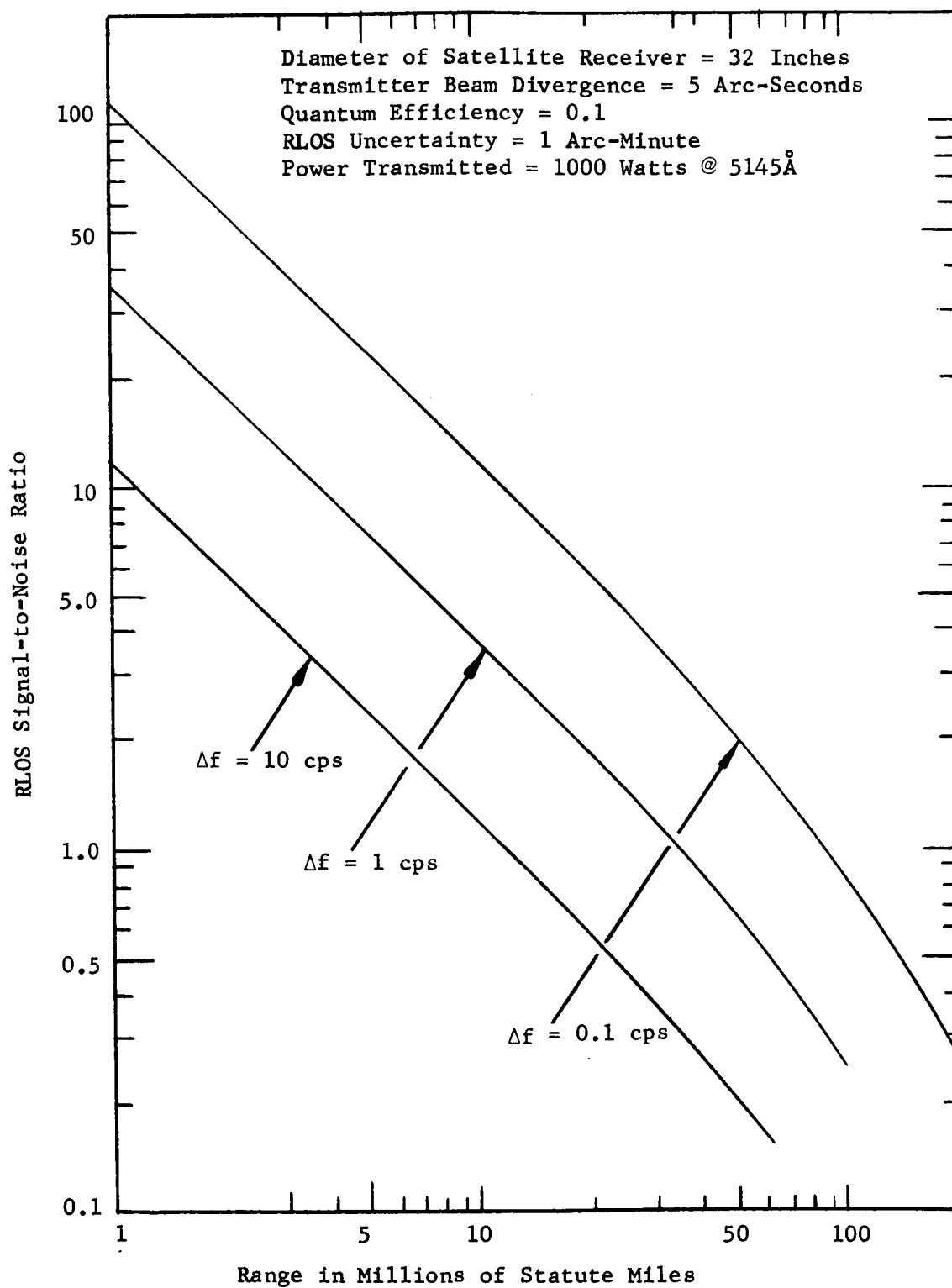
Figure 4-5. RLOS Signal-to-Noise Ratio With Beam Divergence of
5 Arc-Seconds (1000 Watt Laser)
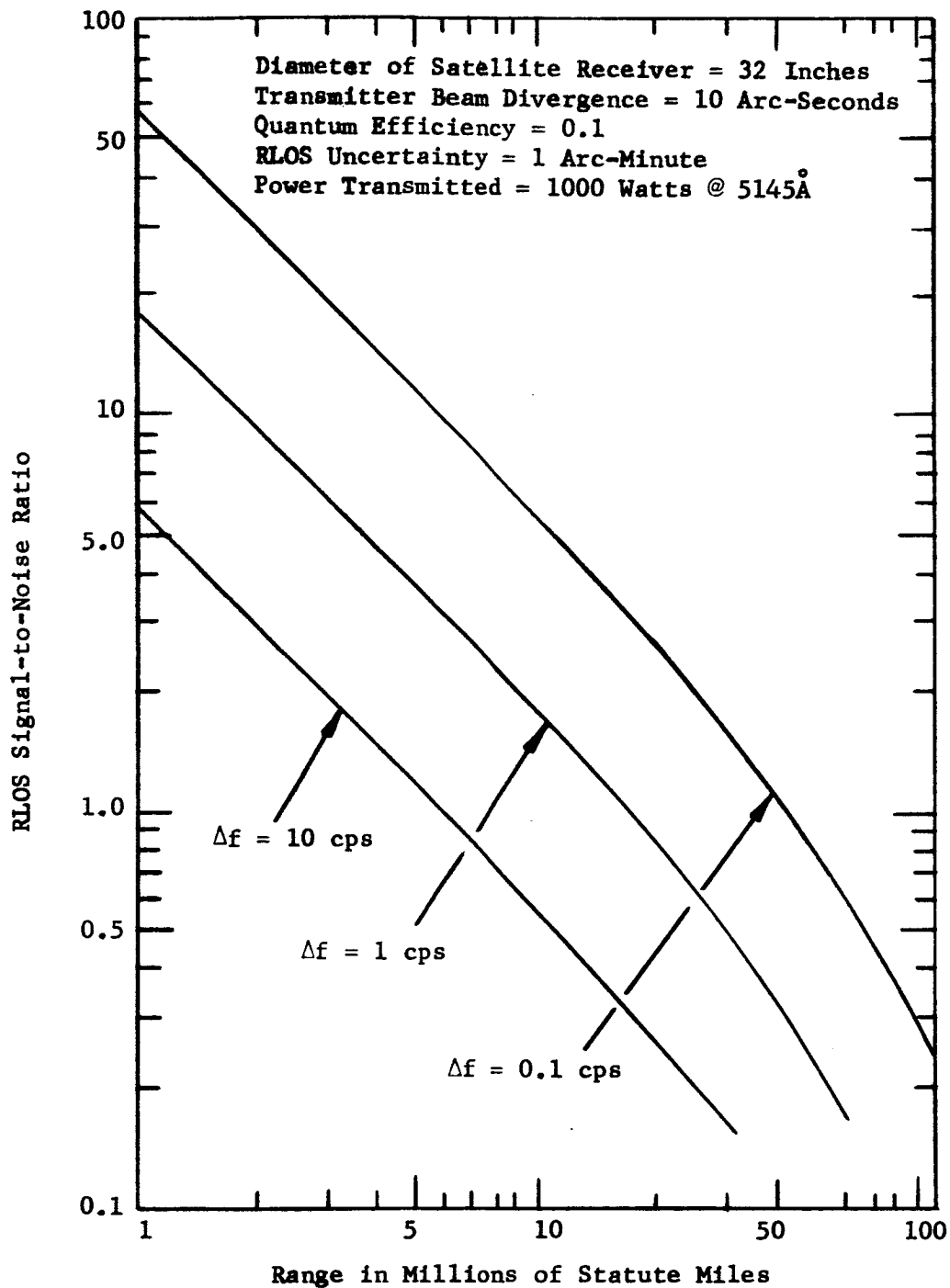
Figure 4-6.   RLOS Signal-to-Noise Ratio With Beam Divergence of
10 Arc-Seconds (1000 Watt Laser)

TABLE 4-1

RLOS POLARIZATION PERFORMANCE - ARGON EARTH BEACON

	Transmitter Beam Divergence (arc-seconds)								
	3			5			10		
Low Pass Filter Bandwidth (cps)	0.1	1	10	0.1	1	10	0.1	1	10
Range in Millions of Statute Miles for Which S/N = 1	45	18	6.2	27	11	3.7	13.5	5.6	1.85

Average Transmitted Earth Beacon P_{ower} = 100 watts
Diameter of Satellite Receiver = 32 inches
Quantum Efficiency = 0.1
RLOS Uncertainty = 1-arc-minute

(a)

	Transmitter Beam Divergence (arc-seconds)								
	3			5			10		
Low Pass Filter Bandwidth (cps)	0.1	1	10	0.1	1	10	0.1	1	10
Range in Millions of Statute Miles for Which S/N = 1	150	58	19.5	86	35	12	43	17.5	6

Average Transmitted Earth Beacon Power = 1000 watts
Diameter of Satellite Receiver = 32 inches
Quantum Efficiency = 0.1
RLOS Uncertainty = 1 arc-minute

(b)

We may therefore conclude that the polarization technique, although highly attractive from an equipment implementation point of view (i.e. simple spacecraft equipment), does not meet the requirements for determining a rotational reference to an accuracy of 1 arc-minute. For this reason, emphasis must revert to alternate schemes for RLOS determination.

4.3   AN INTERFERENCE FRINGE TECHNIQUE FOR RLOS OR TWIST ANGLE DETERMINATION

The interference fringe technique is based on measuring the orientation of a fringe system formed in space by the superposition of two coherent beacons. As will be shown, this approach is an improvement in performance over the polarization approach. Despite the improved signal-to-noise ratio of this approach for predictably practical argon lasers, servo bandwidths of interest, and 100-million mile ranges, the signal-to-noise ratio is less than necessary. It does, however, represent a new and interesting means for twist or RLOS measurement at intermediate distances. Where background light is the limiting source of noise, this technique will extend the range for RLOS from 10 million miles (for polarization sensing) to 50 million miles.

The interference fringe approach is illustrated in Figure 4-7. Two coherent beacons are projected at an angle, α, with respect to each other so as to overlap in a region where RLOS or twist angle is to be measured. In this region, the intensity of the light falling on any plane perpendicular to the symmetry axis is the coherent product of two coherent wavefronts titled with respect to each other by the same angle, α. Interference fringes are formed whose spacing is established solely by angle α and whose axis is normal to the plane of the figure.

Interference Fringes
are Formed in the
Superposition Region

Telescope Placed
in This Region

Signal
Proportional
to RLOS or
Twist Angle

Fringe
Orientation
Measurement
System

N Fringes in
Exit Pupil of
Telescope

N Fringes in
Entrance Pupil
of Telescope

R

d

Frequency
Modulator
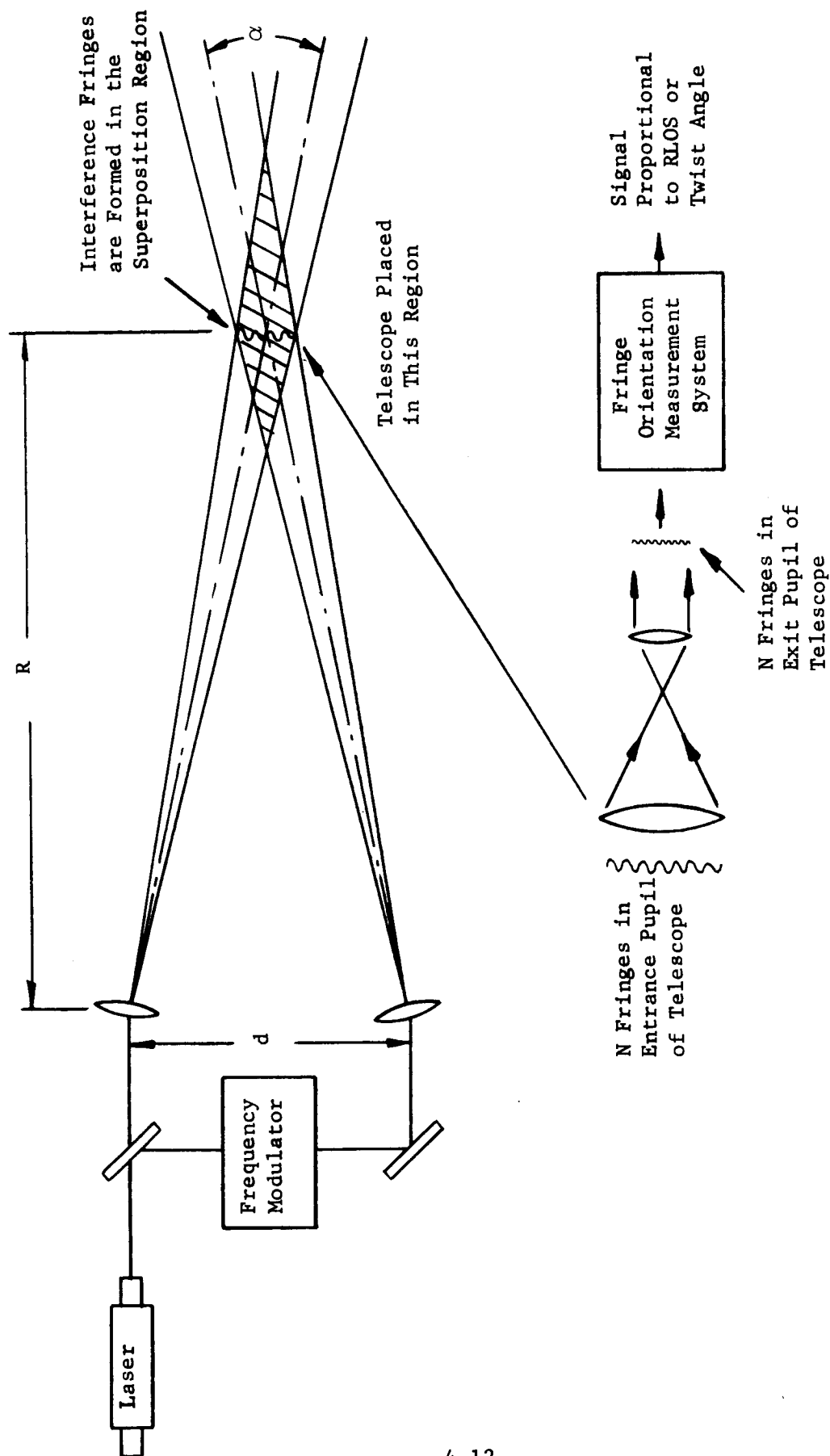
Laser

Figure 4-7. Diagram Showing Principle of Interference Fringe Method RLOS
or Twist Angle Determination

In practice, both beacons may be derived from a common laser source and one beacon may be offset in frequency from the other by a frequency modulator. This will impart a continuous lateral motion to the fringe pattern which will look in fact like an endless, moving sinusoidal grating. Analytically, this is equivalent to the case of stationary fringes. The reason for arranging to have moving fringes is that this might have certain practical advantages in a working RLOS or twist measurement system since this motion permits AC detection without any moving parts on the spacecraft. (AC detection is generally preferred when the limiting noise of a system is other than "white" and is peaked at zero cps.)

The RLOS or twist angle reference may be obtained from the orientation of the fringe pattern as follows. A telescope in the region of overlapping beams accepts N fringes which are transferred at correspondingly diminished spacing to the exit pupil where an arrangement of analyzer gratings and photomultipliers are located. The analyzer gratings function much like the polarizing analyzers of conventional polarization techniques for twist angle measurement. In combination with the luminous fringe pattern, the analyzers form moire fringes. As will be shown in the next section , the light intensity within these moire fringes is a sensitive function of the angular orientation of the analyzers with respect to the interference fringe pattern. This relationship leads to output signals from the photomultipliers which can be used to locate the axis of the interference fringe pattern to a correspondingly high accuracy.

4.3.1   Analysis

The detection system is illustrated in Figure 4-8. If we ignore for the moment the translational effect on the incoming interference bar pattern,

4-13
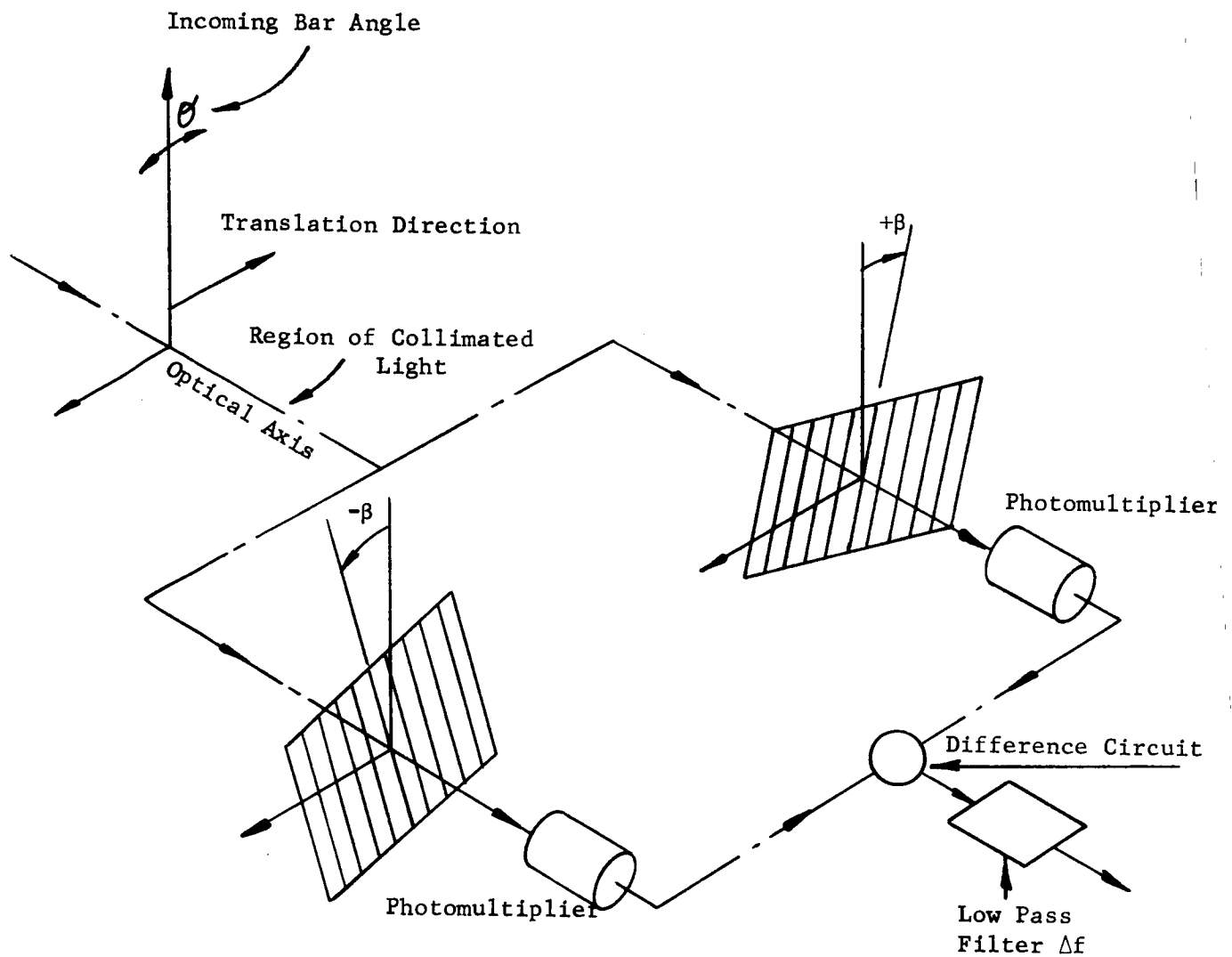
Figure 4-8. Fringe Orientation Measurement System

then the intensity per unit area of the bars received from the earth beams
may be represented as a biased cosinusoidal function.

$$I(X'',Y'') = I_o \left[1 + \cos \frac{\pi X''}{g} \right]$$ (4-1)

where I_o is a maximum intensity per unit area, (X'',Y'') represents the coordinate
system of the bars received, and g is the interference fringe bar width. We
will assume for simplicity that all the light collected by the vehicle tele-
scope system will be detected.

We wish to determine the intensity in a rectangular aperture whose
sides are parallel and perpendicular to the set of "sharp" bars fixed in the
detector. By "sharp" we mean that the transition from a dark bar to a light
bar is discontinuous; the intensity goes from some nominal value to zero
abruptly.

We will further assume the ideal situation, that the optical system
does not change the intensity $I(X'',Y'')$ from the given by Equation (4-1).

Since the incoming interference fringe pattern is superposed on
the detector's sharp bar reference gratings, a system of moire fringes will be
set up at each detector. As can be seen in Figure 4-9, XY represents the co-
ordinate system of the moire fringes; X'Y' represents the coordinate system of
the sharp bars (those fixed on the detector); and as indicated earlier, X"Y"
represents the coordinate system of the incoming fringe pattern.

Let θ be the angle between two sets of bars making up the fringes.
Let g denote the width of the bars making an angle, ϕ, with the moire fringes
(i.e., the sharp bars), as well as the width of the bars, making an angle,
$\rho = \phi + \theta$, with the moire fringes (i.e., the received bar pattern).
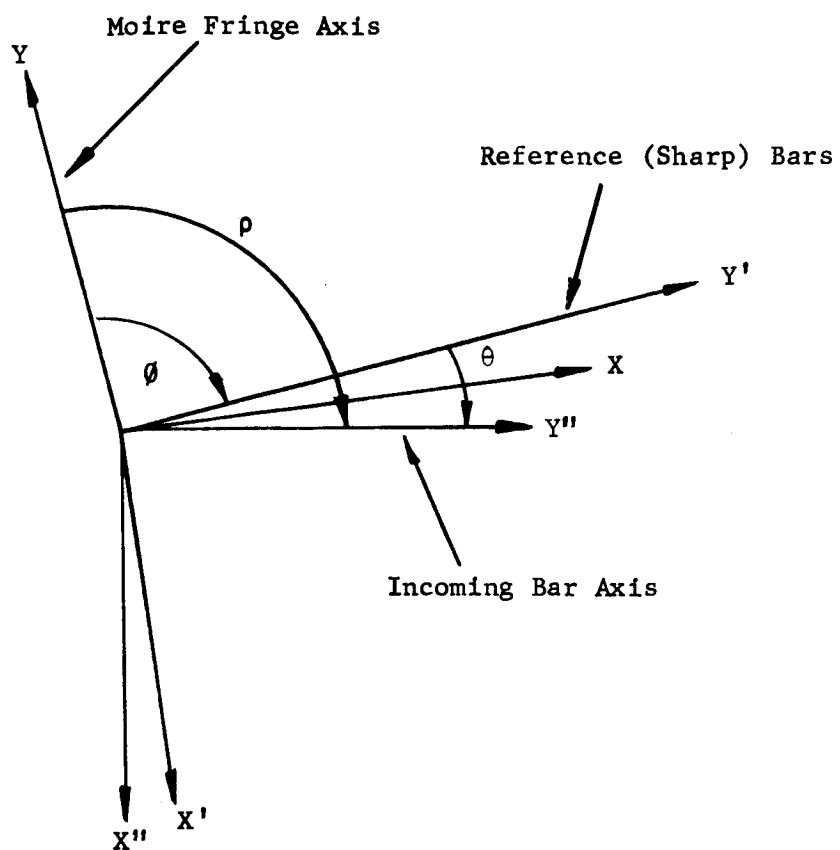
Figure 4-9. Coordinate Systems

From Figure 4-9 we can see that

$$X'' = X' \cos \theta - Y' \sin \theta \qquad (4\text{-}2)$$

$$Y'' = X' \sin \theta + Y' \cos \theta$$

The case of interest is when $\theta \ll 1$. Then

$$X'' = X' - \theta Y' \qquad (4\text{-}3)$$

So in the (X', Y') coordinate system, the intensity per unit area of the bars received from the two interfering beams is

$$I(X', Y') = I_o \left[1 + \cos \frac{\pi}{g} (X' - \theta Y') \right] \qquad (4\text{-}4)$$

Consider the resultant intensity from both sets of bars. The resultant intensity in a slit perpendicular to the bars fixed in the detectors is periodic in the X' direction. The period is equal to 2g. From o to g the intensity per unit area is given by

$$I_o \left[1 + \cos \frac{\pi}{g} (X' - \theta Y') \right]$$

From g to 2g the intensity is zero. In general we need only consider the distribution across half a fringe as the pattern is periodic and symmetric about the center. Also, we should expect that many periods would be contained in a slit of height h, (h $\gg$ 2g). Therefore, neglecting edge effects, the resultant intensity in a slit of h, in the X' direction, is given by,

$$I(Y') = W \int_o^g I_o \left[1 + \cos \frac{\pi}{g} (X' - \theta Y') \right] dX' \qquad (4\text{-}5)$$

where $W = h/2g$. Thus, neglecting edge effects, the height of a slit can be arbitrarily chosen to equal one vertical period. The intensity of a slit of arbitrary size then would equal W times the intensity in the unit slit where W equals the number of vertical periods in the height of the slit.

Performing the indicated integration in Equation (4-5), we obtain

$$I(Y') = WI_o g \left[1 + \frac{2}{\pi} \sin\left(\frac{\pi\theta Y'}{g} \right) \right] \qquad (4\text{-}6)$$

Now the set of bars received from the earth beacon will be translated perpendicular to the direction in which they run. We are ignoring any random jitter in the translational motion of the fringe pattern caused by dynamic atmospheric refractive effects. Any translation along the bars does not effect the pattern. When the bars received from the earth beacon are translated an amount, $X_o{''}$, the fringe pattern in the detector aperture shifts an amount, $-X_o{''}/\theta$ (see Figure 4-10). If the aperture width is equal to $2D$, the total intensity in the aperture is then given by,

$$I(X_o{''},\theta) = \int_{\frac{-D-X_o{''}}{\theta}}^{\frac{D-X_o{''}}{\theta}} WI_o g \left[1 + \frac{2}{\pi} \sin\left(\frac{\pi\theta Y'}{g} \right) \right] dY' \qquad (4\text{-}7)$$

Integrating we obtain

$$I(X_o, \theta) = 2WI_o g D \left[1 - \frac{2}{\pi} \operatorname{sinc}\left(\frac{\pi\theta D}{g} \right) \sin\left(\frac{\pi X_o{''}}{g} \right) \right] \qquad (4\text{-}8)$$

where:

$$\operatorname{sinc}\left(\frac{\pi\theta D}{g} \right) = \sin\left(\frac{\pi\theta D}{g} \right) \bigg/ \frac{\pi\theta D}{g} \qquad (4\text{-}9)$$

$$Y_o' = \frac{-X_o''}{\sin \theta}$$

$$\theta \ll 1$$

$$Y_o' = \frac{-X_o''}{\theta}$$
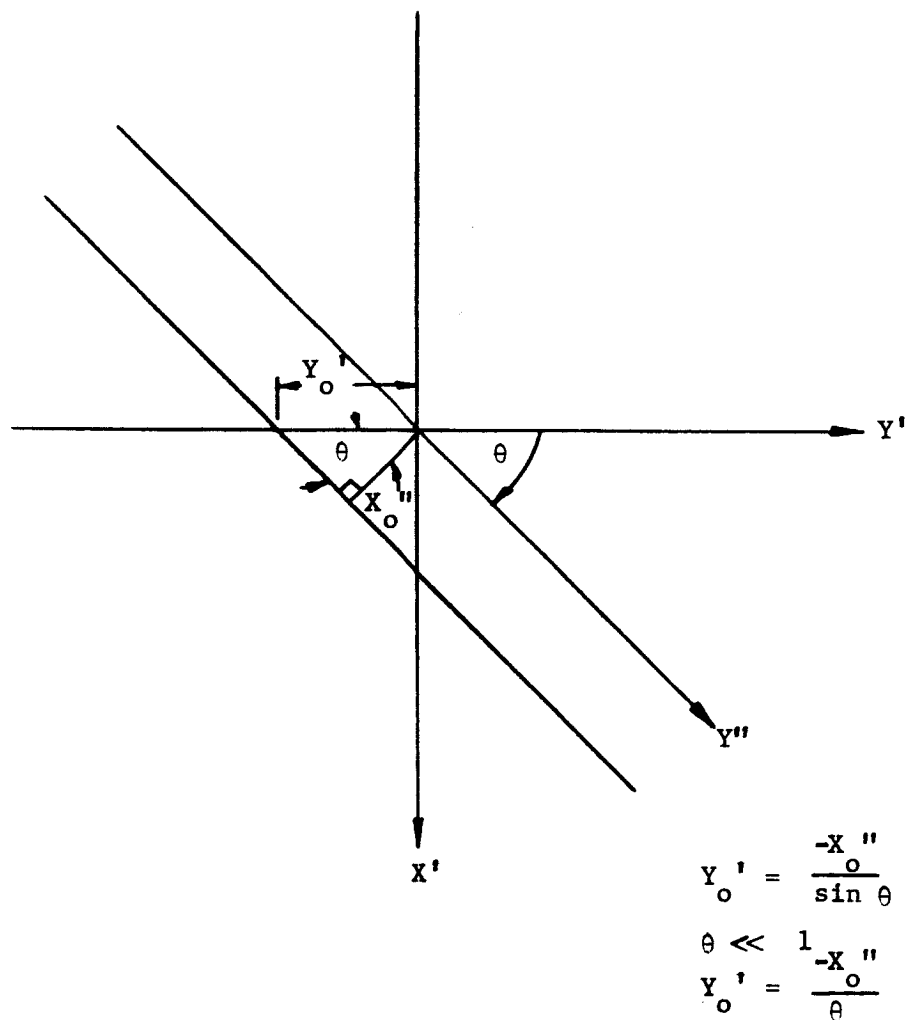
Figure 4-10. Translational Shift of Moire Fringes Due to a
              Translational Shift of the Received Interference Pattern

Recalling that $W = h/2g$, the constant $2WI_ogD$ is then equal to I_ohD which is the maximum input intensity per unit area times the half area of the detector aperture. Since two laser beams are required to generate the interference fringe pattern at the vehicle, the average signal photon arrival rate at the vehicle receiver is $2n_S$ where n_S is the average signal photon arrival rate from a single beam. Therefore, $2WI_ogD = n_S$, and Equation (4-8) can be expressed as

$$I(X_o'', \theta) = n_S \left[1 - \frac{2}{\pi} \text{sinc} \left(\frac{\pi\theta D}{g} \right) \sin \left(\frac{\pi X_o''}{g} \right) \right] \qquad (4\text{-}10)$$

The background earth shine radiation is independent of θ and therefore can be written as

$$I_B = 2WI_BgD = n_B/2 \qquad (4\text{-}11)$$

Now at the output of each sharp bar grating we have intensities

$$\frac{n_S}{2} \left[1 - \frac{2}{\pi} \text{sinc} \left(\frac{\pi D(\theta-\beta)}{g} \right) \sin \left(\frac{\pi X_o''}{g} \right) \right] + \frac{n_B}{4} + n_D \quad \text{for one channel,}$$

and

$$\frac{n_S}{2} \left[1 - \frac{2}{\pi} \text{sinc} \left(\frac{\pi D(\theta+\beta)}{g} \right) \sin \left(\frac{\pi X_o''}{g} \right) \right] + \frac{n_B}{4} + n_D \quad \begin{array}{l}\text{for the other}\\\text{channel,}\end{array}$$

where

n_S = average signal photon arrival rate at vehicle

n_B = average background photon arrival rate

n_D = equivalent dark current arrival rate

Refer to Figure 4-8 for the angles θ and β.

A small rotation about the line of sight $\delta\theta$ of the incident laser beacon signal is detected by intensity changes of the two exit beams. Forming the difference Δ of the two intensities, we obtain

(4-12)

$$\Delta = \frac{2gn_S \sin\left(\frac{\pi X_o''}{g}\right)}{\pi^2 D(\theta^2 - \beta^2)} \left[\beta \sin\left(\frac{\pi D\theta}{g}\right) \cos\left(\frac{\pi D\beta}{g}\right) - \theta \cos\left(\frac{\pi D\theta}{g}\right) \sin\left(\frac{\pi D\beta}{g}\right) \right]$$

Making use of the fact that $\theta < \beta$, the intensity change $\delta\Delta$ is then equal to

(4-13)

$$\delta\Delta = \frac{2n_S \delta\theta}{\pi\beta} \sin\left(\frac{\pi X_o''}{g}\right) \cos\left(\frac{\pi D\theta}{g}\right) \left[\text{sinc}\left(\frac{\pi D\beta}{g}\right) - \cos\left(\frac{\pi D\beta}{g}\right) \right]$$

To convert the intensity changes into number of photons, we multiply the intensity changes by $1/2 \, \Delta f$ where Δf is an electrical narrowband filter bandwidth in cycles per second. This quantity is further multiplied by the quantum efficiency ϵ of the photodetector to obtain the number of photoelectrons. There will be

$$\frac{2n_S \delta\theta\epsilon}{2\Delta f\pi\beta} \sin\left(\frac{\pi X_o''}{g}\right) \cos\left(\frac{\pi D\theta}{g}\right) \left[\text{sinc}\left(\frac{\pi D\beta}{g}\right) - \cos\left(\frac{\pi D\beta}{g}\right) \right]$$

signal photoelectrons at the output of the difference amplifier. The signal shot noise, the background noise contribution and the two detectors dark current noise produce an overall photoelectron uncertainty at the output of the difference amplifier of

$$\left[\frac{\epsilon}{2\Delta f} \left\{ \left[\frac{n_S}{2} - \frac{n_S}{\pi} \sin\left(\frac{\pi K_o''}{g}\right) \text{sinc}\left(\frac{\pi D(\theta-\beta)}{g}\right) + \frac{n_B}{4} + n_D \right] \right. \right.$$
$$\left. \left. + \left[\frac{n_S}{2} - \frac{n_S}{\pi} \sin\left(\frac{\pi X_o''}{g}\right) \text{sinc}\left(\frac{\pi D(\theta+\beta)}{g}\right) + \frac{n_B}{4} + n_D \right] \right\} \right]^{1/2}$$

which is equal to

$$\left[\frac{\epsilon}{2\Delta f} \left\{ n_S \left[1 + \frac{2}{\pi} \text{ sinc} \left(\frac{\pi D\beta}{g} \right) \sin \left(\frac{\pi X_o''}{g} \right) \cos \left(\frac{\pi D\theta}{g} \right) \right] + \frac{n_B}{2} + 2n_D \right\} \right]^{1/2}$$

The signal-to-noise ratio, S/N, at the output of the difference amplifier is therefore:

$$(4\text{-}14)$$

$$\frac{S}{N} \Big]_{Diff} = \frac{\frac{n_S \delta\theta\epsilon}{\pi\beta\Delta f} \sin \left(\frac{\pi X_o''}{g} \right) \cos \left(\frac{\pi D\theta}{g} \right) \left[\text{sinc} \left(\frac{\pi D\beta}{g} \right) - \cos \left(\frac{\pi D\beta}{g} \right) \right]}{\left[\frac{\epsilon}{2\Delta f} \left\{ n_S \left[1 + \frac{2}{\pi} \text{ sinc} \left(\frac{\pi D\beta}{g} \right) \sin \left(\frac{\pi X_o''}{g} \right) \cos \left(\frac{\pi D\theta}{g} \right) \right] + \frac{n_B}{2} + 2n_D \right\} \right]^{1/2}}$$

The angle β must be chosen to maximize S/N_{Diff}. For the case of interest where the background radiation and dark current are sufficiently greater than the signal, we can ignore the β dependence in the denominator of Equation (4-14) for the determination of an optimum β. A solution of a transcendental equation will be required to determine the exact angle of operation of angle β. However, $\beta = \frac{g}{2D} = \frac{1}{N}$, where N is the number of fringes in the aperture, will provide a sufficiently convenient operating point.

Subsituting $\beta = \frac{g}{2D} = \frac{1}{N}$ into Equation (4-14), and setting the translation factor, $\sin \left(\frac{\pi X_o''}{g} \right)$, and $\cos \left(\frac{\pi D\theta}{g} \right)$ factor equal to unity, yields

$$\frac{S}{N} \Big]_{Diff} = \frac{\frac{n_S \delta\theta\epsilon}{\pi\Delta f} \left[\frac{2}{\pi} \right]}{\left[\frac{\epsilon}{2\Delta f} \left\{ n_S \left[1 + \frac{4}{\pi^2} \right] + \frac{n_B}{2} + 2n_D \right\} \right]^{1/2}}$$

$$(4\text{-}15)$$

Simplifying, we obtain

$$\frac{S}{N} \Big]_{Diff} \approx \frac{2n_S \delta\theta N \sqrt{2\epsilon}}{\pi^2 \left[\Delta f(1.4 \, n_S + .5 \, n_B + 2n_D) \right]^{1/2}}$$

$$(4\text{-}16)$$

In terms of the respective incident powers, S/N_{Diff} may be expressed as

$$\frac{S}{N}\bigg]_{Diff} = \frac{2\,P_S\,\delta\theta N\,\sqrt{2\epsilon}}{\pi^2\left[h\nu\Delta f(1.4\,P_S + .5\,P_B + 2\,P_D)\right]^{1/2}} \qquad (4\text{-}17)$$

In order to compare the above signal-to-noise ratio for the interference RLOS method, employing two laser beams with the polarization technique described in the Phase II OTS Report, it is necessary to modify the expression for polarization signal-to-noise ratio. The received signal power level will be taken as $2\,P_S$ instead of P_S in the polarization signal-to-noise ratio expression.

Therefore,

$$\frac{S}{N}\bigg]_{Pol} = \frac{2\,P_S\,\delta\theta\,\sqrt{2\epsilon}}{\left[h\nu\Delta f\left(2\,P_S + P_B + 2\,P_D\right)\right]^{1/2}} \qquad (4\text{-}18)$$

Dividing the S/N for the interference method by the S/N for the polarization method yields

$$\frac{\dfrac{S}{N}\bigg]_{Int}}{\dfrac{S}{N}\bigg]_{Pol}} = \frac{N}{\pi^2}\;\frac{2\,P_S + P_B + 2\,P_D}{1.4\,P_S + .5\,P_B + 2\,P_D} \qquad (4\text{-}19)$$

For the case where $P_B > 2\,P_S$ and P_D is sufficiently samll, we obtain

$$\frac{\dfrac{S}{N}\bigg]_{Int}}{\dfrac{S}{N}\bigg]_{Pol}} \approx 0.1\,N \qquad (4\text{-}20)$$

Hence, the improvement afforded by the interference system over the polarization system is directly proportional to the number of fringes in the detecting aperture.

4-23

4.3.2   Beacon Requirements for Remote Formation of
        Suitable Interference Fringes

The pointing requirements of each of the transmission optics in Figure 4-7 can be shown to be the same as for the single beacon of the conventional deep space system.

The necessary baseline separation, d, depends on the range, R, and the requisite number of fringes, N, following within the entrance pupil of the detection telescope. N is related to the fringe spacing, 2g, and the telescope aperture, A, by the expression

$$N = \frac{A}{2g}$$

It then follows that the baseline separation, d, is related to the other parameters as follows:

$$d = \frac{R\lambda N}{A} = \frac{R\lambda}{2g} \quad \text{for } R \gg d$$

This relationship is plotted in Figure 4-11. Suppose, for example, that we wish to produce 50 fringes across a 1-meter aperture in the region of a space vehicle 10^8 miles ($\sim 1.6 \times 10^8$ km) away using 0.5μ light. As may be seen from Figure 4-11, a baseline separation of about 5000 km is required; i.e., for interplanetary ranges. The 5000 km separation is $\sim 1/2$ the earth's diameter and the system becomes impractical since the beacons must be mutually coherent.

Over shorter distances, however, the requisite baseline separation becomes much easier to manage. For example, a separation of only 20 meters is sufficient to produce 100 fringes across a 1-meter aperture at lunar distances.

4-24

A

B

Cooperative
Earth-Moon
C Stations

Maximum Terrestial
Separation

Practical Terrestial Separation

Earth - Moon Separation = 384,000km

Earth Diameter = 12.7km

Earth 1/2 Diameter = 6km

Number of fringes across 1 meter aperture	1000	100	10
Width of a fringe	1mm	10mm	100mm
	A	B	C

$2g=$

$\lambda = .5\mu$

10^{11} 10^{10} 10^9 10^8 10^7 10^6 10^5 10^4 10^3

R-Range in Meters

10^8 10^7 10^6 10^5 10^4 10^3 10^2 10 1 10^{-1} 10^{-2} 10^{-3}

d-Distance Between Sources In Meters

Figure 4-11. Requirements for Baseline Separation

To produce a like number of fringes within a 20 cm (8-inch) aperture in the vicinity of the moon, the separation of the two earth beacons need be only 100 meters.

4.4 DETERMINATION OF ROTATION ABOUT LINE OF SIGHT BY AUXILIARY STAR TRACKER METHOD[*]

An RLOS angle change $\Delta\beta$ may be measured by means of an onboard star tracker working in conjunction with the vehicle telescope viewing the earth beacon. This provides an alternate to the polarization and interference fringe techniques previously discussed.

The vehicle telescope can determine the direction of the earth beacon to an angular uncertainty of $\Delta\theta_R$. We will assume that the vehicle telescope has a circular aperture of diameter D_R and that a detection arrangement system of the type shown in Figure 4-12 is utilized. The detection scheme is placed at the focal plane of the circular diffraction-limited objective imaging the earth laser beacon source.
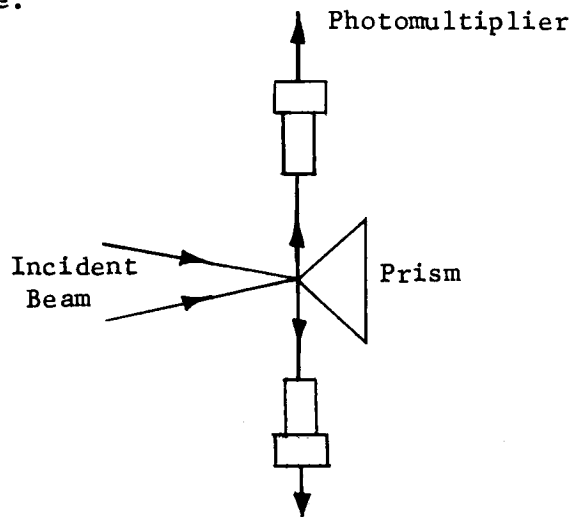
Figure 4-12. Detection Arrangement

[*]The type of star tracker considered in this section is described in context and is linear only over a narrow field.

In the Phase I OTS Report it was shown that the rms pointing error of the telescope, $\Delta\theta_R$, is approximately equal to $.61 \, \dfrac{\lambda_E}{D_R} \left(\dfrac{S_E}{N_1} \right)^{-1}$ where

$$\lambda_E \; = \; \text{wavelength of laser earth beacon}$$

and

$$\frac{S_E}{N_1} \; = \; \text{at the spacecraft, the earth beacon signal-to-noise ratio.}$$

The angular uncertainty contribution to RLOS, $\Delta\beta_E$, as determined by the telescope assuming that the star source is stationary with respect to the spacecraft is

$$\Delta\beta_E \;\; = \;\; .61 \; \frac{\lambda_E}{D_R} \left(\frac{S_E}{N_1} \right)^{-1} \cot \gamma \qquad\qquad (4\text{-}21)$$

where γ is the separation angle between the star tracker and telescope viewing the earth laser beacon. The cot γ term is the projection factor for the vector into the correct plane. Similarly the rms pointing error of the star tracker, $\Delta\phi$, is approximately equal to $.61 \, \dfrac{\lambda_S}{D_S} \left(\dfrac{S_S}{N_2} \right)^{-1}$ (for a single axis) where

$$\lambda_S = \text{average star wavelength}$$

$$\frac{S_S}{N_2} = \text{star tracking signal-to-noise ratio.}$$

Then the magnitude of the angular uncertainty of RLOS as determined by the star tracker, $\Delta\beta_S$, assuming that the earth beacon is stationary with respect to the spacecraft, is:

$$\Delta\beta_S \;\; = \;\; .61 \; \frac{\lambda_S}{D_S} \left(\frac{S_S}{N_2} \right)^{-1} \frac{1}{\sin \gamma} \qquad\qquad (4\text{-}22)$$

In general the factor 0.61 in the above expression is theoretical. In practice this constant is always somewhat less favorable.

If both sources of light move, then the rms RLOS uncertainty,

$\Delta\beta$, as determined by both detectors, is

$$\Delta\beta = \left[\left(\Delta\beta_E \right)^2 + \left(\Delta\beta_S \right)^2 \right]^{1/2} \tag{4-23}$$

Substituting the values of $\Delta\beta_E$ and $\Delta\beta_S$ from Equations (4-21) and (4-22) into Equation (4-23) yields

$$\Delta\beta = .61 \left[\frac{\lambda_E^2 \cot^2\gamma}{D_R^2} \left(\frac{S_E}{N_1} \right)^{-2} + \frac{\lambda_S^2}{D_S^2 \sin^2\gamma} \left(\frac{S_S}{N_2} \right)^{-2} \right]^{1/2} \tag{4-24}$$

Solving Equation (4-24) for the star tracker signal-to-noise ratio necessary to obtain an rms RLOS uncertainty of $\Delta\beta$ gives

$$\frac{S_S}{N_2} = \left[\left(\frac{D_S \Delta\beta \sin\gamma}{.61 \lambda_S} \right)^2 - \left(\frac{\lambda_E}{\lambda_S} \frac{D_S}{D_R} \cos\gamma \right)^2 \left(\frac{S_E}{N_1} \right)^{-2} \right]^{-1/2} \tag{4-25}$$

The following example for this RLOS determination method gives an indication of performance. Refer to Table 4-2 for the vehicle telescope and laser earth beacon parameters. Table 4-3 lists the pertinent star tracker parameters. The star tracker signal-to-noise ratio required to obtain 1 arc-minute RLOS angular uncertainty is computed from Equation (4-25) on the basis that the distance between earth terminal and vehicle is 10^8 miles (daytime operation is assumed). The choice of the star Canopus for stellar tracking has been used since Canopus is a bright star out of the galactic plane which provides large separation angle between earth beacon and star. The minimum angular separation, γ, between Canopus and earth is typically 30 degrees.

The star tracker signal-to-noise ratio $\frac{S_S}{N_2}$ required to obtain the 1 arc-minute RLOS angular uncertainty is appreciably less than unity. This is an

TABLE 4-2

TYPICAL PARAMETERS FOR ARGON EARTH BEACON
AND VEHICLE RECEIVER

Input Parameter	Symbol	Reception in space of Earth Transmission Day Operation
Range (statute miles)	R	10^8
Wavelength Received (Å)	λ_E	5145 (argon)
Transmitted Power (watts)	P	100
Transmitted Beam Divergence (arc-sec)	α_t	5
Diameter of Receiving Aperture (cm)	D_R	100
Receiver Field of View (arc-sec)	α_R	3
Atmospheric Transmission (60° from the zenith)	τ_A	· 0.6
Optical System Transmission (%)	τ_o	50
Pre-Detection Filter Transmission (%)	τ_f	50
Pre-Detection Filter Bandpass (Å)	$\Delta\lambda$	1.0
Received Background Earthshine Power (watts)	P_B	4.08×10^{-12}
Dark Current Radiant Input Power Equivalent	P_D	Negligible in comparison with signal shot noise and background
PMT Quantum Efficiency (%)	ϵ	0.10
Post Detection Low Pass Filter Bandwidth (cps)	Δf	10
Received Signal Power at Vehicle (watts)	P_S	3.13×10^{-13} watts
Earth Beacon Tracking Signal-to-Noise Ratio	$\dfrac{S_E}{N_1}$	90

TABLE 4-3

TYPICAL STAR TRACKER PARAMETERS

Parameter	Symbol	Value
Effective Aperture of Star Tracker Collector (cm)	D_S	10.16 (4 inches)
Cone Angle (degrees)	θ	5
Field of View (steradians)	Ω	6×10^{-3}
Stellar Tracker Optical Efficiency (%)	η_o	50
Post Detection Filter Bandwidth (cps)	Δf	10
S-20 Photocathode Quantum Efficiency	ϵ	0.2
Night Sky Spectral Radiance @ 4000Å (watts/cm^2/star/Å)		1.3×10^{-14}
Star		Canopus
Declination		$-52° 40' 03.67''$
Right Ascension		0.6 hr. 22 min. 50.501 sec.
Visual Magnitude		-0.86
Spectral Class.		Fo
Photoelectric Magnitudes		S-20-0.55 silicon 1.00 S-17-0.59 S-4 -0.45

extremely modest requirement as can be seen from considering the star tracker

signal-to-noise ratio determined from the parameters in Table 4-3. The tracker

signal-to-noise ratio is equal to

$$\frac{S_S}{N_2} = P_S \left[\frac{e}{2h\nu\Delta f \left[P_S + P_B + P_D \right]} \right]^{1/2}$$

Where P_S is the receiver stellar signal power in watts,

P_B - is the background power in watts

P_D - is the detector dark noise power in watts

e - is the detector quantum efficiency

h - is Planck's constant = 6.6256×10^{-34} joules-sec

Δf - is the post-detection filter bandwidth in cps.

A star of zero (visual) magnitude $\left(m_v = 0 \right)$ yields a luminous

flux density I_o of 2.1×10^{-10} lumens per cm^2 or 3.1×10^{-13} watts per cm^2 at

a point outside of the atmosphere of the earth. The relationship between the

flux density, I, received from a star of visual magnitude m_v and a zero magnitude

star is given by,

$$I/I_o = 2.5.^{-m_v}$$

For a star tracker collector of effective aperture diameter D_S

inches, the power, P, in watts available at the collector is given by,

$$P = \frac{1.57 \times 10^{-12} D_S^2}{2.51^{m_v}} \quad \text{watts.}$$

Therefore P_S is equal to $P\eta_o K$ where η_o is the tracker system optical efficiency ($\approx$ 50%) and K is a multiplicative constant determined by star spectral class and responsivity of detector ($\approx$ 0.33). For the tracker parameters given in Table 4-3, $P_S = 9 \times 10^{-12}$ watts. The collected background power is 1.27×10^{-11} watts. Therefore, $P_B = 1.27 \times 10^{-11} \times (.33) = 6.35 \times 10^{-12}$ watts. The detector dark current contribution is negligible in comparison with P_S and P_B. For a 10 cps post-detection low pass filter bandwidth the tracker signal-to-noise ratio is 346! A comparison of this result with what is required to perform 1 arc-minute RLOS determination clearly indicates the adequacy of performance of this type of RLOS system.

No attempt has been made to optimize parameters but merely to indicate the capability of this type of RLOS determination system, and the freedom of choice in design paramters. It is evident that RLOS determination by this star tracker technique is superior to the polarization and interference fringe methods.

However, this conclusion only applies to the argon laser beacon, He-Ne transmitter case. With the advent of the infrared lasers (CO_2 laser operating at 10.6μ), the requirement for the 1 arc-minute RLOS determination is relaxed considerably, and the question of RLOS determination must again be re-examined.

4.5 TORQUE INDUCED LINE-OF-SIGHT ERROR AS A FUNCTION OF POINTING SERVO INTEGRATION TIME

4.5.1 Introduction

In our discussions of RLOS techniques, bandwidths of from 0.1 to 10 cps were used for illustrative calculations. The only source of pointing

error considered was that due to the fluctuation components of the photocathode current in the pointing error sensors. It was evident from the calculations that the error could always be reduced by bandwidth reduction. But as a result the system would become increasingly susceptible to direct torque disturbances which introduce additional error components.

The following discussion summarizes the relationship between the bandwidth of a servo and its ability to resist torque disturbances. Given the specific torque disturbances of a space optical communications system, this discussion will provide a basis for choosing a servo bandwidth to match.

4.5.2 Analysis

In the frequency range where the pointing servo open loop gain, $KG(j\omega)$, is much larger than unity, the pointing error, E_c, of the servo controlled telescope is related to the error, E_u, of the uncontrolled telescope by the relation

$$E_c = \frac{E_u}{KG(j\omega)} \qquad (4-26)$$

where $\left| E_u \right| = \left| \frac{T_o \sin \omega_o t}{J \omega_o^2} \right|$, J is telescope inertia, and To is the peak magnitude of sinusoidal disturbance torque.

Furthermore, the equivalent noise bandwidth of the pointing servo can be established from a knowledge of the open loop gain characteristics. Hence, for a general type of control characteristic, it is possible to determine

the minimum bandwidth required to produce a given low frequency open loop

gain characteristic. In the following open loop plot, unit loop gain occurs

at a point on the -6 db/oct slope.

$$KG(j\omega) = \frac{\omega_o^2}{(j\omega)^2}\left[\frac{1 + j\omega\tau_1}{1 + \frac{j\omega\tau_1}{n}}\right]$$
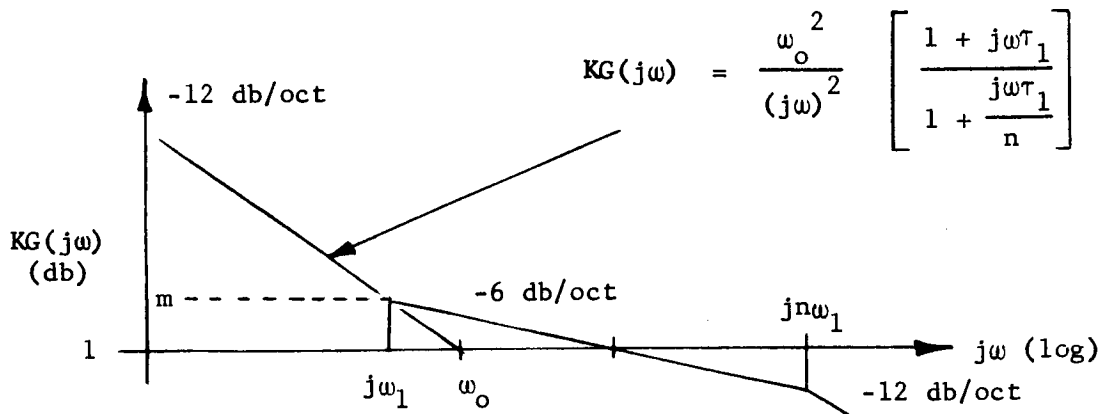
Here m is the value of $KG(j_\omega)$ at ω_1 and n is defined by the diagram. The

noise bandwidth of the system can be shown to be

$$\omega eq = \omega_o\left(\frac{1 + m}{1 - \frac{1}{n}}\right)\frac{\pi}{2\sqrt{m}} \tag{4-27}$$

The low frequency loop gain is expressible as $\left(\frac{\omega_o}{j\omega}\right)^2$. Assuming now that

unity loop gain occurs at the center of the line with the -6 db/oct slope, to

obtain greatest phase margin, then $m = \sqrt{n}$ and

$$\omega eq = \omega_o\left(\frac{1 + m}{1 - \frac{1}{m^2}}\right)\frac{\pi}{2\sqrt{m}} \tag{4-28}$$

which attains a minimum value of 4.07 ω_o when m = 3 (or n = 9). For this case

the low frequency loop gain has a magnitude of

$$\left|\frac{\omega eq}{4.07\omega}\right|^2 \tag{4-29}$$

4-34

The expression is extremely useful since it gives the value of open loop gain (or equivalently the torque disturbance attenuation factor) as a function of bandwidth ωeq , for the assumed type of system.

Another expression would apply if the goal is simply to obtain maximum low frequency torque level and minimum equivalent noise bandwidth (i.e., with m not restricted equal to $\sqrt{n}$). In this case minimum noise bandwidth is obtained when m = 1, regardless of the value of n; hence,

$$\omega eq_{min} = \frac{\pi}{1 - \frac{1}{n}} \tag{4-30}$$

For the previous value of n = 9, ωeq is now 3.53 ω_o instead of 4.07 ω_o and the low frequency loop gain expression becomes

$$\left| \frac{\omega eq}{3.53 \ \omega_o} \right|^2 \tag{4-31}$$

Other types of system characteristics can be so analyzed to obtain similar results. One such alternate, which is shown following, has proportional plus integral control to increase low frequency loop gain without significant effect on noise bandwidth.
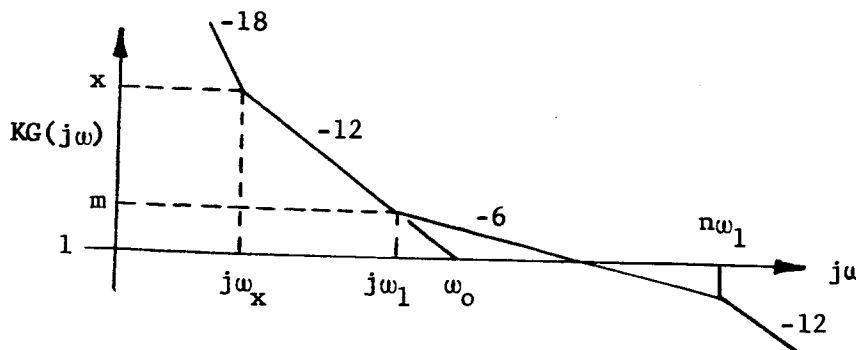
For X $\gg$ m, the noise bandwidth will be nearly

$$\omega eq = \frac{\pi}{2\sqrt{m}} \left(\frac{1 + m}{1 - \frac{1}{n}} \right) \qquad (4\text{-}32)$$

but as X approaches n, the bandwidth increases and is more accurately given by

the expression

$$\omega eq = \omega_0 \ \frac{\pi}{2} \ \frac{m + \dfrac{m}{\sqrt{x}} + \dfrac{1}{m} + \dfrac{1}{x} \left(\sqrt{m} + \sqrt{x} \right) \left(1 - \dfrac{1}{n} \right)}{\left(1 - \dfrac{1}{n} \right) + \dfrac{m}{x} \left(1 - \dfrac{2}{n} \right) - \dfrac{m}{x} - \dfrac{1}{mx}} \qquad (4\text{-}33)$$

The expression for open loop gain at frequencies $\omega \leq \omega_x$ is

$$\left(\frac{\omega_0}{\omega} \right)^3 \ \frac{1}{x} = KG(j\omega) \qquad (4\text{-}34)$$

These equations could be utilized to obtain results imilar to
Equations (4-30) and (4-31) preceding. However, this is unnecessary in
order to obtain approximate yet representative results. One procedure is
to sketch particular open loop gain characteristics (making sure that a
stable system will be thus provided) and use the preceding equations to
evaluate ωeq. ·

Systems which resort to slopes even steeper than -18 db/oct at
low frequency are possible and may be advantageous. However, expressions
for ωeq and $KG(j\omega)$ have not yet been derived for such cases.

EXAMPLE: A telescope $(J = 100 \text{ slug ft}^2)$ shall be positioned by torquers in a loop that is lead-lag stabilized. A single sinusoidal torque disturbance of To = 0.001 lb-ft and at $\omega_o = 0.01$ **rad/sec** is acting on the telescope. The peak uncompensated error which results (see Equation 4-26) is

$$\left| E_u \right| = \frac{.001}{(100)\ (.01)^2} = .1 \text{ rad} = 5.7°$$

and it is desired that this be reduced to 1 arc-minute rms or 1.4 arc-minute peak. This requires an open loop gain of

$$\left| KG(j\omega) \right|_{min} = \frac{5.7 \times 60}{1.4} = 244$$

This can be obtained with an equivalent noise bandwidth of

$$\omega eq = 4.07\ (.01)\ \sqrt{244} = 0.635 \text{ rad/sec from Equation (4-29)}$$

$$\omega eq = 3.53\ (.01)\ \sqrt{244} = 0.550 \text{ rad/sec from Equation (4-31).}$$

SECTION V

MEASUREMENTS OF INTENSITY STABILITY
IN THE FAR FIELD OF A GAS LASER

5.1 INTRODUCTION

Calculations of signal power received on earth from an optical communications sytem located in deep space generally assume diffraction-limited concentration of light in the transmitted beam. The practical extent to which this degree of concentration can be stably achieved has been investigated by measuring the beam intensity distribution and fluctuation characteristics in the far field of a typical, high quality gas laser.

5.2 CAUSES OF FLUCTUATIONS

Anything influencing the structure of laser cavity modes is capable in principle of influencing the phase and amplitude distributions of an emerging laser beam. As a result, the intensity distribution of the laser beam in its far field may exhibit time-dependent fluctuations and corresponding time-variations of the received signal power. The laser cavity modes (and hence the far field distributions) can be disturbed by (a) an effect which tends to alter the transverse distribution of the optical path between the laser mirrors and (b) an effect which tends to change the transverse gain distribution within the plasma tube and hence alter the amplitude distribution with each pass through the active medium. Such disturbances may be produced, for example, by mechanical changes of the mirror alignment or by random changes

of the gas density distribution within the plasma tube. The subject of in-
homogeneous gain distributions has previously been studied theoretically by
Statz and Tang.[1]

5.3 EXPERIMENTAL PROCEDURE

Experiments were devised to assess the beam properties and to meas-
ure the intensity fluctuations in the far field of the Helium-Neon laser pre-
viously illustrated in Figure 3-11.

The plasma tube was designed for a nominal output power of 10 milli-
watts in a single transverse mode. The structure supporting the plasma tube
and the laser mirror was made extremely rigid so as to play a neutral role in
the experiments. The laser was operated in the lowest order transverse mode[2]
(TEM$_{oo}$) at 6328Å.

The experimental arrangement was as shown in Figure 5-1. The laser
beam was focused to its diffraction limited spot (its far field pattern) which
was then magnified by a short focal length lens and imaged onto a distant screen.
This arrangement produced a conveniently large image of the far field pattern
and facilitated the subsequent measurements.

Photoelectric measurements were made with the four photomultipliers
shown in the figure. Three were used to measure the intensity fluctuation at
different points in the far field using the fiber optics light pipes as probes.
One was used to monitor the direct laser output at the low output end of the laser

---

[1]H. Statz and C.L. Tang: Problem of Mode Deformation in Optical Masers.
J.Appl.Phys., Vol.36, No.6, June 1965, pp. 1816-1819.

[2]As shown in Figure 5-1, a near-hemispherical mirror configuration was used
to ensure stable single transverse mode operation.
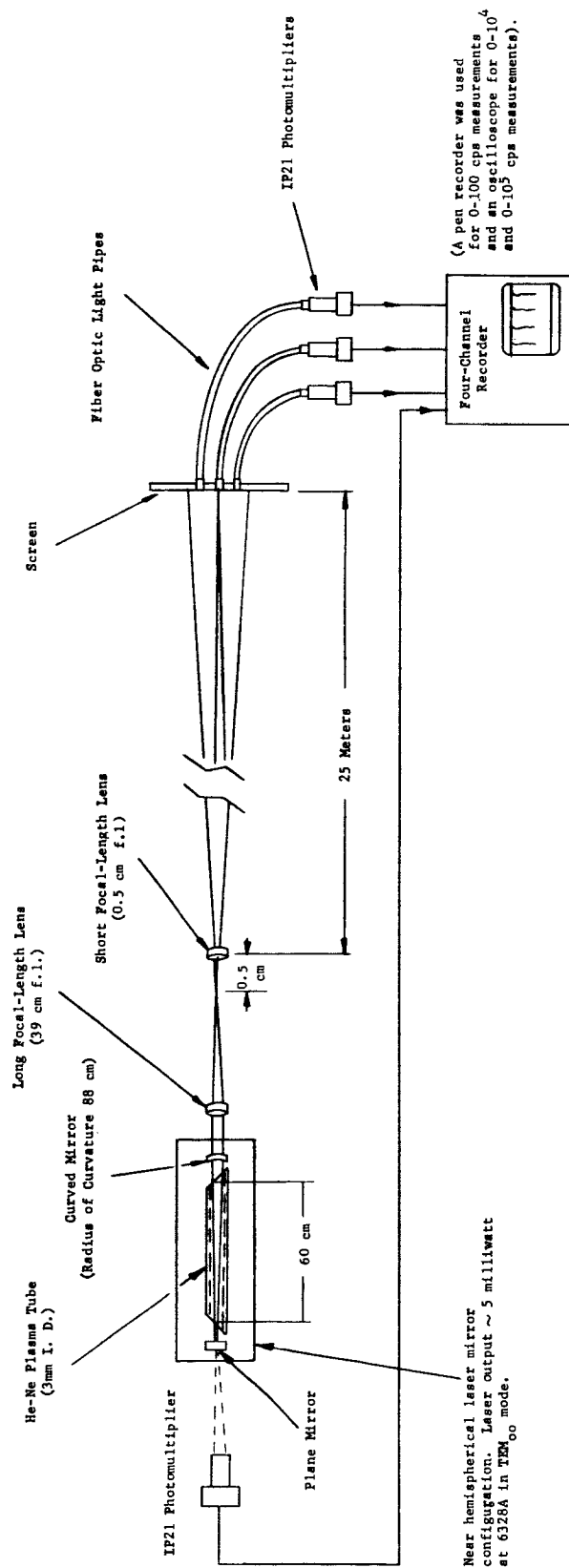
Figure 5-1.   Diagram of Experimental Setup for Measurement of
Intensity Stability in the Far Field of a Laser Beam

All photomultipliers were powered from the same supply with a voltage setting that produced a maximum anode current of 50 μa; i.e., half the maximum rating of the 1P21's that were used. Variations in sensitivity among the photomultipliers were balanced out by varying the load resistors so as to produce identical responses to the same light input.

5.4 RESULTS

The principal results were as follows:

(a) The diameter of the far field pattern was found to be in agreement with diffraction theory. Measurements of the diffraction spread of the laser beam (shown in Figure 5-2) corresponded with the limiting aperture which in this case was the 3 mm bore diameter of the plasma tube.[3]

(b) Neither intensity fluctuations within the far field pattern nor gross lateral motions of the entire far field pattern were found to be observable visually.

(c) By means of the photoelectric measurements, the relative magnitude of far-field intensity fluctuations was shown to be approximately constant across the whole far field pattern and to have an rms value of between 0.5% and 1% of the maximum intensity in the center of the pattern. This was only slightly more

---

[3] cf., for example, D. Dutton, M.P. Givens, R.E. Hopkins: Some Demonstration Experiments in Optics Using a Gas Laser. Am.J.Phys., Vol.32, No.5, May 1964, pp. 355-361.
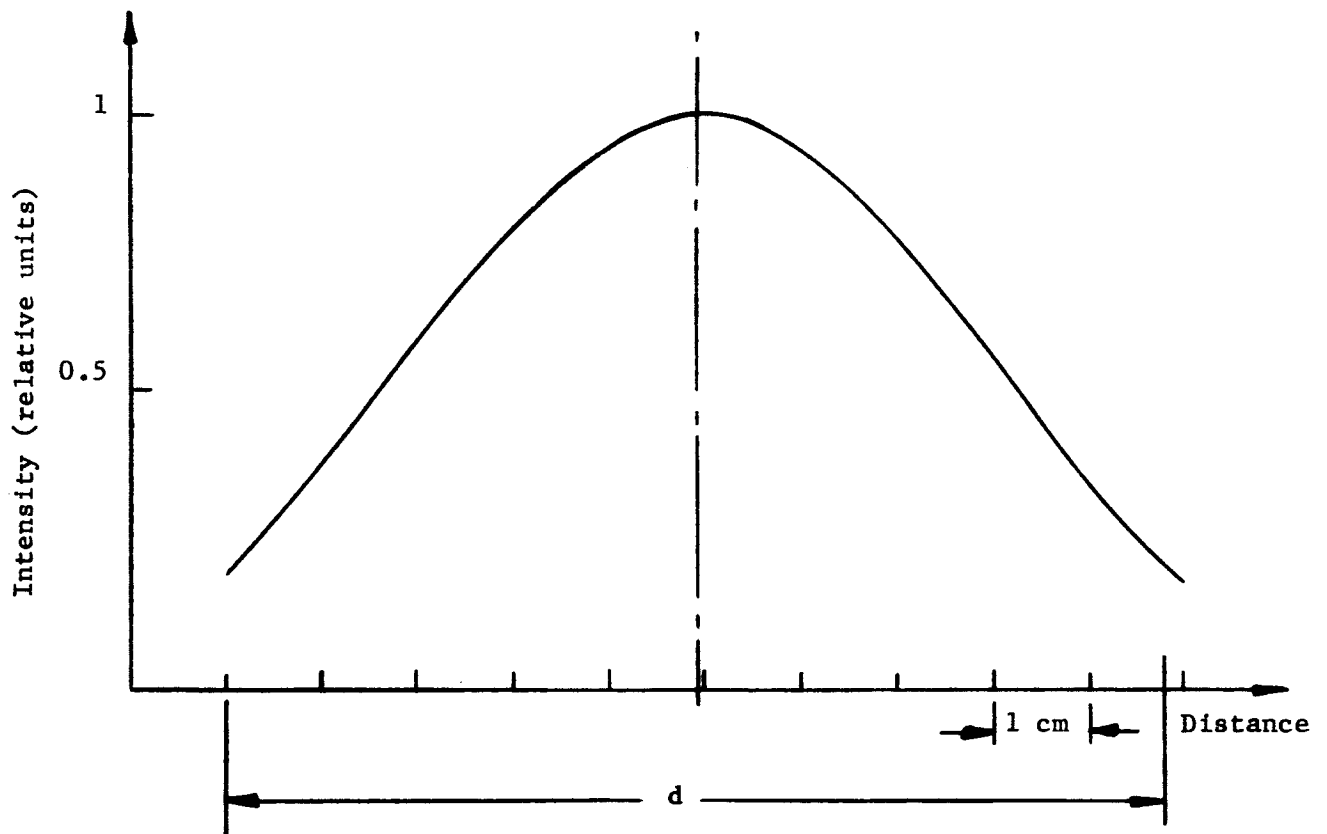
Figure 5-2. Intensity Across Magnified Far Field Pattern of Laser.
d = Diameter of Airy Disc for Homogeneously Illuminated
Circular Aperture of Same Diameter as Laser Tube.

than the relative magnitude of fluctuations appearing
in the entire laser output measured in the near field.

(d)   There was close cross-correlation of the intensity

fluctuations at different points of the far field

pattern with respect to each other and with respect

to the intensity of the entire laser beam. When the

laser output power was reduced (by increasing the

mirror spacing of the near-hemispherical resonator,

which produces higher diffraction losses) the inten-

sity fluctuations increased considerably.

(e)   When the output of the photomultipliers was observed

with an increased bandwidth of 0 to 10^4 cps, the

intensity fluctuations in the far field were found

to be only slightly increased. The effect of further

increasing the bandwidth to 10^5 cps was merely to raise

the level of the shot noise to a comparable magnitude.

Some of the more interesting fluctuation recordings are repro-
duced in Figures 5-3 through 5-6. In making these measurements the usual
initial procedure was to completely block the laser and to trace out the
reference baseline for about a minute. Then, direct readings of the inten-
sity fluctuations were recorded, the values of which were established by
the initial reference traces. When increased resolution was wanted,
the recorder was switched to a more sensitive scale without regard to
the baseline. At the end of certain recordings, the baseline and the
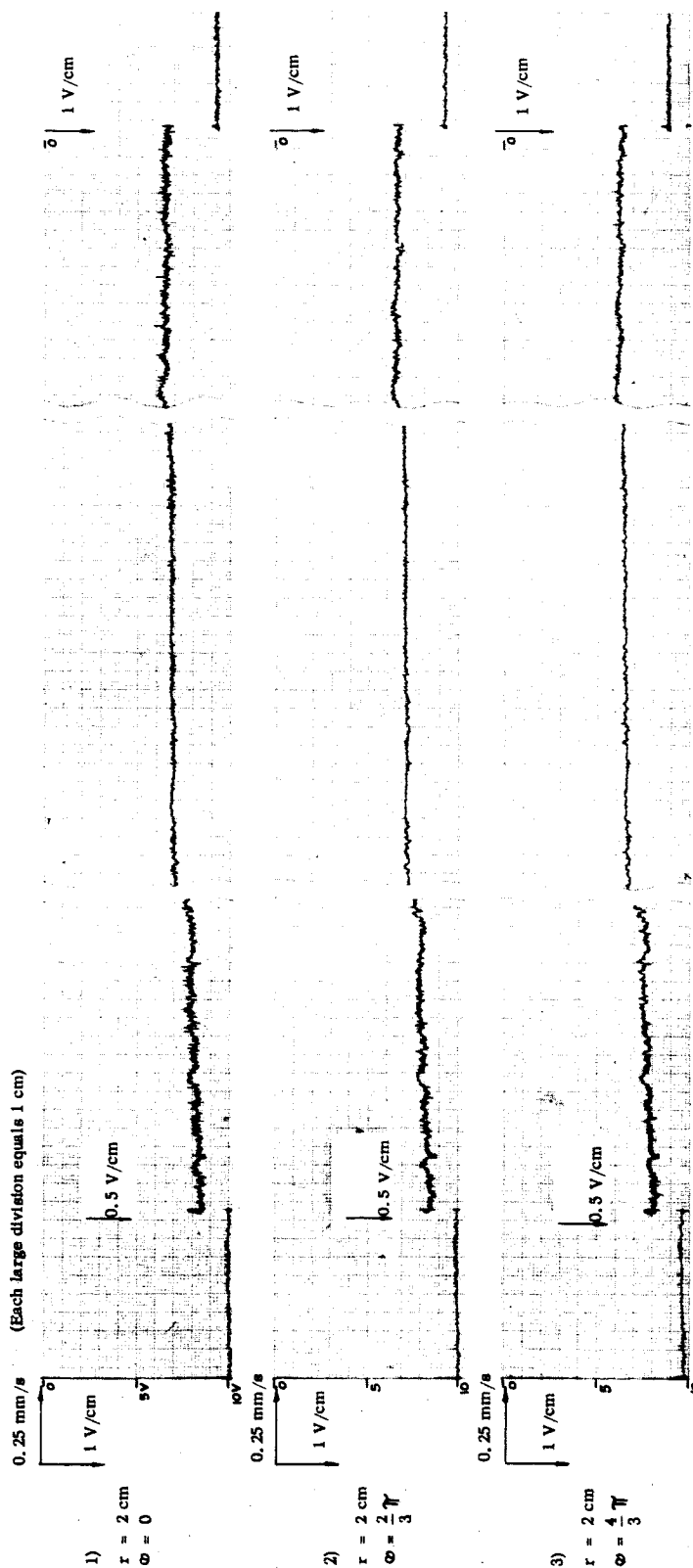
Figure 5-3. Recording of Long-Term Behavior of Intensity Fluctuation
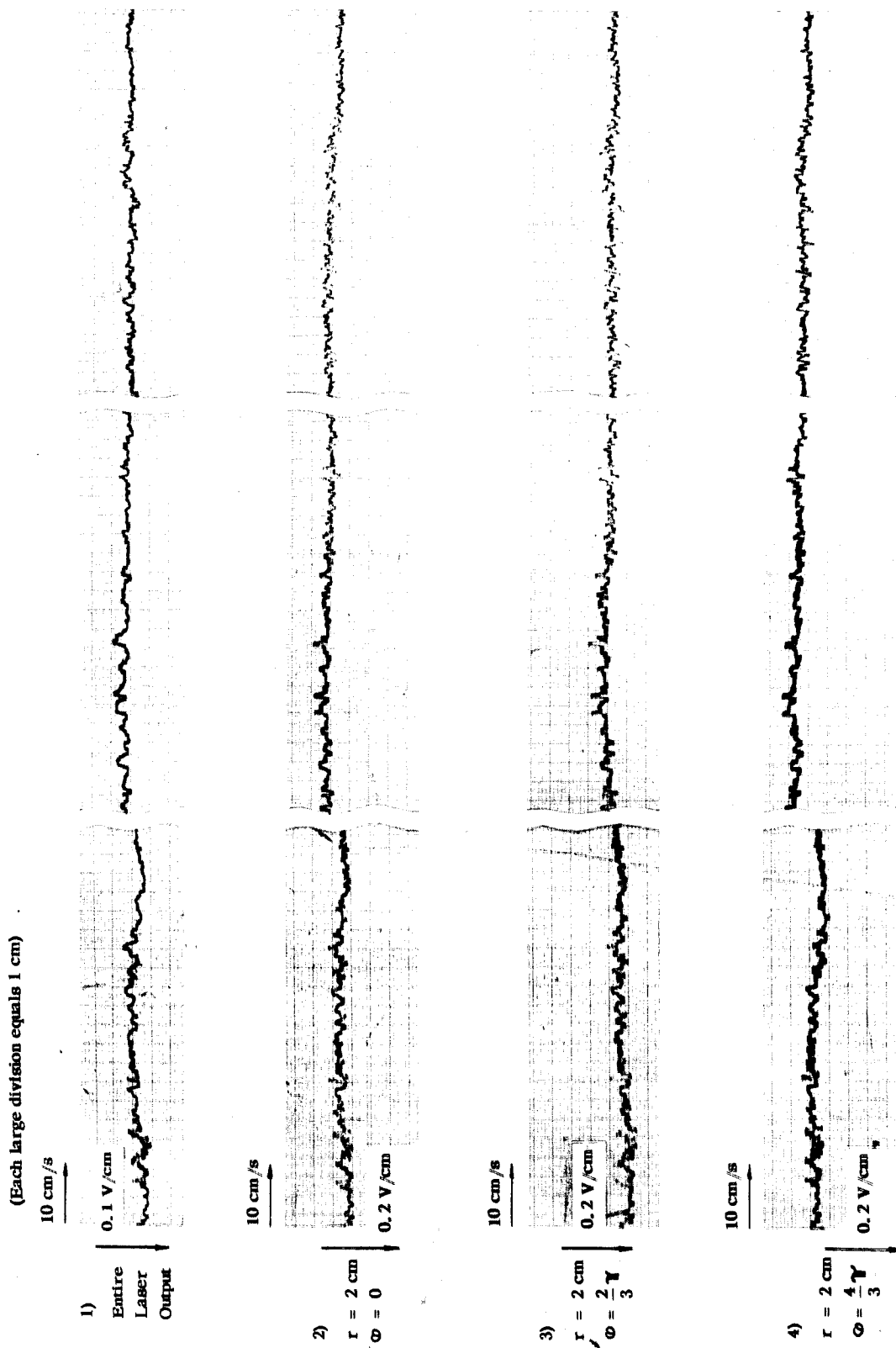
Figure 5-4. Recording of Short-Term Behavior of Intensity Fluctuation

(Each large division equals 1 cm)

0.5 mm/s

0.2 V/cm

1 V/cm

1)

Entire
Laser
Output

0.5 mm/s

1 V/cm

0.5
V/cm

2)

r = 0 cm

0.5 mm/s

1 V/cm

0.5 V/cm

3)

r = 1.5 cm

0.5 mm/s

1 V/cm

0.5 V/cm

4)

r = 3.0 cm

0.5 mm/s

1 V/cm

0.5 V/cm

5)

r = 4.5 cm

0.5 mm/s

1 V/cm

0.5
V/cm

6)

r = 6 cm
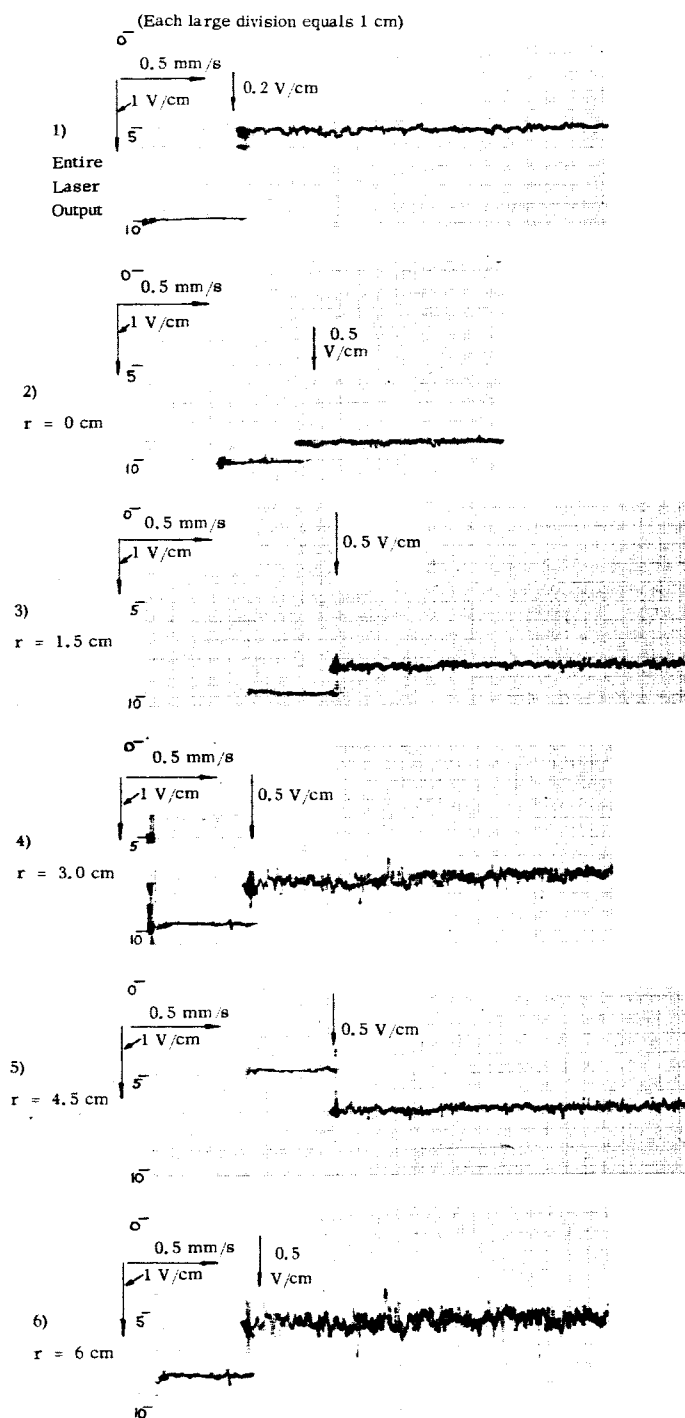
Figure 5-5.   Recordings Used to Measure Relative RMS
Fluctuations at Various Distances of the
Sampling Points from the Center of the
Far Field Pattern.

5-9
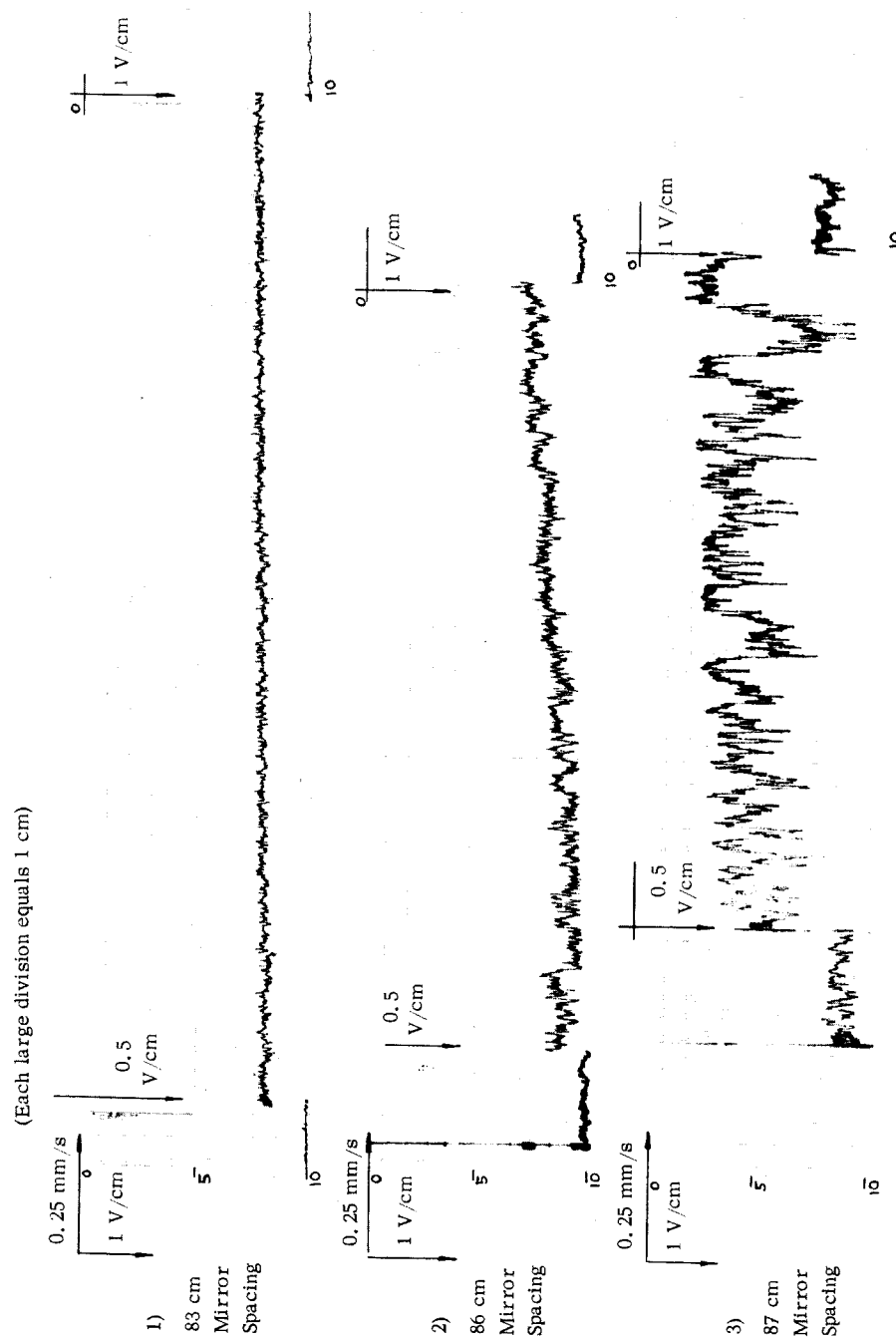
Figure 5-6. Recordings of Fluctuations When the Laser Power is Reduced by Increasing the Mirror Spacing

absolute value of the fluctuations were reestablished to provide a check on
the consistency of the measurements.

In the figures, r denotes the radial distance of a given light
pipe from the centroid of illumination in the far field pattern and φ denotes
its azimuth position.

Estimates were made of the rms values of the recorded intensity
fluctuations based on the process being Gaussian. In a Gaussian process the
peak-to-peak value of the fluctuating intensities, during 95% of the obser-
vation time, is four times the rms value.

Figure 5-3 illustrates portions of the recorded long-term behavior
of intensity fluctuations. The traces are seen to decline at an equal rate
which indicates a continuous decrease in laser output during the observation
period. This decrease was evidently caused by dust particles settling onto
the resonator mirrors and onto the Brewster-angle windows of the plasma tube.
The relative intensity fluctuations were estimated to be 0.9% rms.

Figure 5-4 illustrates portions of the recorded short-term behavior.
Simultaneous recordings are shown of the intensity fluctuations at three points
in the far field pattern positioned the same as for Figure 5-3. In addition,
a recording of the entire laser output is shown. This figure illustrates the
high degree of cross correlation between the fluctuations at the different
points in the far field, and between these points and the full beam cross
section. Minor deviations from unity cross correlation do occur but only at
a comparatively slow rate of up to a few cycles/sec. These deviations are
likely due to local atmospheric effects.

Figure 5-5 is meant to illustrate the dependence of the relative rms intensity fluctuations on the distance of the sampling point from the center of the far field pattern. The relative rms fluctuation in the center amounted to about 0.5%, which was about the same value as for the total laser output. For the traces illustrated in the figure, the respective rms values are as follows:

Trace No.	Conditions	rms Fluctuations
1	Full beam cross section	0.4%
2	r = 0 cm (center of pattern)	0.5%
3	r = 1.5 cm	0.7%
4	r = 3.0 cm	1.2%
5	r = 4.5 cm	1.8%
6	r = 6.0 cm	2.5%

To a good approximation the fluctuations do not exceed about 1% across the majority of the far field pattern as may be seen by comparing the above values with the intensity distribution shown in Figure 5-2 and obtained with the same setup.

Figure 5-6 illustrates the considerable increase in the intensity fluctuations that results when the laser power is reduced by increasing the mirror spacing so as to increase the diffraction loss of the resonator. The first trace corresponds to a mirror spacing of 83 cm which produced a total output of 5 mw. The second is for a spacing of 86 cm, for which the output was 2 mw. The third is for a spacing of 87 cm and a total output of 0.5 mw. At the exact hemispherical spacing of 88 cm the output dropped to zero.

5.5 CONCLUSIONS

From the nature of the fluctuation recordings we may infer that the sources of the fluctuations were predominantly smaller than the width of the cavity mode and statistically independent. Thus it is likely that the majority of the observed fluctuations stem from dust particles floating into the resonant path between the Brewster-angle windows and the laser mirror and floating also into the near-field region of the laser beam.

As the fluctuations in the far field turned out to be relatively small, the possibility of troublesome inhomogeneities in the gain distribution within the plasma tube could be ruled out. This is in agreement with the calculations by Statz and Tang.[1]

Based on the intensity stability data above, and provided the laser operates in a fundamental transverse mode, the following conclusions are warranted:

(a) The laser beam does not exhibit intensity fluctuations of sufficient magnitude to be detrimental to a deep-space optical communications system. As was shown by sampling various regions in the far field of the laser beam, the fluctuations are typically about 1% and this amount will not degrade the signal-to-noise ratio of a communications channel.

(b) Discernible intrinsic angular fluctuations of the laser beam were absent; i.e., there was no tendency

---

[1]Statz and Tang, *Op.Cit.*

of the centroid of illumination in the far field
to fluctuate spatially. Positive indication of
such "beam wander" would have been as follows:

(1) The time average distribution of light
     in the far field is larger than can be
     accounted for by diffraction theory.

(2) Appreciable negative cross correlation
     exists between records of the intensity
     fluctuations taken at opposite sampling
     points across a diameter of the far field
     pattern.

Both of these effects were absent to within the sensitivity of
our measurements which we estimate to be at least within a few percent of
the basic beam spread angle. And since any _fractional_ variation of the
laser beam spread angle is unaffected by the telescope of an optical com-
municator, it is therefore demonstrated that a mechanically stable He-Ne
laser, as far as beam-angle fluctuations are concerned, is suitable for a
deep-space optical communications system.

SECTION VI

CHANNEL SEPARATION

6.1   INTRODUCTION

Development of effective techniques for adequate channel separation is the key to using common telescope optics for both the receiving (beacon tracking) function and the transmitting function of a spaceborne optical communications system. This problem can be stated as follows: How can we arrange for the fine guidance photomultipliers to be signal quantum noise limited at 4880Å and 5145Å in the presence of scattered light at 6328Å from the neighboring high-power He-Ne laser transmitter? More particularly, how can we accomplish optical duplexing without resort to time sharing techniques?

6.2   SOURCES OF UNWANTED LIGHT

Any transmit light incident on the receive detectors is derived from reflection and scattering from the surfaces of the optical elements common to both the transmit and receive channels. Referring back to Figure 2-1, the main sources are evidently:

(a)   Scattering at the beamsplitter

(b)   Subsequent scattering of residual collimated light transmitted through the beamsplitter

(c)   Reflection from the transfer lens L_1

(d)   Reflection from the central dead zone of the telescope secondary mirror

The amount of light back-reflected from the transfer lens L_1 and

the telescope can be expected to be small although not necessarily negligible,

compared with the transmit light diffusely scattered from the beamsplitter on

reflection of the transmit beam.

6.3 CHANNEL SEPARATION REQUIREMENTS

The magnitude of channel separation needed in the Laser/Optics

Techniques type of optical system may be established by considering the signal

requirements of the tracking servo detectors as follows.

The most difficult case (i.e., when maximum exclusion of transmit

light from the receive channel is required) is when, with negligible background

light, the amount of incoming beam light is barely sufficient for the tracking

function to be carried out. Suppose, for example, that the integration time

of the tracking servos is of the order of 10^{-2} seconds. Then, for reasonable

servo performance with a bandwidth of some tens of cycles per second, a mini-

mum of about 10^4 signal photoelectrons are needed per second. Given a de-

tector quantum efficiency of 10% and an optical efficiency of 33% leading to

the detectors, it follows that a minimum of 3×10^5 photons per second of

signal light (provided by the beacon) are needed by the tracking channel.

Therefore, the channel separation problem reduces to ensuring that the track-

ing channel detects fewer than 3×10^5 photons per second of the high-power

laser light present in the neighboring transmit channel.

As a specific example, let the transmit laser power be 100 milli-

watts (3×10^{17} photons/second). What the tracking channel detects of this

must be small compared with 3×10^5 photons per second. Thus, the required channel separation must exceed the ratio of these numbers, which is about 10^{12}.

Twelve decades of channel separation are a worst case number for the He-Ne communicator considered in the OTS Reports. The actual needs may vary by several orders of magnitude one way or the other. With such considerations in mind our efforts were directed towards demonstrating approximately 12 decades of channel separation (120 db) by techniques that can be extrapolated to more or less separation as dictated by exact requirements of future systems.

A reduction in receive-channel sensitivity to beacon light may result from the methods used to suppress unwanted transmit beam light. Moreover, the receive channel detectors will in general have different sensitivities at the receive and transmit laser wavelengths.

An appropriate figure of merit M for channel separation which takes these considerations into account can be defined as follows:

$$M \text{ (in db)} = 10 \log \frac{P_t}{P_d}$$

where P_t is the power of the transmit laser, and P_d is the response of the receive channel photodetectors to light originating from the transmit laser put in terms of equivalent signal power (i.e., referred to detector sensitivity at the received signal wavelength).

If the transmit laser power is P_t then

$$P_d = \frac{\tau_t \epsilon_t}{\tau_r \epsilon_r} P_t$$

where τ_r is the optical transmission at the receive wavelength, τ_t is the optical transmission at the transmitter wavelength, ϵ_t is the detector quantum efficiency at the transmit wavelength and ϵ_r is the detector quantum efficiency at the receive wavelength.

6.4 APPROACH

From the outset it appeared feasible to achieve adequate channel separation mainly by the use of conventional all-dielectric filters and lens coatings. Our subsequent investigations showed that indeed this was the case. The approach taken was based on the following reasoning:

(1) Any red laser light incident in the direction of the detector will be derived from back-scatter and reflection from the surface of the transfer lens and from the beamsplitter surfaces. There will also be a component reflected back by the telescope's secondary mirror. Scattered light will be attenuated by an amount proportional to the square of the distance away, so it is advisable to make the spacing of optical components as large as possible. Reflected light from the lenses will be attenuated to a higher degree if the surface curvatures are as small as possible, provided that multiple imaging does not produce bright focused "ghosts". Each lens surface should therefore be coated with a VLR (very low reflectance) coating tuned to the laser wavelength. This will tend to reduce each surface reflectivity by about a factor of 10^3.

The central area of the secondary mirror will reflect axial rays back through the hole in the primary mirror. The extent of this area is easily computed

and, if necessary, to prevent the axial rays from returning in the direction of their source, this portion of the secondary mirror can be occulted.

(2) It is feasible to make a dichroic beamsplitter, with special design but using conventional dielectric multilayer techniques, that reflects almost completely the 6329Å band (99%) and transmits about 80% of the 4880Å - 5145Å band.

(3) The receiver photomultipliers can be protected from residual 6328Å light by the provision of one, or more, filters having high reflectance for 6328A and good transmission for the 4880Å - 5145Å band. A figure of 99.9% reflection and 80% transmission for these two regions, for each filter, should be achievable. If more than one such filter is needed, a slight wedge should be provided between them to avoid interaction of the coherent light.

(4) To pursue the all-dielectric approach the above filters should be designed, fabricated, and their spectral response measured, especially the value of transmission where this is very low. Special test gear is necessary to measure the resulting channel separation and must be set up accordingly.

When a dichroic beamsplitter and say two rejection filters are used, attenuation of the 6328A light by a factor of at least 10^9 can be expected with a transmission of 50% of the shorter wavelengths. With the further precautions cited above, an additionally large factor of attenuation can be expected by minimizing scatter and reflections and additionally by use of a non-red-sensitive photomultiplier.

6.5 MEASUREMENT TECHNIQUES

A tremendous range of light levels is encountered in the development of channel separation techniques. As we have already discussed, the ratio of direct transmit laser power to what ultimately can be tolerated by the receive

channel detectors is about twelve decades. It is necessary to have an accurate, reproducible technique that is capable of assessing the attenuation of He-Ne laser light within a range of at least this magnitude.

In principal, this requirement is straightforward. In practice, it is accompanied by many difficulties. For one thing a given photodetector has a linear response only over a relatively few decades. For another, it is necessary to make measurements at very low light levels where results may be suspect on account of spurious laser reflections and interference effects.

We employed a measurement technique that tends to avoid the serious pitfalls and readily enables one to make systematic radiometric measurements over a range of more than 13 decades.

A low noise, highly red-sensitive photomultiplier is used as the sensor. Specially constructed stacks of neutral density filters are used as input attenuators. A measurement procedure is followed using the photomulti-plier-filter combination which ensures that the photomultiplier always works in its calibrated linear range.

The linear range of the photomultiplier was established as follows. The test setup was as shown in Figure 6-1. The method of calibration was to measure the anode current of the photomultiplier when the laser power falling on the photocathode was increased by exactly equal steps.

Light from the test laser was attenuated by a continuously variable neutral density wedge followed by one or more neutral density filters of the desired step value. Each filter was demountable from an exactly reproducible position. A typical measurement sequence for an attenuator consisting of the wedge and one step filter was as follows:
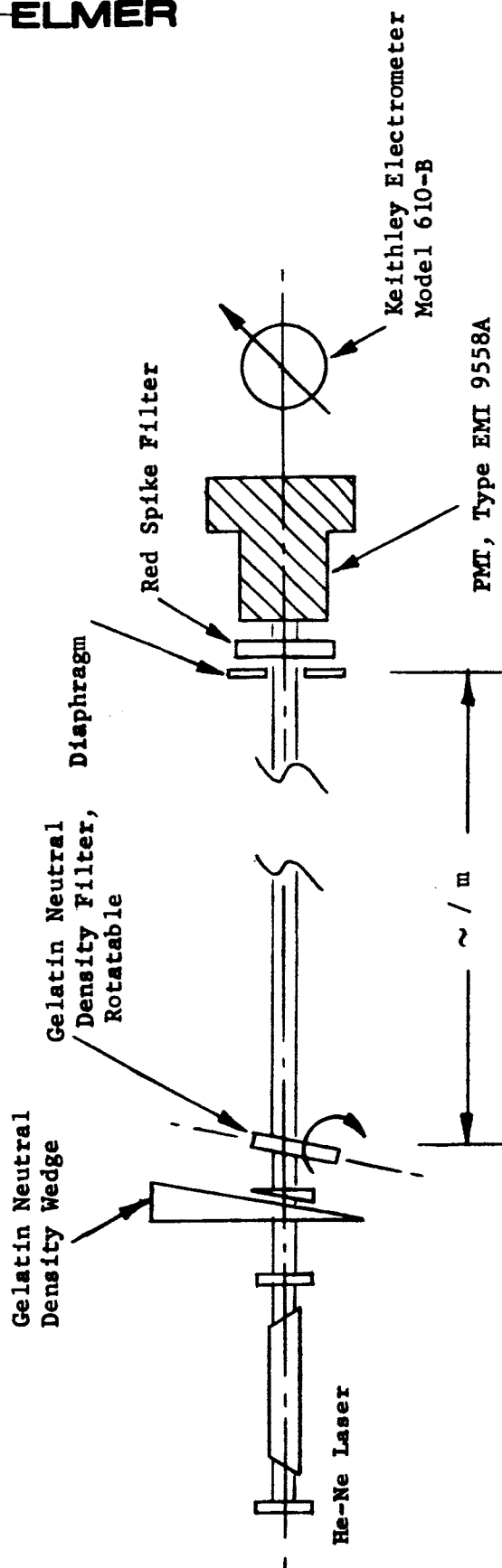
Figure 6-1.   Setup for Evaluating the Linear Range of the Photomultiplier

The wedge was set to near minimum transmission such that, without the step filter in place, the anode current of the photomultiplier was just above the dark-current level. Next the step filter was inserted and the wedge was backed off to exactly compensate for the increased attenuation. Then the step filter was removed and the anode current was measured. Following this, the step filter was replaced, the wedge was backed off to produce the previous anode current reading, the step filter was removed again, and another reading of the anode current was taken. This last sequence of events was repeated until, as shown by a semilog plot of the anode current readings vs increasing light intensity, it was seen that the photomultiplier was saturating. The variable-density wedge (illustrated in Figure 6-2) could be varied over a range of about four decades. By preceding the wedge with additional step filters and by following a similar procedure, it was possible to calibrate the photomultiplier over a much larger range. A typical experimental setup for making radiometric measurements over many decades is illustrated in Figure 6-3.

Inevitable reflection and scattering from the neutral filter produces a certain amount of stray light which may cause measuring errors. It was possible to make this effect negligible by locating the photomultiplier about 1 meter away from the neutral filters and by inserting a diaphragm in front of the photomultiplier. In addition, all neutral filters were tilted slightly so as to deviate spurious reflections safely out of the field of view of the detector.
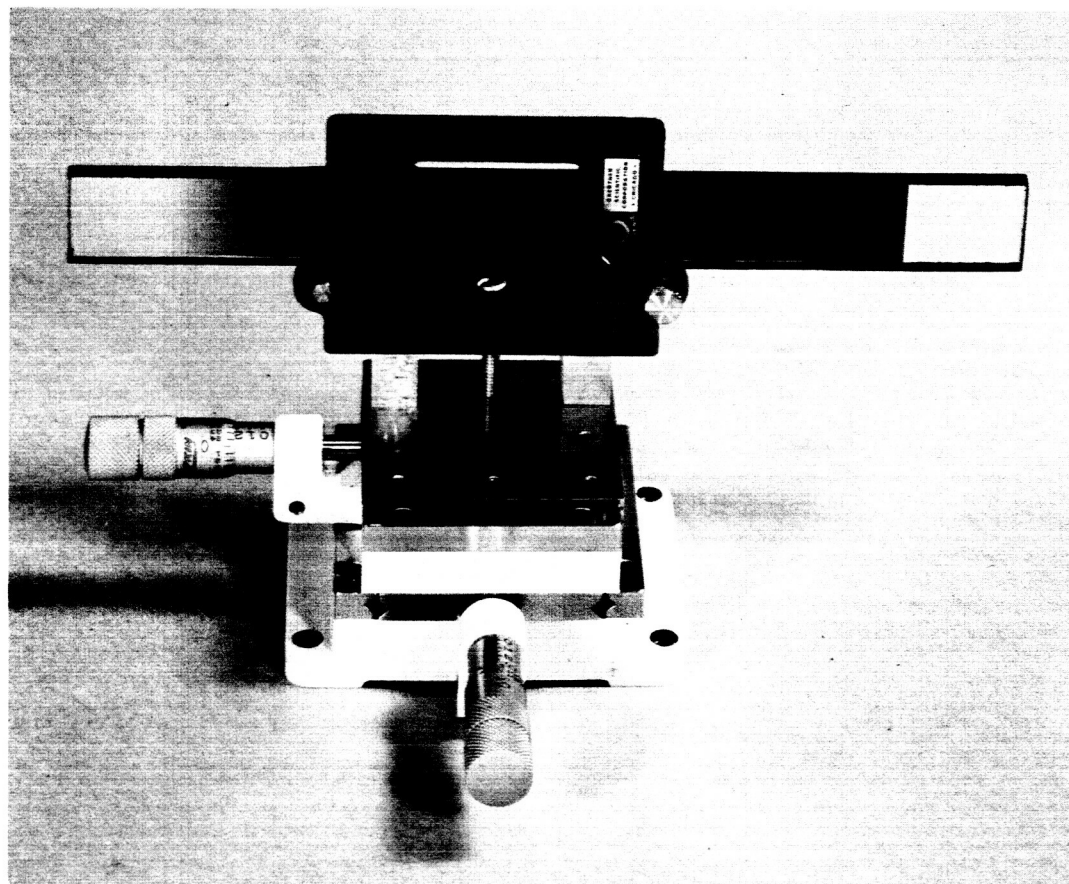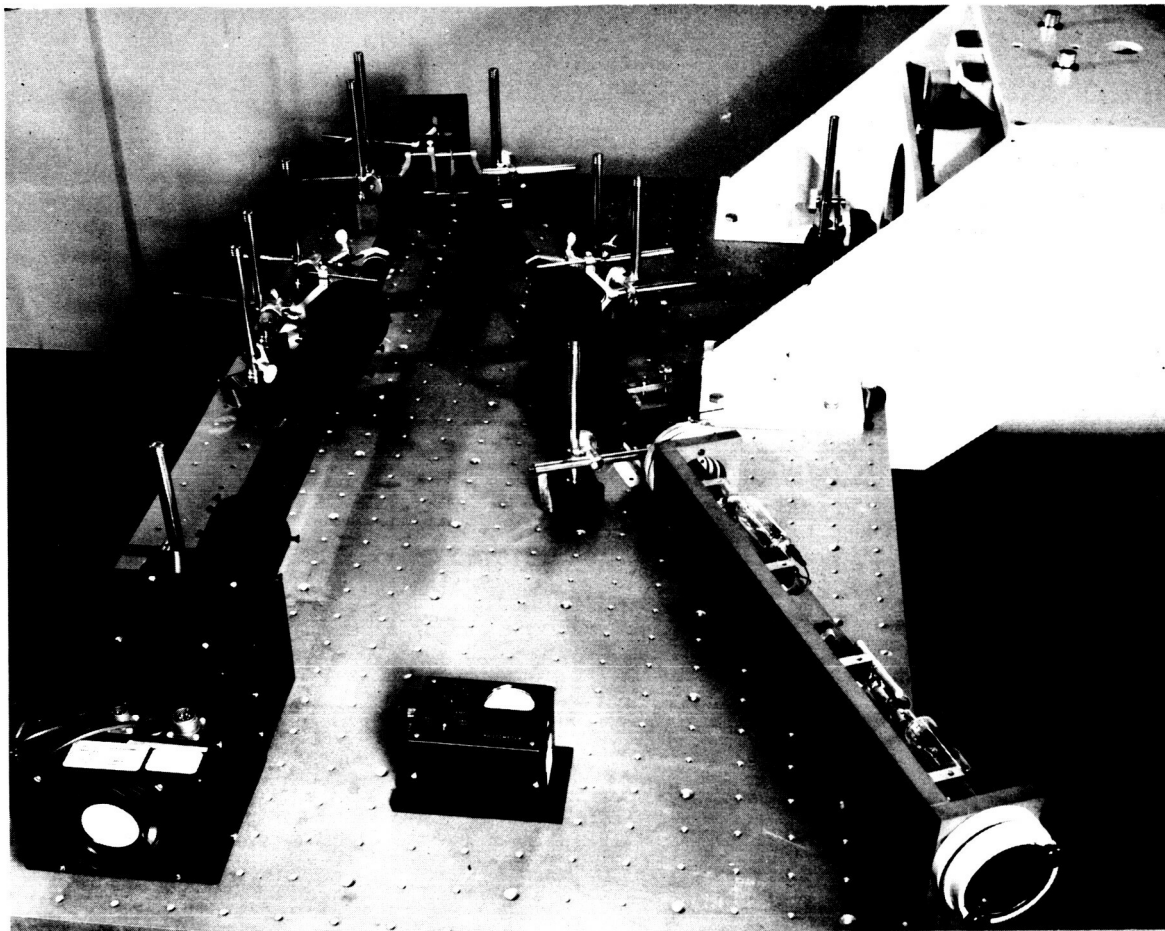
Figure 6-3. View of Optical Bench Showing
Equipment for Measuring Isolation
Properties of Test Dichroic Coatings

It will be noted that this technique of evaluating the linear range of a photomultiplier does not require exact knowledge of the densities of the neutral filters. In fact the density of each filter is automatically calibrated along the linear part of the anode current plot. These calibrations then serve, in turn, to calibrate the adjoining non-linear range.

6.5.1   Precautionary Measures in Stacking Neutral Filters

The amount of attenuation introduced by the addition of a neutral density filter to a given stack may be different from the value measured for the filter alone. This is due to stray light arising within the stack. However, the method adopted does not rely on the specific attenuation for the single filters. It establishes the attenuation of each filter after its insertion into the path of the laser beam with the aid of the variable neutral density wedge filter.

As a variant to the above procedure a component of variable high attenuation may first be used to reduce the output of the He-Ne laser to a level within the linear range of the photomultiplier. Then a filter stack can be built up by inserting one filter after another into the light path and by measuring the contribution of each filter to the overall attenuation with each step. At the same time the variable component is step-wise reduced to keep the power of the laser beam within a convenient linear measuring range of the photomultiplier. Here also, slightly tilting the neutral filters relative to the light path and reducing the field of view of the photomultiplier help in obtaining reproducible results.

The neutral density filters used to build up highly attenuating stacks had values of attenuation of 10 to 80 db and were either metal films

(inconel) produced by Perkin-Elmer or gelatin films from Kodak. Gelatin

filters could only be exposed to light levels up to about 0.1 mw in order

not to suffer deformation by local heating effects of the laser beam.

It was previously mentioned that EMI type 9558A photomultipliers

were selected for the channel separation measurements. A semilog plot of one

of these tubes, obtained by the procedure described above, is shown in Figure 6-4.

The nominal tube characteristics are; 184 μa/lumen luminous sensitivity,

3×10^4 ampere/watt radiant sensitivity at 6328Å, 1.8×10^{-9} ampere dark

current at room temperature, and 2×10^{-11} ampere dark current at -10°C.

As may be seen from Figure 6-4, this tube exhibits a five-decade linear range

at room temperature and an additional two decades are gained by refrigerating

to -10°C. The onset of non-linearity at high levels was probably due to

saturation effects at the last dynode. It was not due to saturation of the

photocathode, since widening the incident laser beam did not significantly

affect the anode current.

An interesting feature of the dark current was noted when the

photomultiplier was refrigerated to -10°C. The dark current exhibited a

burst-like character with a standard deviation of about three times the value

attributable to a Poisson sequence of independent current pulses of the same

average value. Figure 6-5 shows typical recordings of the dark current, measure-

ments having been taken with the setup shown in Figure 6-6. A thermoelectrically

cooled housing was used to stabilize the temperature of the photomultiplier at

-10°C for these and related laboratory experiments.
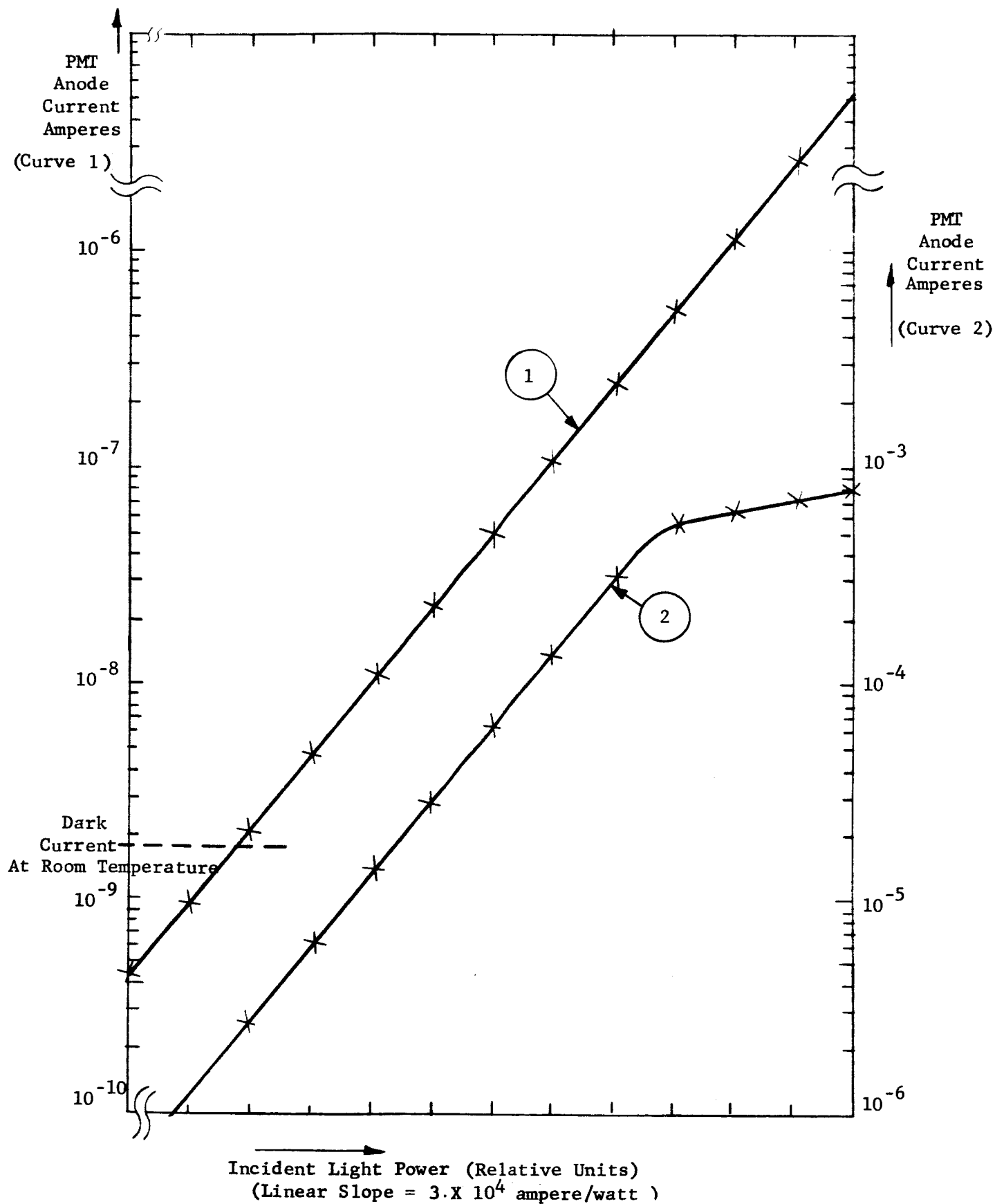
Figure 6-4.   Measured EMI 9558A Photomultiplier
Anode Current Output vs Light Input
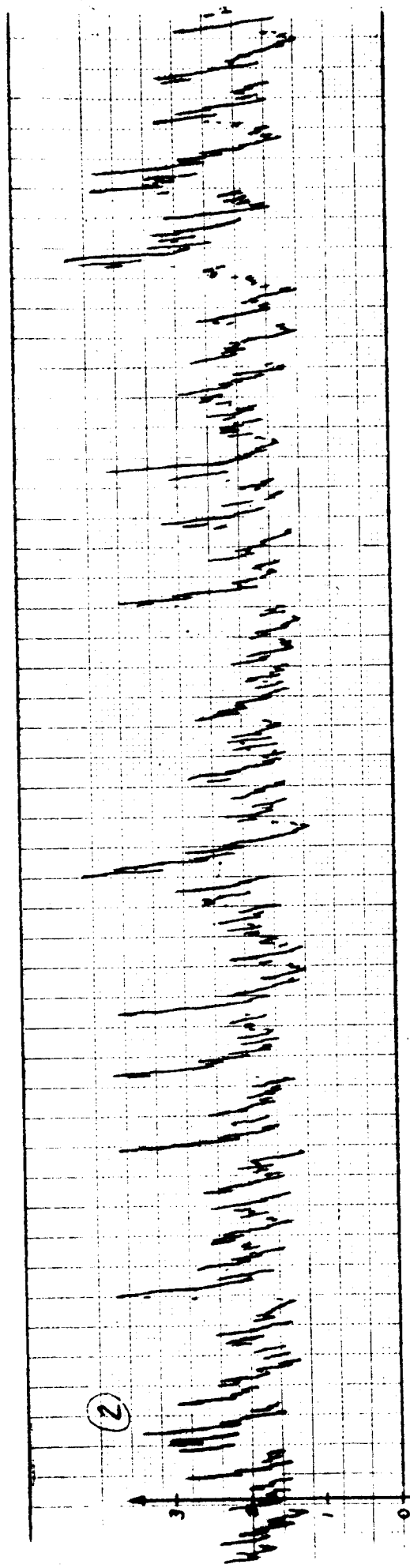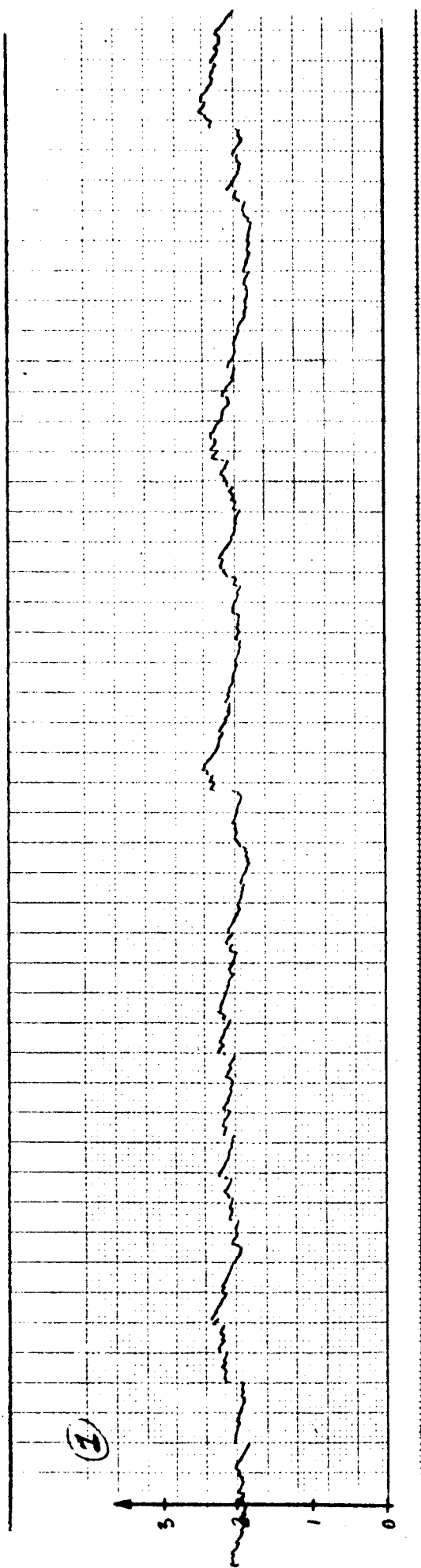
Figure 6-5. Typical Dark-Current Recordings at -10°C; Vertical Units 10^{-11} Amperes, Recording Speed 1 mm/sec; Time-Constant of RC-Circuit: 20 Seconds in Trace 1, 2 Seconds in Trace 2.
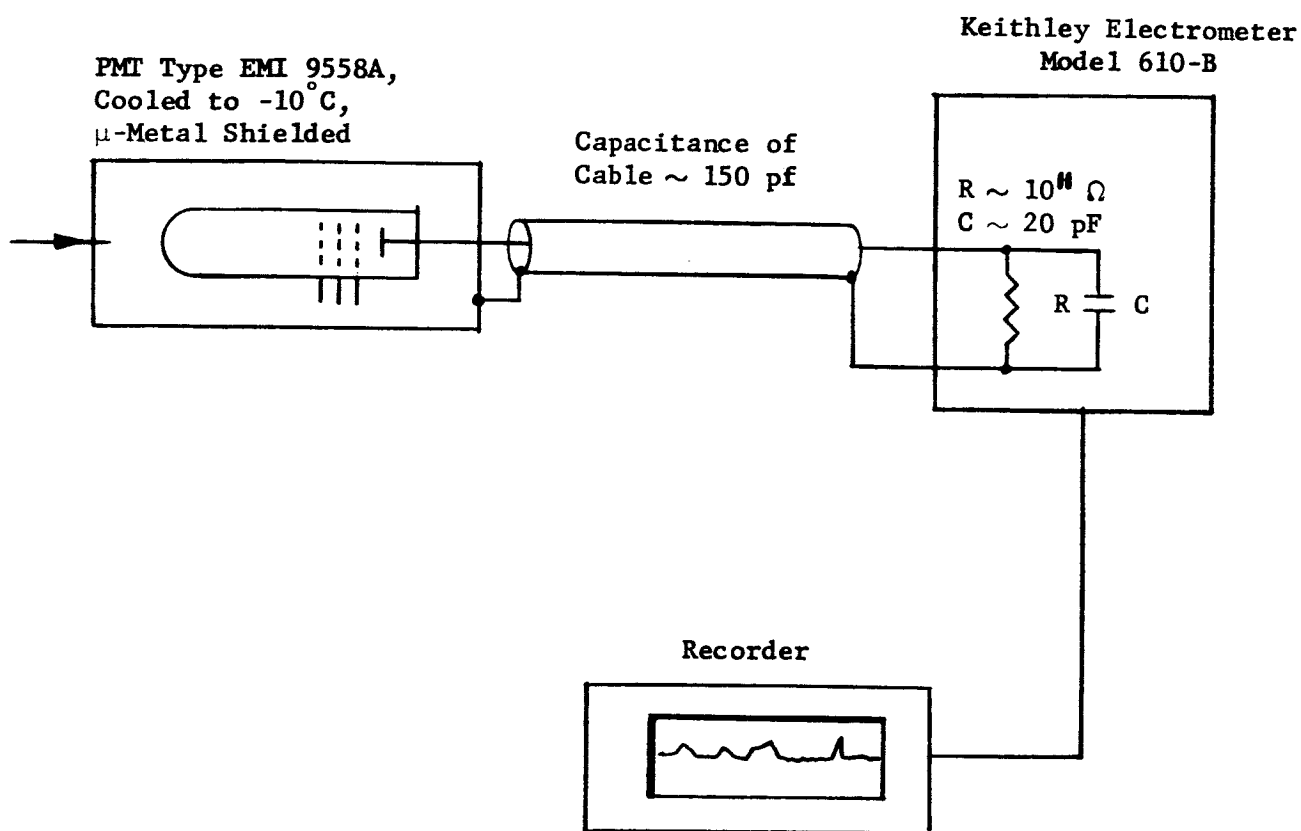
Figure 6-6. Schematic Diagram of the Recording Setup

The observed non-Poisson behavior of the refrigerated photomultiplier agrees with reports by others[1] and seems to be a common feature of this type of photomultiplier with an S-20 cathode. This point should be borne in mind when dark current is an important parameter influencing system signal-to-noise ratio.

6.5.2 Measuring Procedure and Range

The following procedure was followed to evaluate the amount of red transmit light leaking into the receive channel of our breadboard optical communications system. First the photomultiplier anode current was related to the output of the He-Ne laser by building up an attenuator comprising a stack of neutral density filters as indicated in Figure 6-7. The red spike filter was placed in front of the photomultiplier to block the fluorescence light of the He-Ne gas discharge. The direct power of the laser was measured by a calibrated radiometer. A typical scale factor was 300 μa anode current per 5×10^{-8} watt of laser output. Then the photomultiplier was installed into the breadboard as shown in Figure 6-7 to measure the fraction of laser light detectable via the receive channel. The procedure is susceptible to a systematic error as the sensitivity of a photocathode fluctuates significantly across its surface and calibration of the photomultiplier and subsequent measurements will, in general, not use the same portion of the photocathode. This defect, however, is clearly negligible for our application of measuring attenuations of 100 db and more.

The overall measuring range of this method is determined by the output of the He-Ne laser on the one hand and by the sensitivity of the photomultiplier on the other. By using the same photomultiplier for which recordings

---

[1] J. P. Rodman, and J. J. Smith: Applied Optics, 2, 287 (1963)
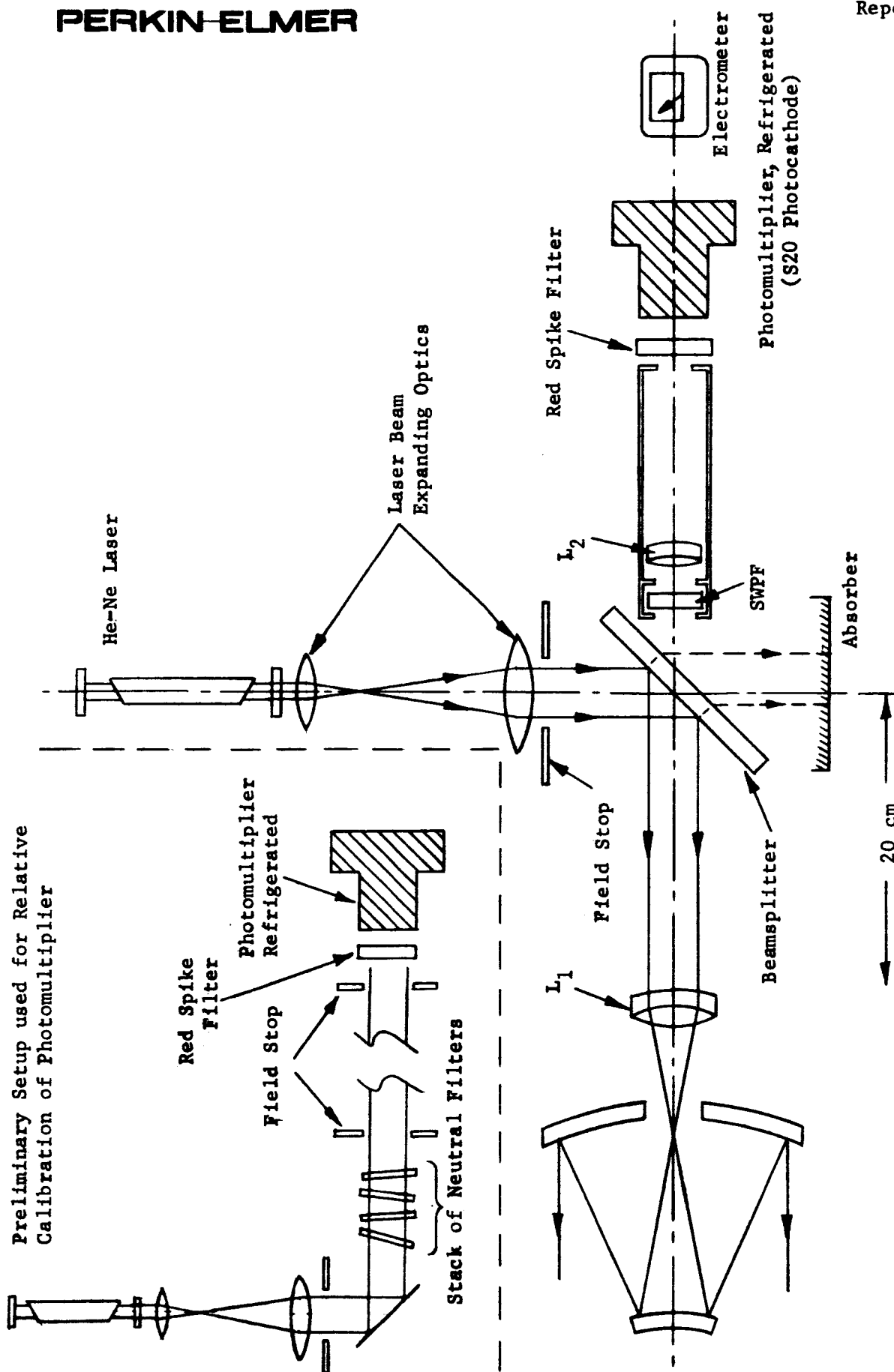
Figure 6-7. Test Setup for Channel Separation Measurements

the dark current at -10°C are shown in Figure 6-5, a light-induced increase of the anode current of this tube by as little as 10^{-11} ampere may be well established according to Figure 6-4. This corresponds to an input light power of 0.3×10^{-12} mw at 6328A. Used in conjunction with a He-Ne laser of about 10 mw output this photomultiplier calibration allows us to measure the attenuation at 6328$\overset{\circ}{A}$ of a given optical arrangement over more than 13 decades, as needed for the transmit-receive channel separation experiments.

6.6 CHANNEL SEPARATION TECHNIQUES

The all-dielectric approach to the channel separation problem has led to the development of some remarkable dielectric multilayer coatings. A summary description of the different designs now at our disposal follows, preceded by a discussion of a number of precautions which were followed in the mechanical design of the breadboard optical system. Finally, the results of channel separation measurements on the complete breadboard optical communications system are presented to show the combined effectiveness of the various techniques.

6.6.1 Mechanical Considerations

Scattering from a dielectric multilayer coating on a conventional substrate is partly caused by minute scattering centers in the coating itself and partly by small cracks in the surface of the substrate. These cracks develop during a conventional grinding process. They may be avoided to some degree by following an assiduous grinding and polishing procedure. Evaporating a low-scatter dielectric coating on such a "control ground" substrate helps in obtaining a beamsplitter with the least attainable scattering, and for this reason we used substrates prepared in this way wherever appropriate.

A circular diaphragm of 2 cm in diameter was introduced at the f/70 focal plane as an aperture for the scattered light. It reduces the solid angle of light rays from a scattering center of the beamsplitter which reach the receiver light detectors, to $\pi/25$ steradian. The converging lens system L_2 in front of the fine guidance beam divider has an entrance pupil of order 1.4 cm. As it cannot be located too far away from the beamsplitter for mechanical stability, it will not reduce the received bundle of scattered light rays any further than the 2 cm diaphragm in the f/70 focal plane.

The central area of the secondary mirror will ordinarily reflect axial transmit light rays back towards the receive light detector. Although it turned out not to be necessary, we were prepared either to leave this area blank when coating the mirror or to obstruct it mechanically with a light-absorbing disc.

6.6.2 Dielectric Multilayer Coatings

Reference is made in this discussion to Figures 1-1 and 6-7 which illustrate the location in the breadboard of the following coating designs:

(a) Dichroic Beamsplitter: This is the central element of the optical system. It has the properties of a color-sensitive mirror. Its requirements are for high transmission at the argon laser wavelengths and high reflectivity at the He-Ne laser wavelength. The current state of development of dielectric multilayers for the dichroic beamsplitter is illustrated in Figure 6-8. Designed for 45° incidence, this beamsplitter is seen to transmit about
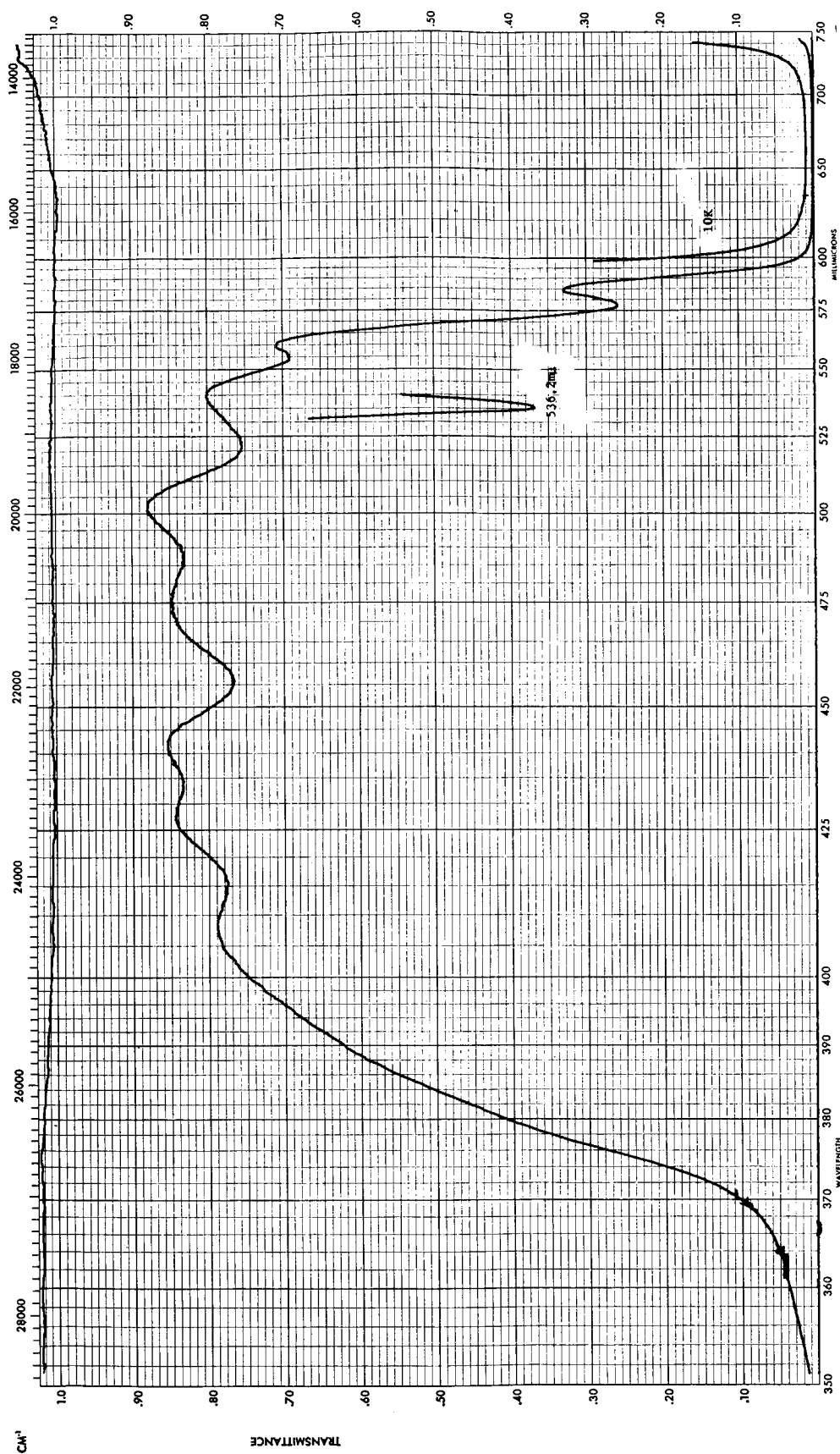
Figure 6-8. Transmittance vs. Wavelength Plot of Dichroic Beamsplitter Designed for 45° Incidence

80% at 4880Å and 5145Å and only about 0.1% at 6328Å .
Although this is notable performance for a dichroic
beamsplitter at such oblique incidence, it is ex-
pected that further refinements in design and tech-
nique can improve this performance another step.

(b) <u>Very-Low-Reflectance Coatings (VLR Coatings):</u> A
very-low-reflectance coating design tuned to 6328Å,
is required for minimizing reflection from the surfaces
of the elements of the transfer lens L_1. These re-
flections consist in general of slightly divergent
beams tending to propagate at small angles toward
the receive channel photomultiplier. We employed
a special design that was also tuned to the argon
wavelength so as to maximize the amount of argon
beacon light reaching the fine-guidance detectors.
A reflectance plot is reproduced in Figure 6-9.
and shows that the reflectance of an uncoated surface
becomes reduced from about 0.04 to about 5×10^{-4}
at 6328Å and to about 5×10^{-3} at the argon wavelengths.

(c) <u>Short-Wavelength Pass Filter (SWPF):</u> This kind of filter
is located between the beamsplitter and receive channel
detectors, and in practice is best located as shown in
Figure 6-7, immediately in front of lens L_2. It functions
as a final blocking filter to prevent surviving transmit
light from entering the receive channel. Its required
properties are similar to those of the beamsplitter as
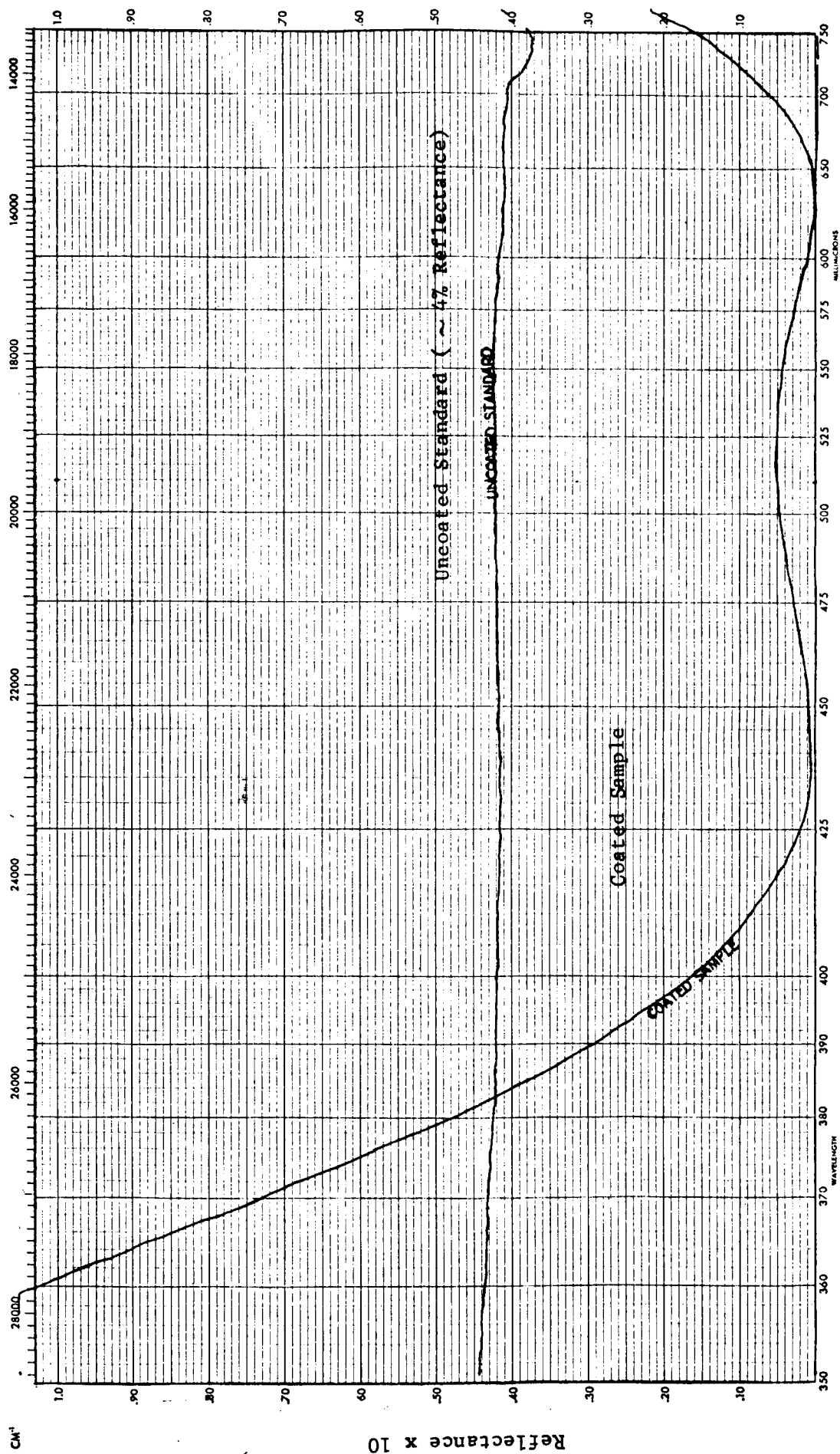
Figure 6-9. Reflectance vs Wavelength Plot of Very-Low-Reflectance Coatings Applied to Transfer Lens. Reflectance at 6328A Measured with Setup Described in Paragraph 6.5.

it must reject red transmit light by reflection and

pass blue beacon light. A special coating design was

worked out for the SWPF requirement, and filters with

the transmittance characteristics shown in Figure 6-10

resulted. The transmittance at 6328$\overset{o}{A}$ is on the order

of 1 part in 10^5 (as measured with the radiometric

procedure described previously.) At 4880$\overset{o}{A}$ and 5145$\overset{o}{A}$

the transmittance is seen to exceed 0.94. Some of

the incident blue light is lost on reflection from the

uncoated surface of the substrate. Thus, by putting

antireflection coatings on this surface one can expect

to improve the transmission by an additional few percent.

The SWPF design is additionally useful as a long-wave

blocking filter in conjunction with a Fabry-Perot

type spike filter such as may be employed for predetection

filtering in the project breadboard.

(d) Spike Filter With Enhanced Red Suppression: The receive

channel of the project breadboard is designed to in-

corporate a narrowband spike filter centered on one

or both of the argon laser lines. This filter may be

located immediately in front of the decollimating lens

L_2 and either be a substitute for or be used in con-

junction with the SWPF shown in Figure 6-7.
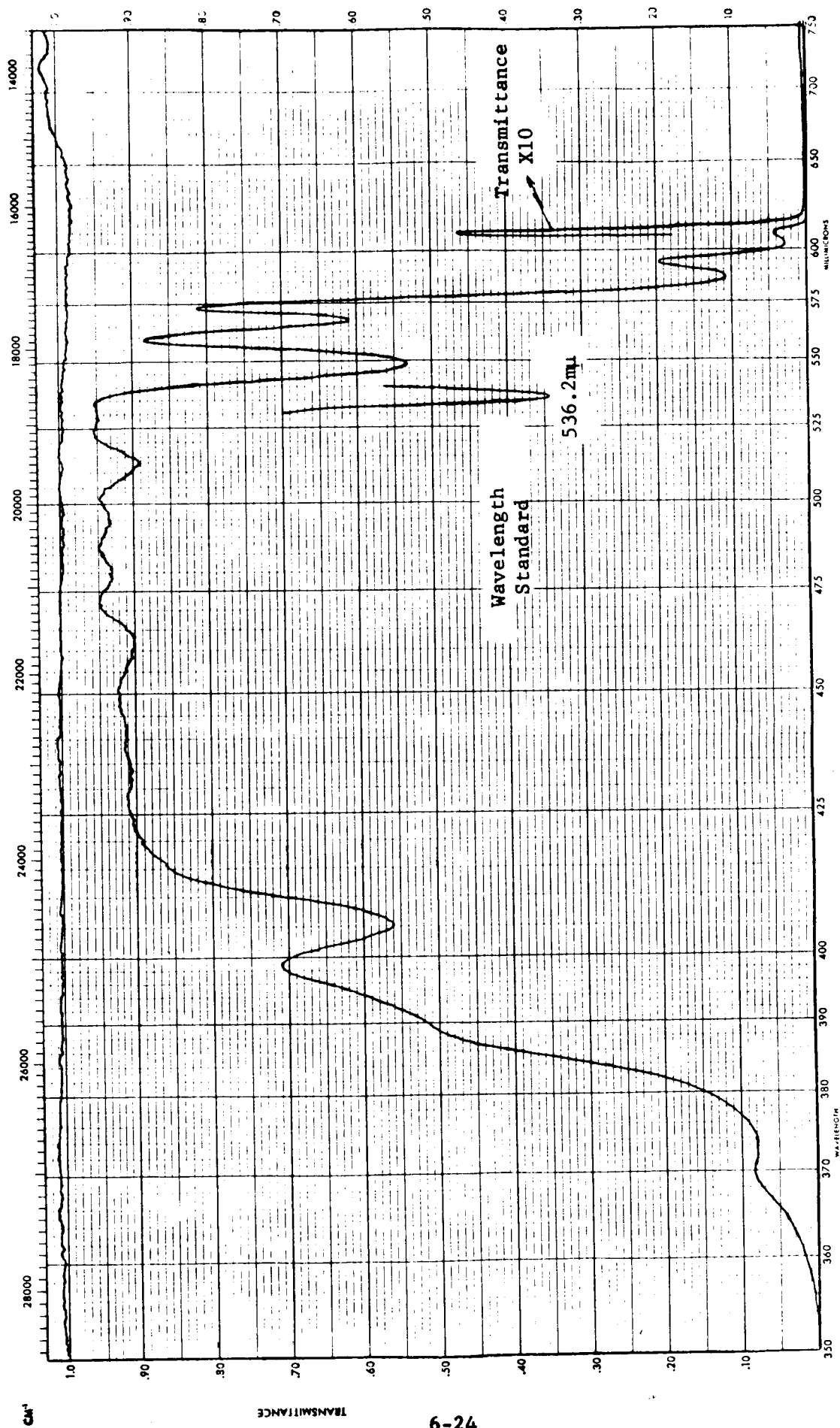
Figure 6-10. Transmission Spectrum of Short-Wavelength-Pass Filter.

Dielectric spike filters of conventional design employ colored glass elements as blocking filters. As a result of the sandwiching of absorbent filters and dielectric substrates, optical quality and peak transmission tend to suffer.

We therefore investigated the possibility of constructing a spike filter from purely dielectric stacks. This approach was successful, and the transmittance plot shown in Figure 6-11 was obtained by a design comprising four separate dielectric multi-layer stacks; a Fabry-Perot type multilayer to produce the principal narrow spike, a bandpass filter centered on the spike wavelength to block the immediate side maxima of the spike, a long-wavelength blocking filter and a short-wavelength blocking filter. The remaining leakage of unwanted light in the wings and, in particular, the leakage at $6328\overset{o}{A}$ is determined by the blocking filters. By incorporating the SWPF design for the long-wavelength blocking filter, the transmittance of the compound spike was reduced to less than 10^{-7} at $6328\overset{o}{A}$! As shown by Figure 6-11, the half-width of the all-dielectric spike filter is about $25\overset{o}{A}$ and the peak transmission at $4880\overset{o}{A}$ is 58%.

6.7 MEASUREMENTS OF SYSTEM CHANNEL SEPARATION

The setup shown in Figure 6-7 was used to evaluate the net channel separation that resulted from using a minimum of optical elements bearing a combination of the above coatings in the project breadboard.
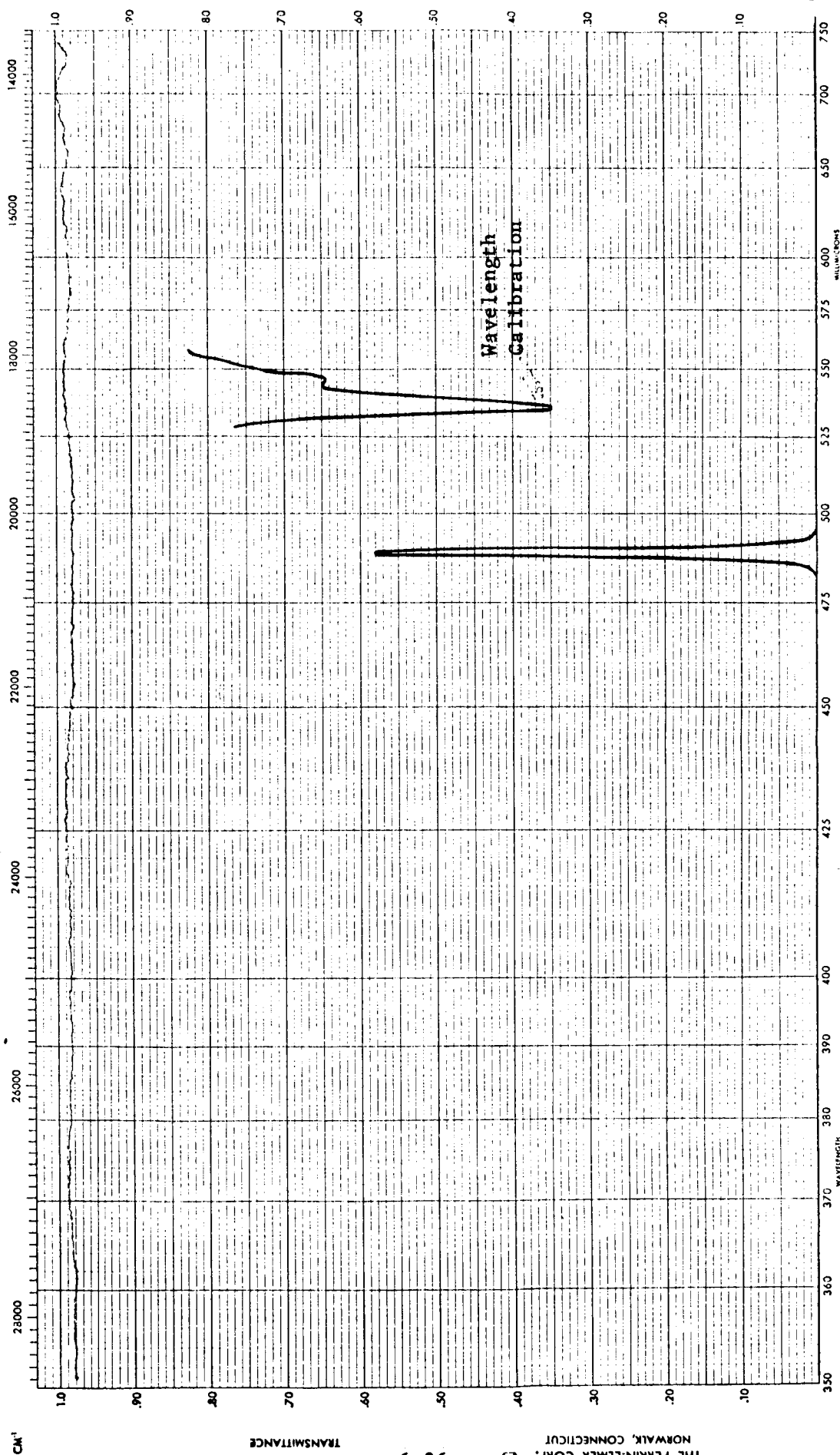
Figure 6-11. Transmittance vs. Wavelength Plot of Special Blue
Spike Filter.

One set of measurements was made under the following set of conditions: the surfaces of the transfer lens were coated with VLR coatings having the transmittance shown in Figure 6-9, the beamsplitter corresponded to Figure 6-8; the compound spike filter of Figure 6-11 was used in place of the SWPF shown in Figure 6-7; the telescope was not yet incorporated into the setup, and the outgoing He-Ne laser beam was terminated by a black, absorbing surface about 5 meters away from the beamsplitter.

This arrangement, which mainly relied on only two components for channel separation (the beamsplitter and the spike filter) attenuated the red light of the He-Ne laser reaching the detector by 95 db. Furthermore, all background radiation was blocked outside the 25Å passband of the spike filter centered on 4880Å where the net transmission was about 58%.

According to our previous definition, the figure of merit for channel separation becomes 95 db less 3 db (for the transmission term) plus 15 db (assuming substitution of S-cathode photomultiplier for the S-20 with which the measurements were taken) for a total of approximately 110 db.

These measurements were repeated for the entire optical system including the 16-inch aperture telescope. Inclusion of the telescope clearly had an important bearing on the channel separation problem because part of the transmit light incident on the central region of the secondary mirror is re-flected directly back into the receive channel. The optical arrangement was essentially the same as for the previous measurements except that the SWPF was used rather than the spike filter. The measurements revealed that adding the telescope to the breadboard only accounted for about 10% more light reaching the photomultiplier. The other 90% stemmed almost entirely from

reflections off the four surfaces of the transfer lens L_1. Scattering from the beamsplitter and from the absorber behind the beamsplitter contributed less than 1%.

The overall attenuation of the red laser light detected by the photomultiplier in the breadboard setup amounted to about 100 db. This does not include the additional attenuation of 15 db to be expected by using receive photomultipliers with reduced red response.

The blue spike filter with enhanced red suppression of the type described was not used for these last measurements. It was found with this filter that suppression of 6328Å light was virtually complete except for a minute amount which was transmitted diffusely through pinholes in the four sets of dielectric coatings on its four constituent substrates. Since, as described in Section VII the post-launch alignment scheme requires a finite amount of collimated red light to be transmitted by such a filter, the original one was ruled out for this use. A modified design was later manufactured and its properties are described in connection with the investigation of remote alignment techniques discussed in Section VII.

The blue glow from the He-Ne laser turned out to be an unexpected source of background light reaching the photomultiplier detector in these measurements. It was necessary to exclude this light by, for example, inserting red filters directly after the laser or in front of the photomultiplier, and this is the reason for its inclusion in Figure 6-7.

6.8   DISCUSSION

The all-dielectric approach has now been shown to be capable of achieving channel isolation very effectively. It should be emphasized that the figure of 100 db quoted above results mainly from two treated surfaces, one of which is the beamsplitter and the other must be provided anyway as part of the predetection filter. Future refinements can be expected to yield greater separation without additional optical elements and we are still free to add additional SWPF's to increase arbitarily the amount of separation obtained.

It has been suggested previously that channel separation can also be affected with the help of dispersing elements. However, at best this approach would complicate the problem of post-launch alignment techniques. Further difficulties might arise due to the fact that the received earth-beacon light consists of several wavelengths which would be subject to differing dispersions. By contrast, the all-dielectric approach features noteworthy versatility in that future changes in operating wavelengths can be accommodated by straightforward redesign of the dielectric multilayers.

A number of general conclusions appear to be warranted:

(a) The dielectric techniques used in the laboratory experiments and described in the preceding paragraphs can readily provide more than 110 db of channel separation between a helium-neon transmitter and an argon beacon-receiver.

(b) This approach is simple to implement. Most of 110 db separation is produced by two optical elements that have to be provided anyway: the beamsplitter and the spike filter.

(c) This approach can be modified for more or less channel

separation as wanted. For example at least 20 db of

improvement is feasible as a result of improving the

dichroic beamsplitter. Alternatively, another SWPF

can be inserted in the optical system for an increased

channel separation of ~ 50 db.

(d) This dielectric technique permits an attractively

simple approach for boresighting the transmit channel

with respect to the receive channel. For example,

let us arrange for the amount of channel separation

to be no more than necessary for the tracking function.

Then, by inserting a cube corner prism between the beam-

splitter and the transfer lens, a certain additional

amount of collimated light from the transmit laser will

be reflected back into the receive channel where an

image will be formed in red light. The additional in-

tensity can be enough for the receive channel detectors

to tell where the image is located. Alignment can then

be accomplished by adjusting the transmit channel optics

until the red image falls exactly on the apex of the

image divider. This subject is discussed more fully in

the next section.

An appendix that accompanies this section contains a discussion of

polarization aspects of dichroic mirrors of the type used extensively in our

laboratory experiments. This study was carried out as technical background

for building PCM/PL capability into a given transmitting or receiving optical

system. The principal conclusion is that polarization-dependent effects will

not significantly influence the current breadboard optical system when it

functions as a PCM/PL transmitter, and that PCM/PL is fully compatible with

our channel separation techniques.

APPENDIX VI-A

POLARIZATION EFFECTS OF DICHROIC MIRRORS
IN A PCM/PL TRANSCEIVER

SUMMARY

This Appendix analyzes the polarization effects of dichroic mirrors
in a PCM/PL transceiver. Equations are derived which state the effect on the
communication link of introducing a dichroic mirror into the optical path. The
PCM/PL binary digital optical signal may be either right- and left-hand circu-
lar polarized or two-perpendicular-plane polarized signals. The derived bit-
error-rate equations show that the dichroics insert a smaller error into the
system if the PCM/PL system using circularly polarized light is used. With a
poor dichroic (transmission in the "p" and "s" planes of 0.6 and 0.45, re-
spectively), a PCM/PL transceiver, using circular and plane polarizations in-
cident on the dichroic, required signal increases of 2.8 db and 3.5 db, re-
spectively, to make up for signal deterioration. Better dichroics, which in
practice are readily obtained, cause correspondingly smaller signal deterior-
ation. Several methods for reducing the effect of the errors introduced by
dichroics are also discussed.

INTRODUCTION

Dichroic mirrors introduce amplitude losses and phase errors in
both transmitted and reflected signals. These errors change linearly polarized
light into elliptically polarized light. The performance of PCM/PL (Pulsed Code
Modulation with Polarized Light) and optical heterodyne demodulation techniques

will be degraded by these errors in polarization.[1] Introduction of compensators

and proper alignment of the plane of polarization for the local oscillator laser

will correct any ellipticity introduced in the optical heterodyne receiver. The

effect of polarization errors in a PCM/PL system is more complicated. This

Appendix examines the relation between polarization errors and bit-error-rate

of the PCM/PL system. Several techniques for reducing the effect of polarization

errors are discussed.

The Laser/Optics breadboard is a functional transceiver for an

optical communications link. A dichroic mirror is located "behind the mirror"

to produce two conjugate optical paths. One of these paths contains a PCM/PL

transmitter laser and modulator (Figure 6-12). The second path contains the

fine tracking sensor and, possibly, a receiver for the optical communication

link. Although a PCM/PL receiver is not envisioned as part of the Laser/Optics

breadboard, we have added such a receiver to the breadboard optical configur-

ation shown in Figure 6-12 for illustrative purposes in the following dis-

cussion. The receiver components are typical of what are needed in general for

PCM/PL detection.

POLARIZATION-DEPENDENT EFFECTS OF DICHROIC MIRRORS

The transmittance T (at 4880$\overset{\circ}{A}$ and 5145$\overset{\circ}{A}$) and reflectance R (at

6328$\overset{\circ}{A}$) characteristics of a typical dichroic are given in Figure 6-13. The sub-

scripts "s" and "p" in the identities below denote the polarization perpendicular

_____

[1]W. N. Peters: Incoherent Optical Polarization Pulse Code Modulation Communica-
tion System, National Electronics Conference, Chicago, October 1965.
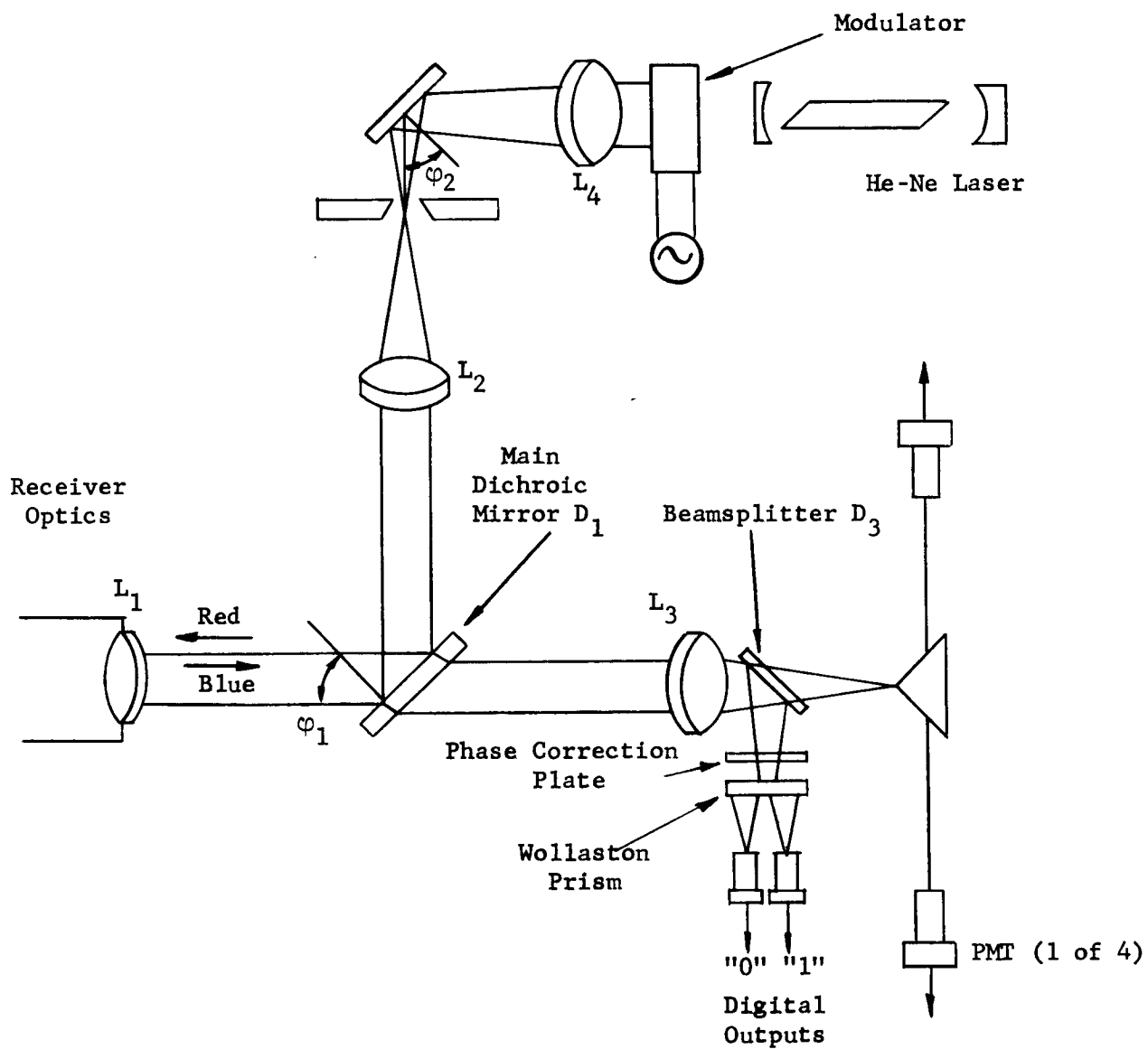
Figure 6-12. Optical Communications Transceiver
with PCM/PL Detection
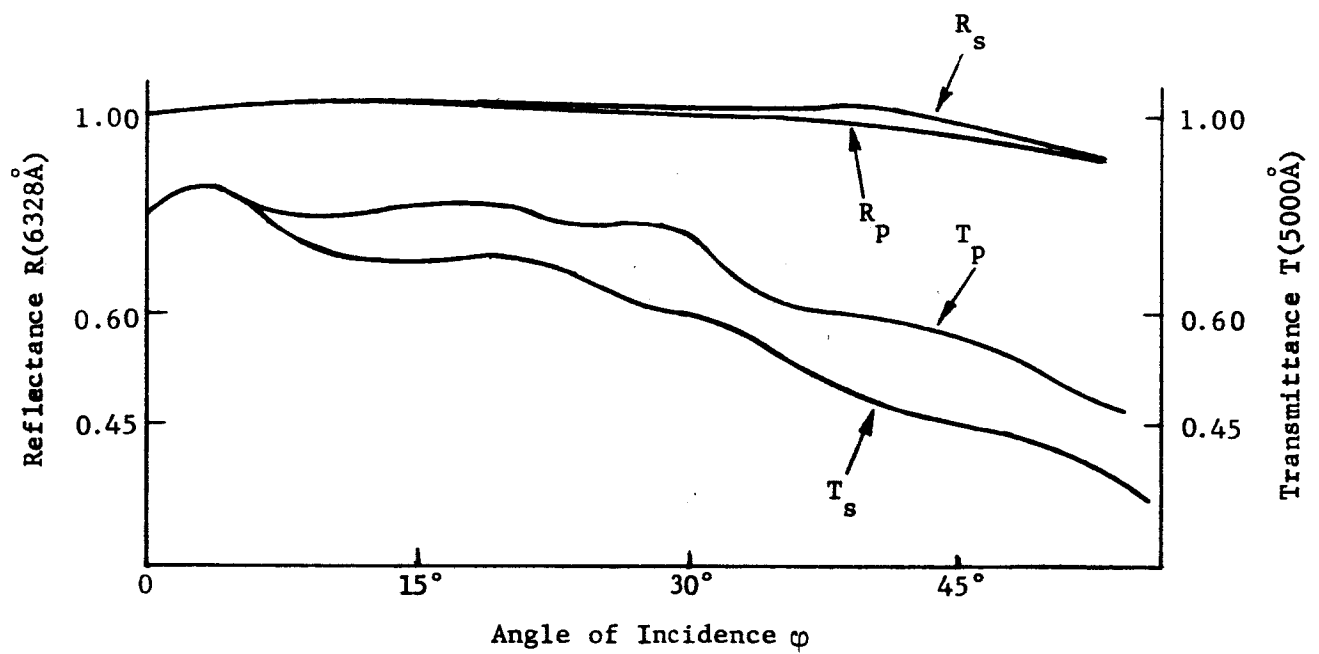
Figure 6-13. Transmittance and Reflectance of Dichroic Mirror

to, and parallel to the plane of incidence, respectively. That is, in

Figure 6-12 the "s" vector is perpendicular to the paper and the "p" vector

is parallel to the paper. We may define the following general parameters as

follows:

$$\beta_T = \text{Max} \left\{ T_p, T_s \right\} \qquad \beta_R = \text{Max} \left\{ R_p, R_s \right\} \qquad (6\text{-}1)$$

$$\epsilon_T = \frac{|T_p - T_s|}{\beta_T} \qquad \epsilon_R = \frac{|R_p - R_s|}{\beta_R}$$

Let δ denote the phase difference between the "s" and "p" vectors at the entrance

face of the Wollaston prism resulting from uncorrected system errors and random

fluctuations of the transmission medium.

When several mirrors are placed in the optical path, the polariza-

tion errors are cumulative. For example, the parameters describing the polar-

ization of the optical signal at the Wollaston prism in Figure 6-12 are:[2]

$$\beta = {}^1T_p \times {}^3R_p$$

$$\epsilon = \frac{{}^1T_p \times {}^3R_p - {}^1T_s \times {}^3R_s}{\beta} \qquad (6\text{-}2)$$

$$\delta = {}^1\delta + {}^3\delta + \delta_c , \quad -\pi/2 \leq \delta \leq \pi/2$$

where

δ = residual phase error

δ_c = phase introduced by phase correction plate

---

[2] This example assumes that the "s" and "p" components have the relative magni-
tudes shown in Figure 6-13.

The superscripts 1 and 3 in Equation (6-2) denote the dichroics D_1 and D_3 of Figure 6-12. Thus, the parameter ^1T_p is the transmission of dichroic number 1 in the "p" plane.

Sources of Polarization-Dependent Errors:

Since the received optical signals will be circularly polarized, a phase correction of $\delta_c = \pi/4$ must be inserted to obtain the required plane polarized orthogonal signals at the Wollaston prism. Phase errors introduced by the dichroics may also be corrected. For example, if the dichroics introduce a 15° phase error, the phase correction $\delta_c = 45 \pm 15°$ will make the "0" and "1" signals plane and orthogonal at the Wollaston prism. The choice between the plus or minus signs is determined by the orientation of the dichroics and phase correction plate.

The phase errors created in the atmosphere and received optics will give a statistical distribution to the phase error δ. Since the value of δ becomes time varying, it is impossible to insert a constant phase correction δ_c which will compensate for atmospheric phase errors.

An additional source of phase error is the PCM/PL modulator. If the voltage impressed on the electro-optic modulator is in error, phase errors are introduced in the transmitted optical signal. If the phase errors of the "0" and "1" signals have the same sign and are equal, the errors may be calibrated and compensated at the receiver. No compensation is possible when the phase errors have different signs.

<u>Receiver-Optical Considerations:</u>

Since the maximum obtainable β_R is greater than the maximum obtainable β_T, the isolation requirements between the transmitter and receiver dictate the basic arrangement of Figure 6-12. The advantages of changing the angles ω_1 , ω_2 and the insertion of additional phase compensators will be discussed later.

The two orthogonal polarizations which are transmitted and received by the telescope should be right-hand (RH) and left-hand (LH) circular polarization. A PCM/PL communication system operating against a plane polarized noise source (e.g., blue sky) has a minimum bit-error-rate when circular polarization is utilized (Reference 1). This has the added advantage that the receiver optics operate with arbitrary rotational orientation. They do not need an RLOS (Rotation about Line of Sight) determination to decode the received optical signal because the plane of polarization of the light incident on the Wollaston prism will be determined solely by the orientation of the quarter-wave plate.

The output of the He-Ne laser is plane polarized. Thus, if the modulator is operated at the ± quarter-wave voltages, the light passing through L_4 will be circularly polarized as required for PCM/PL.

DERIVATION OF PCM/PL ERROR RATES

<u>Case 1: $\epsilon = 0$, $\beta = 1$, $\delta = 0$</u>

The bit-error-rate of PCM/PL system is, under these conditions,

$$P_B = 1/2 \sum_{K=1} P_K \left(S + N/2 \right) \left[\overline{Q_K \, (N/2)} \quad \overline{Q_{K+1}(N/2)} \right] \qquad (6-3)$$

The derivation of Equation (6-2) is treated in Reference 1, and the variables are defined as follows:

$$P_K \ (S + N/2) = \frac{\exp \ (-S - N/2) \ (S + N/2)^K}{K!}$$

$$Q_K \ (N/2) = \sum_{K=0}^{K-1} P_K \ (N/2)$$

The derivation of Equation (6-3) assumes that the signal and noise photoelectrons detected during the sampling interval are Poisson distributed and have expectations of S and N, respectively. Equation (6-3) is plotted in Figure 6-14.

Case 2: $\underline{\epsilon = 0, \ \beta \neq 1, \ \delta = 0}$

The above conditions occur when the optical signal is normal to the multilayer film. By inspection, the bit-error-rate becomes

(6-4)

$$P_B = 1/2 \sum_{K=1}^{\infty} P_K \ \left(\beta S + \beta N/2 \right) \left[\overline{Q_K \ (\beta N/2)} - \overline{Q_{K+1} (\beta N/2)} \right]$$

Figure 6-14 may again be used to graphically determine the required operating parameters by substituting βS and βN for S and N, respectively. S and N are the signal and noise counts with the dichroics removed.

In the above sample, the signal-to-noise ratio (S/N) remains constant during the transformation (i.e., $S/N = \beta S / \beta N$). However, the decrease in the signal count per decision increases the relative contribution of the quantum noise. Thus, it is important to maintain both the maximum possible S/N and average signal counter decision.
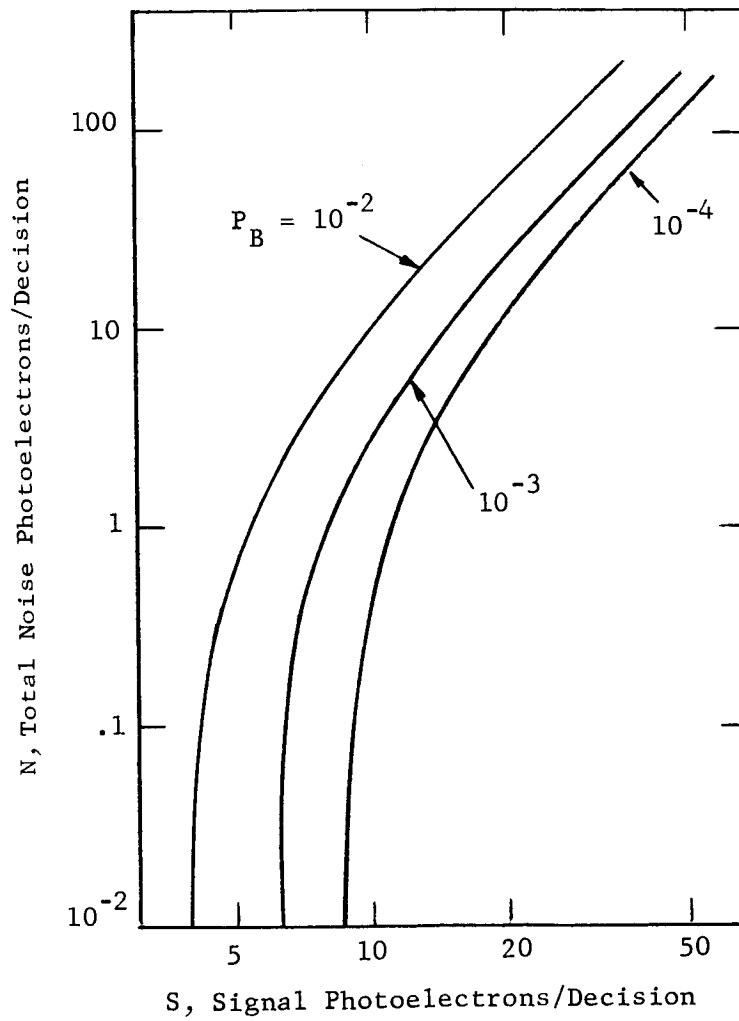
Figure 6-14. Signal vs. Noise Count as Given by Equation(6-3)
(Reference <u>loc cit</u> 6-33)

Case 3: $\epsilon \neq 0$, $\beta \neq 1$, $\delta \neq 0$

The general solution of the bit-error-rate for a PCM/PL receiver with both phase and amplitude polarization errors will now be derived. The relative intensity of elliptically polarized light passing through an analyzer at azimuth angle α is:[3]

$$I = \frac{1}{2} \left(a_1^2 \cos^2 \alpha + a_2^2 \sin^2 \alpha + a_1 a_2 \sin 2\alpha \cos \delta \right) \qquad (6\text{-}5)$$

The variables are defined in Figure 6-15.

The expected phase error δ is assumed to be small. Using the cosine expansion for small angles, Equation (6-5) becomes

$$I = \frac{1}{2} \left[a_1^2 \cos^2\alpha + a_2^2 \sin^2\alpha + 2a_1 a_2 \sin\alpha \cos\alpha \left(1 - \frac{\delta^2}{2!} \right) \right]$$

$$= \frac{1}{2} \left\{ \left[a_1 \cos\alpha + a_2 \sin\alpha \right]^2 - \frac{a_1 a_2 \delta^2 \sin 2\alpha}{2} \right\} \qquad (6\text{-}6)$$

counts per second.

The optimum PCM/PL receiver will have plane, orthogonal and equal intensity optical signals at the Wollaston prism for the "0" and "1" signals. However, the dichroic mirrors will insert both phase and amplitude errors. Referring to Figure 6-15, suppose the original signal has an intensity S and was plane polarized in a plane of $\alpha = \pi/4$. The intensity of this original signal is

$$I = \frac{1}{2} \left\{ \left[\sqrt{S} \cos \pi/4 + \sqrt{S} \sin \pi/4 \right]^2 - 0 \right\}$$

---

[3] W. Budde,: Photoelectric Analysis of Polarized Light. Applied Optics, vo. 1, no. 3, Mar. 1962, pp 201-205.
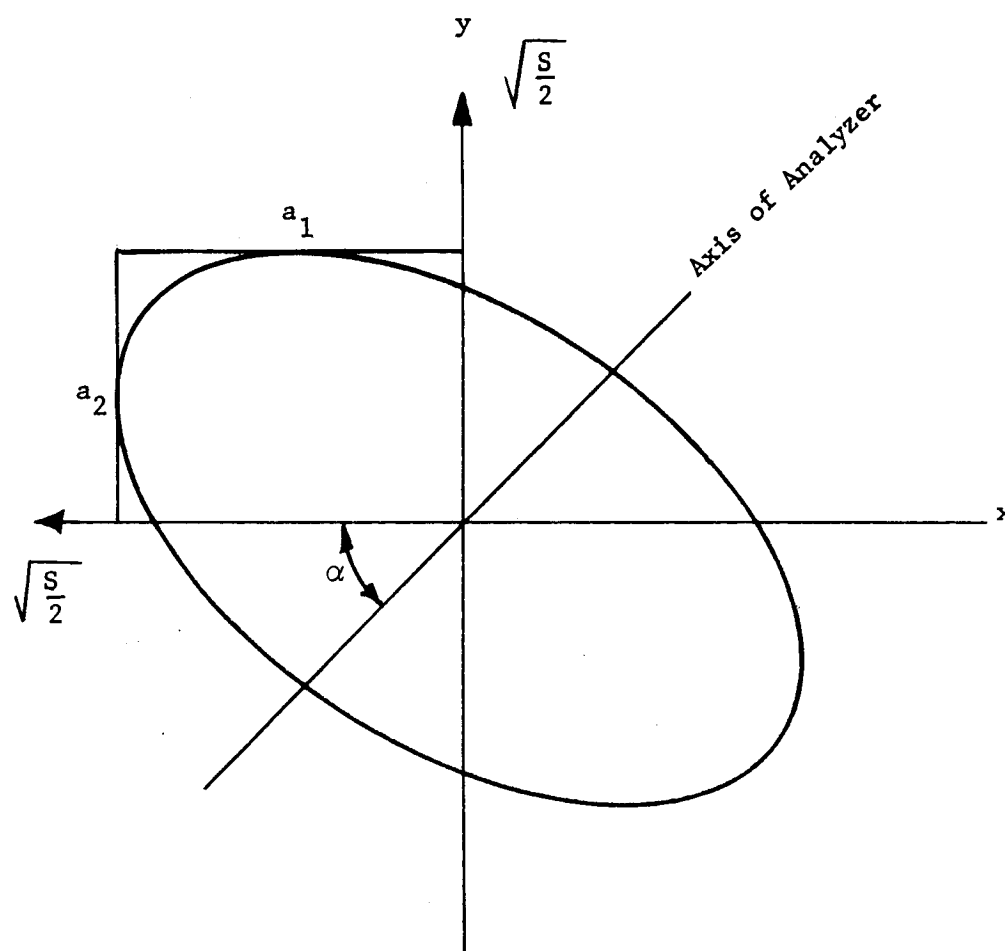
$$E_x = a_1 \cos (wt)$$

$$E_y = a_2 \cos (wt + \delta)$$

Figure 6-15. Geometry of Elliptically Polarized Light
With Respect to Optical System

Assuming that the x and y planes coincide with the s and p planes of the dichroic, respectively, the transmitted intensity at the output of the dichroic is

$$I = \frac{1}{2} \left\{ \left[\sqrt{ST_p} \cos \pi/4 + \sqrt{ST_s} \sin \pi/4 \right]^2 - \frac{S \sqrt{T_s T_p}\, \delta^2 \sin \pi/2}{2} \right\}$$

$$= T_p \frac{S}{2} \left\{ \left[\cos \pi/4 + \frac{\sqrt{T_s - T_p + T_p}}{\sqrt{T_p}} \sin \pi/4 \right]^2 - \frac{\frac{\sqrt{T_s - T_p + T_p}}{\sqrt{T_p}}\, \delta^2}{2} \sin \pi/2 \right\}$$

If $T_p \geq T_s$, the variables may be relabeled

$$I_{sig} = \frac{\beta S}{2} \left\{ \left[\cos \pi/4 + \sqrt{1+\epsilon} \sin \pi/4 \right]^2 - \frac{\sqrt{1-\epsilon}\, \delta^2 \sin \pi/2}{2} \right\}$$

$$= \frac{\beta S}{2} \left\{ 1 - \frac{\epsilon}{2} + \sqrt{1-\epsilon} \left(1 - \frac{\delta^2}{2} \right) \right\} \tag{6-7}$$

This is the signal count received in the correct photodetector. Note that if $\beta = 1$, $\epsilon = 0 = \delta$, Equation (6-7) reduces to S, as expected. When polarization errors are introduced into a PCM/PL signal, the "0" and "1" polarizations are not orthogonal. That is, it is impossible to select a proper azimuth angle for the analyzer at which all the "0" energy enters one photomultiplier and all the "1" energy enters the opposite photomultiplier. The amount of energy entering the incorrect detector (i.e., noise) is:

$$I_N = \frac{\beta S}{2} \left\{ \left[\cos \left(\frac{-\pi}{4} \right) + \sqrt{1-\epsilon} \sin \left(\frac{-\pi}{4} \right) \right]^2 - \frac{\sqrt{1-\epsilon}\, \delta^2 \sin \left(\frac{-\pi}{2} \right)}{2} \right\}$$

$$= \frac{\beta S}{2} \left\{ 1 - \frac{\epsilon}{2} - \sqrt{1-\epsilon} \left(1 - \frac{\delta^2}{2} \right) \right\} \tag{6-8}$$

Since the background noise is assumed to have random polarization and the angle of the analyzer is $\alpha = \pm \pi/4$, both detectors will have a modified average background noise count per decision of

$$\left(\frac{N}{2}\right)_{background} = \frac{N}{2}\left(\frac{T_s + T_p}{2}\right)$$

The modified average count of the "signal" photomultiplier when the circularly polarized optical signal is incident upon the dichroic is

$$(S + N/2)' = I_{sig} - I_N + (N/2)'_{background} \tag{6-9}$$

$$= \frac{\beta S}{2}\left\{2 \sqrt{1-\epsilon} - \delta^2 \sqrt{1-\epsilon}\right\} + \frac{N}{S}\left(\frac{T_s + T_p}{2}\right)$$

The modified count of the "noise" photomultiplier is

$$(N/2)' = I_N + (N/2)_{background} \tag{6-10}$$

$$= \frac{N}{2}\left(\frac{T_s + T_p}{2}\right) + \frac{\beta S}{2}\left\{1 - \frac{\epsilon}{2} - \sqrt{1-\epsilon}\left(1 - \frac{\delta^2}{2}\right)\right\}$$

Equations (6-9) and (6-10) may be explained by referring to Figure 6-16. Part (a) shows the partition of the received energy between the two detectors where there is no polarization error (i.e., $\epsilon = 0 = \delta$). Parts (b) and (c) show the received energy partition with phase and amplitude polarization errors and the redefined signal and noise levels, respectively.

Case 4: $\beta = 1$, $\epsilon = 0$, $\delta \neq 0$

If $\beta = 1$, $\epsilon = 0$, $\delta \neq 0$, Equations (6-9) and (6-10) substituted into Equation (6-3) give the expression for the bit-error-rate with polarization phase
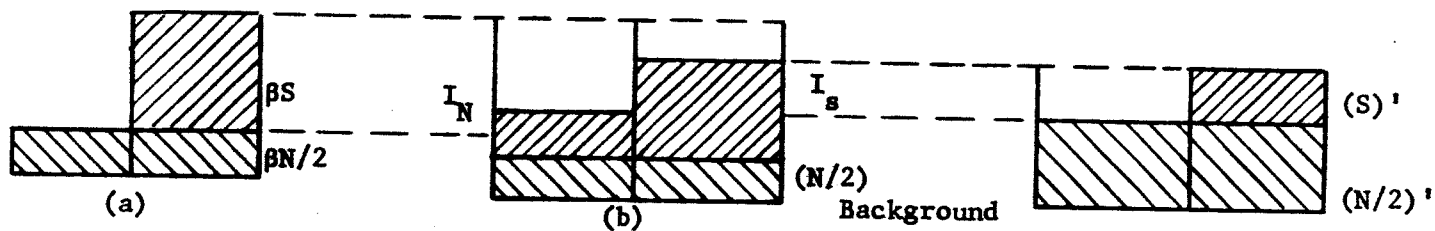
Figure 6-16. Partition of Received Energy

errors. The resulting equation is plotted in Figure 6-17. This graph demon-
strates that the residual phase errors expected from the system are not detri-
mental to a PCM/PL communication link.

Case 5: $\delta = 0$, $\beta \neq 1$ (Zero Phase Error, Appreciable Amplitude Error)

The error rate equation can be simplified if the following assump-
tion is made:

$$\frac{N}{2} \left(\frac{T_s + T_p}{2} \right) \approx \frac{\beta N}{2} \qquad (6-11)$$

The above approximation is appropriate since the system is assumed to be operat-
ing at high S/N and $\epsilon < 0.25$. The bit-error-rate equation for amplitude polar-
ization errors is obtained by substituting Equation (6-11) in Equations (6-9)
and (6-10), which in turn are substituted in Equation (6-3). The resulting
expression is plotted in Figure 6-18.

As a typical example of the transmissibility for poor dichroic
let T_p = 0.60, T_s = 0.45, δ = 0, β = 0.6, and ϵ = 0.25.

The quantum limit with the dichroic removed (ϵ = 0, β = 1) is 6.22
signal photons per decision (from Figure 6-15). By inserting the dichroic into
the optical path, the new quantum limit becomes (Figure 6-18):

$$S_{q\ell} = \frac{7.1}{0.6} = 11.8 \text{ counts}$$

This increased quantum limit can be overcome by increasing the
transmitter power by 2.8 db. The required increase in power reduces to approx-
imately 2.6 db for higher signal and noise powers (also from Figure 6-15).
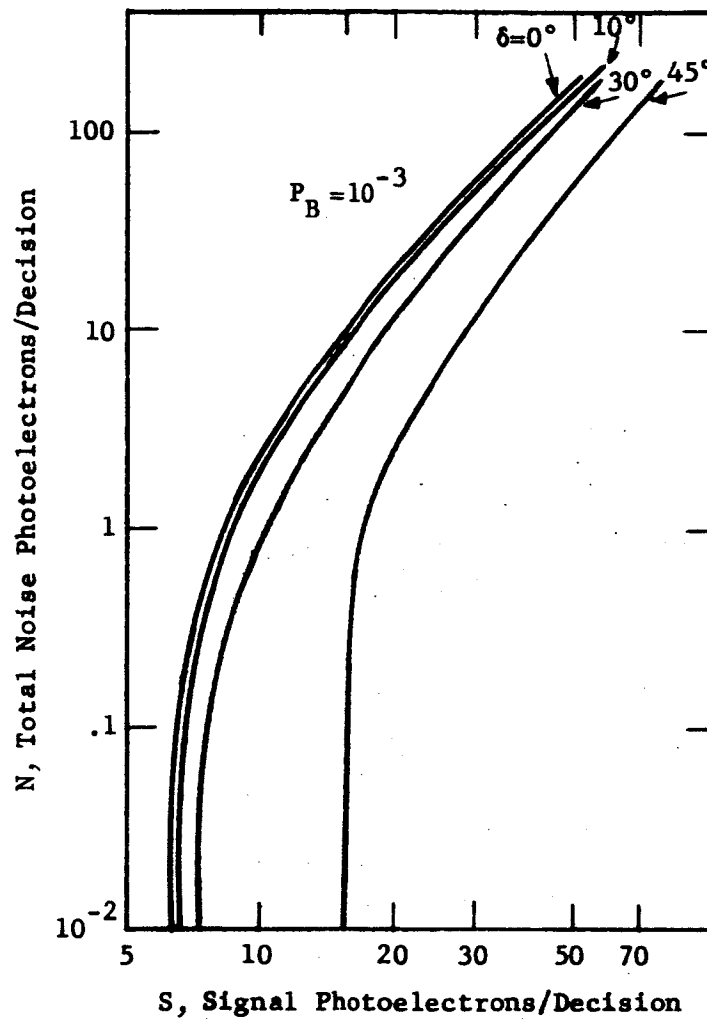
Figure 6-17. Signal Count vs. Noise Count for Various Polar-
ization Phase Errors for a Bit-Error-Rate $P_B = 10^{-3}$
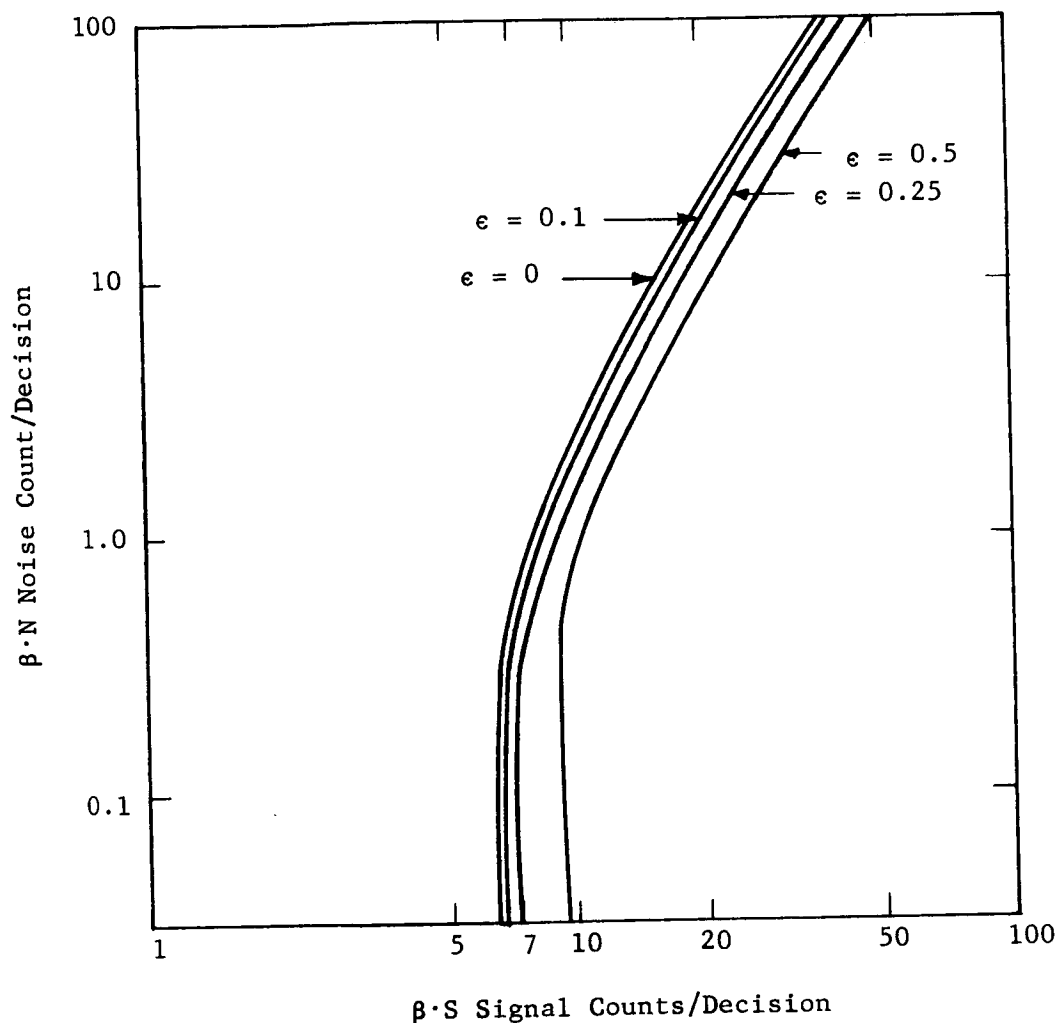
Figure 6-18. Average Signal Count vs. Average Noise Count
$P_B = 10^{-3}$, PCM/PL Modulation
Circular Polarization at Dichroic (Also Plane
Polarization at Dichroic with $\alpha = \pi/4$)

PLANE POLARIZATION INCIDENT ON DICHROIC

The foregoing discussion assumed circular polarization incident on the dichroic as illustrated in Figure 6-12. But if the phase correction plate in Figure 6-12 is moved to a position between L_1 and D_1 as shown in Figure 6-19, plane polarized blue light will be incident on the dichroic mirror and the effect on a PCM/PL receiver[4] will be changed in general.

Two axial orientations of the quarter-wave plate are of interest. If the axis is placed at $\pi/4$ to the "s" and "p" planes of the dichroic, the optical intensities of Equations (6-7) and (6-8) result. Thus, there is no advantage to placing the quarter-wave plate axis at $\pi/4$ to the plane of incidence for the dichroic mirror.

However, a different result occurs when the quarter-wave plate and dichroic "s" or "p" axes are parallel ($\alpha = 0$). In this special case, we no longer have a symmetric channel. That is, the bit having its polarization in the "p" plane (say, "0") will have a larger average energy than the other bit representing the "s" plane ("1"). Thus, the bit error contributions of the two channels must be considered separately.

---

[4] Since both the optical thickness and index of refraction of the phase correction plate are functions of wavelength, additional phase compensation is needed in the transmit optical signal. This phase correction may be accomplished simply by adding a DC bias voltage to the optical modulator.

Modulator

D_2

0, $\lambda/2$ Voltages

DC
Bias

L_1

D_1

PCM/PL
Receiver

Phase
Correction Plate
($\sim \lambda/4$)
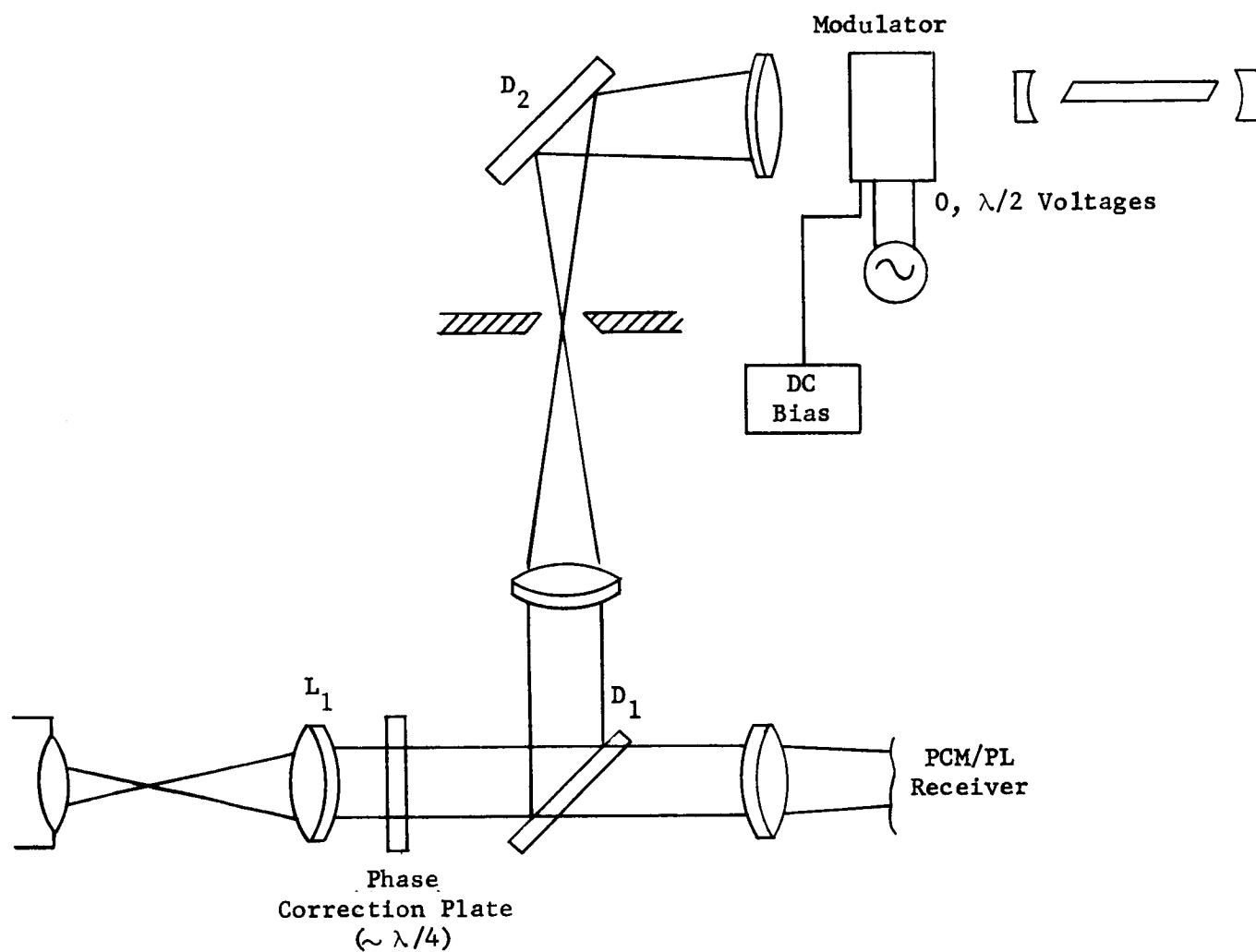
Figure 6-19. . Plane Polarization at Dichroic D_1

Assuming random data, the bit-error-rate for a plane polarized PCM/PL signal incident upon a dichroic mirror when $\alpha = 0$, $\delta = 0$, is

$$P_B = \frac{1}{2} \sum_{K=0}^{\infty} \frac{P_K (\beta S + \beta N/2)}{2} \left[\overline{Q_K (\beta N/2)} + \overline{Q_{K+1}(\beta N/2)} \right]$$

$$+ \frac{1}{2} \sum_{K=0}^{\infty} \frac{P_K (\zeta S + \zeta N/2)}{2} \left[\overline{Q_K (\zeta N/2)} + \overline{Q_{K+1} (\zeta N/2)} \right]$$

(6-13)

where

$$\zeta = \beta(1-\epsilon)$$

$$= \text{Min} \left\{ T_p, T_s \right\} \text{ or Min} \left\{ R_p, R_s \right\}$$

Equation (6-13) is plotted in Figure 6-20. Assuming the values of the previous example dichroic, namely; $\beta = 0.6$, $\epsilon = 0.25$ and $\delta = 0$, the power increase required to have the system operated at the quantum limit at the original bit-error-rate is 3.5 db. This is somewhat worse than the 2.8 db previously calculated for circular polarization incident on the dichroic.

CONCLUSIONS

1. Comparison of Figures 6-18 and 6-19 shows that if $\epsilon > 0.25$, it is best to have the PCM/PL signal circularly polarized at the dichroic.

2. The PCM/PL signal is not significantly degraded even with residual phase errors of 10° to 20° (from Figure 6-17). Since errors exceeding this magnitude can be avoided by proper dichroic design, polarization phase errors will not be a significant design problem.

Figure 6-20. $P_B = 10^{-3}$, PCM/PL Modulation Plane Polarization
at Dichroic with $\alpha = 0$

3.   The amplitude losses considered will affect both the signal and

the noise. Thus, in the special condition, $\beta \neq 1$, $\delta = 0$ and $\epsilon = 0$, the signal-

to-noise ratio will remain constant ($S/N = \beta S/\beta N$). However, the reduction of β

increases the relative contribution of quantum noise. Thus, for example, in

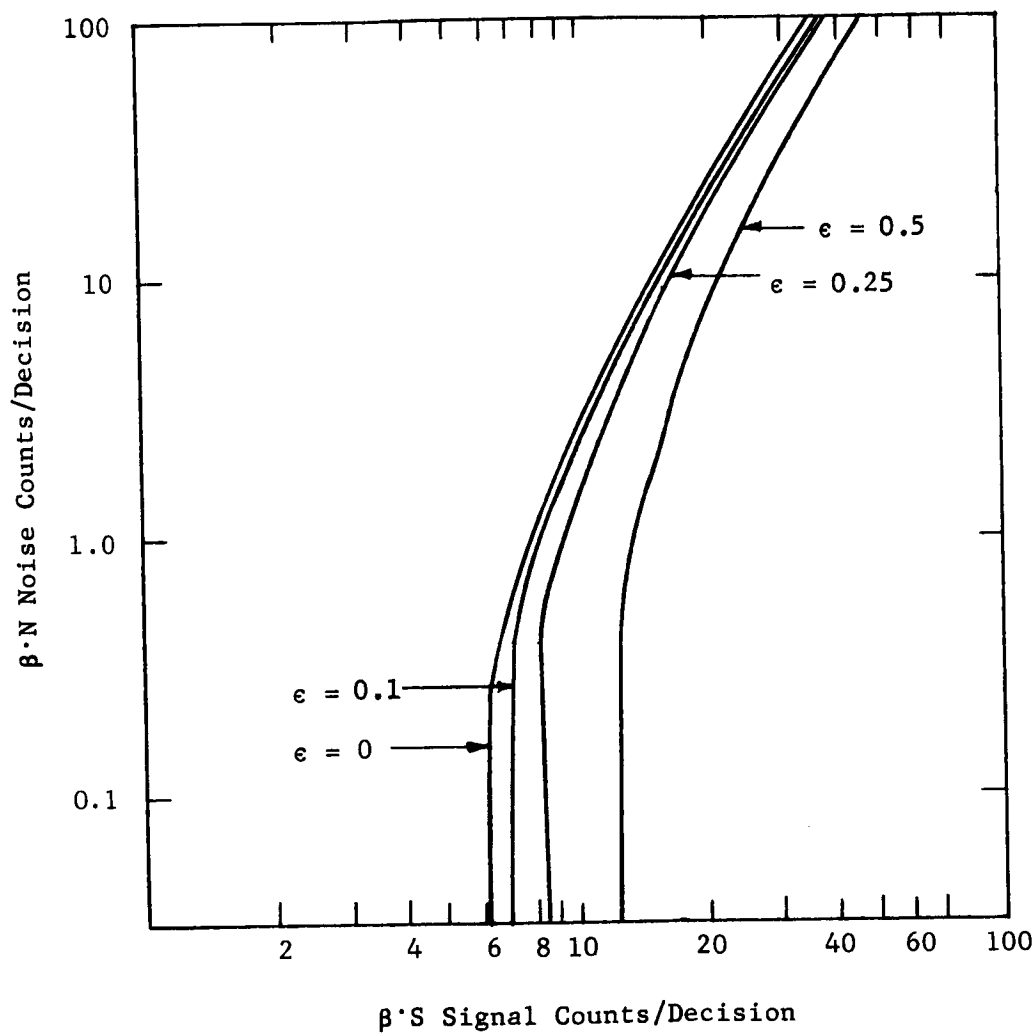a system operating near the quantum limit, both the transmissibility of 0.51μ

signal and reflectivity of 0.63μ signal should be as large as possible.

4.   The optical arrangement shown in Figure 6-12 may be used if

the dichroic complies with the following specifications: δ_T, $\delta_R < 15°$; ϵ_T,

$\epsilon_R < 0.10$; $\varphi_1 = \pi/4$; $\beta_R \gtrsim 99.9$; and β_T correspondingly is as near unity as possible.

5.   The prime requirement of the dichroic D_1 is that the reflectivity

of the red light should be close to 1.0. This insures proper isolation between

the transmit and receive signals. Figure 6-13 demonstrates that the transmit

He-Ne laser signal suffers insignificant polarization errors. Thus, PCM/PL is

an allowable choice for the transmit modulation technique.

6.   PCM/PL is susceptible to polarization errors. However, the

detection of a received amplitude modulated optical signal is nearly independent

of the polarization. Thus, the AM signal will suffer only a normalized power

loss between $1-\beta$ and $1-\beta + \beta\epsilon$. The use of AM modulation also significantly

simplifies the receiver, illustrated for example in Figure 6-21. This arrange-

ment uses the received optical energy for both telemetry and the fine guidance

of the transfer lens. By using the subcarrier amplitude modulation on a carrier

frequency greater than 10 Kc, the telemetry spectrum can be independent of the

amplitude variations of the fine guidance for a low-data-rate channel.
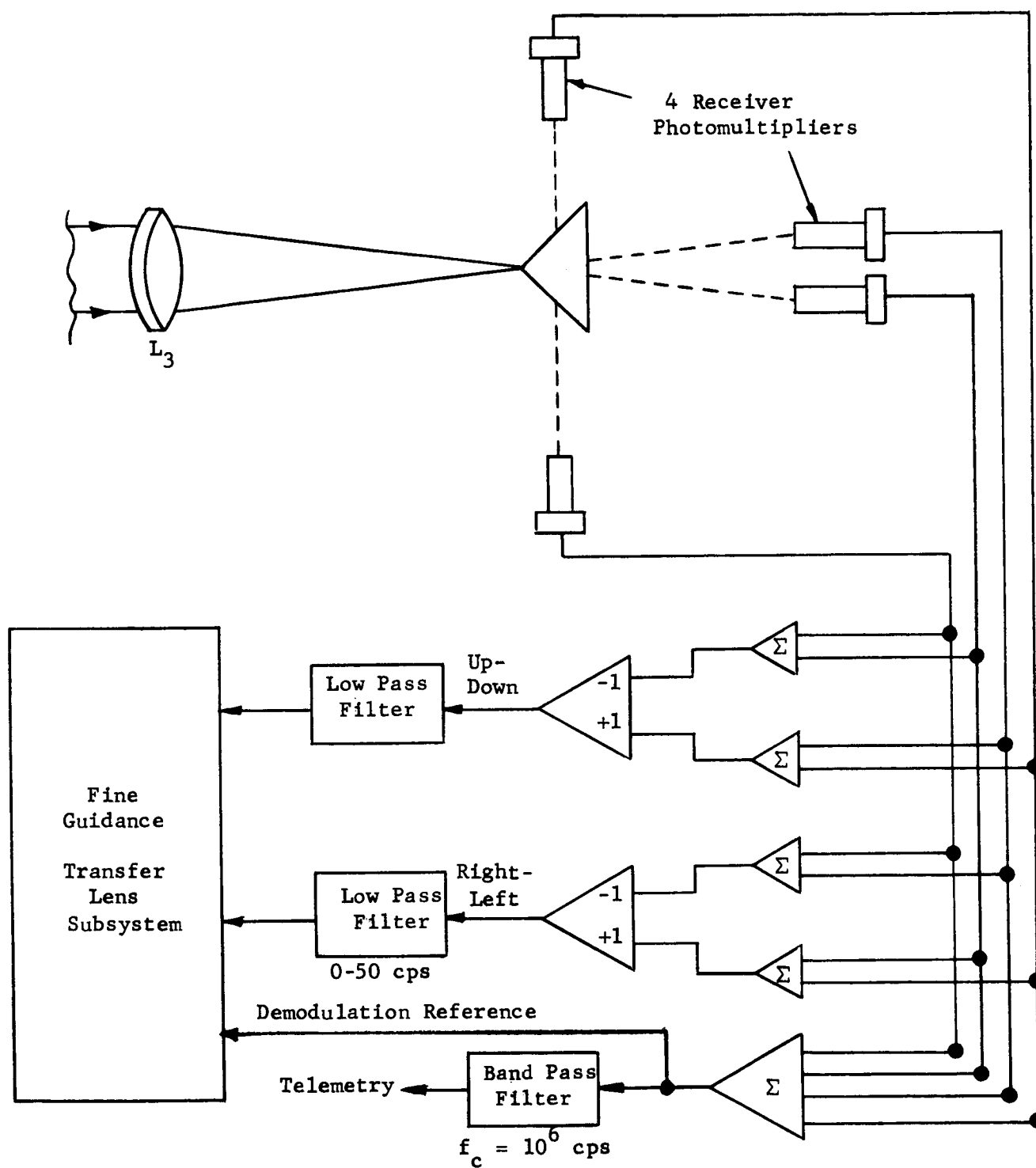
Figure 6-21. Subcarrier AM Receiver

7. The angles φ_1 and φ_2 may be reduced to reduce the polarization errors of the received PCM/PL blue light (Figure 6-13). However, severe space allocation problems may occur for angles $\varphi_1 < 30°$ because of focal-length limitations of L_2, L_3, and L_4. The optimum angle of φ_1, may be found by analyzing the transmissibility of available dichroic mirrors and the PCM/PL error rate curves.

8. A comparison between Figures 6-18 and 6-19 demonstrates that circularly polarized light incident upon the dichroic provides only a marginal advantage.

SECTION VII

CHANNEL ALIGNMENT AND TRANSMIT BEAM OFFSET CONSIDERATIONS

7.1. INTRODUCTION

In this section we shall assume that system focus has been taken care of by the procedure outlined in Section III. To reiterate, the axial location of each lens behind the main telescope is assumed to be permanently fixed after initial mechanical adjustments have been made to within the appropriate tolerances. The spacing of the secondary mirror with respect to the primary is left as the only remaining adjustment. To refocus the system an electrical dither signal is applied to the transfer lens while the system is tracking a beacon. (In the case of our laboratory experiments, a 16-inch collimator furnishes collimated light as if from a beacon at infinity. In the spaceborne case, the beacon light originates from an argon laser on the ground.) The resulting motion of the transfer lens is then monitored while the secondary mirror is moved in the direction of or away from improved focus. Optimum focus then is found by searching for the point at which the transfer lens experiences a minimum of motion induced by the dither signal.

When the complete system is focused, the problem remains as to how alignment of the transmit channel with respect to the receive channel can be simply and accurately determined. Also, once mutual boresight has been established, it is necessary to provide a mechanism to point the transmit channel away from this reference. In particular the transmit beam must be offset from

the receive line of sight by as much as 36 arc-seconds to make up for the

transit time and Bradley effects over interplanetary ranges.

This section is concerned with our investigation into ways of

building alignment and beam offset capabilities into the project breadboard.

7.2   ALIGNMENT REQUIREMENTS

The best approach to the problem of ensuring that the transmit

channel is accurately aligned with the receive channel is the one that uses

the least number of components to do the job. What exactly is this job?

Consider Figure 7-1 which illustrates the layout of the two channels and imagine

that we are looking into the beamsplitter in the direction shown. The condition

of mutual channel alignment is when, from this point of view, an image of the

equivalent f/70 laser source appears to be exactly coincident with an imaginary

f/70 diffraction image centered on the apex of the image divider. Note that

this is completely independent of the rest of the optical system. The tele-

scope and transfer lens merely serve to magnify the diameter of a collimated

axial bundle.in the region of the beamsplitter 100 times, from about 4 mm to

400mm (16 inches), and to demagnify ray angles in that region by the same amount.

There are two possible kinds of misalignment between the two channels;

parallel displacement of the optical axes and angular misorientation of the axes.

The first of these is illustrated in Figure 7-2 and results when the axes of the cone

of diverging laser light in the transmit channel is not coincident with the axis of

the cone of converging light with the receive channel. Since the receive channel

axis coincides with the telescope axis, then in the presence of this defect some

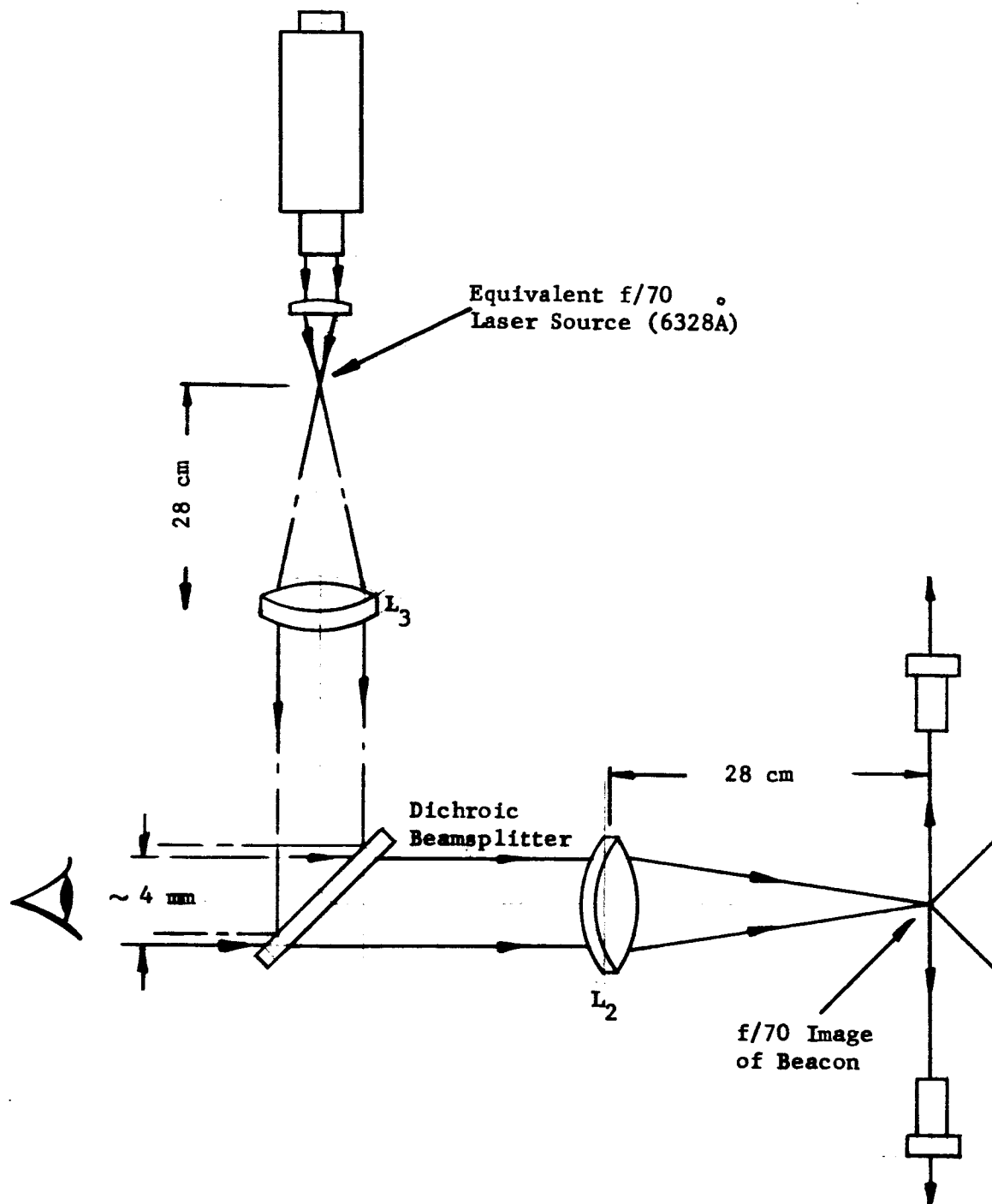marginal rays of the transmit laser light are vignetted.

Figure 7-1. Basic Optical Elements for Channel
Alignment Considerations.

Effective
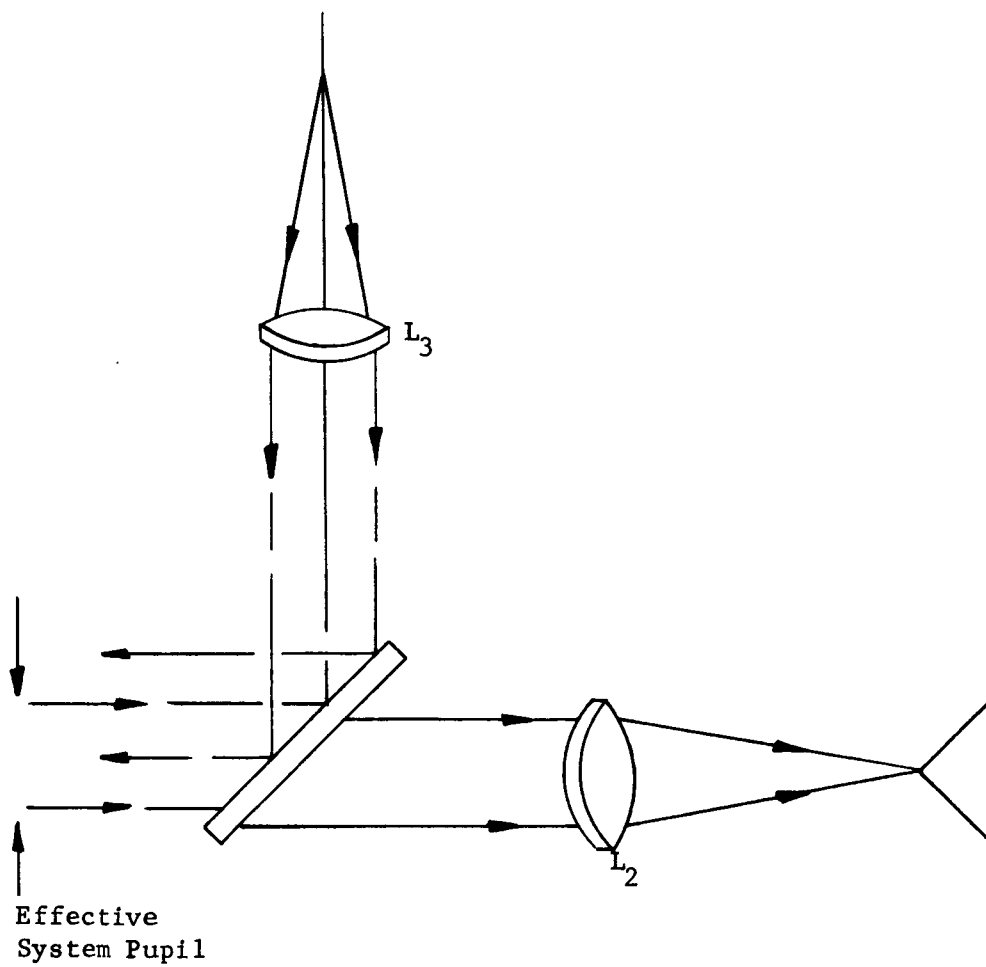System Pupil

Figure 7-2.   Illustration of Parallel Displacement
             of Channel Axes.

A nominal amount of vignetting can be tolerated by the system.
For example, if when merged by the beamsplitter the axes of the two channels
depart by say 5% of the 4mm axial bundle diameter, then approximately 6%
of the transmitted light power will be lost through vignetting which is not
too serious. Related back to a positioning tolerance on the laser, this means
that the axis of the laser must be located to within a suitable fraction,
say ±5%, of the output beam diameter. Typical He-Ne lasers have an output
beam diameter of a few millimeters. Taking 3mm as an example, an appropriate
positioning tolerance for the laser axis is ±0.15mm. (±.006 inch). This is
a liberal mechanical tolerance and shows there should be no need for post-launch
repositioning of the laser axis in a spaceborne optical communications system.

What about angular misalignment of the channels? Assuming the
receive channel to be the reference once again, to an observer looking into the
beamsplitter as in Figure 7-1 this defect causes the image of the transmit laser
source to form off center with respect to the apex of the fine guidance image
divider. If this relative image displacement equals the diameter of an f/70
diffraction disc, then the transmitted beam will be mispointed by an amount
equal to the diffraction cone angle of the primary mirror if the system is dif-
fraction limited. Back on the earth the center of the beam will miss its mark
be one full beam diameter. Smaller misalignments will have correspondingly
smaller effects and less important consequences.

As a reasonable tolerance for this form of misalignment, let us
demand that the transmitted cone of light shall be pointed with an absolute
accuracy of ±10% of the cone angle.

To the observer of Figure 7-1 this means that the center of the equivalent f/70 transmit laser image must be in a circle centered on the apex of the image divider and having a radius of 10% of an f/70 diffraction-limited image. Assuming the image diameter to be equal to the diamter, D, of the first dark ring of the Airy pattern, which is given by the formula

$$D = 2.44 \lambda f$$

where λ is the wavelength of operation and f is the final f-number of the system, the image position tolerance amounts to $\pm.011$ ($\sim \pm.0004$ inches). This is also the lateral positioning tolerance of lens L_3 shown in Figure 7-1 and previously in Figure 2-1. An equivalent statement is that the axis of the transmit laser beam must be oriented with an angular accuracy given by the ratio of $\pm.011$mm to the focal length of L_3, which in our case is 250mm. The angular tolerance is therefore 4.4×10^{-5} radians (9.5 arc-seconds). (Note that this corresponds to about 1/10 arc-second on **demagnification** by the 16-inch aperture project telescope.)

The post-launch alignment tolerance of ±9.5 arc-seconds in the general region of the transmit channel possibly can be met by rigorous mechanical design alone. However, fairly long optical pathlengths are involved as are components of substantial mass (such as the laser itself).

These factors may unduely complicate the problem of space qualification of the system and are likely to necessitate some form of backup post-launch alignment equipment. The same equipment is needed in any event to perform the important diagnostic function of measuring, on ground command, whether the channels are aligned correctly.

7.3 ALIGNMENT TECHNIQUE

An attractively simple technique to measure, and therefore to read-just, the relative angular alignment of the two channels becomes feasible as a fortunate consequence of using the channel separation techniques discussed in Section IV. Only one additional optical element is required - in this case a cube-corner prism - and advantage is taken of the residual sensitivity of the receive channel to light originating from the transmit channel. This technique is illustrated in Figure 7-3 and was built into the project breadboard.

The cube-corner prism is located in the unused region behind the dichroic beamsplitter and is ordinarily blocked by a retractable shutter. When the shutter is withdrawn, the small amount of collimated transmit laser light passed by the beamsplitter is reflected directly into the receive channel. This light is further attenuated by the pre-detection spike and/or SWPF and the remainder converges to a focus at or near the apex of the image divider. If the additional attenuation is only as much as dictated by the channel separation requirements, then the image will be bright enough for its positon to be measured by the fine-guidance photomultiplier. To the extent indicated by such a measurement, the image can then be centered by a lateral translation of lens L_3 or alternatively by means of the Risley prisms.

Alternative approaches were complicated by comparison and therefore were less desirable. For example, Figure 7-4 illustrates one of the discarded, but nevertheless feasible, alignment techniques.

A dichroic mirror is used to pass blue light from an auxiliary source and form an image that is conjugate to the equivalent transmit laser source. A shutter retracts from in front of a cube-corner prism that retroreflects light
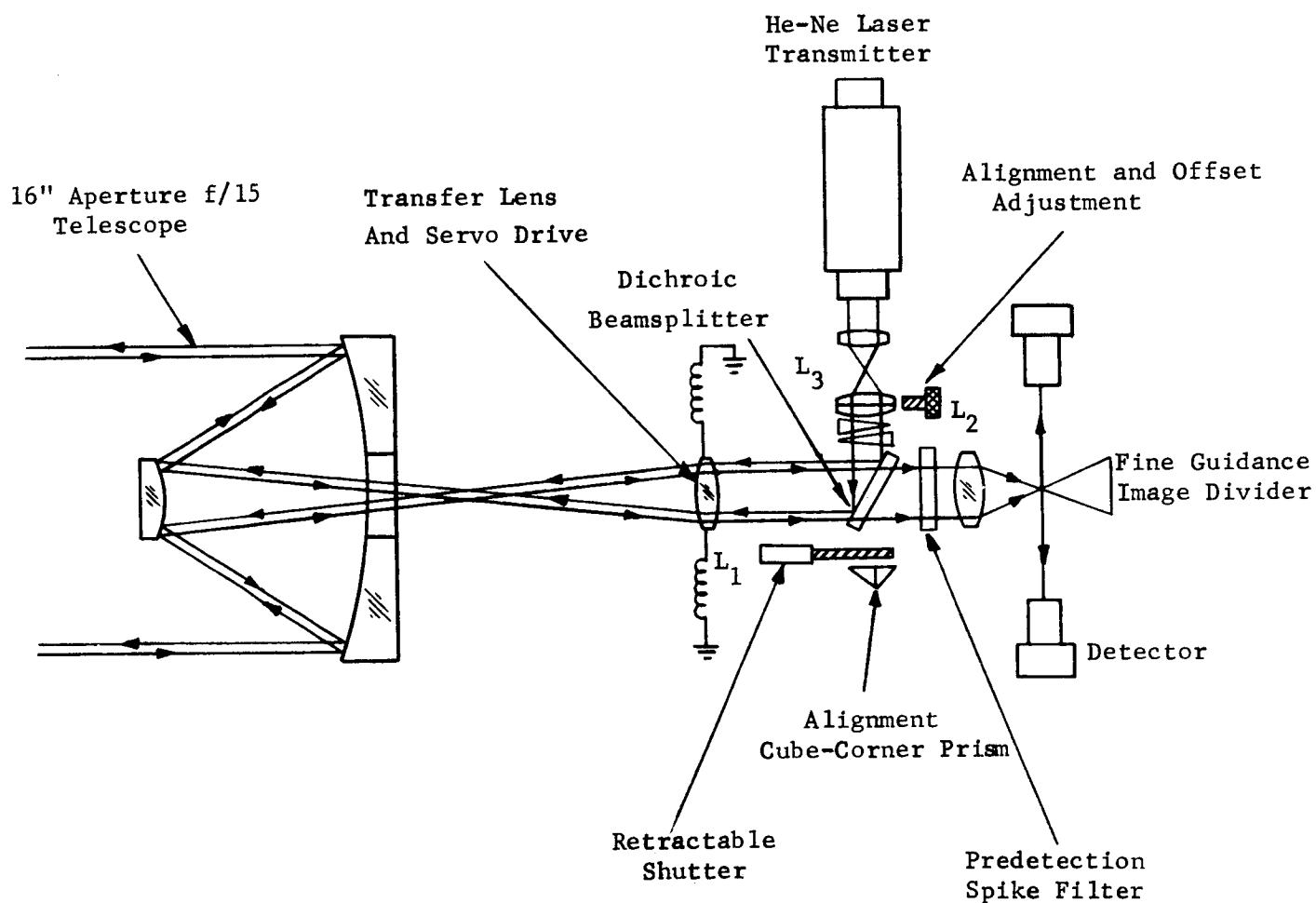
Figure 7-3.   Optical Layout of Project Breadboard
              Showing Auxiliary Cube-Corner Alignment Scheme.
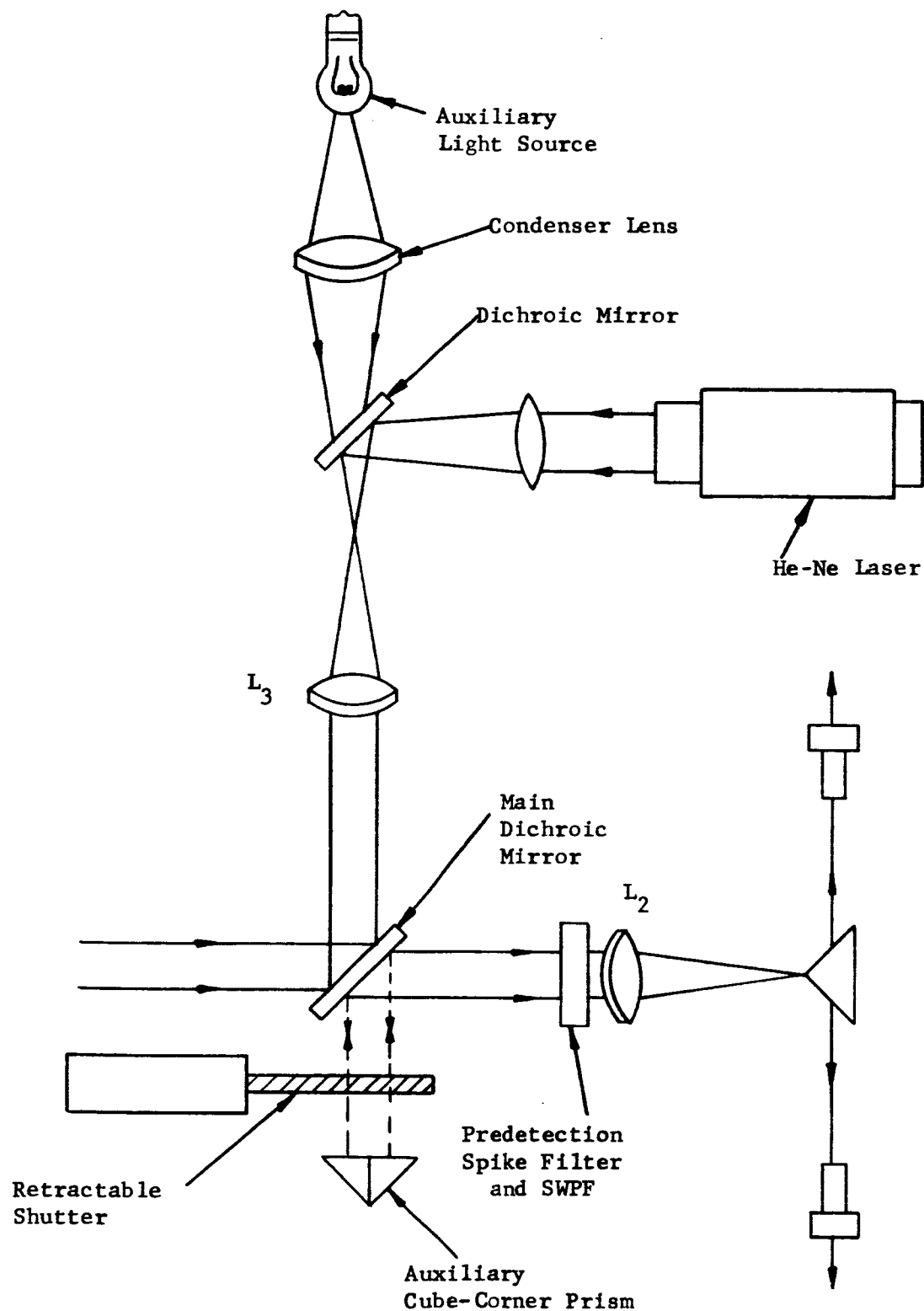
Figure 7-4.   Alternate Equipment Arrangement for Remote
              Boresight Alignment of Optical System

passing through the main dichroic mirror (which we recall is not perfectly transparent to blue light). An image of the auxiliary light source is sub- sequently formed near the nose of the fine-guidance beam dividing prism. This image is in blue light which is passed by the "spike" predetection filter. It is detected by the photomultipliers just as for incoming beacon light. To accomplish channel alignment, the laser collimating lens L_3 (or a Risley prism) is adjusted to make this image divide equally into four quadrants at the image divider (as measured by the four fine-guidance photomultipliers). This technique assumes that the auxiliary light source and associated optics can be accurately afixed with respect to the laser and thus be able to serve as an accurate post- launch alignment reference. On the other hand, the prior technique references the transmit channel directly to the receive channel and clearly is preferable for this reason alone.

7.4 METHODS FOR OFFSETTING THE TRANSMIT BEAM

The same optical or mechanical elements that are used to make the axis of the transmit channel collinear with the receive channel can also be used to offset the transmit beam and compensate for Bradley and transit time effects. The amount and direction of forward bias can be controlled by either

(a) translating the transmit laser collimating

lens L_3 in its plane or,

(b) manipulating a pair of Risley prisms situated

between this lens and the dichroic beamsplitter.

The lateral motion required in the current breadboard system by (a) is about 0.0004 inches per 1/10 arc-second of post-telescope beam offset. The angular deflection required by (b) amounts to about 10 arc-seconds at the Risley prisms to offset the beam transmitted by the telescope by 1/10 arc-second. The transmitted beam can be offset 30 arc-seconds by translating L_3 0.12 inches, or by wedging the optical path with the Risley prisms, by 50 arc-minutes.

By either method, the zero bias reference is the lens position or the Risley prism adjustment determined by the initial channel alignment procuedure.

7.5   OPERATIONAL DEMONSTRATIONS

The complete project breadboard was set up as illustrated in Figure 7-5 to demonstrate qualitatively the main features of the channel separation, alignment and point ahead functions in a working system. A 16-inch aperture collimator in the rear of the view shown in Figure 7-5, functioned as an argon-beacon simulator.

7.5.1   Channel Separation

The entire project breadboard was set up to show visually whether any traces of transmit laser light appeared in the receive channel. The arrangement behind the telescope was as illustrated in Figure 7-6 with the observer substituting for the image divider and photomultipliers. In the presence of about 7 milliwatts of power from the transmit laser at 6328Å impinging on the dichroic beamsplitter and subsequently leaving the telescope, no traces of scattered or directly reflected red light were visible to the eye in the receive channel. At the same time the artifical beacon, which in reality was a
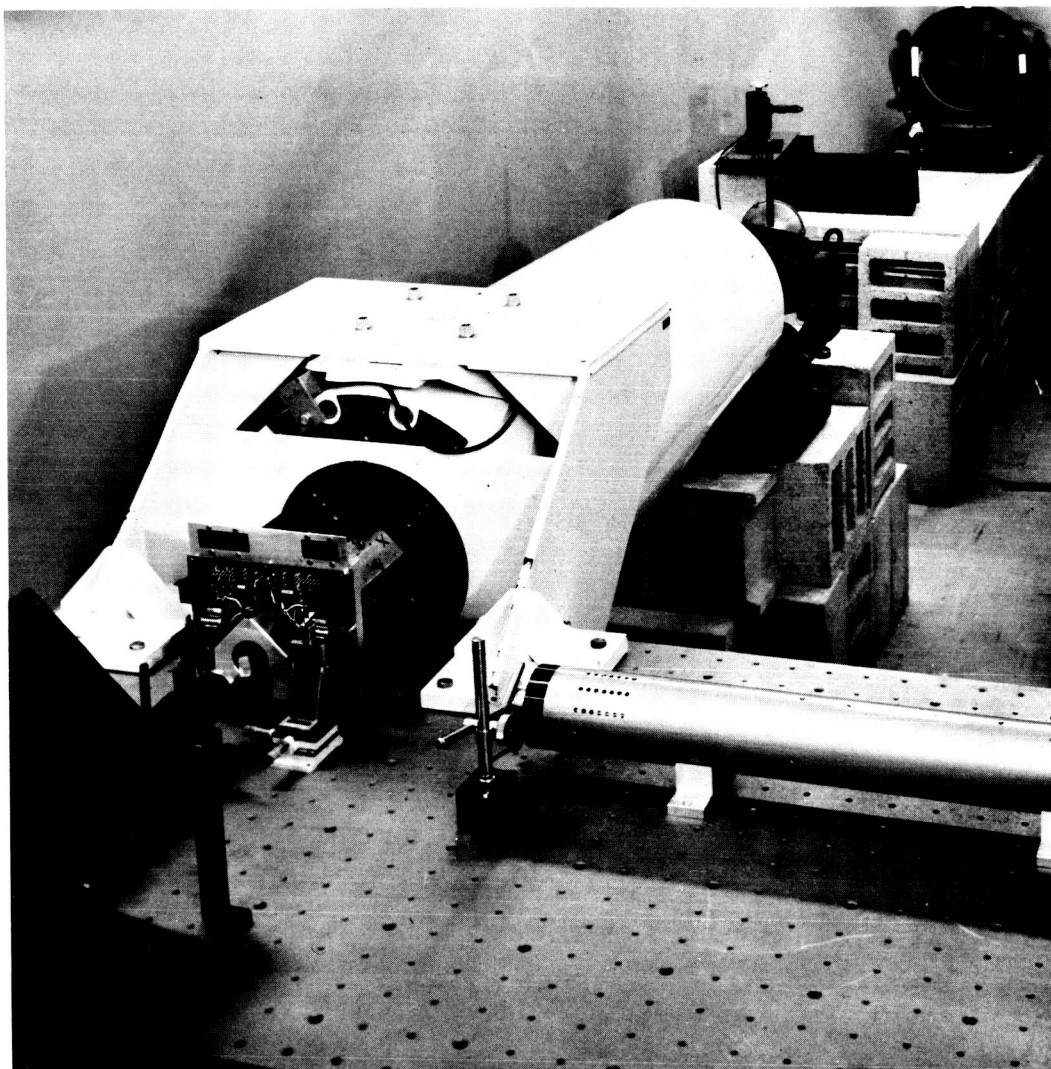
Figure 7-5. View of Complete Project Breadboard
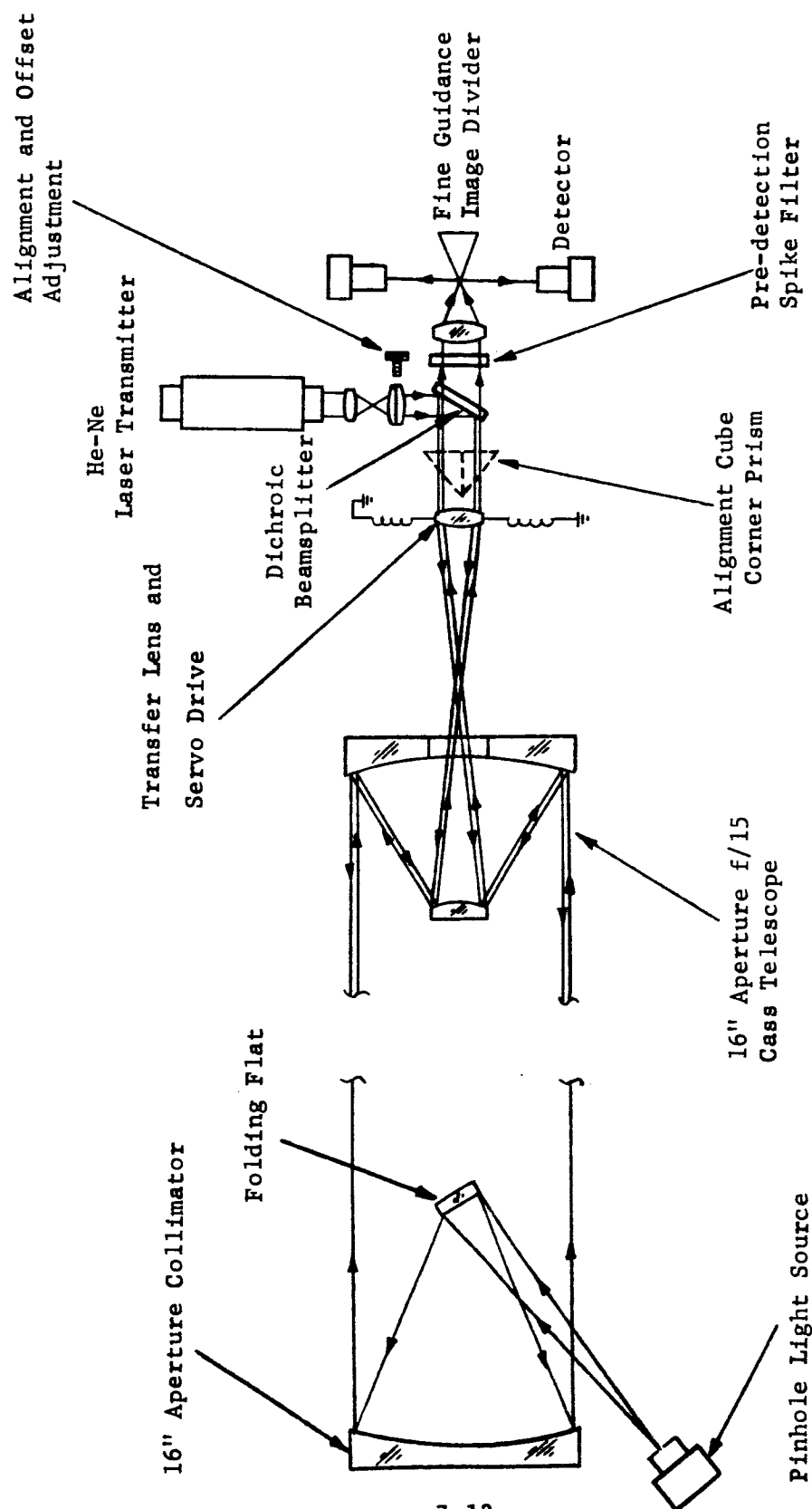   Including 16-Inch Aperture Beacon
             Simulator

Figure 7-6. Layout of Deep-Space Optical Communications System Breadboard and Associated Beacon Simulator

tungsten filament source illuminating a pinhole and seen through a 25Å wide spike filter at 4880Å, was brightly visible in the receive channel. This demonstration illustrated qualitatively the effectiveness of the channel separation techniques described in Section VI.

7.5.2   Alignment and Point Ahead

For alignment purposes a cube corner prism was inserted into the region shown in Figure 7-6. This location is an alternative to the arrangement shown in Figure 7-3. The channel separation figure of merit was previously established at $M \sim 115$ db.

The alignment technique of Paragraph 7.4 relies on the fact that with 11 decades of separation between transmit and receive channels, an adequate amount of light at 6328Å is reflected into the receive channel to use for system alignment when the auxiliary prism is put in place. By this means the equivalent f/70 laser source is imaged in the image-dividing prism. The apex, it should be noted, defines the axis as well as the f/70 focal plane of the entire optical system.

The laser collimating lens was translated manually to bring the 6328Å image exactly onto the apex of the image divider. This caused the image to be divided into equally intense quadrants, which demonstrated visually (corresponding to an electronic measurement at the intensities with the fine-guidance photomultipliers) that the channels were aligned. Hence, the transmit laser beam (outgoing) and the beacon laser beam (incoming) were made precisely coaxial. That this was the case was easily seen by removing the alignment prism and noting that an image was formed in red light back at the test collimator's source pinhole.

From this boresight reference the transmit beam was offset from 0 to various point-ahead angles of tens of arc-seconds by translating the laser collimating lens shown in Figure 7-6.

7.6   INFLUENCE OF SYSTEM COMPONENTS ON CHANNEL ALIGNMENT

7.6.1   <u>Relative Spectral Response of Receive Channel Photomultipliers</u>

The design of the Laser/Optics Techniques optical system calls for receive channel photomultipliers selected for minimum red response commensurate with near-maximum blue response. We discussed in Section VI how this helps to prevent transmit light from disturbing the proper functioning of the receive channel (beacon tracker). On the other hand we discussed in Paragraph 7.3   how, after adequate channel separation is obtained by the various dielectric multilayer techniques at our disposal, the residual red response can be utilized for sensing mutual alignment of the two channels.

The subsystem of the project breadboard, which senses beacon image position or channel alignment, employs four photomultipliers and a four-quadrant optical image divider. This scheme necessitates using photomultipliers with nominally identical blue and red responses. Otherwise, if the photomultipliers are balanced when beacon light is imaged at the apex of the image divider, they can, nevertheless, register imbalance to an identical image in red transmitter light and result in a corresponding alignment error.

It turned out in practice that when the four EMI 9514S fine-guidance photomultipliers were balanced in response to light at 4880Å, a 2 to 1 spread was measured in their relative responses to light at 6328Å. This result is in keeping with the fact that 6328Å is well into the tail of this kind of photomultiplier response curves.

To avoid this possible source of alignment error, such photo-multipliers can be carefully selected for matching spectral responses. Alternatively, unequal responses can be corrected for by the alignment and/or tracking circuitry. In either case, it must be determined whether the spectral response of a given photomultiplier is subject to variations during the operating life of the spaceborne subsystem in which it is to be used.

7.6.2   Characteristics of Short-Wave-Pass Filter

As discussed in Section VI, more than 100 db of channel separation was achieved in the project breadboard by taking advantage of a special kind of short-wave-pass filter (SWPF) which is highly reflective at 6328$\overset{\circ}{\text{A}}$ and which typically transmits less than 1 part in 10^5 of incident light at this wavelength. To be able to carry out remote alignment with such a filter in place, it is necessary that this residual amount of light remains collimated and not be due primarily to scattering through coating imperfections.

We evaluated our existing SWPF's in this regard and have found that, while some samples are freer of imperfections than others, this is an area where improvements are needed.

Much of the residual transmittance of SWPF's with maximum rejection of red transmit light stems from tiny holes occurring at random over the dielectric multilayer. This is illustrated by Figure 7-7 which shows a magnified image of a typical SWPF illuminated from behind by a He-Ne laser. These holes are as small as 10 microns in diameter and are, therefore, responsible for light being diffracted into the entire acceptance angle of the fine-guidance subsystem.
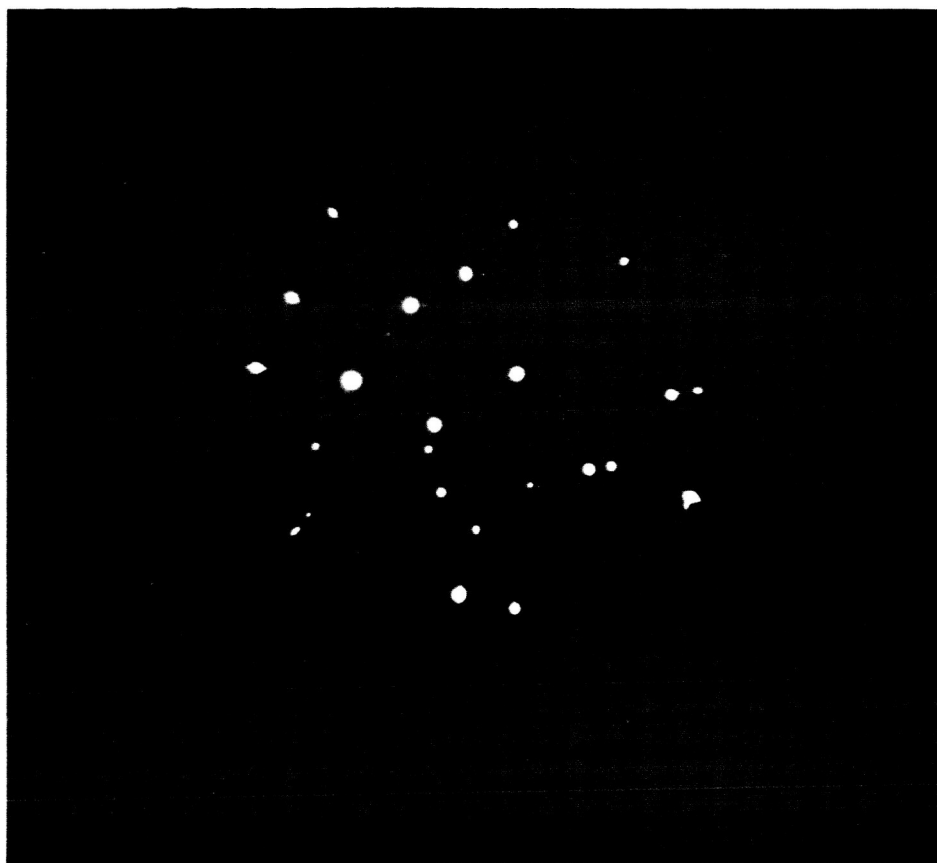
Figure 7-7. Photograph of Transmission of He-Ne
Laser Light Through Pinholes in
Dielectric Coatings on Short-Wave-
Pass Filter

To evaluate the influence of these imperfections on the alignment
scheme, measurements were taken with the arrangement illustrated in Figure 7-8.
In effect, the receive channel was separated from behind the beamsplitter of
the breadboard setup, and its clear aperture of 1.2 cm was illuminated by a
He-Ne laser.

The image in the focal plane of lens L_2 consisted of a bright spot
in the center embedded in a diffraction pattern resulting from the numerous
holes of the SWPF. Figure 7-9 shows a magnified photo of the central area of
the image plane. The structure of the background diffraction pattern is due
to ghost reflections by the imaging optics and its detail is irrelevant in this
context. The center spot consists of an Airy pattern of diffraction-limited
size - not resolved on the photo - and its relative intensity is determined
by the amount of laser light that passes the SWPF without change in wavefront.
Clearly, only this portion of transmitted red light can be utilized for remote
alignment, and it has to be detected against the diffraction-pattern background
resulting from coating imperfections.

Measurements on a number of SWPF's showed that the intensity of
the central spot amounts variously to 50%, 20%, or even very much less of the
total red light received by the fine guidance system. This renders them not
completely satisfactory for the remote alignment scheme in their present
form.

However, we believe that SWPF's that are essentially pinhole-free
can be prepared in the future by special deposition techniques. This develop-
ment is desirable both for enhanced isolation properties and for simplicity
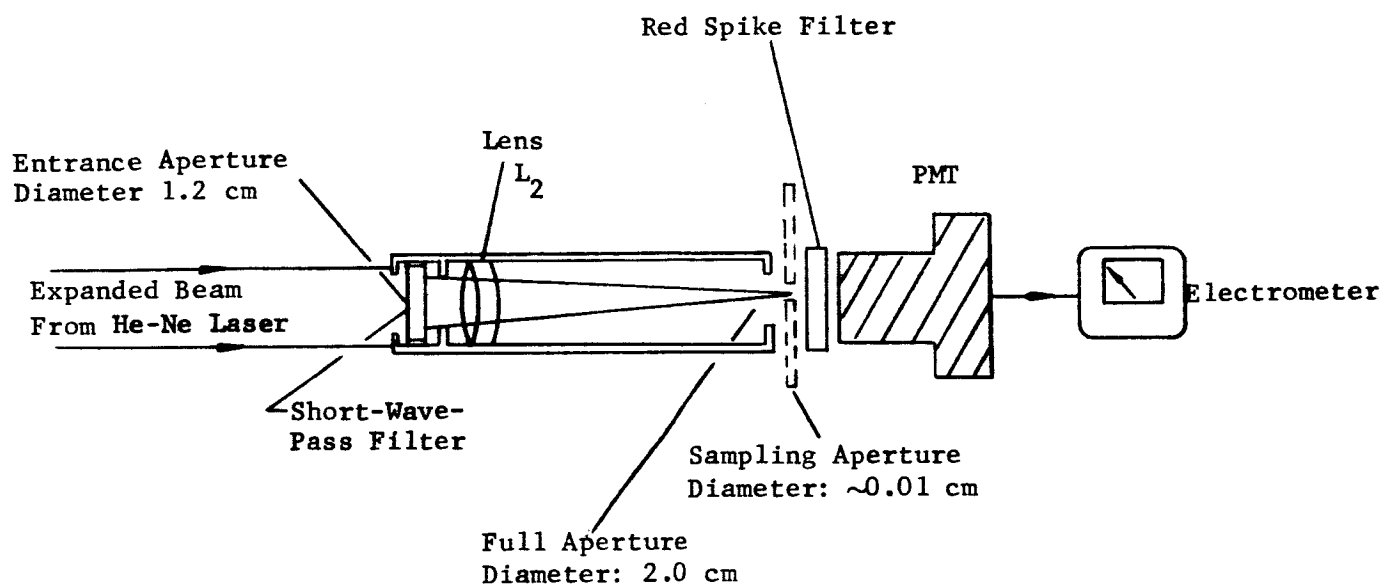
Figure 7-8. Experimental Setup used to Evaluate Short-Wave-Pass Filters in Connection With Alignment Scheme.
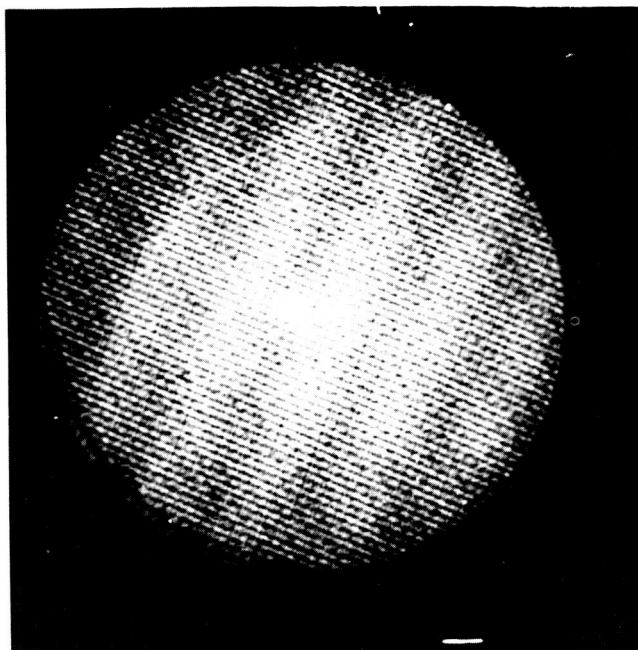
Figure 7-9.   Photograph of Image Formed by Lens L_2
of Light Transmitted by Short-Wave-
Pass Filter

of the alignment technique. In regard to the latter, it would eliminate any need for a filter-removal mechanism which otherwise might be required while alignment is being carried out.

7.6.3   Single Substrate Spike Filter

Towards the end of the contract period a spike filter was manu-factured consisting of four dielectric stacks deposited serially on a single substrate. Its characteristics are nominally the same as those of the spike filter with enhanced red suppression described previously. The latter was built up from four individual coating stacks on separate substrates, suffered from multiple ghost reflections and relatively poor optical quality, and im-paired the image quality in the fine-guidance channel. The new filter has neither of these defects. However, in common with some of the SWPF's dis-cussed earlier (which comprises one of the four stacks) this one sample ex-hibits an unsatisfactorily large ratio of scattered to collimated residual red transmission. This is not expected to be a fundamental limitation on the use of this device.

It is noteworthy that the newly developed single substrate spike filter replaces a cemented assembly of dielectric coatings and colored glass filters. The benefits that accrue are:

      (a)   higher peak transmission

      (b)   improved optical quality.

7.7   DISCUSSION

As we have shown in Paragraph 7.2, it cannot be stated categorically that post-launch channel realignment will be absolutely necessary and that

equipment should be provided as part of the optical communications system for this purpose. Such a need can only be proven in the course of developing a space-qualified version of the project breadboard. However, a strong case can be made for providing a way of monitoring channel alignment purely for diagnostic and backup purposes.

The technique we implemented in the project breadboard and investigated in close association with the work on channel separation is foolproof in this sense. But it is not foolproof if the pre-detection filters or any other element must be removed to obtain enough red sensitivity in the receive channel.

We are certain that the technique can, in fact, be employed with an arbitrary amount of attenuation as dictated by channel separation requirements. But it should be understood that the residual transmission of transmit light into the receive channel must be a result of coherent transmission by the dielectric multilayers, not because of transmission by minute surface imperfections. This criterion should be borne in mind when extremely narrowband pre-detection filters and improved dichroic mirrors are developed in the future for similar systems.

SECTION VIII

TRANSFER LENS SERVO SUBSYSTEM

8.1 INTRODUCTION

A brief description of the transfer lens servo subsystem was given in Section III of this report. Here we shall go into considerably more detail to provide a better understanding of how it functions in the project breadboard. This section is also intended to illustrate the technology involved in developing this subsystem for the current needs of the breadboard and for future spaceborne optical communications systems.

Small "cross-line of sight" pointing errors in an optical telescope can be removed by introducing compensating motions to a transfer lens within the optics. The basic technique, shown in Figure 8-1, was designed into the project breadboard to obtain automatic laser tracking capability. The arrangement originated in the Stratoscope II Astronomical-Telescope (Figure 8-2).

The mechanical assembly (Figures 8-3, 8-4, and 8-5) consists of two magnetic drives, optical elements housed in a movable lens cell, a counter-weighted lens cell support device utilizing flexure bearings (and allowing only lens translations perpendicular to the optical axis), mechanical stops to provide both soft and hard limiting action plus collars convenient for lens cell centering, and capacitive type position pickoffs whose outputs are differentiated to obtain velocity feedback signals. The construction features
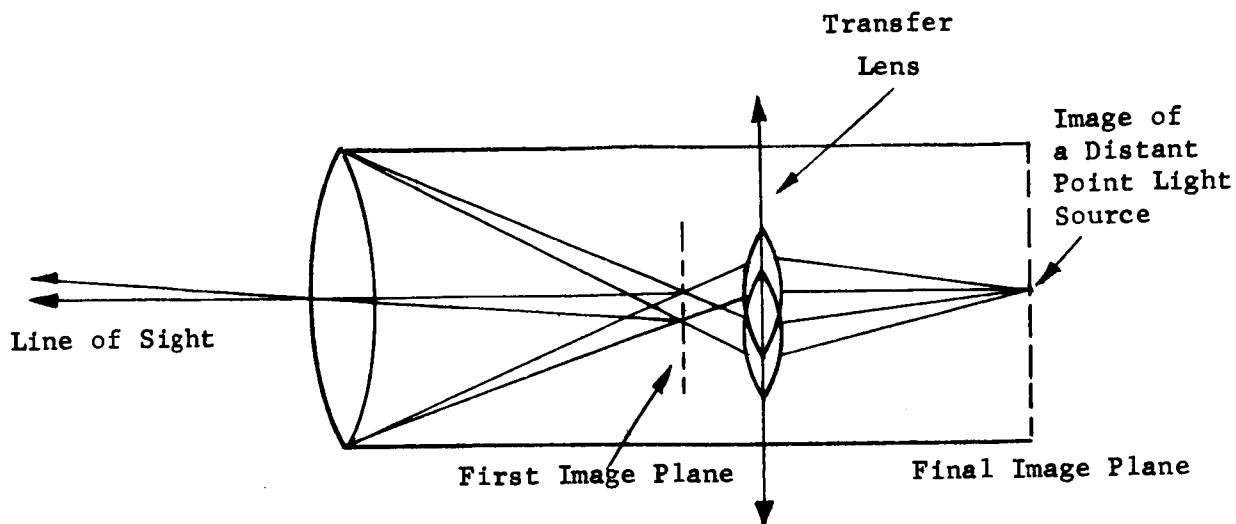
Figure 8-1.   Transfer Lens Motions Which Compensate for
              Image Motions Due to Telescope (or Object)
              Movements.
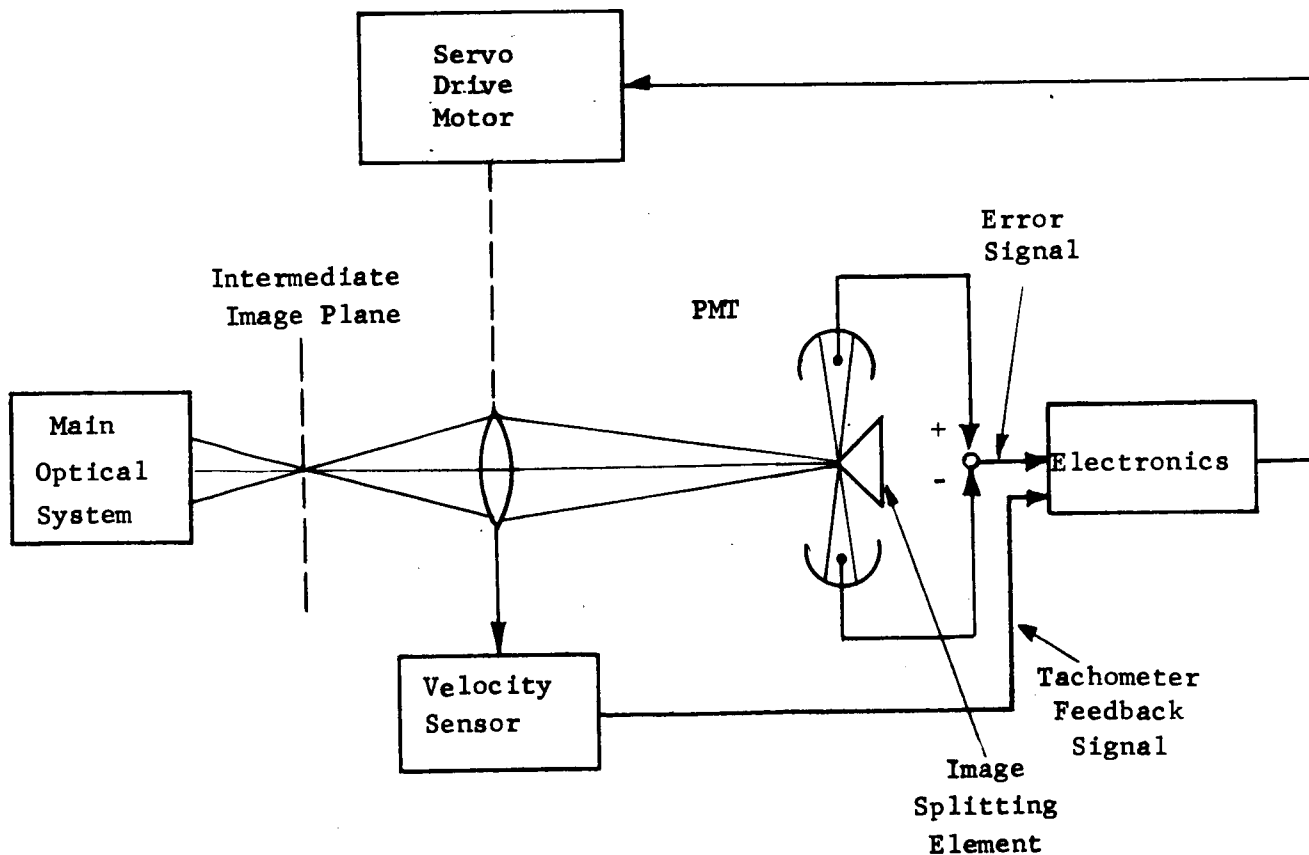
Figure 8-2.   Single Axis Arrangement Illustrating The
              Stratoscope II Star Tracking Method
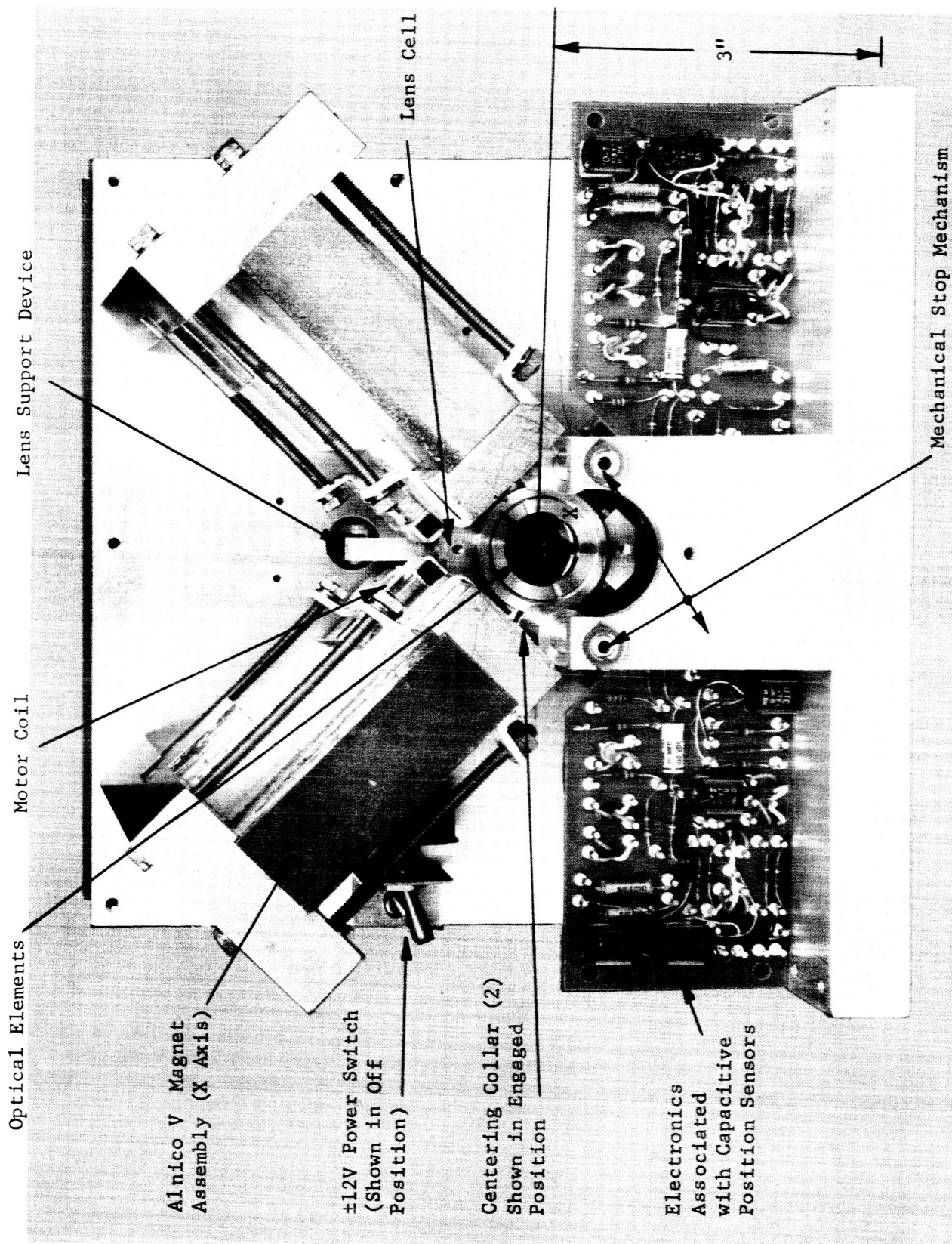
Figure 8-3. Transfer Lens Mechanical Subassembly, Front View

Optical Elements

Motor Coil

Lens Support Device

Lens Cell

Alnico V Magnet Assembly (X Axis)

±12V Power Switch (Shown in Off Position)

Centering Collar (2) Shown in Engaged Position

Electronics Associated with Capacitive Position Sensors

Mechanical Stop Mechanism

3"

Flexure Bearings
(6004-600, 5004-800)

Electronics Associated
with Motor Coil Excita-
tion and Coil Velocity
Feedback

X-Axis
Drive Motor

Movable Portion
of Stop Mechanism

Free End of
Cantilevered
BeCu Stop Quill

Stop Mechanism
(Shown with Centering
Collars Disengaged)

Quill Housing

Moving Capacitor
Plate Support

Counterweight
Housing

Lens Cell Support
Rods (4)

Y Axis Capacitive
Position Sensor

Figure 8-4. Transfer Lens Mechanical Subassembly, Side View

Vertical Plate

X Axis Drive Motor

Counterweight Housing

Horizontal Support Base

Y Axis Drive Motor

Two Axis Flexure Bearing Support

Counterweights (4) On Ends of Lens Cell Support Rods

To Image Splitting Prism

Figure 8-5. Transfer Lens Mechanical Subassembly, Rear View

mechanical design changes from that of Stratoscope to obtain compatibility with a long term hard vacuum environment and, additionally, to avoid wherever possible potential problem areas as revealed by previous work. A prime exa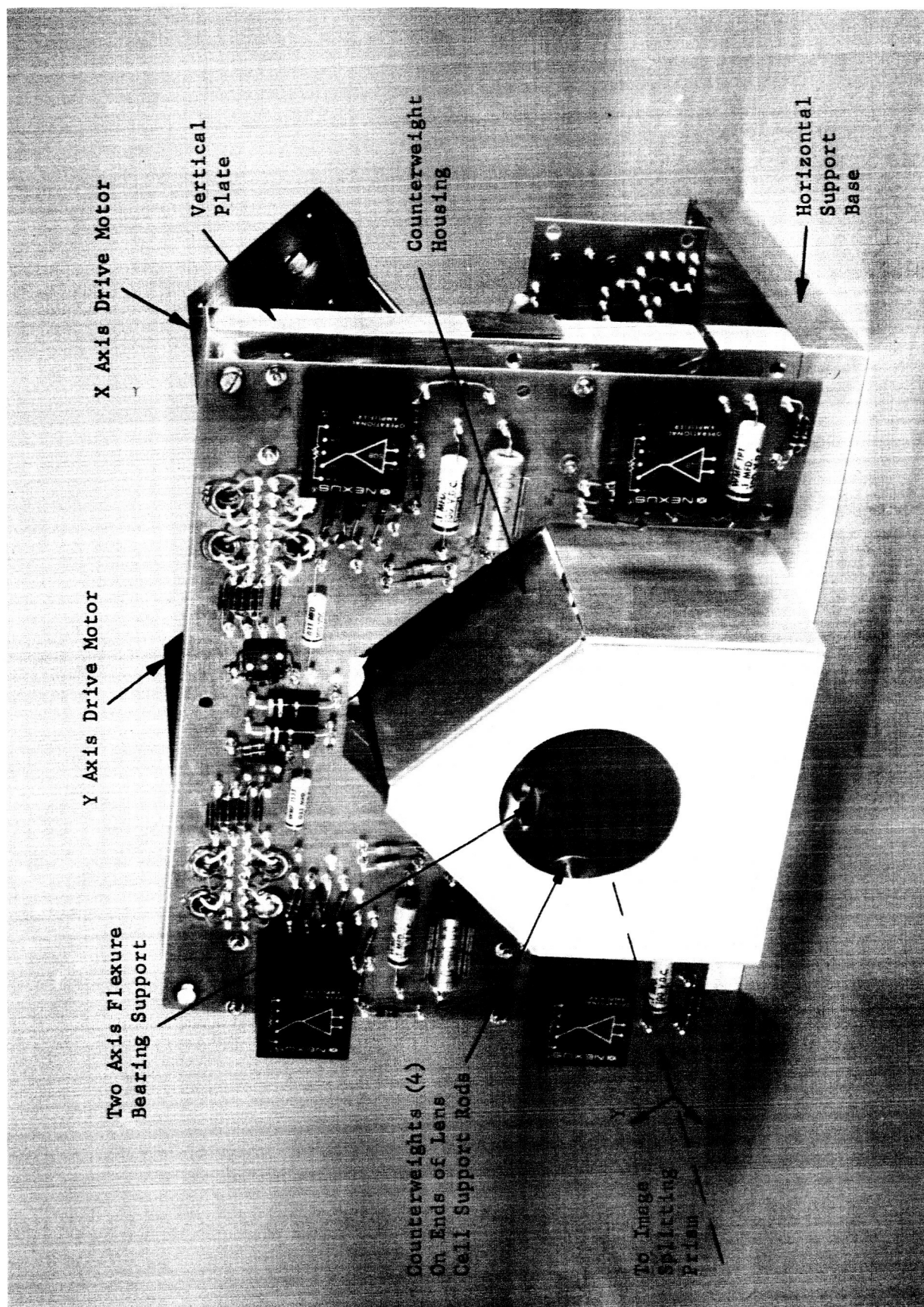mple of the latter type change, which also allowed placement of the optical axis at a nominal 3 inches off the support table (refer to the original design specification of Table 8-1), involved replacement of bulky and heavy magnetic velocity sensors by small and light capacitive position sensors. This alternate approach avoided electrical feedback difficulties associated with magnetic field coupling between motor and tachometer coils.

The electronics associated with the mechanical assembly is packaged on two circuit cards (visible in Figures 8-3, 8-4, and 8-5) and in the separate enclosure shown in Figure 8-6. The phototubes and image splitter are contained in a separate subassembly.

TABLE 8-1

ORIGINAL SPECIFICATIONS FOR TRANSFER LENS ASSEMBLY

Nominal Range of Translational Motion	±0.07 in., two axis
Type of Motor	Free-coil magnetic drive
Allowed Motion in Lens Axis Direction	0.005 in. maximum
Nominal Height of Optical Axis	3 in. above table (desired); any (acceptable)
Type of Support	Counterweighted (design compatible with zero-gravity hard vacuum environment, but counterweighted for use with non-zero gravity)
3db Bandwidth	≈ 50 cps
Weight of Lens (Glass Elements)	20 gm
Light Level	$>10^{10}$ P/S
Wavelength	5148 or 4880Å
Photosensors	Four EMI 9514S photomultiplier tubes
Image Splitter Location	f/70 image plane
Ratio of Image Motion to Transfer Lens Motion	4.7/1

Figure 8-6.   Electronics Control Box, Front Panel

8.2   PRINCIPLES OF OPERATION (See Figure 8-7)

An image of a modulated point source is relayed by the transfer lens to the image splitting prism where it is divided into four parts and sent to a brace of four phototubes. Since each tube receives any light falling on its associated prism face or quadrant, the phototube output signals (e_1, e_2, e_3, e_4) are preamplified and summed to obtain a signal (Σe) which at all times indicates total received light level. Sums and differences between the preamplifier output signals, moreover, are taken to obtain AC signals $(\Delta E_x$ and $\Delta E_y)$ indicating transfer lens position errors. Conversion of these signals to DC is performed via chopper demodulators which use the amplified sum Σe as a reference. The drive motor amplifiers, receiving these signals, excite their associated motors which produce lens motions that tend to reduce the error signals to zero; i.e., to return the optical image to the apex of the splitting prism.

AC exited capacitance bridges are used to detect the position of the lens. Each bridge is arranged as shown in Figure 8-8 to sense translational motion along one axis while being insensitive to motions in the other two directions. This is accomplished through use of both high input impedance preamplifiers (for Z axis insensitivity) and proper choice of geometry. Subsequent to demodulation and filtering, the position signals are differentiated to obtain lens velocity feedback signals which are used to servo stabilize the two axis control loops.
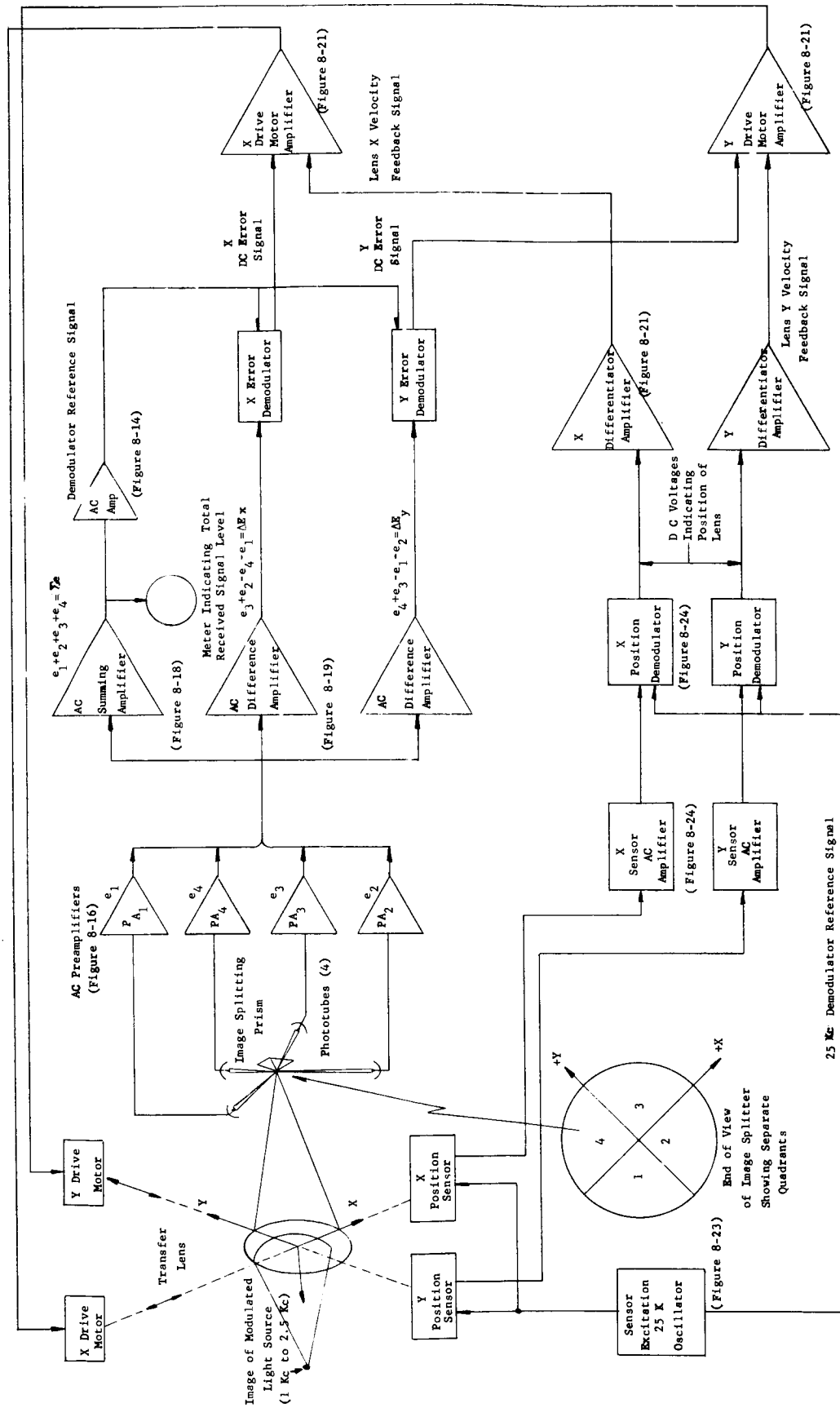
8-9

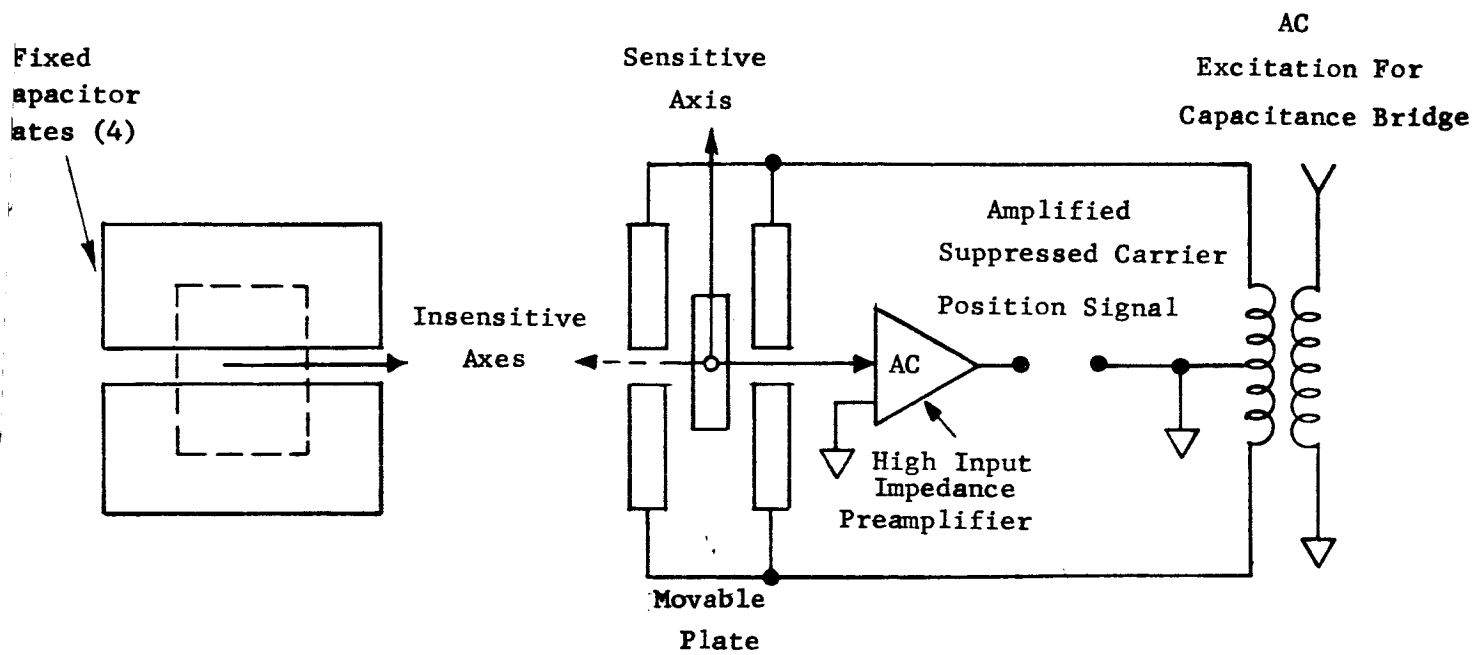Figure 8-7. Transfer Lens Servo Subsystem

Figure 8-8. Capacitance Operated Position Sensor Arrangement

Figure 8-9, a servo block diagram, indicates the system scale factors (to be discussed later) and a few of the electronic features of the subsystem. A shorting type phone jack allows monitoring of total phototube output current and is convenient for checking tube dark current and detecting excessive background light levels. While the phototube gains are nominally equalized within a factor of two by separately trimming bleeder string values, the preamplifiers are adjusted by screwdriver over a five to one range for vernier capability. Separate jacks for monitoring the preamplifier output signals are located on the front panel. A front panel meter (see Figure 8-6) facilitates rapid setting of light level and high voltage, to obtain proper electronics scale factors which prevail only with a 300 μa reading <u>provided the optical imagery is correct.</u>[1]

Lag-lead compensation networks to accentuate low frequency servo loop gain are incorporated following the differencing amplifiers and demodulators. The static gain of the system is increased even more by an integrating type servo amplifier, which also increases the low frequency gain of the velocity (minor) loop. The system was nominally designed to have a unity (position or major) loop gain at approximately 20 cps which corresponds to a 3 db closed loop response of nearly 40 cps.

8.3 SERVO ANALYSIS

The nominal scale factors of Figure 8-9 were obtained from the following analyses:

---

[1] Image must be diffraction limited and focused at the apex of the prism, and must correspond in size to f/70 .
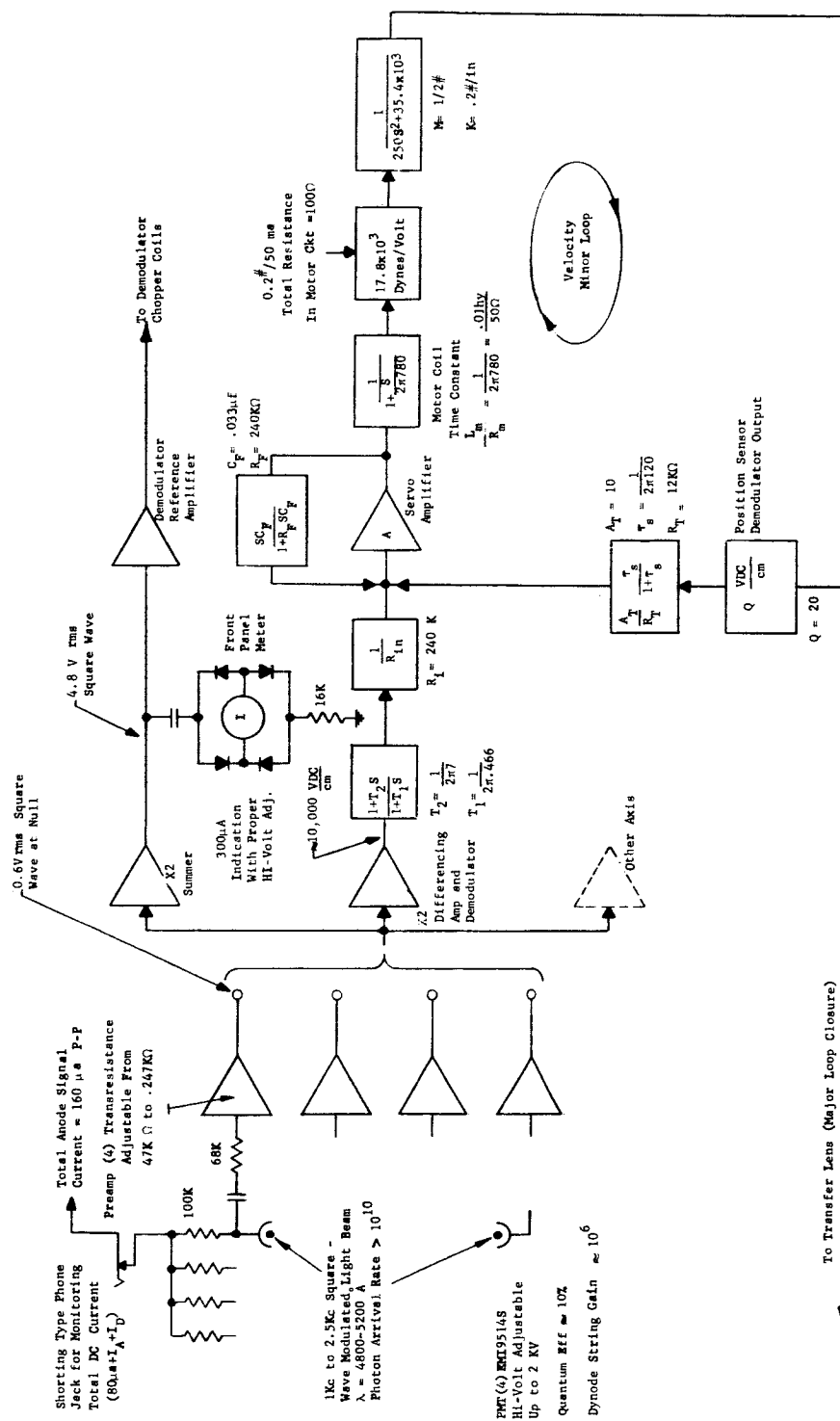
Figure 8-9. Servo Block Diagram

8.3.1 Velocity (Minor) Loop Analysis

Open loop gain $\triangleq$ O.L.G. $= A_T \dfrac{(1+R_F \, SC_F) \, \tau_s}{SC_F \, R_T \, (1+\tau_s)} \cdot \dfrac{17.8 \times 10^3 \, Q}{250S^2 + 35.4 \times 10^3}$

Assume C_F is tentatively infinite to obtain

O.L.G. $= A_T \dfrac{R_F}{R_T} \dfrac{\tau_s}{1+\tau_s} \dfrac{17.8 \times 10^3 \, Q}{250S^2 + 35.4 \times 10^3}$

Assume now that minor loop unity gain will occur at 60 cps and that τ can therefore be $1/(2\pi 120)$ which leads to

$$A_T \frac{R_F}{R_T} = \frac{250\left(S^2 = \overline{2\pi 60}^{\,2}\right)}{17.8 \times Q \times 10^3} \times 2 = 200$$

Hence, if $Q = 20$ and $A_T = 10$, then $\dfrac{R_F}{R_T}$ must be 20; or, if $R_F = 240$ K, then $R_T = 12$ K. Figure 8-10 indicates that a C_F value of 0.033 uf, corresponding to a low frequency break of 12db/oct at 20 cps, can be incorporated to obtain increased minor loop gain at lower frequencies.

8.3.2 Position (Major) Loop Analysis

With the foregoing minor loop parameter values, the closed mirror loop gain, for cases where O.L.G. $\gg 1$, is given by

$$C.L.G. = \frac{R_T \, (1+\tau_s)}{Q \, R_{in} \, A_T \, \tau_s}$$

For cases where $\tau_s \ll 1$, this equation reduces to

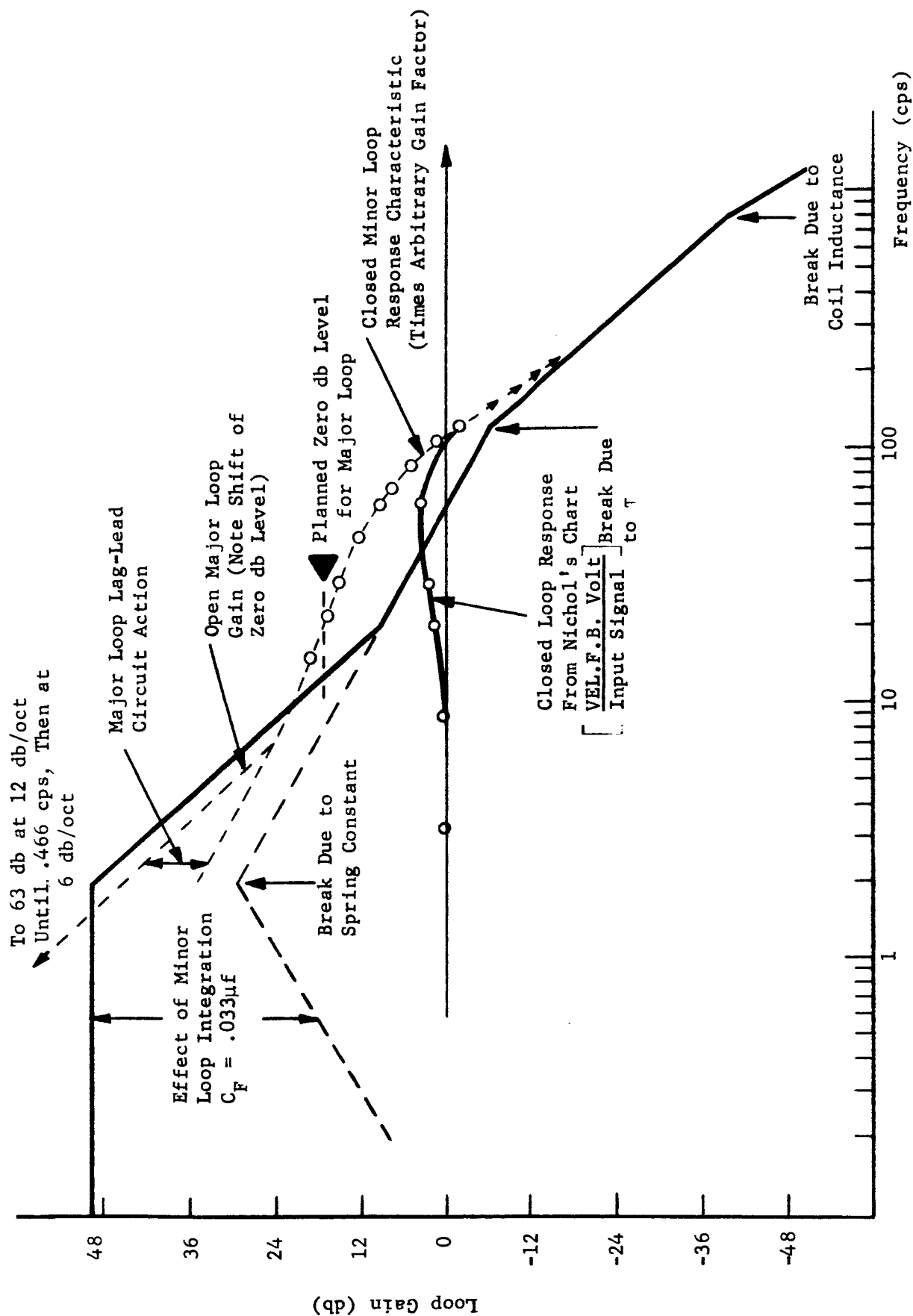$$C.L.G. = \frac{R_T}{Q \, R_{in} \, A_T \, \tau_s}$$

Figure 8-10.. Servo Response

To obtain unity major loop gain crossover at 20 cps, a gain of K is required
of the sensor where

$$K = \frac{Q \, R_{in} \, A_T \, \tau_s}{R_T} \bigg|_{s=2\pi20} = 667 \text{ V/cm}$$

Since the DC error signal scale factor is 10^4 V/cm, a loss of $10^4/667$ or 15
can be tolerated. This can be implemented with a lag-lead circuit to produce
the loss only at higher frequencies (near and above 20 cps) for stability without
sacrifice of lower frequency gain. One choice would be a circuit which produced
a 6db falloff between 0.466 and 7 cps.

8.3.3 Expected Frequency Response

The transfer lens servo will act to reduce the low frequency motions
of the optical image with respect to the apex of the image divider. The ratio of
the motion with the transfer lens operative (M_o) to that with the lens inoperative
(M_i) is called the error response which is determinable from the expression:

$$\text{Error Response} = \frac{M_o}{M_i} = \frac{1}{1+GH} = \frac{1}{1+G}$$

where

> GH is the open loop gain of the major loop and
>
> H is the feedback factor which is unity for the major loop.

It should be clear that, at low frequencies where the loop gain greatly
exceeds unity, the error response is closely equal to 1/G. At high frequency, on
the other hand, where the loop gain is much less than one, the error response is
closely equal to unity. The nominal error response expected of the transfer lens
servo system is shown in Figure 8-11 along with the major open loop gain function
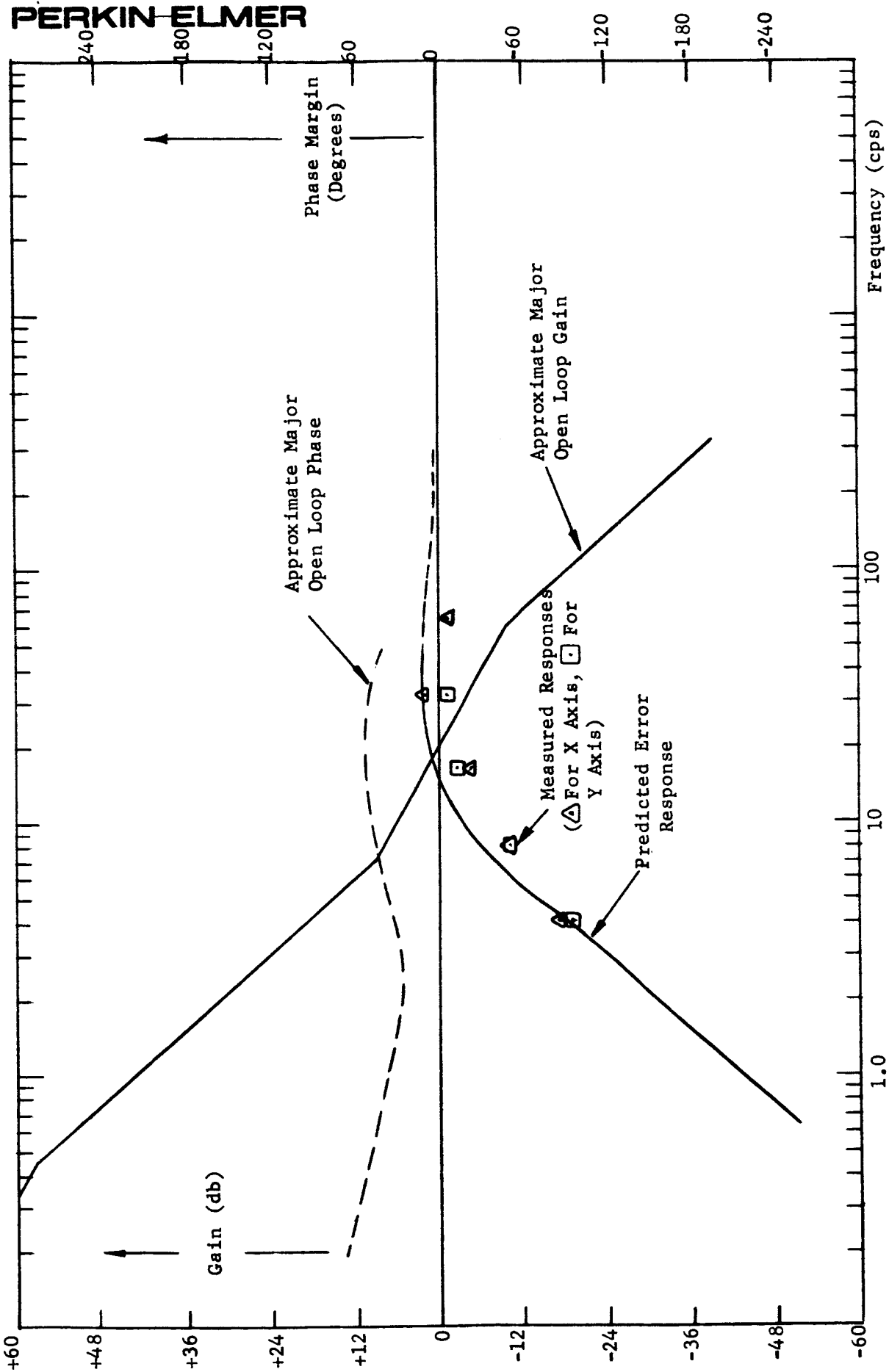
PERKIN ELMER

Figure 8-11.   Nominal Response Characteristics of Major Loop

(G and GH) and its associated phase shift characteristic. The figure also includes measured results (for both the X and Y axis channels) taken to verify predicted performance.

Figure 8-12 shows the closed loop response,

$$\frac{\theta_o}{\theta_i} = \frac{G}{1+GH} = \frac{G}{1+G} \; ,$$

of the system as obtained from a Nichol's chart plot of the open loop gain and phase characteristics.

Figures 8-13 and 8-14 are derived in fashion identical to Figures 8-11 and 8-12, respectively, but utilize a Nichol's chart derived minor loop transfer function instead of assuming the straight line characteristic (minus 6 to minus 12 db/oct). As such, the latter two figures take into account the steady state response over-shoots of the minor loop.

8.4   CIRCUIT DETAILS AND CALCULATIONS

8.4.1   Optical Scale Factor

The photosensor scale factor, when operating in the linear range, corresponds to full change of error signal (from its positive to negative maximum) for an image motion of 1.22 $\frac{\lambda}{D}$ (f/#) or approximately 43×10^{-4} cm. Since the ratio of image to transfer lens motion is 4.7:1, then full signal change occurs for 9.2×10^{-4} cm of lens motion.
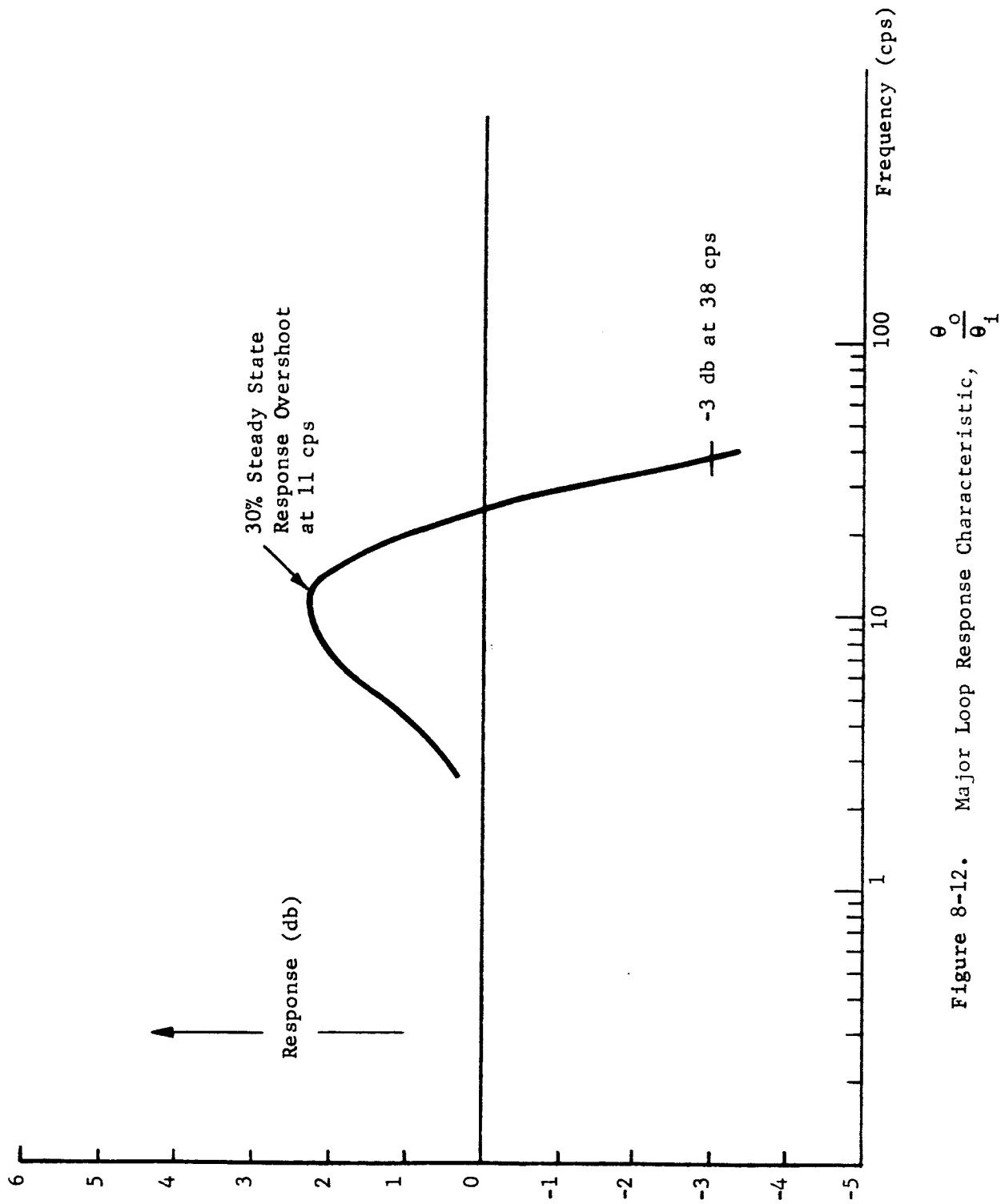
Figure 8-12.   Major Loop Response Characteristic, $\dfrac{\theta_o}{\theta_i}$
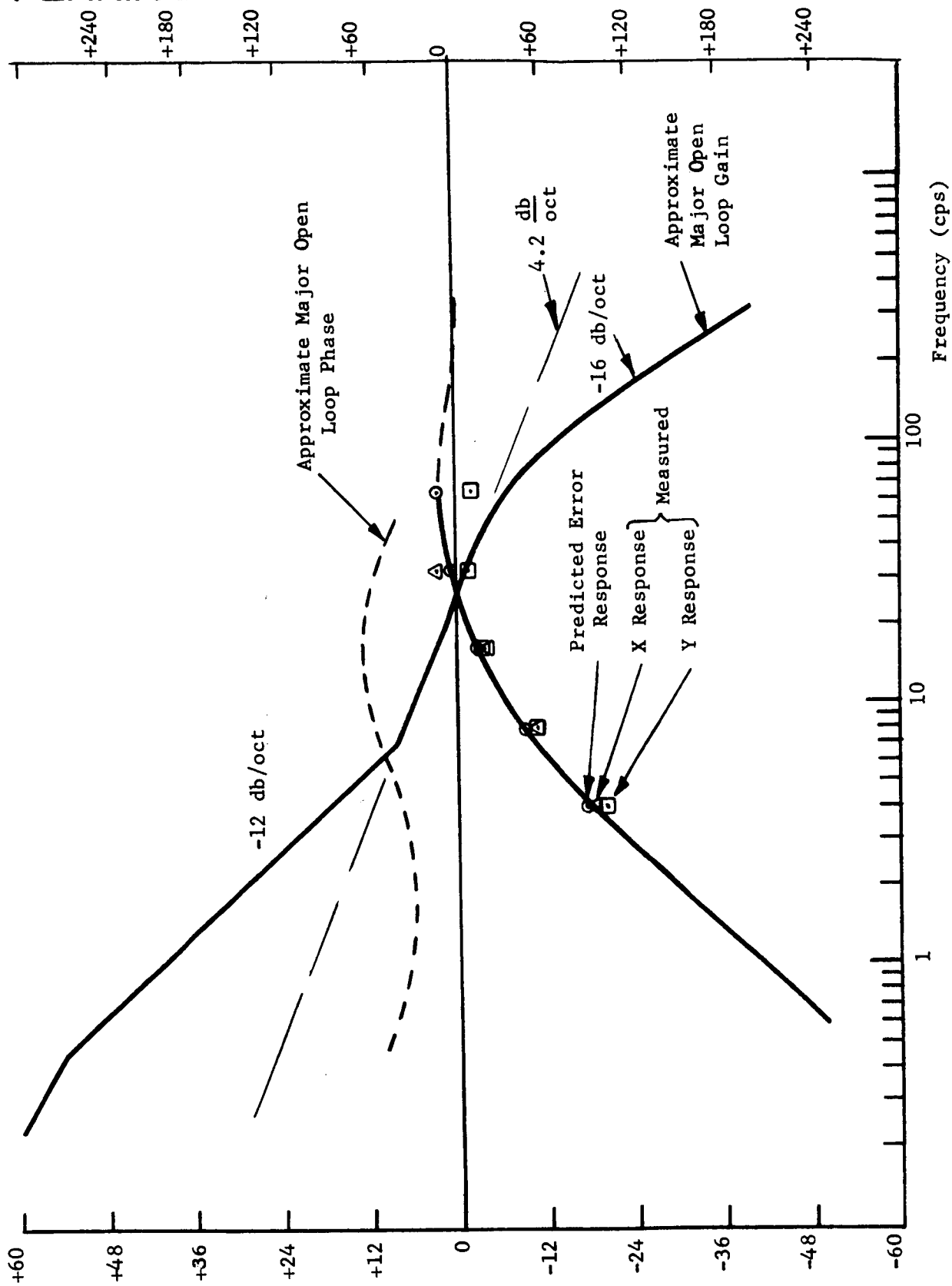
Figure 8-13.   Nominal Response Characteristics of Major Loop Utilizing Nichol's Chart
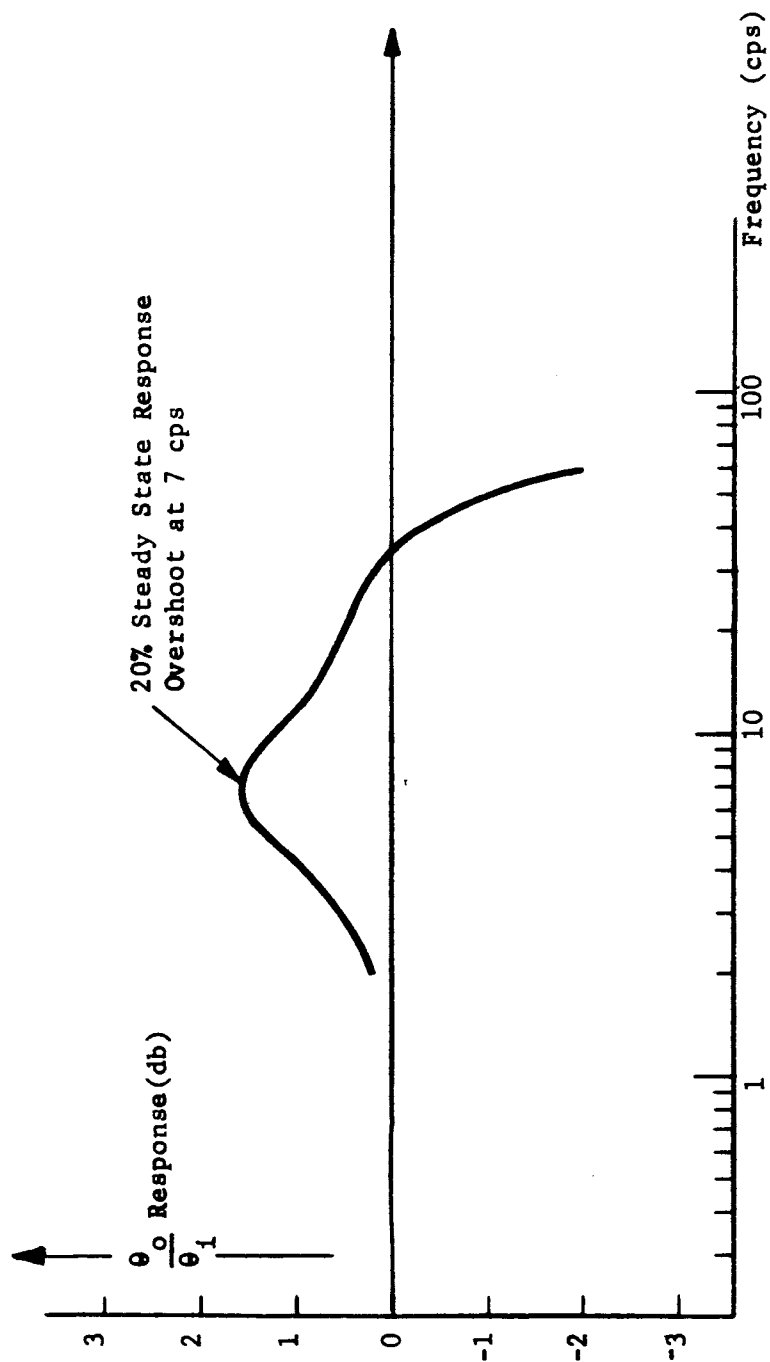   Derived Minor Loop Transfer Function

Figure 8-14. Major Loop Response Utilizing Nichol's Chart Derived Minor
Loop Transfer Function

8.4.2   Phototube Response

The photocathode current expected with 10^{10} photons/sec is 0.6×10^9 electrons/sec or about 100 pa. Since a dynode string gain of 10^6 is possible, a total output current variation due to chopped signal light could be 0.1 ma p-p (or about 25 ua/tube) while DC dark current may be in the order of 0.02 ua. The signal-to-noise ratio corresponding to a 100 cps equivalent noise bandwidth (neglecting background light) will be over 2000 which indicates that noise in signal should not be troublesome.

8.4.3   Preamplifier (see Figures 8-15 and 8-16)

The 25 ua p-p phototube signals are reduced to 15 ua, by the current division action of the 100K and 68K ohm resistors, and fed to the SQB-1 summing junction. Since the transresistances of the SQB-1 operation amplifer circuits are variable from 47K to 247K ohms, the output rms signal levels will be in the order of 0.35 to 1.75V rms, a range which encompasses the desired 0.6V rms level indicated in Figure 8-9. The circuit design features a .0.1 uf input DC blocking capacitor to avoid preamplifier saturation on background light induced anode currents. The two 1N914 diodes connected to this capacitor are included to avoid excessive SQB-1 input current transients generated by high voltage transients. The other two diodes plus two transistors and the 33K and 68K ohm resistors operate to avoid excessive output signals. The clipping level for the arrangement shown is given by the expression

$$V_c = \frac{33K}{68K} \ (V_D + V_{BE} + V_S) + (V_D + V_{BE}) \approx 7.3V$$
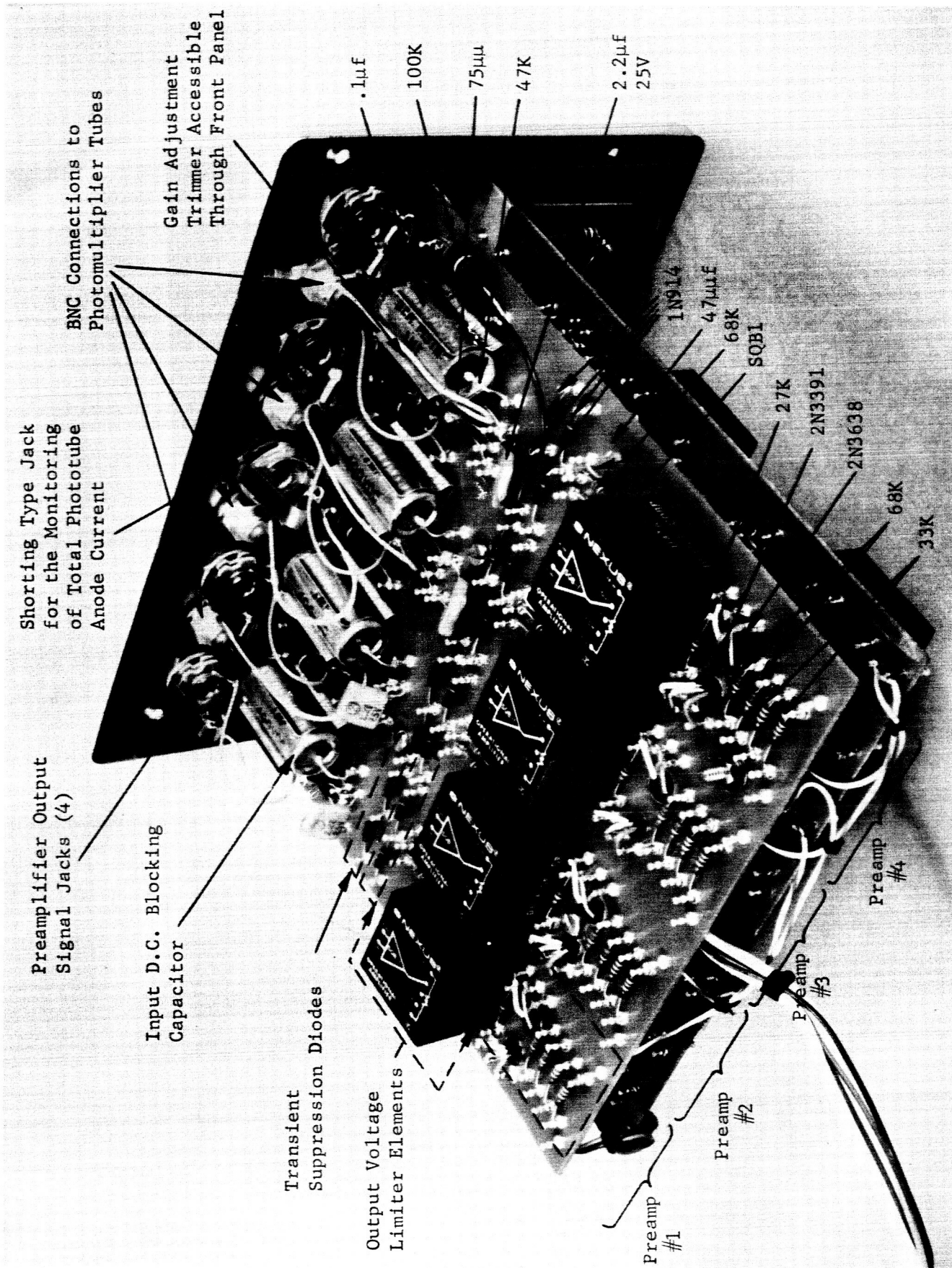
Figure 8-15. Electronics Package with Cover Removed, Bottom View

Labels:
- Gain Adjustment Trimmer Accessible Through Front Panel
- BNC Connections to Photomultiplier Tubes
- Shorting Type Jack for the Monitoring of Total Phototube Anode Current
- Preamplifier Output Signal Jacks (4)
- Input D.C. Blocking Capacitor
- Transient Suppression Diodes
- Output Voltage Limiter Elements
- .1μf
- 100K
- 75μμ
- 47K
- 2.2μF 25V
- 1N914
- 4.7μμF
- 68K
- SOB1
- 27K
- 2N3391
- 2N3638
- 68K
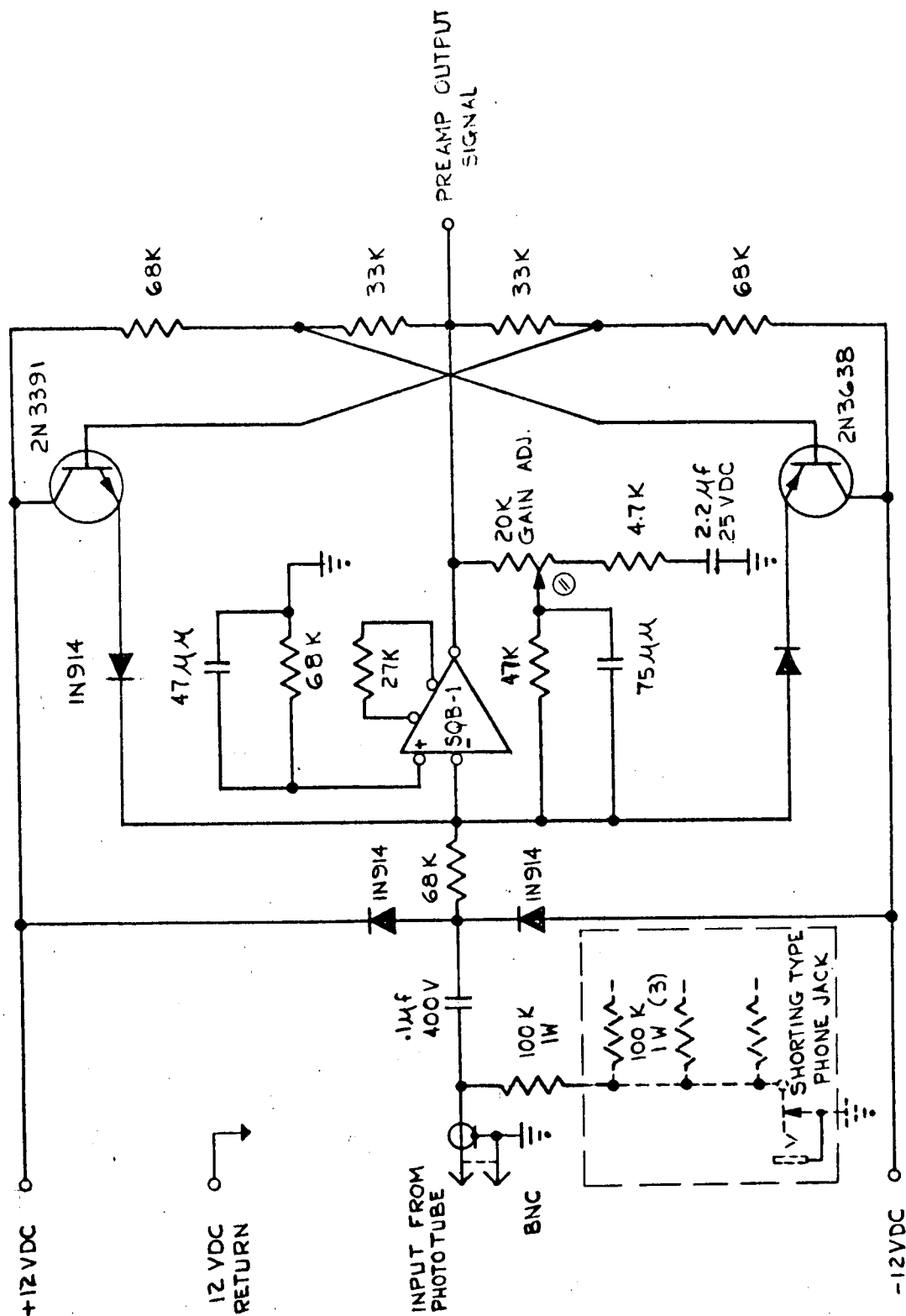- 33K
- Preamp #1
- Preamp #2
- Preamp #3
- Preamp #4

Figure 8-16. Photomultiplier Tube Preamplifier, Schematic Diagram

where

V_D is diode drop ($\approx$ 0.5V)

V_{BE} is the base emitter drop of a conducting transistor ($\approx$ 0.5V)

and

V_S is the supply voltage (±12V)

8.4.4   Meter and Demodulator Reference Amplifiers (see Figures 8-17 and 8-18)

The four preamplifier signal levels are both summed and amplified by the meter amplifier to provide a nominal output signal level of 4.8V rms. The AC component of the meter amplifier is diode routed through the front panel meter to the parallel combination of the 20K and 82K ohm resistors, thus causing a 300 ua indication free of amplifier DC drift effects. The DC feedback path, provided through the 39K ohm resistors and the 0.1 uf capacitor, together with the AC path are nearly equivalent to an 80K ohm feedback resistor. The meter amplifier output is AC coupled to the following amplifier circuit which provides high gain, clipping action, and power output sufficient to drive two Airpax 6025 chopper reference windings. It is noteworthy that slow frequency variations of the light modulating mechanism over the design range of 1.0 to 2.5 Kc are perfectly acceptable.

8.4.5   Demodulator Amplifier (see Figures 8-17 and 8-19)

This amplifier takes the difference between sums of signal pairs, provides a gain of two, incorporates an output buffer amplifier (2N3391 and 2N3638 cathode follower arrangement), as well as a clipper, and drives a conventional demodulator-filter combination at the output. The 20K ohm trimpot
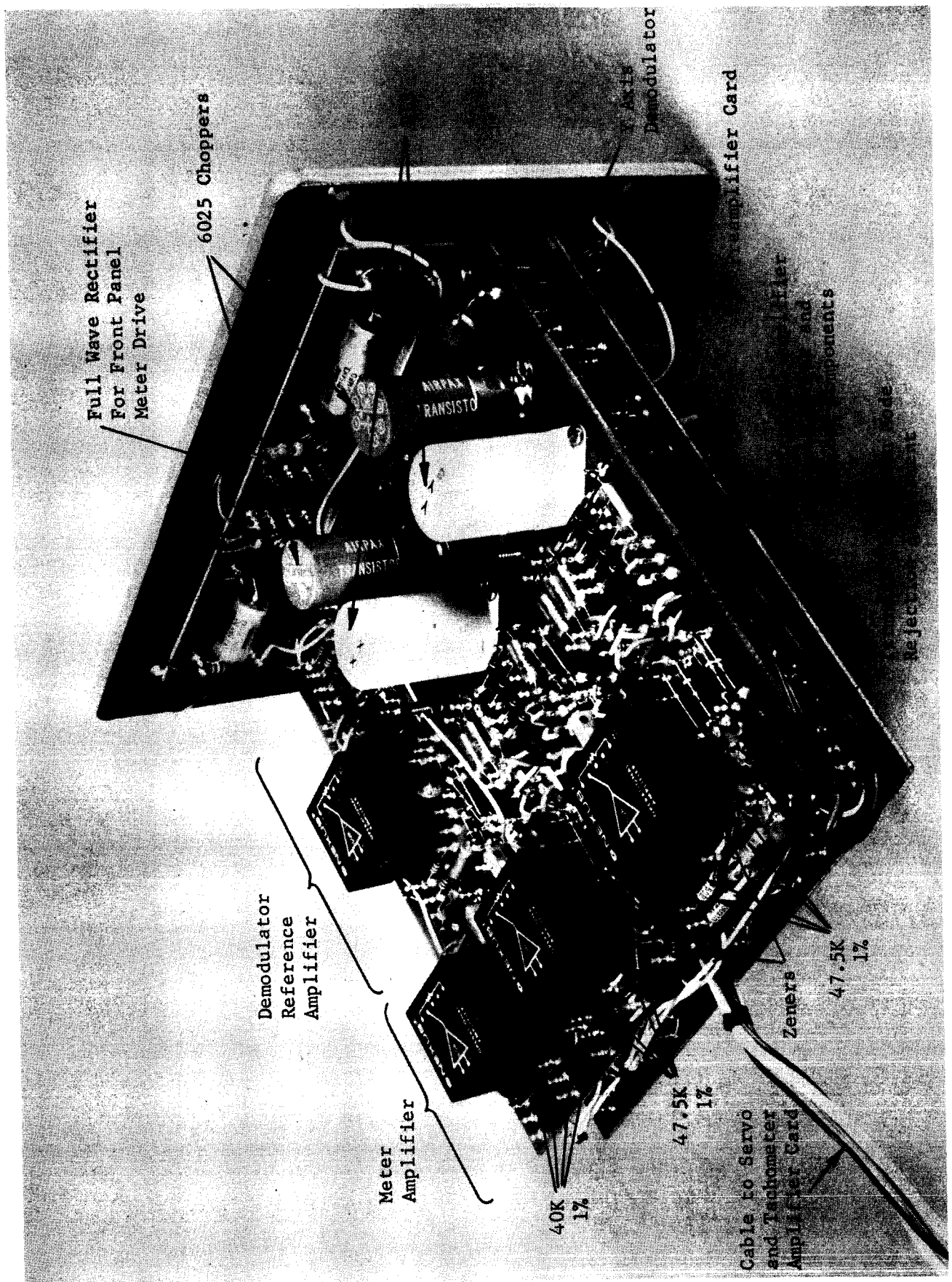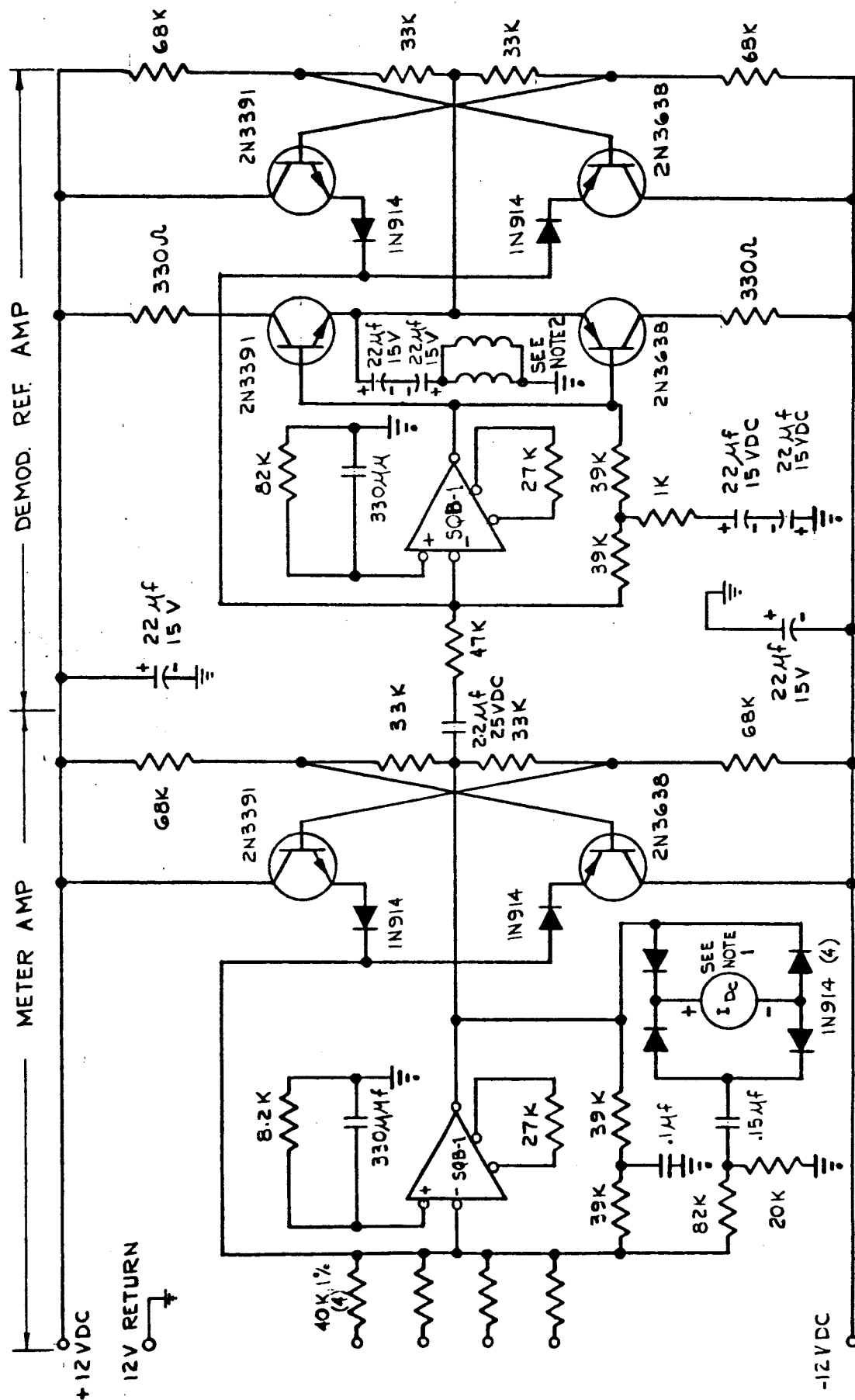
Figure 8-17. Electronics Package With Cover Removed, Top View

NOTE 1: PARKER TYPE S25 0-500μa DC FRONT PANEL METER
NOTE 2: AIRPAX G025 CHOPPER EXCITATION COILS
(SEE CHOPPER FIG.19)

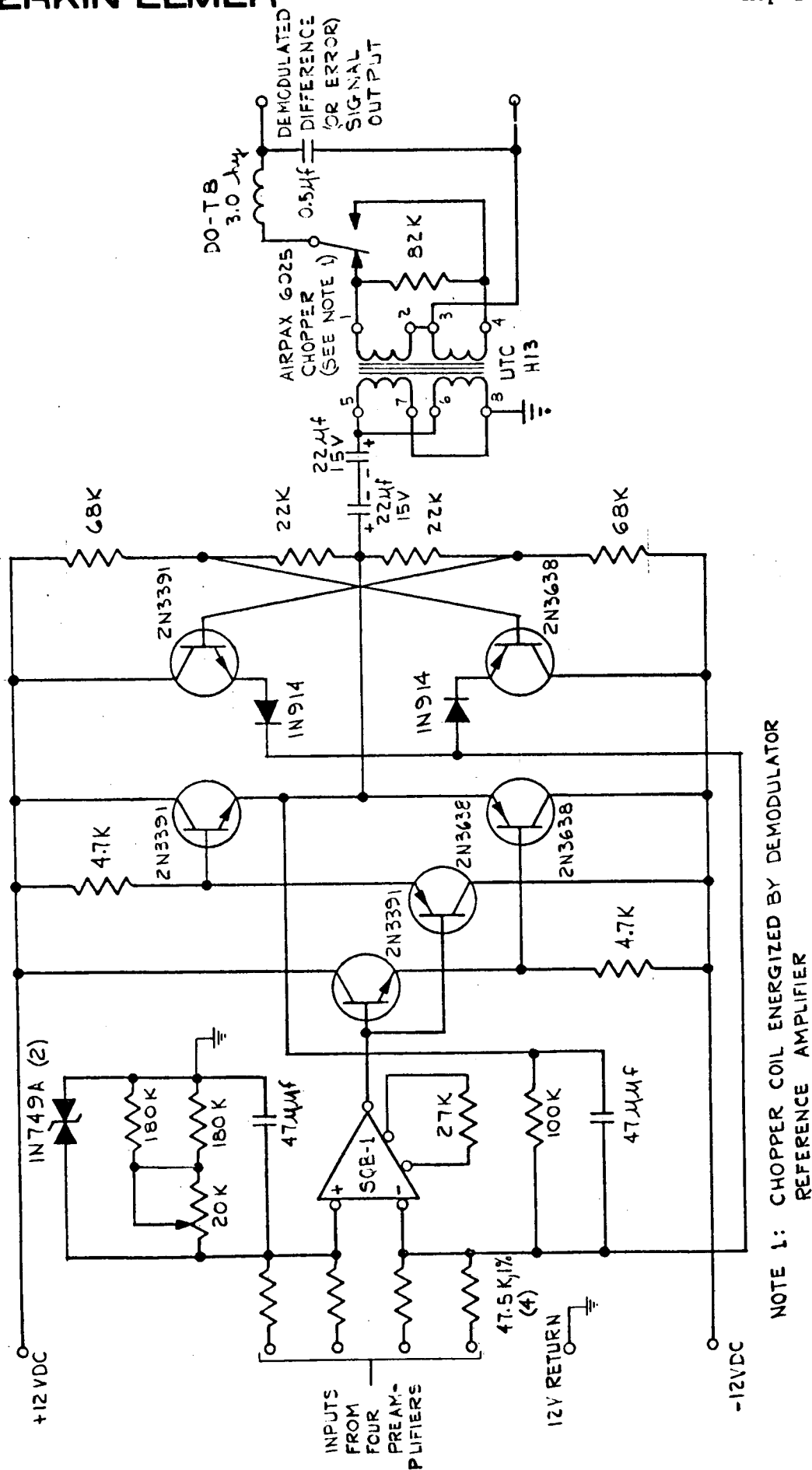Figure 8-18. Meter and Demodulator Reference Amplifiers, Schematic Diagram

Figure 8-19.   Demodulator Amplifier

NOTE 1: CHOPPER COIL ENERGIZED BY DEMODULATOR
         REFERENCE AMPLIFIER

is an adjustment for common mode rejection and is accessible only after the
outer metal case is removed from the electronics container. While the amplifier
was designed with an output limiter circuit, similar to that of the preamplifier
but with a 5.2V clipping level, it was later discovered that the clipping level
varies depending upon the inputs applied to the "plus" terminal of the SQB-1.
The zener diode was included as a quick fix to avoid SQB-1 internal saturation
under large signal conditions, a circumstance which fortunately should never
occur under nominal operating conditions.

The demodulator filter is a 3.0 hy - 0.5 uf combination loaded with
a shunt resistance of about 23.5K ohms. This combination ($F_r \approx 125$ cps, $\zeta = .05$)
introduces only very small phase lag near the 20 cps major loop gain crossover
frequency and has, therefore, been neglected in the previous analysis. Since
the demodulator input AC error signals are nearly squarewave in shape, filtering
requirements are at a minimum. The 82K ohm resistor on the H-13 secondary avoids
transformer output signal transients associated with stray capacitance.

8.4.6   **Tachometer and Servo Amplifiers** (see Figures 8-20 and 8-21)

The tachometer amplifier furnishes an output signal which is the
derivative of its input signal and uncorrupted by erroneous outputs due to DC
amplifier offset voltages. The transfer function is of the form

$$\frac{10TS}{1+TS}$$

and the value of T is $(2\pi 120)^{-1}$.

Figure 8-20.   Servo and Tachometer Amplifier Card

Servo Operational
Amplifier Output
Buffer Emitter
Follower Circuit

12K

6.8K

240K(2-470K
Paralleled)

39Ω

2.4K(2-4.7K
Paralleled)

10Ω

Servo Amplifier

1N456(2)

1.1μf { 0.1μf
1.0μf

1.5K
1.2K
12K
12K

24K (2-47K Paralleled)

Note:
2μf and 15μf
Capacitors Shown
on Schematic are
not on This Card
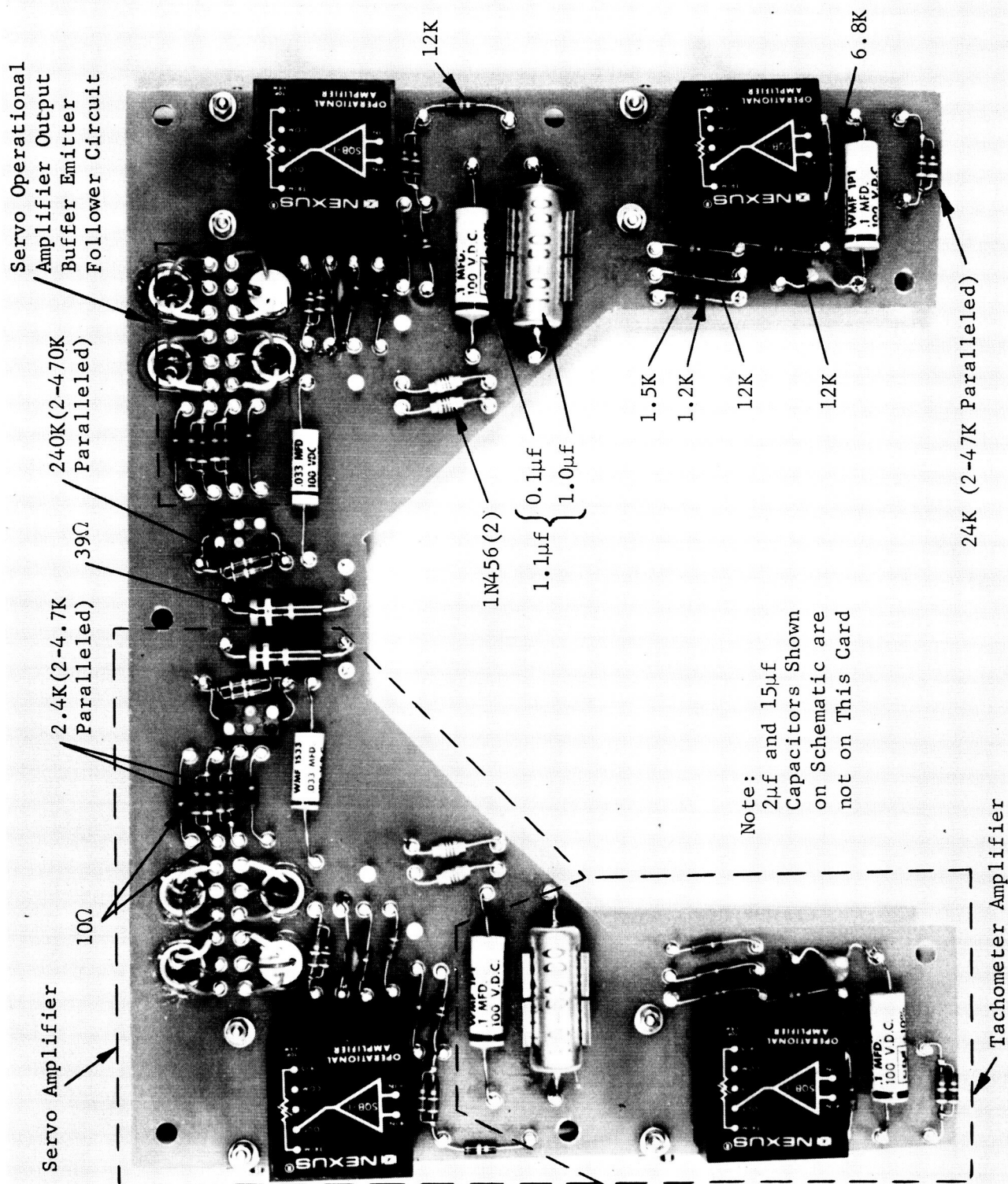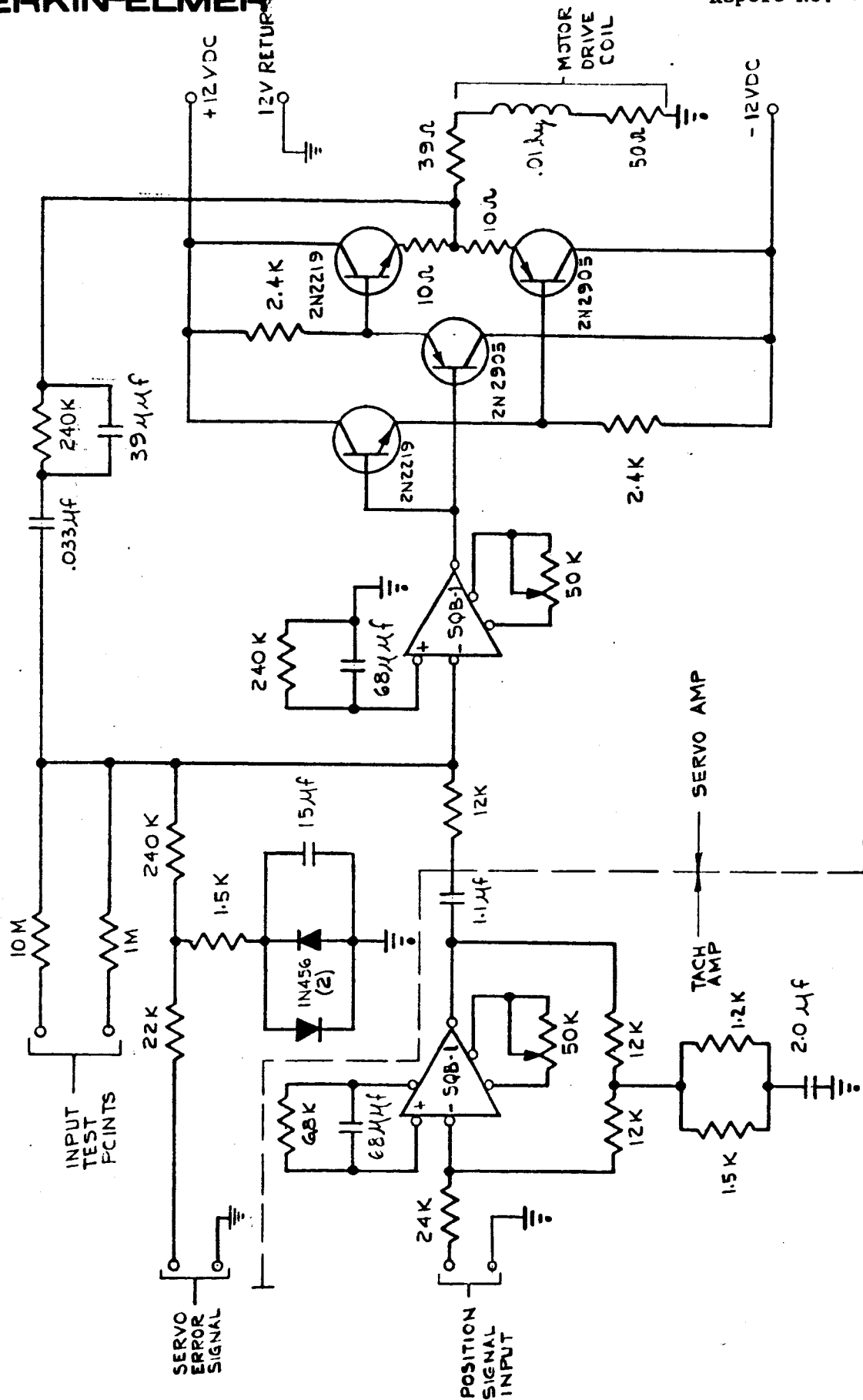
Tachometer Amplifier

Figure 8-21. Servo and Tachometer Amplifiers, Schematic Diagram

The servo amplifier is straight forward in design as is the servo error signal compensation network (22K ohms, 240K ohms, 1.5K ohms, 15 μf). The IN456 diodes, however, have been incorporated across the capacitor to limit energy storage action which might otherwise give rise to intolerable image acquisition transients. The 50K ohm trimmers were included for obtaining minimum operation amplifier DC unbalance which is important only for the servo amplifier. The adjustment, made after shorting from the 22K, 240K, 1.5K ohm junction to ground and removing the tachometer amplifier SQB-1, is simply to obtain the least amplifier output voltage integration rate with the tachometer amplifier summing junction grounded.

Input test points have been provided for use during servo response measurements.

8.4.7   25 Kc Oscillator (see Figures 8-22 and 8-23)

The design consists of a conventional astable multivibrator re-sistively coupled to two 2N2905 transistors whose collectors drive an output transformer in push-pull fashion.

The half-period of oscillation is given by the expression

$$t = .693 \ RC = .693 \ (56K) \ (500 \ \mu\mu f)$$

and the nominal frequency is therefore

$$F = \frac{1}{2t} = \frac{.722}{RC} = 25.75 \ Kc$$

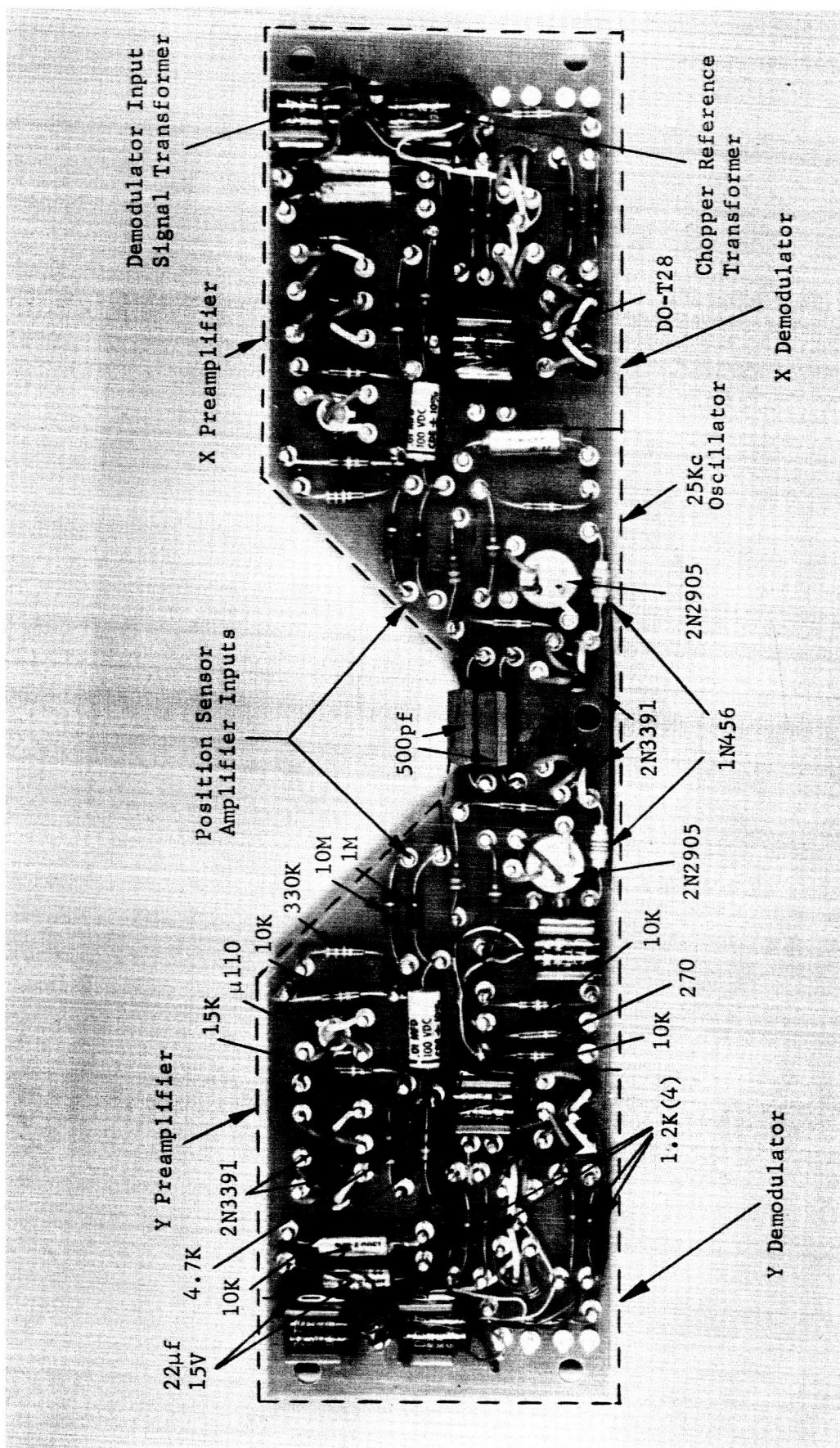It should be noted that the amplitude of the AC ouput signal depends upon the ±12 VDC power supply settings.

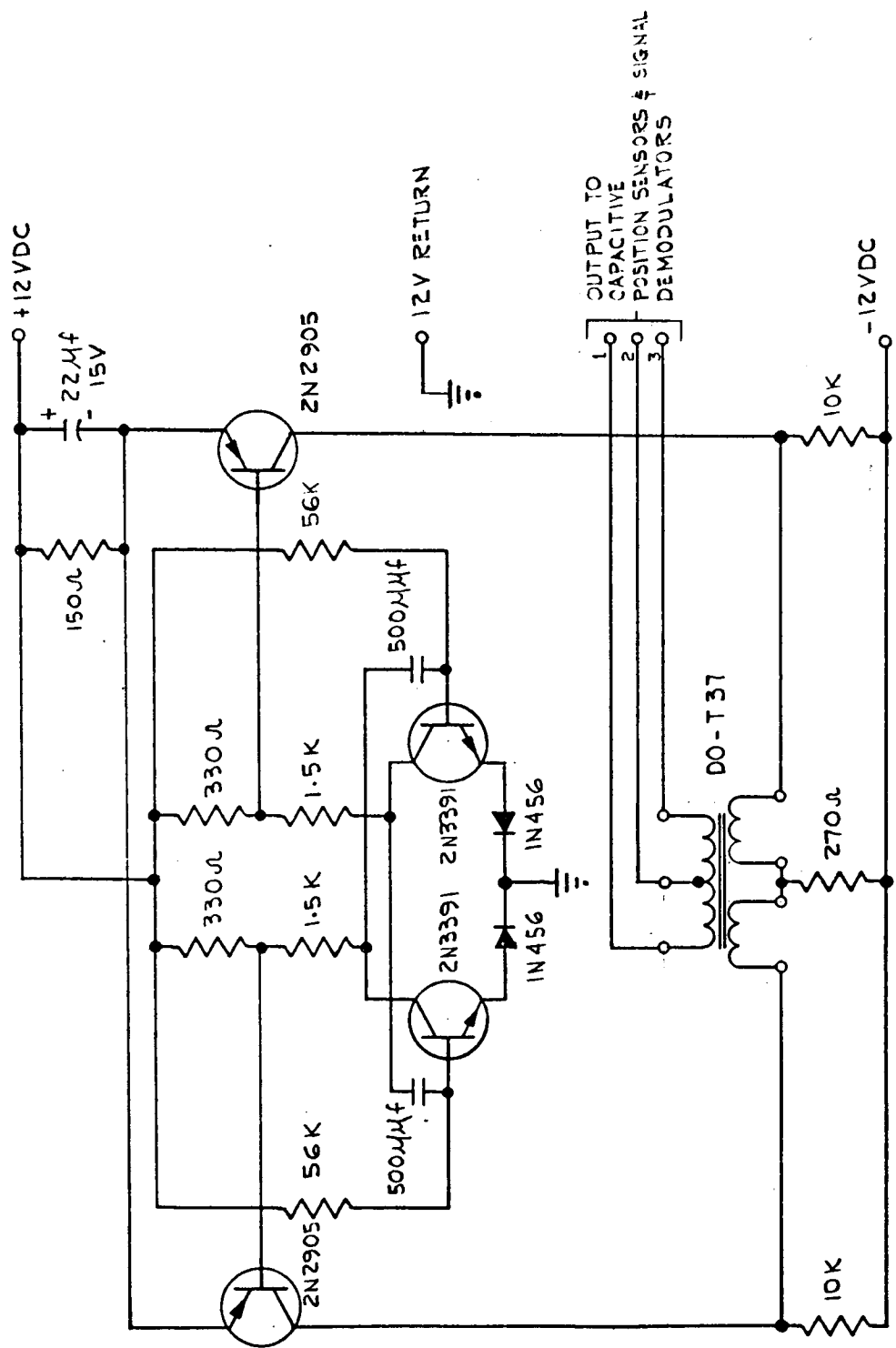Figure 8-22. 25Kc Oscillator, Position Sensor Amplifier, And Demodulator Circuit Card

Figure 8-23.   25 KC Oscillator, Schematic Diagram

8.4.8 <u>Position Sensor Amplifier and Demodulator</u> (see Figures 8-22 and 8-24)

8.4.9 <u>Mechanical Configuration</u>

Each servo drive motor basically consists of two 7,000 Gauss magnetic fields in which a 328 turn (nominal) No. 36 wire coil is free to move in translation as a result of coil current. The coil resistance is approximately 50 ohms and the inductance is near 10 mhy, both when in and out of the gap. The ±0.15 inch motor motional range was selected in excess of the required ±0.065 inch in order to provide for a soft stop range, and thereby avoiding the excessive flexure bearing load possible when hitting hard stops.

The stop permits a measured ±0.073 inch range of unrestricted motion and an additional radial motion of nearly 0.077 inch with soft stop action. Two collars are fitted over the soft stop housings and can be gently engaged with mating pieces on the movable lens coil to accomplish centering.

The weight of the moving mass excluding counterweight is estimated as 120 gms (4.2 oz). The bearings (Bendix type 6004-600 and 5004-800) are very fragile and can be damaged by misapplying small loads either axially or radially (viz: force levels under one pound). The breadboard unit should therefore be handled very carefully and only when absolutely necessary. Launch vibration and shock can be applied only when the assembly is caged. For the project breadboard, there is no caging mechanism at present so that care must be exerted in shipping and handling. Future work should be devoted to a space qualifiable assembly.

8.5 OPERATING PRECAUTIONS FOR THE BREADBOARD APPARATUS

(a) Do not handle the mechanical unit except with the utmost of care. <u>The flexure bearings can be ruined by introducing even modest static and/or dynamic loads.</u>
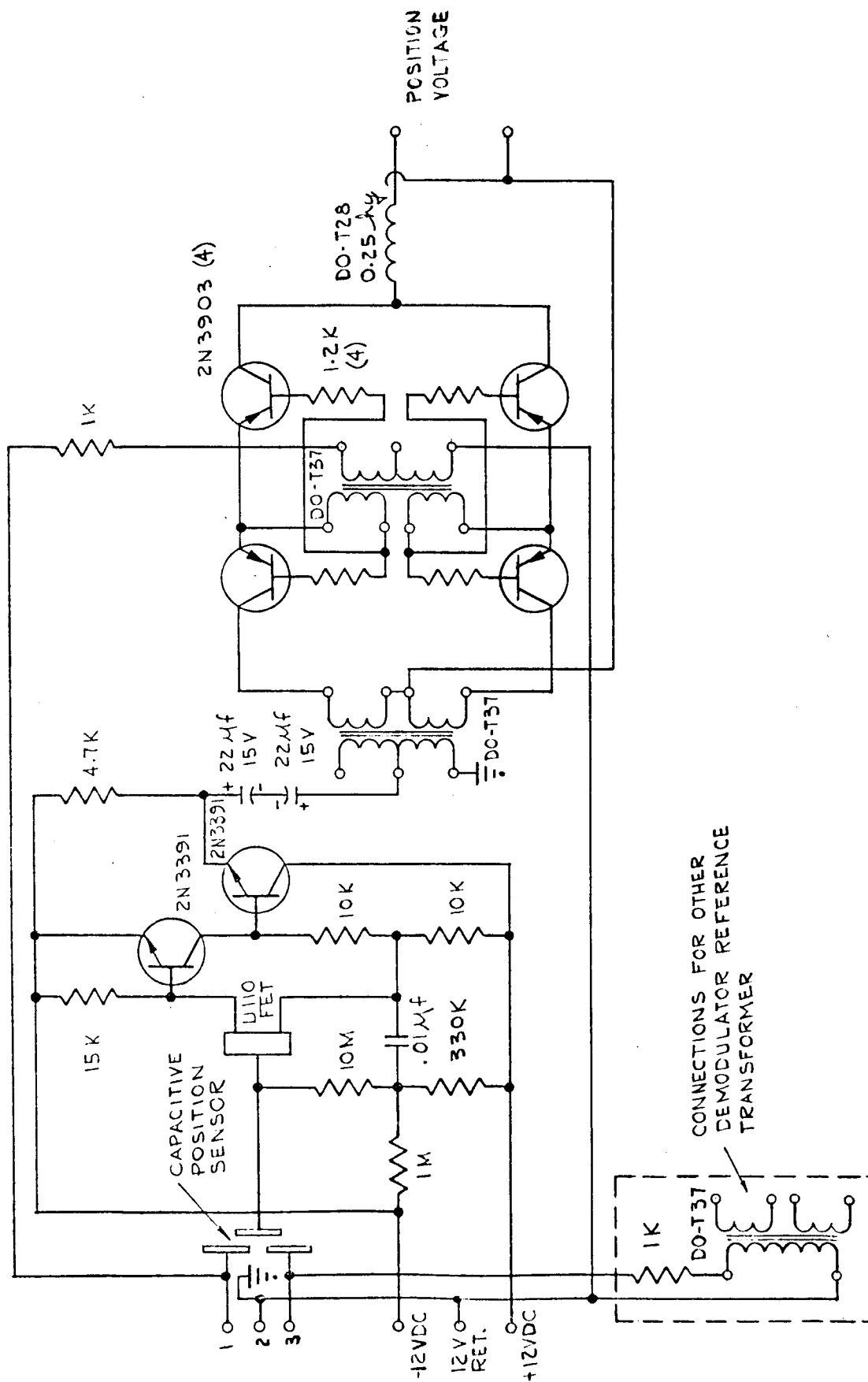
Figure 8-24. Position Sensor Amplifier and Demodulator, Schematic Diagram

(b)   The external magnetic fields of the drive motors
       are very high. Magnetic tools will be subjected
       to strong forces and may therefore cause unin-
       tentional damage upon impact. . Keep watches and
       other sensitive items well clear of the motors.
       Extreme care should also be exercised to avoid small
       magnetic particles which will be attracted into the
       magnetic gaps and will be extremely difficult to
       remove without mechanical disassembly.

(c)   The Nexus amplifiers are rated for maximum applied
       voltages of ± 15VDC. The values should never be
       exceeded even momentarily. Power supply settings
       (± 12VDC) should be checked prior to turning the
       equipment on. Power should always be controlled by
       means of the on-off switch on the mechanical assembly
       to avoid power supply turn-on and turn-off transients.

8.6   MEASURED RESULTS

The various measurements performed on the transfer lens servo
subsystem are described in the following subparagraphs.

8.6.1   Position Pickoff Scale Factors

With ±12 VDC applied to the electronics, the output from the 25 Kc
oscillator transformer secondary was measured as 19.25 VAC. Next the transfer
lens was placed in a hold mode controlled by adjustable potentiometers, and
moved to several positions within its motional range. The position (determined
by optical equipment), the command potentiometer setting, and the position
pickoff voltage were recorded at each position. The results obtained are
given in Table 8-2. Figures 8-25 and 8-26 show the results graphically to
better indicate linearity characteristics.

8.6.2   Motor "Force Current" Relationship

A 20 gm weight was placed onto the lens cell to produce a nominal
load change of 14.14 gms on each axis. The result obtained for the Y axis was
2.781 pounds per ampere as compared to an expected value of 2.93. The result
for the X axis, 3.15 pounds per ampere, is believed to be in error on the high
side since the current reversed direction and the assembly was later observed
to exhibit hysteresis. The result is nevertheless in reasonably good agree-
ment with the 2.93 expected value. It was noted that both motors produced
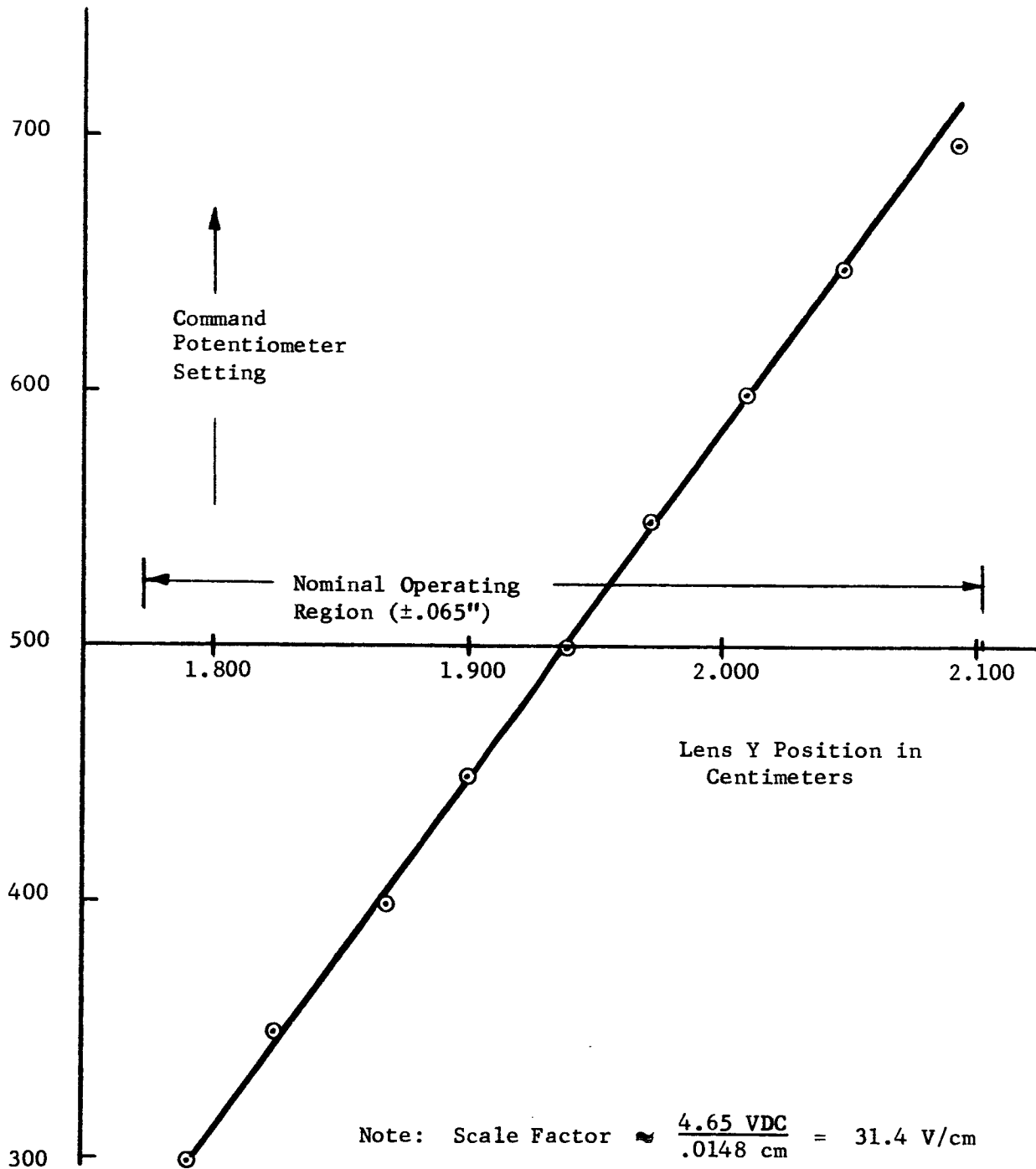forces in the positive directions when positive motor coil voltages were present.

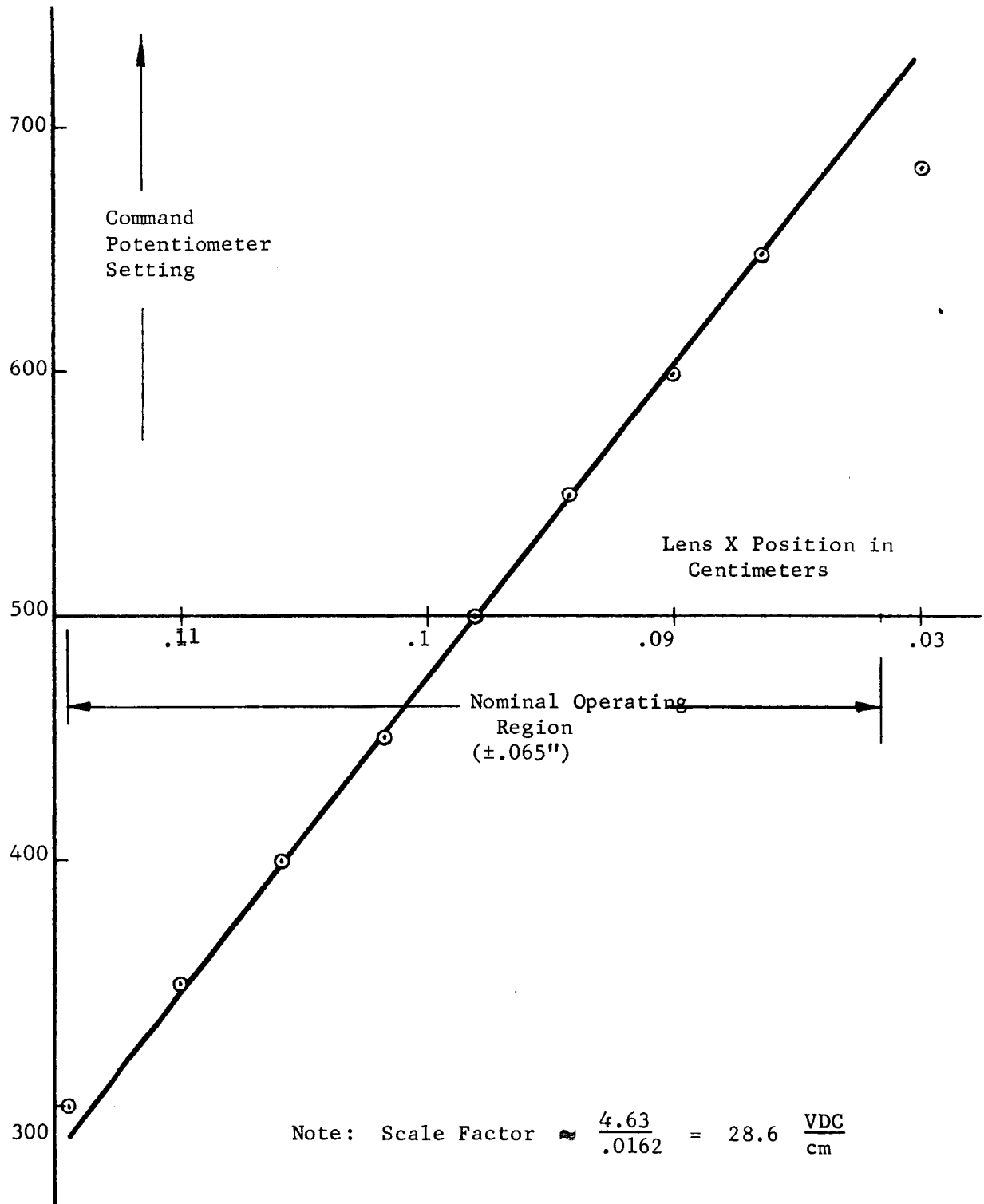**Figure 8-25..** Y Position Sensor Characteristic

Figure 8-26.. X Position Sensor Characteristic

8.6.3   Tachometer Amplifier Characteristics

The small signal transfer functions of both tachometer amplifiers were measured and found to be in remarkably good agreement with expected results (see Figure 8-27).

		TABLE 8-2			
		DATA ON POSITION PICKOFF			
X Position Pickoff Voltage (VDC)	Y Position Pickoff Voltage (VDC)	X Command Pot ----	Y Command Pot ----	X Pos (cm)	Y Pos (cm)
-4.33	0	685	0	0.080	0
-3.54	0	650	0	0.0865	0
-2.4	0	600	0	0.0901	0
-1.23	0	550	0	0.0943	0
0	0	500	0	0.0981	0
+1.17	0	450	0	0.1017	0
+2.34	0	400	0	0.1058	0
+3.46	0	350	0	0.1099	0
+4.63	0	300	0	0.1143	0
0	-4.87	0	710	0	----
0	-4.65	0	700	0	2.092
0	-----	0	650	0	2.048
0	-2.33	0	600	0	2.009
0	-----	0	550	0	1.972
0	0	0	500	0	1.939
0	-----	0	450	0	1.900
0	+2.35	0	400	0	1.868
0	-----	0	350	0	1.825
0	+4.65	0	300	0	1.791

NOTES: 1) The position pickoff voltages were measured at the demodulator outputs.

2) As the transfer lens was moved in the positive directions, the pickoff voltages became more positive.
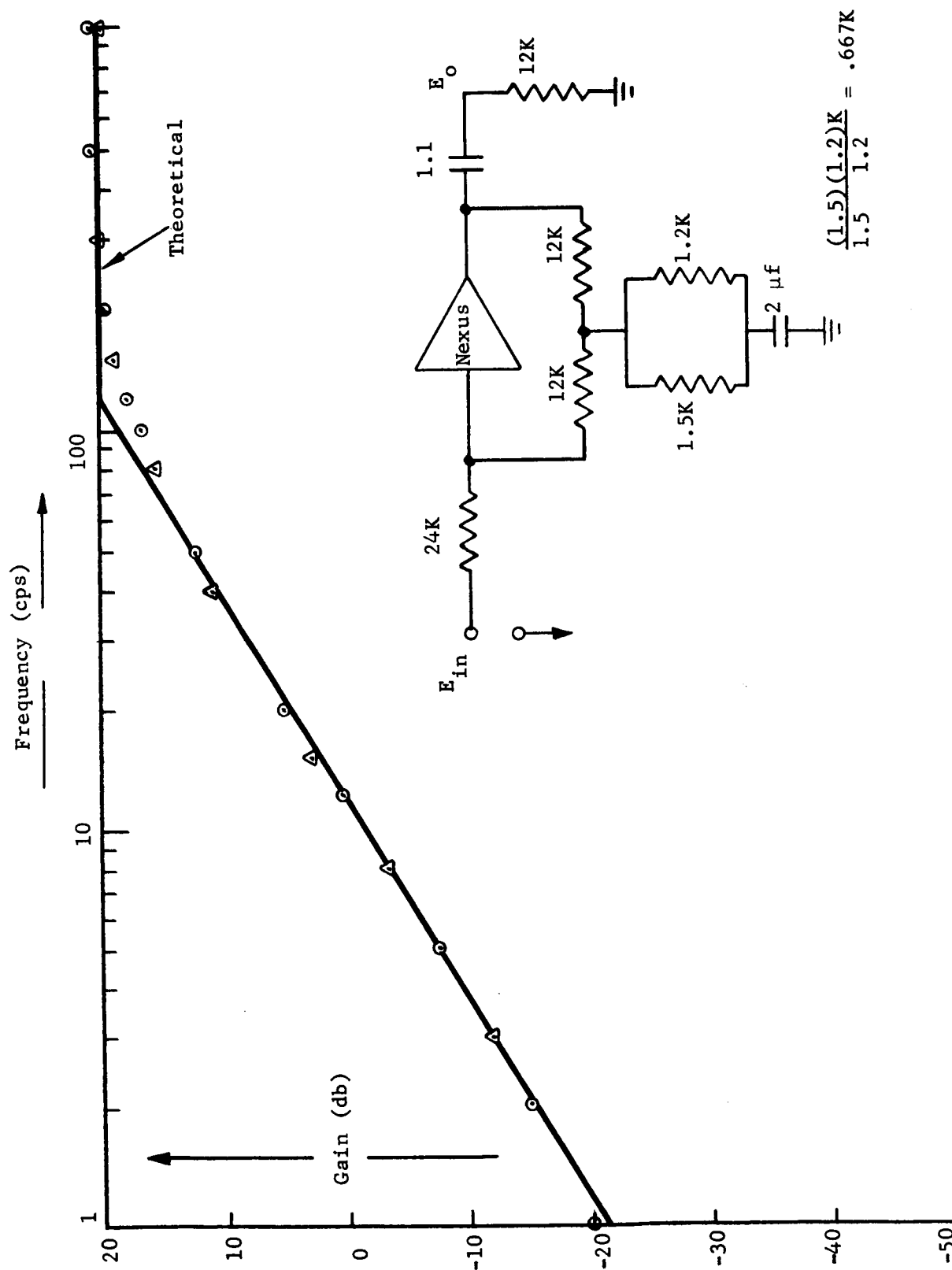
Figure 8-27.   Tachometer Amplifier Measured Transfer Function Compared with
                Theoretical Transfer Function

8.6.4 Minor Loop Transfer Characteristic

Both loops were spot checked to determine whether the minor closed loop responses were in agreement with the design value. It was anticipated, since the position pickoff scale factors were measured as 30V/cm rather than 20V/cm, that the servo input resistors (R_{in} = 240K ohms) would have to be reduced to about 160K ohms to compensate. The units were placed in a hold mode, with positional dither electrically induced, and the required input resistors were experimentally determined to be 150K ohms, a value in good agreement with theory. Figure 8-28 indicates the nature of the measurement approach.

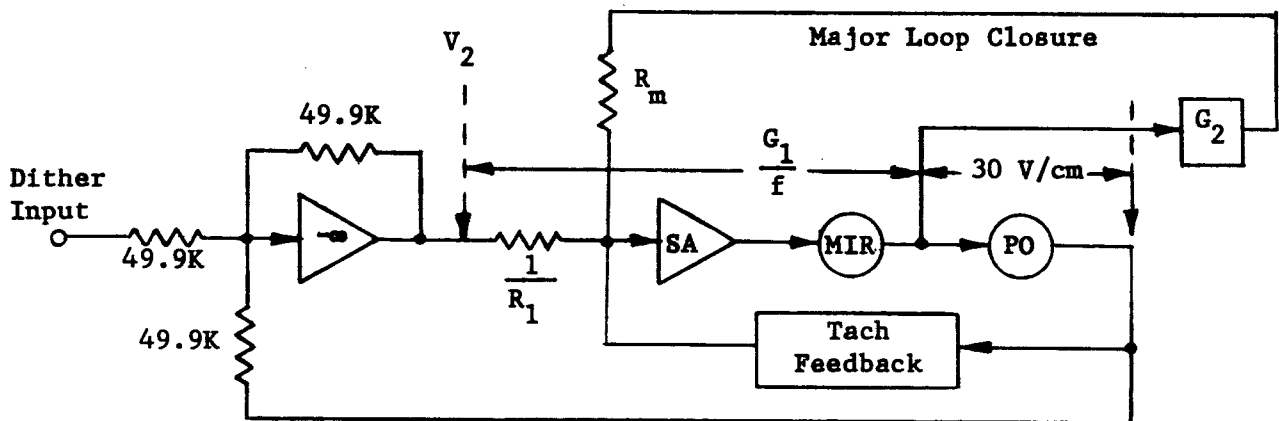Figure 8-28. Minor Loop Test

The response to an input applied to R_{in} with R_i removed should be such that the major loop gain is unity at 20 cps. Since the value of G_2 for the major loop is 662, then

$$\frac{1}{R_1} \times \frac{G_1}{f} \times 30 = 2.9 = \frac{V_1}{V_2} \; ; \text{ measured at 1 cps}$$

and

$$\frac{1}{R_{in}} \times \frac{G_1}{(f=20)} \times (G_2=662) = 1; \text{ at 20 cps}$$

Hence the required R_{in} can be shown to be 150K ohms. The results were essentially identical for both axes as shown by inspection of Table 8-3.

8.6.5   Major Loop Response

The error response of each transfer lens servo axis was measured at five frequencies. The data are shown in Table 8-4 and are also compared with theoretical response curves in Paragraph 8.3.3.

TABLE 8-3				
MINOR LOOP RESPONSE DATA				
Axis	V_2* (Volts P-P)	V_1* (Volts P-P)	f cps	G_1/f
X	2	5.8	1	2.9
X	5	3.2	5	0.64
X	5.5	0.7	25	0.127
Y	2	5.6	1	2.8
* Reading accuracy estimated as ±5%.				

TABLE 8-4									
MAJOR LOOP RESPONSE DATA									
Frequency (cps)	4		8		16		32		64	
Axis	X	Y	X	Y	X	Y	X	Y	X	Y
Input P-P (volts)	6.6	6.6	3.5	3.5	3.5	3.5	1.35	1.35	2.7	2.7
Output P-P (volts)	0.8	0.76	1.1	1.1	2.3	2.5	1.7	1.2	2.3	2.3
Error Response (db)	-18.3	-18.8	-10.0	-10.1	-3.5	-3.0	+2.0	-1.0	-1.4	-1.4

NOTES:

1) Input applied in series with error demodulator output.

2) Output is the total of applied input and error demodulator output signals.

3) The average noise level was 0.5 and 0.6 V P-P for the X and Y axes, respectively.

4) The preamplifier output voltages were adjusted to yield an output voltage of 5 V P-P for condition of maximum light to the associated PTM. . The high voltage was 1640 VDC for tubes 1, 2, and 3, and 1176 VDC for tube 4. The total DC current observed was 25 μa.

8.7   TEST AND CONTROL ELECTRONICS

8.7.1   Functions

A hold-mode and electronics control unit (HMECU) illustrated in Figure 8-29 was developed for use in conjunction with the transfer lens servo subsystem.

The HMECU has the following functions:

(a)   A two-axis hold-mode servo provides a stable central lens position for acquisition, or allows precise location of the lens for alignment and test purposes. The lens position is controlled in both X and Y axes by 10-turn calibrated potentiometers on the panel. A two-position panel switch selects hold-mode or tracking operation. The hold-mode function is provided by disconnecting the error demodulator and substituting the position pickoff output for each axis. The circuit utilizes a unity-gain summing amplifier to provide a phase reversal and allow extra inputs.

(b)   Two panel meters monitor the demodulated outputs of the capacitive position pickoffs. They are calibrated in arc-seconds of equivalent pointing error of the primary optics. The meters operate independently of any control functions.

Figure 8-29. Hold-Mode and Electronics Control Unit, Front Panel

(c) A selector switch and a pair of binding posts are located on the panel to provide a means of injecting disturbance signals or offsets into either axis of the hold-mode or tracking servos. These inputs may be used to facilitate dynamic response measurements of the servos, or to aid in evaluating the optical performance of the system.

(d) Two test point selector switches and pairs of binding posts allow simultaneous measurements of two voltages in either or both axes of the servos. Scale factors at the test points are determined with precision resistors and unity gain amplifiers so that gain can be measured directly without awkward coefficients. The switches also provide measurement of the plus and minus DC power supply inputs.

(e) Four color-coded wires carry the system DC power from two external 12 volt regulated power supplies to the HMECU. [Color coding: Positive supply: Red (plus), Black (minus). Negative supply: Black (plus), Violet (minus).] The incoming power is controlled by a double-pole switch on the panel.

(f) Six large capacitors associated with the servo electronics are remotely located in the HMECU because of lack of room on the transfer lens assembly.

Figure 8-30 illustrates the internal components of the HMECU. The circuit of the HMECU is given in Figure 8-31. A simplified block diagram, from which the various functions of the HMECU are self-evident, is given in Figure 8-32.
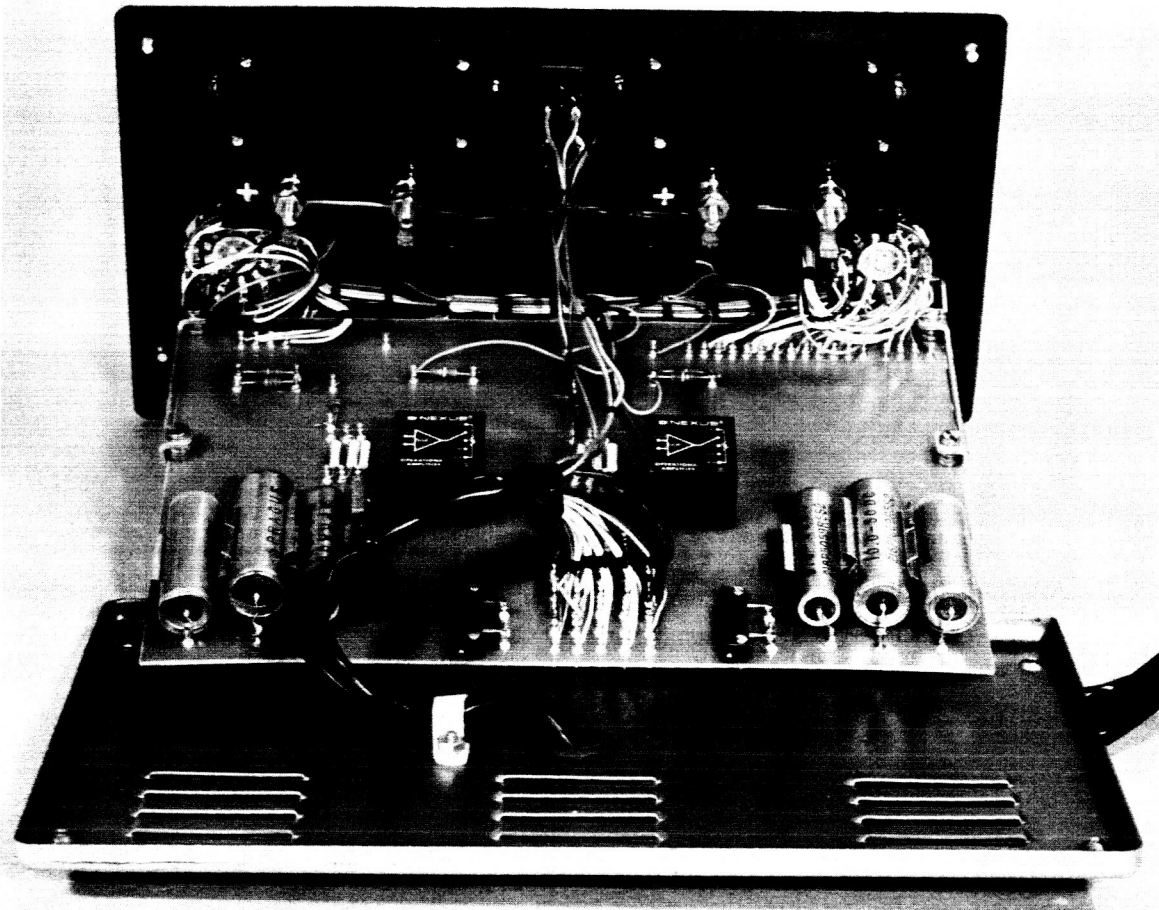
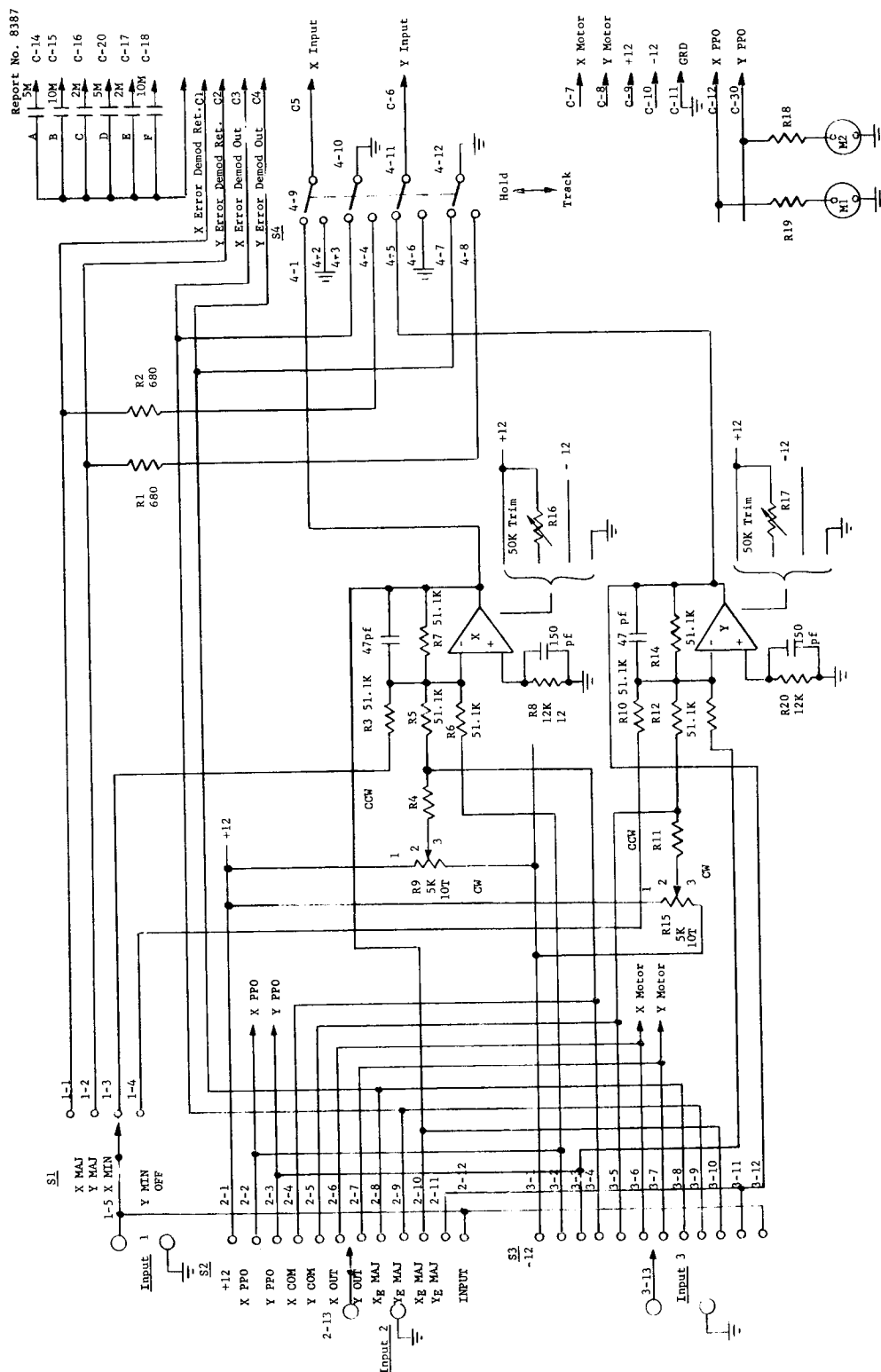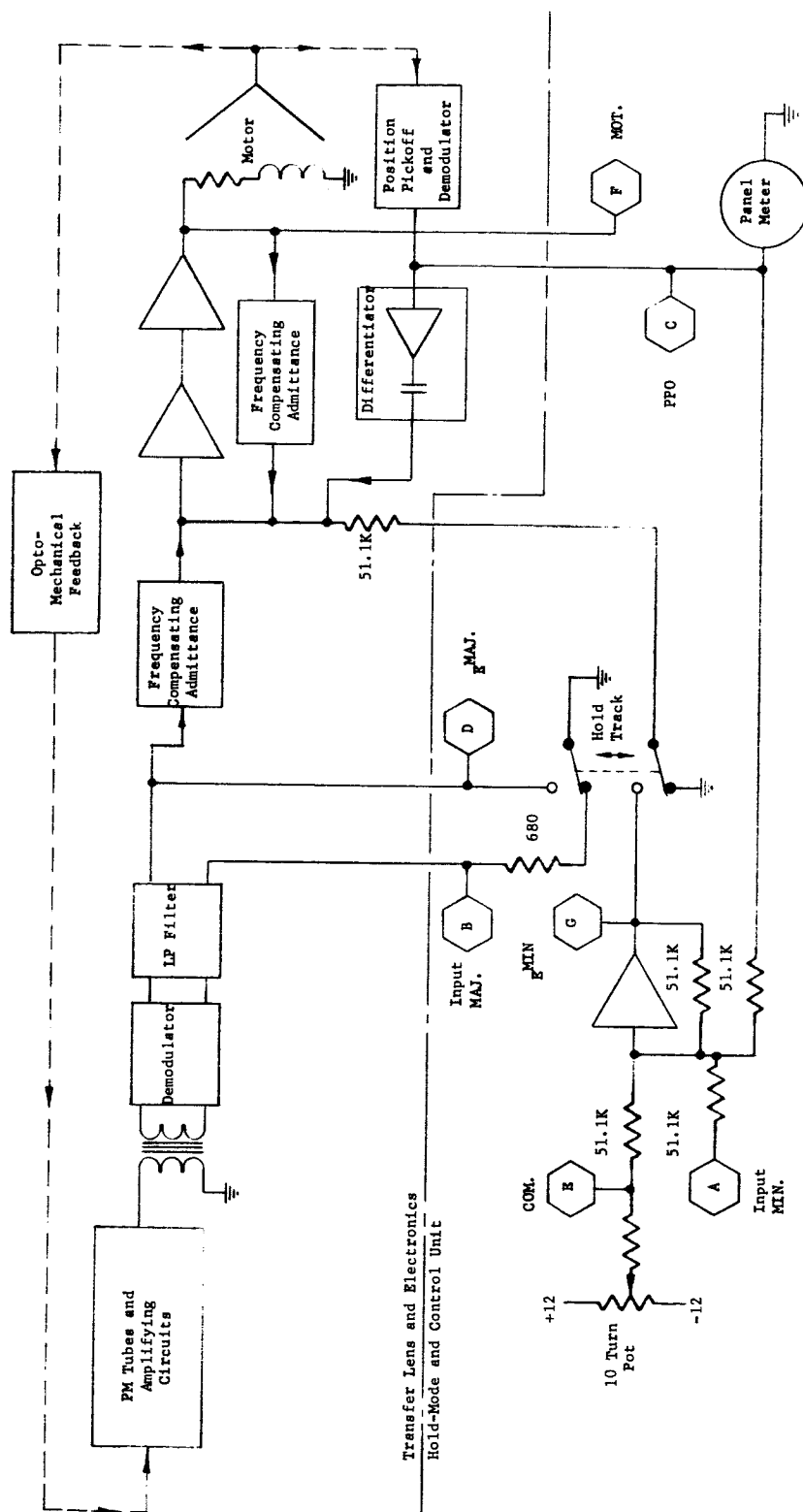Figure 8-30. Hold-Mode and Electronics Control Unit, Rear View
with Case Removed

Figure 8-31. Hóld-Mode and Electronics Control Unit, Schematic Diagram

Figure 8-32. Hold-Mode and Electronics Control Unit, Simplified Block Diagram Showing Test Point and Hold-Mode Connection

8.7.2   <u>Measurements and Tests</u>

The following are examples of typical measurements that can be made using the HMECU. The block diagram, Figure 8-32, is referenced.

(a)   The overall closed loop transfer function in the tracking mode can be measured by inserting a signal into "B" (via the input binding post and with the input selector in the X MAJ or Y MAJ position), and measuring the output voltage differentially between "B" and "D" (with the TPI selector in the X_E MAJ or Y_E MAJ position). The scaling is unity gain. This test is most useful near or above the unity loop-gain frequency.

(b)   The tracking loop error function can be measured by inserting a signal into "B" and measuring the output at "D". This is the simplest test and the most pertinent to system performance.

(c)   The open loop transfer function of the tracking servo can be measured by inserting a signal into "B", defining and measuring the input at "D" and measuring the output differentially between "B" and "D".

(d)   The hold-mode closed loop transfer function can be measured by inserting a signal into the appropriate minor loop input "A" and measuring the output at "C". The output will appear inverted.

(e)   The hold-mode error function is measured by inserting a signal into input "A" and measuring the error at "G". The output is inverted.

(f) Acquisition behavior can be tested by monitoring one or both PPO outputs "C" on a strip chart recorder and switching from hold-mode to track mode. The position controls may be preset for any desired initial position. An initial velocity can be provided by injecting a triangular wave into one axis at point "A" via the input selector.

(g) The force-per-volt constant at the motor can be determined while in hold-mode by measuring the motor voltage at point "F" (TP1 or TP2, "MOT" or "MOT"), and applying a known force against the transfer lens.

(h) Friction in the transfer lens support can be measured in hold-mode by slowly moving the X and Y position potentiometers while observing the motor voltage at point "F". The force-per-volt constant, as determined above, can be used to convert the readings to units of force.

SECTION IX

CONCLUSIONS

It is commonly recognized that much of the potential advantage of an optical communications system stems from the high degree of beam direction- ality that can be attained with lasers. Unfortunately, it is also commonly thought that extremes of directionality are the same as near-impossibilities of pointing and tracking. To be sure, these are not simple problems, but experience is showing that the necessary tools are within the present state of the art of high-precision optics.

During the course of the Laser/Optics Techniques Program, it was shown that, when suitable design precautions are taken, helium-neon lasers can be made to be perfectly suited to the task of filling a wide-aperture diffraction- limited telescope for transmission from deep space.

It also was shown that the same telescope used for transmission can be used simultaneously for reception of light from a distant earth beacon without appreciable interference from the transmit channel. Special dielectric multilayer techniques were developed for this "optical duplex" function.

The common telescope approach minimizes the boresighting and alignment problems. It was shown that now focus, alignment, and beam offset requirements all can be managed by straightforward and basically simple techniques.

The technology of transfer lens servo drives was advanced by development of a special laser tracking and pointing subsystem for the project breadboard. Techniques were employed which lend themselves to future space qualification.

The current program is clearly demonstrating in the laboratory that lasers and high-quality electro-optics are available for use in deep space communications. Breadboards of working subsystems have taken shape and experiments at signal levels suitable for deep space optical communications have been conducted with the hardware.